



**UNIVERSITÀ DEGLI STUDI DI PALERMO**

**Dottorato in Ingegneria Civile, Ambientale, dei Materiali**

**Ingegneria Strutturale e Geotecnica**

**Dipartimento di Ingegneria**

**S.S.D. ICAR/08 – ING-IND/26**

**NOVEL TOOLS FOR THE MECHANICAL  
ANALYSIS OF THIN PLATES  
AND RELEVANCE ON MEMBRANE-BASED  
TECHNOLOGIES**

**IL DOTTORE**

**Ing. Giuseppe Battaglia**

**IL COORDINATORE**

**Ch.mo Prof. Antonina Pirrotta**

**IL TUTOR**

**Ch.mo Prof. Antonina Pirrotta**

**IL CO TUTOR**

**Ch.mo Prof. Giorgio Micale**

**CICLO XXXII**

**ANNO CONSEGUIMENTO TITOLO 2020**



*To my grandmother and my grandfather*

They taught me the true meaning of love

## Table of Contents

INTRODUCTION ..... XI

### CHAPTER I

#### ANALYSIS OF THIN PLATES AND MEMBRANES

<b>1.1)</b>	<b>Introduction.....</b>	<b>1</b>
<b>1.2)</b>	<b>Constitutive equations for anisotropic and isotropic materials .....</b>	<b>2</b>
1.2.1)	Stresses .....	3
1.2.2)	Strains and displacements of a body .....	4
1.2.3)	Anisotropic, orthotropic and isotropic materials .....	7
<b>1.3)</b>	<b>Thin Plate and Membrane analysis .....</b>	<b>12</b>
1.3.1)	Kirchhoff's plate bending theory .....	13
	<i>1.3.1.1) Strain expressions .....</i>	<i>14</i>
	<i>1.3.1.2) Stress-strain relation for the case of small deformations .....</i>	<i>16</i>
	<i>1.3.1.3) The governing equation for the deflection of plates in Cartesian coordinates .....</i>	<i>18</i>
	<i>1.3.1.4) The strain energy of plates .....</i>	<i>21</i>
	<i>1.3.1.5) Transverse vibrations of thin plates .....</i>	<i>23</i>
1.3.2)	Membranes ( $a/h > 50$ ).....	24
	<i>1.3.2.1) The strain energy of membranes .....</i>	<i>26</i>
1.3.3)	Boundary conditions .....	28



<b>1.4) Numerical methods.....</b>	<b>30</b>
1.4.1) Methods based on Fourier series .....	31
1.4.1.1) Navier methods (double series solution) .....	31
1.4.1.2) Levy method (single series solution).....	32
1.4.2) Variational methods .....	33
1.4.2.1) The Rayleigh-Ritz Method .....	35
1.4.2.2) The Galerkin Method .....	36
1.4.3) Domain Discretization methods .....	37
1.4.3.1) The Finite Element Method (FEM).....	38
1.4.3.2) The Boundary Element Method (BEM) .....	38

## **CHAPTER II**

### **AN INNOVATIVE PROCEDURE FOR THE ANALYSIS OF THIN PLATES OF ARBITRARY SHAPES UNDER STATIC LOADS**

<b>2.1) Introduction .....</b>	<b>39</b>
<b>2.2) LEM for shear and torsion of beam .....</b>	<b>40</b>
<b>2.3) The analogy between the torsion beam problem and the plate bending problem.....</b>	<b>45</b>
<b>2.4) LEM for plates.....</b>	<b>46</b>
2.4.1) LEM for simply supported plates .....	46
2.4.2) LEM extension for the analysis of arbitrarily shaped plates with different boundary conditions.....	47

2.4.2.1) <i>Simply-supported polygonal plate</i> .....	51
2.4.2.2) <i>General plate analysis</i> .....	53
2.4.3) Numerical applications .....	61
2.4.3.1) <i>Exact solutions</i> .....	62
2.4.3.2) <i>Concentrated load</i> .....	67
2.4.3.3) <i>Mixed BCs</i> .....	70
2.4.3.4) <i>Arbitrarily shaped plate</i> .....	73

**CHAPTER III**

**AN INNOVATIVE PROCEDURE FOR THE ANALYSIS OF THIN  
PLATES OF ARBITRARY SHAPES UNDER DYNAMICS LOADS**

<b>3.1) Introduction</b> .....	<b>75</b>
<b>3.2) Pb-2 Rayleigh-Ritz method for general orthotropic plate analysis</b> .	<b>76</b>
<b>3.3) Extension of the Pb-2 Rayleigh-Ritz method to arbitrary shaped plates .....</b>	<b>81</b>
<b>3.4) Numerical applications .....</b>	<b>83</b>
3.4.1) Elliptical plate .....	84
3.4.2) Triangular plate .....	85

**CHAPTER IV**

**IDENTIFICATION OF THE MECHANICAL PROPERTIES OF  
ORTHOTROPIC PLATES AND MEMBRANES**

<b>4.1) Introduction .....</b>	<b>87</b>
<b>4.2) Mechanical properties identification of orthotropic plates .....</b>	<b>88</b>
4.2.1) Literature comparison.....	91
4.2.1.1) <i>Elliptical plate</i> .....	91
4.2.1.2) <i>Triangular plate</i> .....	93
4.2.2) Vibration based frequency identification of stiffened plates.....	94
4.2.2.1) <i>Experimental campaigns</i> .....	94
4.2.2.2) <i>Mechanical properties identification of 3D printed plates</i> .....	99
<b>4.3) Mechanical properties identification of orthotropic membranes. 105</b>	
4.3.1) The energy minimization principle for orthotropic membranes	107
4.3.2) Mechanical properties identification .....	108
4.3.2.1) <i>Membrane properties from virtual bulge tests</i> .....	109

**CHAPTER V**

**ANALYSIS OF THE MECHANICAL BEHAVIOUR OF ION EXCHANGE  
MEMBRANES IN MEMBRANE BASED TECHNOLOGIES**

<b>5.1) Introduction .....</b>	<b>114</b>
5.1.1) Electrodialysis and Reverse Electrodialysis processes .....	114
5.1.2) Trans-membrane pressure in membrane-based processes.....	116

5.1.3)	Trans-membrane pressure in ED and RED cases .....	118
<b>5.2)</b>	<b>Experimental characterization of Ion Exchange Membranes .....</b>	<b>120</b>
5.2.1)	Uniaxial tensile tests .....	122
5.2.1.1)	<i>Uniaxial tensile tests of samples conditioned in different solutions .....</i>	<i>124</i>
5.2.1.2)	<i>Uniaxial tensile tests of samples conditioned at different conditioning time .....</i>	<i>125</i>
5.2.2)	Loading and un-loading tests .....	127
<b>5.3)</b>	<b>Finite element model of profiled AEMs and CEMs.....</b>	<b>128</b>
5.3.1)	Boundary Conditions and computational grids .....	131
5.3.2)	Model validation .....	133
5.3.2.1)	<i>Bulge tests of an anion exchange membrane.....</i>	<i>133</i>
5.3.2.2)	<i>Comparison between experimental and FE bulge test results</i>	<i>135</i>
5.3.2.3)	<i>Comparison between FE predictions and analytical solution</i>	<i>136</i>
5.3.3)	Results .....	137
5.3.3.1)	<i>Influence of Pitch to Height Ratio (P/H) and limiting values.</i>	<i>137</i>
5.3.3.2)	<i>Membrane and Channel Deformation for the Selected Geometries .....</i>	<i>139</i>

**CHAPTER VI**

**INVESTIGATION ON FLUID DYNAMICS AND MASS TRANSFER IN  
DEFORMED CHANNELS**

<b>6.1) Introduction .....</b>	<b>142</b>
<b>6.2) Governing Equations and Definitions .....</b>	<b>143</b>
<b>6.3) Boundary Conditions and FV Mesh for CFD Simulations .....</b>	<b>147</b>
6.3.1) FV Mesh for OCF .....	148
6.3.2) FV Mesh for RP .....	149
<b>6.4) Results .....</b>	<b>150</b>
6.4.1) OCF profiled membrane type of $P/H = 8$ .....	150
6.4.1.1) <i>Undeformed Configuration</i> .....	150
6.4.1.2) <i>Deformed Configurations</i> .....	152
6.4.1.3) <i>Global Parameters</i> .....	155
6.4.2) RP pillar type of $P/H = 10$ .....	158
6.4.2.1) <i>Undeformed Configuration</i> .....	159
6.4.2.2) <i>Deformed Configurations</i> .....	160
6.4.2.3) <i>Global quantities</i> .....	162
6.4.3) Comparison between OCF and RP profiled membranes .....	164

**CHAPTER VII**

**FLOW REDISTRIBUTION IN ED AND RED CHANNELS IN THE  
PRESENCE OF LOCAL MEMBRANE DEFORMATIONS**

<b>7.1) Introduction.....</b>	<b>166</b>
<b>7.2) From a small- to a large-scale description of membrane-bounded channels.....</b>	<b>167</b>
<b>7.3) Computational domain and modelling assumptions.....</b>	<b>169</b>
<b>7.4) Discretized governing equations .....</b>	<b>172</b>
7.4.1) Discretized continuity equation .....	172
7.4.2) Discretized Darcy equation for the case of low velocity.....	172
7.4.3) Model adjustment for non-Darcyan flow regime .....	175
<b>7.5) Flow arrangement and boundary conditions .....</b>	<b>179</b>
<b>7.6) Results .....</b>	<b>182</b>
7.6.1) Cross Flow arrangement .....	182
7.6.1.1) Low velocity case ( $U_s \approx 1$ cm/s) .....	182
7.6.1.2) Higher velocity case ( $U_s = 10$ cm/s) .....	186
7.6.1.3) Pressure profiles for all cross flow cases .....	190
7.6.2) Counter Flow arrangement.....	191

**CHAPTER VIII**

**IMPACT OF MEMBRANE DEFORMATION ON THE  
PERFORMANCES OF CROSS-FLOW ELECTRODIALYSIS UNITS  
FOR WATER DESALINATION**

<b>8.1) Introduction .....</b>	<b>195</b>
<b>8.2) 2-D process simulator of ED units: model and methods .....</b>	<b>196</b>
8.2.1) Mass balances and fluxes .....	197
8.2.2) Electric variables, ohmic and non-ohmic resistances .....	200
8.2.3) Stack simulation .....	204
<b>8.3) Algorithm of solution.....</b>	<b>206</b>
<b>8.4) Grid dependence analysis and model validation for the parallel flow     configuration.....</b>	<b>210</b>
<b>8.5) Grid dependence analysis for the Cross Flow configuration.....</b>	<b>214</b>
<b>8.6) Results .....</b>	<b>216</b>
8.6.1) No membrane deformation.....	216
8.6.2) Effects of membrane deformation .....	218
8.6.2.1) <i>Mild deformation effects</i> .....	218
8.6.2.2) <i>Heavy deformation effects</i> .....	220
<b>CONCLUSIONS .....</b>	<b>223</b>

<b>Appendix A: Expression of the Boundary Conditions in terms of Harmonic Polynomials .....</b>	<b>228</b>
<b>Appendix B: Dependence of equivalent channel height and channel hydraulic permeability on TMP .....</b>	<b>232</b>
B1) Equivalent channel height .....	232
B2) Channel permeability for non-Darcyan flow .....	233
<b>Appendix C: Grid dependence and validation against CFD results .....</b>	<b>234</b>
C1) Grid dependence .....	234
C2) Comparison with CFD results .....	235
<b>Appendix D: Correlations used for the physical and transport properties of NaCl solutions. ....</b>	<b>238</b>
<b>NOMENCLATURE.....</b>	<b>239</b>
<b>BIBLIOGRAPHY.....</b>	<b>245</b>
<b>LIST OF ISI PUBLICATIONS AND INTERNATIONAL CONFERENCES PAPERS AND ABSTRACTS .....</b>	<b>267</b>
<b>ACKNOWLEDGEMENTS.....</b>	<b>270</b>



## **INTRODUCTION**

The increasing energy demand and the decline in availability of drinking water are two of the major challenges that humanity has to face in the coming decades. Many technologies have been explored, which can produce electricity from renewable resources and drinking water from non-conventional sources.

In this scenario, Electrodialysis (ED) and Reverse Electrodialysis (RED) processes have drawn much attention. In particular, RED and ED are two promising membrane-based technologies for electricity production and for saline water desalination, respectively.

The key components of ED/RED units are the Ion Exchange Membranes (IEMs), which contain fixed charges in their polymeric matrix, that allow for selective transport of ions through them. In ED and RED units, Anion and Cation Exchange Membranes (AEMs and CEMs) are alternately stacked and separated by means of net-spacers or built-in profiles, which create the channels where solutions flow. An assembly of an AEM and a CEM combined with two fluid channels, adjacent to them, forms the repetitive unit of an ED/RED stack, which is referred to as a “cell pair”.

So far, the performance of ED and RED stacks have been extensively studied by both modelling tools and experimental campaigns. However, membrane deformation phenomena and their effects on process performance have been neglected. On the other hand, several studies have highlighted the significant detrimental effects of membrane deformation on the performance of many other membrane-based processes, such as forward osmosis, pressure assisted osmosis, pressure retarded osmosis, reverse osmosis and proton exchange membranes fuel cells. In ED/RED units, a different pressure distribution between the two channels may occur, giving rise to a transmembrane pressure (TMP) distribution. The TMP can induce deformations of the membrane/channels assembly, which, in turn, may work under very different conditions (e.g. flow, mass transfer and electrical resistance) compared to the nominal (undeformed) ones. As a result, the performance of ED/RED units can be affected.

In this context, the aim of this PhD thesis is to assess, for the first time, the effects of membrane deformation in ED and RED systems induced by a transmembrane pressure difference (TMP) related to an uneven pressure distribution in the fluid channels, which may occur in industrial applications.

To achieve this objective, it has been essential to combine knowledge from solid mechanics, fluid dynamics and electrochemistry fields.

Firstly, the mechanical behaviour of plates has been thoroughly analysed and novel tools for their study have been proposed. In fact, the term “plate” encompasses many structural elements, such as thin plates and membranes. In particular, membranes have been studied as thin plates with large deflections.

Thin plates are commonly studied by means of Finite Element Methods or Boundary Layer Methods, which require a discretization of the domain or the boundary of the element, respectively. However, the possibility of investigating plates without any discretization has recently gained much attention to overcome the problem related to meshing and remeshing of the above-mentioned methods.

In this PhD thesis, innovative procedures have been proposed for the analysis of both thin plates and membranes, which do not require any discretization neither in the boundaries or the domain. In particular, a novel procedure has been introduced for the analysis of isotropic thin plates of an arbitrary shape and boundary conditions with small deflections. The procedure employs harmonic polynomials to express the plate deflection and computes only line integrals.

An optimization procedure has been also developed for the identification of the mechanical parameters of orthotropic arbitrarily shaped plates based on vibration data. In particular, the proposed procedure combines the so-called pb-2 Rayleigh-Ritz method, specifically extended for the analysis of orthotropic plates, with a Particle Swarm Optimization (PSO) algorithm. The pb-2 Rayleigh-Ritz method has also been applied for the study of arbitrarily shaped plates by taking advantage of Green lemma to convert double integrals into simpler line integrals. To assess the procedure’s accuracy, an extensive experimental campaign has been conducted at the Laboratory of Experimental Dynamics at the University of Palermo to identify the modal parameters of structurally orthotropic plates made by a 3D printer.

Then, the behaviour of thin plates with large deflections (membranes) has been considered. In particular, an optimization procedure has been introduced for the identification of the mechanical properties of orthotropic membranes based on static bulge test measurements. Specifically, a genetic optimization algorithm has been coupled with the principle of minimum energy applied to the analysis of rectangular orthotropic membranes.

Based on the aforementioned studies, the behaviour of Ion Exchange Membranes for ED and RED applications has been analysed. The deformation of two adjacent profiled membranes has been investigated by conducting finite-element three-dimensional structural mechanics simulations at the small scale of a “periodic portion” of the membranes for different values of applied TMP, using the Finite Element Ansys Mechanical® software. Afterwards, the fluid dynamics and mass transport characteristics have been assessed in undeformed, compressed and expanded fluid channel configurations, found from the previous mechanical simulations, by finite-volume three-dimensional Computational Fluid Dynamics (CFD) simulations employing the commercial Ansys-CFX® software.

Then, a two-dimensional numerical model, based on an original iterative algorithm, has been developed in order to simulate, at the higher scale of a cell pair, the fluid-structure interaction and the associated flow redistribution phenomena in channels where distributed membrane deformations occur. This model employs correlations on the hydraulic friction factor coming from the results obtained with the small scale models.

Finally, a two-dimensional multi-scale process model has been developed to simulate ED units for water desalination. Transport and electrochemical phenomena have been simulated, computing the distribution of the main variables, thus predicting the process’ performance. Deformation and its effects have been included by using the results of the previous numerical simulations (structural mechanics and CFD) and of the fluid-structure interaction model as input data.

The thesis consists of eight chapters:

Chapter I presents a brief survey of the theory of elasticity and theories for the analysis of thin plates and membranes, e.g. Kirchhoff’s plate bending theory

and Von Karman equations. Moreover, the most common methods for the solution of problems concerning thin plates and membranes are discussed.

Chapter II describes the innovative procedure developed for the analysis of isotropic thin plates of arbitrary shapes and boundary conditions.

In Chapter III, the pb-2 Rayleigh-Ritz method is presented and extended for the analysis of orthotropic arbitrarily shaped plates.

Chapter IV presents the two optimization procedures developed for the identification of the mechanical properties of orthotropic plates and membranes. First, the results of the experimental campaign conducted on the 3D printed plates are presented. Then, the proposed approach is applied for the mechanical identification of plates based on vibration data from both literature, and the experimental campaign. In the second part of the chapter, the mechanical characterization of orthotropic membranes based on bulge test data is presented.

Chapter V presents, first, uniaxial tensile tests of Ion Exchange Membranes, conducted at the Tilburg Research Laboratory of the FUJIFILM Manufacturing Europe B.V. in the Netherlands. Then, it reports the finite element model developed for the analysis of membrane deformations at the small scale and its results for two different geometries of profiled membranes. Model validation is also reported.

In Chapter VI, the analysis of flow and mass transport properties in undeformed and deformed channels predicted by CFD simulations at the small scale is reported.

Chapter VII presents the fluid-structure model for the higher scale (cell pair) simulation aimed at predicting flow and deformation distributions in ED channels. Results on cross flow and counter flow arrangements are reported and discussed.

Finally, Chapter VIII describes a comprehensive ED process model adopted for a sensitivity analysis of the operation of cross-flow units for water desalination. The process performance is evaluated under different geometrical and operating conditions and the effects of membrane deformations are discussed.





## CHAPTER I

### ANALYSIS OF THIN PLATES AND MEMBRANES

#### 1.1) Introduction

Plates are widely employed in many engineering fields, including civil, mechanical and chemical engineering [1-3]. The term plate encompasses a vast variety of structural components such as thick plates, thin plates and membranes. Plates are initially flat, plane, two-dimensional members, which are geometrically bound by two parallel planes, faces, and a cylindrical surface, edge or boundaries. The distance between the faces is called the thickness,  $h$ , whose dimension is typically much smaller than the others (e.g. length and width). These structural elements are typically subjected to the action of lateral loads and their load-carrying action has been associated with that of grid-works of an infinite number of beams or cables. This two-dimensional action makes plates lighter and stiffer compared to beams of the same thickness and span. Consequently, plates are largely used in weight-sensitive structures, such as foundation slabs, lock-gates, bridge decks, aircraft's wings and fuselage, and ships' hulls, as shown in Figure 1. 1.

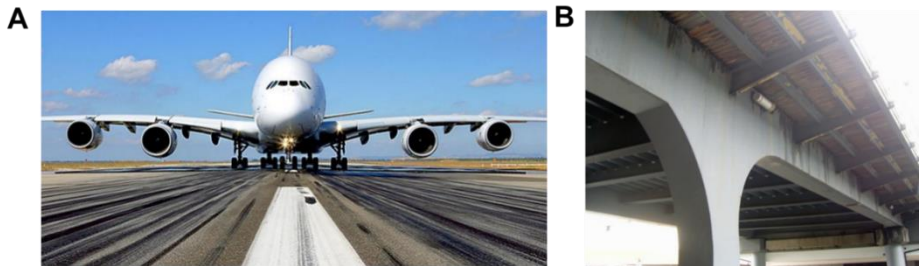


Figure 1. 1 Examples of plate applications: a) aircraft components; b) bridge decks.

As far as the plate analysis is concerned, the ratio  $a/h$  between the plate thickness and the typical plate dimension (e.g. the length size  $a$ ) subdivides plates into four categories [4]:

- i) Membranes ( $a/h > 50$ ); they are very thin plates devoid of flexural rigidity. Membrane carrying-action is predominantly associated with axial shear forces acting in the membrane surface. These forces are often defined as membrane forces. Specifically, the component of the membrane forces along the direction normal to the surface balances the applied lateral loads.
- ii) Stiff plates ( $10 < a/h < 50$ ); these are thin plates, which withstand loading by bending and torsional moments, and transverse shears. In this case, membrane forces are often neglected. It is worth noting that, the term thin plate is usually associated with the meaning of stiff plate.
- iii) Moderately thick plates ( $5 < a/h < 10$ ); they are thicker than stiff plates. In this case, the effects from shear forces are taken into account in the description of stress components.
- iv) Thick plate ( $a/h > 5$ ); they are mathematically studied as three-dimensional bodies by considering internal stress conditions.

The plate categories give, in an engineering sense, an indication about plate's behaviour. Naturally, it is worth noting that, intermediate conditions may exist.

In this Chapter, the theories developed to deal with the behavior of plates and membranes are presented. To introduce these theories, the concepts of stresses, strains and displacements of a body are discussed and constitutive equations for anisotropic, orthotropic and isotropic plates are reported. Finally, the most common methods for solving plate and membrane problems are described.

## **1.2) Constitutive equations for anisotropic and isotropic materials**

The theories of plates and membranes are framed in the theory of elasticity, which studies the relationships of forces, displacements, stresses and strains in an



elastic body. A solid body subjected to the action of an external force deforms, producing internal strains and stresses. Many relationships have been developed to correlate stresses and strains generated in a body. In the following sections, attention is focused on *linear elastic materials*, i.e. materials in which the relationship between stress and strains is linear, which are ruled by the Hooke law, and no residual deformations and stresses remain in the body after removing external forces.

### 1.2.1) Stresses

Consider an arbitrarily shaped body subjected to external loads, which are in equilibrium. If a Cartesian coordinate system  $x, y, z$  is employed, an infinitesimal parallelepiped of edges  $dx, dy, dz$  can be taken at a point anywhere in the interior of the body, as shown in Figure 1. 2. The stresses acting on the faces of this parallelepiped describe the magnitude of the internal forces. A stress vector of three components can be defined at each face of the element. The normal component of the stress vector to the element face is referred to as the normal stress  $\sigma_{ii}$ . The tangential components of the stress vector to the element face are defined as shear stresses  $\tau_{ij}$ . Please note that, the first subscripts of the stress vector refer to the outer normal of the face on which stress vector acts; while the second subscripts refer to the direction of the stress itself. The subscripts  $i, j$  vary from 1 to 3, which refer to the coordinates  $x, y, z$ .

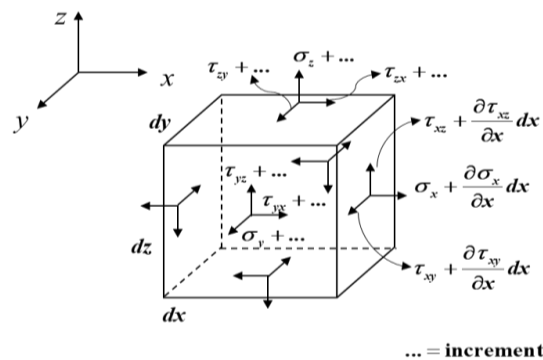


**Figure 1. 2** Stresses acting on an infinitesimal part of a body at anywhere in an interior of a body [4].

As convention, normal and shear stresses are considered positive if the direction of the outer normal and that of the specific stress are in the same direction, vice-versa they are negative [4]. Positive normal stresses are denominated *tensile stresses* and cause an extension of the body. Conversely, negative normal stresses are defined as *compressive stresses* and cause a compression of the body. On this basis, stresses of Figure 1. 2 are positive and the stress tensor  $T_s$  can be defined as:

$$T_s = \begin{pmatrix} \sigma_x & \tau_{xy} & \tau_{xz} \\ \tau_{yx} & \sigma_y & \tau_{yz} \\ \tau_{zx} & \tau_{zy} & \sigma_z \end{pmatrix} \quad (1.1)$$

Please note that repeated subscripts have been omitted, i.e. the normal stresses have only one subscript indicating the stress direction. The stress tensor is symmetric with respect to the principal diagonal because of the *reciprocity law of shear stresses*, i.e.  $\tau_{xy} = \tau_{yx}$ ,  $\tau_{xz} = \tau_{zx}$  and  $\tau_{yz} = \tau_{zy}$  ).

### 1.2.2) Strains and displacements of a body

Let A and B be two points of the infinitesimal body of Figure 1. 2 before the application of any external forces. A system of coordinates  $x_1, x_2, x_3$  can be chosen so that the position of a point A of a body will have coordinates  $x_i$  ( $i=1, 2, 3$ ) and the position of a point B will have coordinates  $x_i + dx_i$ , as shown in Figure 1. 3.

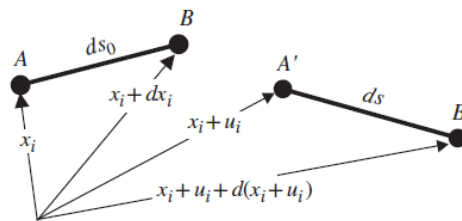


**Figure 1. 3** Strain measure of a segment [5].

After the action of an external load, the points A and B move to point A', B' of positions  $x_i + u_i$  and  $x_i + u_i + d(x_i + u_i)$ , respectively. The length of the segments AB ( $ds_0$ ) and A'B' ( $ds$ ) can be calculated as follows:

$$ds_0^2 = dx_1^2 + dx_2^2 + dx_3^2 \quad (1.2)$$

$$ds^2 = d(x_1 + u_1)^2 + d(x_2 + u_2)^2 + d(x_3 + u_3)^2 \quad (1.3)$$

where  $ds_0$  and  $ds$  are the undeformed and deformed segment length, respectively.

Considering:

$$du_i = \frac{\partial u_i}{\partial x_1} dx_1 + \frac{\partial u_i}{\partial x_2} dx_2 + \frac{\partial u_i}{\partial x_3} dx_3 \quad i = 1, 2, 3 \quad (1.4)$$

After same manipulations, one has:

$$ds^2 = dx_1^2 + dx_2^2 + dx_3^2 + \sum_{i=1}^3 \sum_{j=1}^3 \left( \frac{\partial u_i}{\partial x_j} + \frac{\partial u_j}{\partial x_i} + \sum_{k=1}^3 \frac{\partial u_k}{\partial x_j} \frac{\partial u_k}{\partial x_i} \right) dx_i dx_j \quad (1.5)$$

Defining the components of the Green's symmetric strain tensor, [5, 6], as:

$$\varepsilon_{ij} = \frac{1}{2} \left( \frac{\partial u_i}{\partial x_j} + \frac{\partial u_j}{\partial x_i} + \sum_{k=1}^3 \frac{\partial u_k}{\partial x_j} \frac{\partial u_k}{\partial x_i} \right) \quad (1.6)$$

the length increment of the segment AB can be written as follows

$$ds^2 - ds_0^2 = 2 \sum_{i=1}^3 \sum_{j=1}^3 \varepsilon_{ij} dx_i dx_j \quad (1.7)$$

The Green's symmetric strain tensor is a second-order tensor quadratic in the displacements  $u_i$ , and its elements have a physical meaning:

1.  $\frac{\partial u_i}{\partial x_i} \quad i = 1, 2, 3$  (1.8)

represents the linear strains of a body.

2.  $\frac{\partial u_i}{\partial x_j} \quad i \neq j$  (1.9)

accounts for the rotations of a body subjected to the action of an external force. It should be noted that under the assumptions of small rotations and

infinitesimal extensions, the terms  $\sum_{k=1}^3 \frac{\partial u_k}{\partial x_j} \frac{\partial u_k}{\partial x_i}$  in Eq. (1.6) vanish and the components of Green strain tensor becomes linear in the displacements  $u_i$  [5]

$$\varepsilon_{ij} = \frac{1}{2} \left( \frac{\partial u_i}{\partial x_j} + \frac{\partial u_j}{\partial x_i} \right) \quad (1.10)$$

Please note that, hereinafter, the displacements  $u_1, u_2, u_3$  of a point P ( $x, y, z$ ) are referred to as  $u, v, w$ , and the unabridged notation ( $x, y, z$  for  $x_1, x_2, x_3$  [6]) is used. Further, repeated subscripts will be omitted, thus the subscript will refer to the direction of the strain. The  $w$  component of the displacement of a point P is usually referred to as the deflection.

To better understand the quantities of Eqs. (1.8-1.9), Figures 1. 4 a-f show the six simplest deformations, which a body may encounter [4].

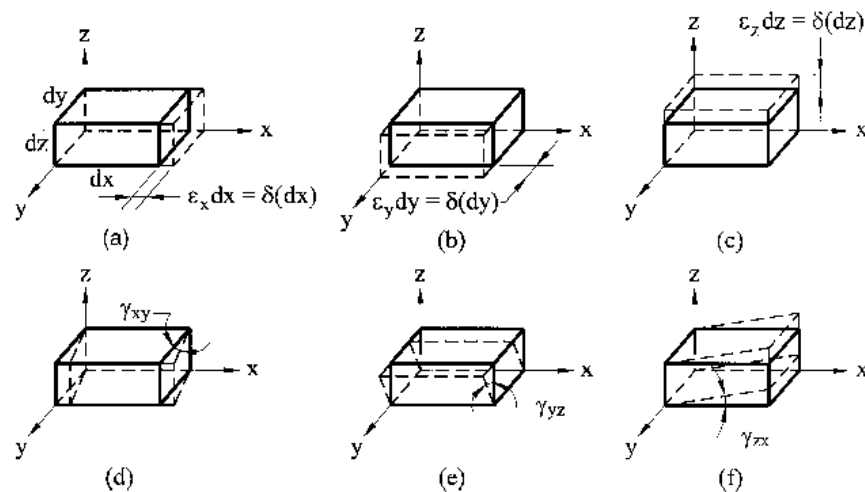


Figure 1. 4 Representation of: a-c) normal strains; d-f) shear strains [4].

Figures 1. 4 a-c, present the normal strain (*extension* or *contraction*) of a body along the three directions of a system using Cartesian coordinates:

$$\varepsilon_x = \frac{\partial u}{\partial x}, \quad \varepsilon_y = \frac{\partial v}{\partial y}, \quad \varepsilon_z = \frac{\partial w}{\partial z} \quad (1.11)$$

Moreover, Figures 1. 4 d-f show the so called shear deformation. Shear deformations cause a distortion of an initially right angle between edges of the parallelepiped. They are indicated as  $\gamma_{xy}, \gamma_{xz}, \gamma_{yz}$ , where subscripts indicate the coordinate planes in which the shear strains occur. Under the assumption of a small deformation, the shear strain can be expressed as:

$$\gamma_{xy} = \frac{\partial v}{\partial x} + \frac{\partial u}{\partial y}, \gamma_{xz} = \frac{\partial u}{\partial z} + \frac{\partial w}{\partial x}, \gamma_{yz} = \frac{\partial v}{\partial z} + \frac{\partial w}{\partial y} \quad (1.12)$$

As for stresses, in the case of a small deformation and a small rotation, the strain tensor  $T_D$  can be expressed as:

$$T_D = \begin{pmatrix} \varepsilon_x & \frac{1}{2}\gamma_{xy} & \frac{1}{2}\gamma_{xz} \\ \frac{1}{2}\gamma_{yx} & \varepsilon_y & \frac{1}{2}\gamma_{yz} \\ \frac{1}{2}\gamma_{zx} & \frac{1}{2}\gamma_{zy} & \varepsilon_z \end{pmatrix} \quad (1.13)$$

### 1.2.3) Anisotropic, orthotropic and isotropic materials

Most of the common engineering materials are both homogeneous and isotropic [7], i.e.:

- Homogeneous: the properties of the material are independent of the position in the body.
- Isotropic: the properties of the material are independent of the orientation at a point in the body.

It is worth noting that homogeneity does not imply isotropy. For instance, the density of a body could be a function of temperature, but the mechanical properties of the body can be still independent of the body's orientation.

However, in many cases, materials exhibit different properties with respect to body orientation. Specifically, materials can be classified as:

- Anisotropic, all the material properties change as a function of the body orientation;

- Orthotropic, material properties are different in three mutually perpendicular directions at a point in the body. These directions are defined as principal directions of orthotropy.
- Isotropic, the material properties do not change as the body orientation changes.

Anisotropic, orthotropic and isotropic materials have different behaviour under the application of forces. Figure 1. 5 presents the mechanical behaviour of anisotropic, orthotropic and isotropic materials subjected to the action of a tensile stress (first row) and shear stresses (second row) [7].

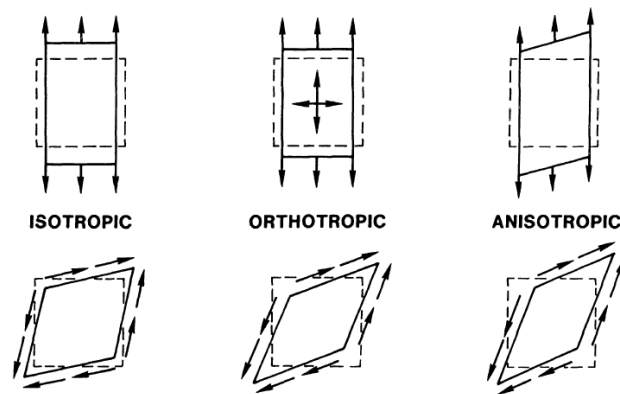


**Figure 1. 5** Mechanical behaviour of anisotropic, orthotropic and isotropic materials subjected to the action of a tensile stress (first row) and shear stresses (second row) [7].

Under pure normal stresses, see Figure 1. 5 (first row), isotropic materials stretch along the stress direction and contract in the perpendicular direction without any shearing deformation. Under shear stresses (Figure 1. 5 (second row)), the body presents only shear deformations without extension or contraction in any direction. This behaviour is detected for any material orientation. Therefore, only two mechanical parameters are required for the characterization of isotropic materials: the Young's modulus  $E$ , which relates material longitudinal elongations with the normal stress applied, and the Poisson's ratio  $\nu$ , which is the ratio between lateral contractions and longitudinal extensions measured during the application of the normal stress.

As far as orthotropic materials are concerned, if the normal stress acts along one of the principal directions of orthotropy of the material, no shearing deformations are detected (Figure 1. 5 (first row)). It is worth noting that the magnitude of extensions and contractions changes when the normal stress is applied along the different principal directions of the material. Therefore, Young's moduli and Poisson's ratios along the principal directions of orthotropy cannot be the same. Moreover, shear stresses (Figure 1. 5 (second row)), cause shearing deformations, whose magnitude could be independent of Young's moduli and Poisson's ratios of the material. Consequently, in a two-dimensional space, an orthotropic material requires at least five material properties, i.e. two Young's moduli, two Poisson's ratio and one shear modulus  $G$ . The shear modulus gives information about the response of the material when shear forces are applied. It is worth noting that, shearing deformations are also detected in orthotropic materials when normal stresses are not applied along the principal directions.

Finally, an anisotropic material subjected to normal stresses or shear stresses always show extensions, contractions and shearing deformations at all orientations of the body. Therefore, to characterize an anisotropic material many mechanical parameters are required.

In the case of linear-elastic materials, the relationship between stresses and strains of a body is described by Hooke's law:

$$\sigma_{ii} = C_{ij} \varepsilon_{ij} \quad i, j = 1, 2, 3 \quad (1.14)$$

where  $\sigma_{ii}$  are the stress components acting on a body,  $\varepsilon_{ij}$  are the strain components and  $C_{ij}$  is the stiffness matrix. Indexes  $i, j$  refer to the component  $x, y, z$  of a Cartesian system. Please note that, in the following equations, repeated subscripts will be omitted.

Hooke's law can also be written as a strain-stress relationship:

$$\varepsilon_{ij} = S_{ij} \sigma_{ii} \quad (1.15)$$

where  $S_{ij}$  is the compliance matrix.

For three-dimensional materials, the stiffness matrix  $C_{ij}$  and the compliance matrix  $S_{ij}$  have 36 constants, which reduce to 21 due to the symmetry of the stress and strain tensors [7]. Therefore, an anisotropic material needs 21 constants to be fully characterized. On the other hand, taking into account the above-mentioned material behaviour of isotropic and orthotropic materials, nine and two constants are needed for the characterization of orthotropic and isotropic materials, respectively.

Components of the compliance matrix are easier to be determined than those of the stiffness matrix. In fact, they can be derived simply by performing experimental tests. For the sake of brevity, only the compliance matrix for an orthotropic material, whose principal directions of orthotropy are assumed to be parallel to the  $x, y, z$  components, is reported as a function of the mechanical parameters [7]:

$$[S_{ij}] = \begin{bmatrix} 1/E_x & -\nu_{yx}/E_y & -\nu_{zx}/E_z & 0 & 0 & 0 \\ -\nu_{xy}/E_x & 1/E_y & -\nu_{zy}/E_z & 0 & 0 & 0 \\ -\nu_{xz}/E_x & -\nu_{yz}/E_y & 1/E_z & 0 & 0 & 0 \\ 0 & 0 & 0 & 1/G_{yz} & 0 & 0 \\ 0 & 0 & 0 & 0 & 1/G_{zx} & 0 \\ & & & & & 1/G_{xy} \end{bmatrix} \quad (1.16)$$

Where  $E_x, E_y, E_z$  are the three Young's moduli along the principal axes of orthotropy of the materials;  $\nu_{ij}$  are the Poisson's ratios defined as  $\nu_{ij} = -\frac{\epsilon_j}{\epsilon_i}$  with  $i, j = 1, 2, 3, i \neq j$ ; and  $G_{xy}, G_{yz}, G_{zx}$  are the shear moduli.

Further, since no shear-extension or normal-shear stress coupling occurs when orthotropic materials are stretched along a principal direction, a relationship between Poisson's ratios and Young's moduli can be defined [8]:

$$\frac{\nu_{ij}}{E_i} = \frac{\nu_{ji}}{E_j}, \quad i \neq j \text{ and } i, j = 1, 2, 3 \quad (1.17)$$



For an orthotropic plate, taking into account the compliance matrix Eq. (1.16), the strain-stress equations can be written as:

$$\varepsilon_x = \frac{\sigma_x}{E_x} - \nu_{yx} \frac{\sigma_y}{E_y}; \quad \varepsilon_y = \frac{\sigma_y}{E_y} - \nu_{xy} \frac{\sigma_x}{E_x}; \quad \gamma_{xy} = \frac{\tau_{xy}}{G_{xy}} \quad (1.18 \text{ a, b, c})$$

After some manipulations, the corresponding stress-strain equations can be obtained:

$$\begin{aligned} \sigma_x &= \frac{E_x}{1 - \nu_{yx}\nu_{xy}} (\varepsilon_x - \nu_{yx}\varepsilon_y); \\ \sigma_y &= \frac{E_y}{1 - \nu_{yx}\nu_{xy}} (\varepsilon_y - \nu_{xy}\varepsilon_x); \\ \tau_{xy} &= G_{xy}\gamma_{xy} \end{aligned} \quad (1.19 \text{ a, b, c})$$

For the sake of brevity, equations for  $\sigma_z$ ,  $\tau_{xz}$  and  $\tau_{yz}$  have been omitted, as their description is not necessary in this work.

As discussed above, the shear moduli of an orthotropic material do not depend on Young's moduli or Poisson's ratios, however, an estimation of the shear values are often calculated as follows [4]:

$$G_{xy} \approx \frac{\sqrt{E_x E_y}}{2(1 + \sqrt{\nu_{yx}\nu_{xy}})} \quad (1.20)$$

In the case of an isotropic material (i.e.  $E_x = E_y$ ,  $\nu_{yx} = \nu_{xy} = \nu$ ), Eqs. (1.18 a-c) and (1.19 a-c) become:

$$\varepsilon_x = \frac{1}{E} (\sigma_x - \nu\sigma_y); \quad \varepsilon_y = \frac{1}{E} (\sigma_y - \nu\sigma_x); \quad \gamma_{xy} = \frac{\tau_{xy}}{G} \quad (1.21 \text{ a, b, c})$$

$$\sigma_x = \frac{E}{1 - \nu^2} (\varepsilon_x - \nu\varepsilon_y); \quad \sigma_y = \frac{E}{1 - \nu^2} (\varepsilon_y - \nu\varepsilon_x); \quad \tau_{xy} = G\gamma_{xy} \quad (1.22 \text{ a, b, c})$$

It should be noted that, in the case of isotropic materials,  $G$  is a function of both Young's modulus and Poisson's ratio:

$$G = \frac{E}{2(1 + \nu)} \quad (1.23)$$

### 1.3) Thin Plate and Membrane analysis

The mechanical behaviour of plates has been investigated in great depth since the early 18th century. In the following section, attention is focused on the analysis of thin plates ( $10 < a/h < 50$ ) and membranes ( $a/h > 50$ ). Specifically, considering a plate of constant thickness  $h$  and arbitrary geometry, the plate can be subdivided into two equal parts by a plane orthogonal to the thickness in Figure 1.6. This plane is commonly known as the *middle plane* or the *midplane* of the plate. In the elastic theory of plates, plate behaviour is well described by investigating only the *midplane* deformations.

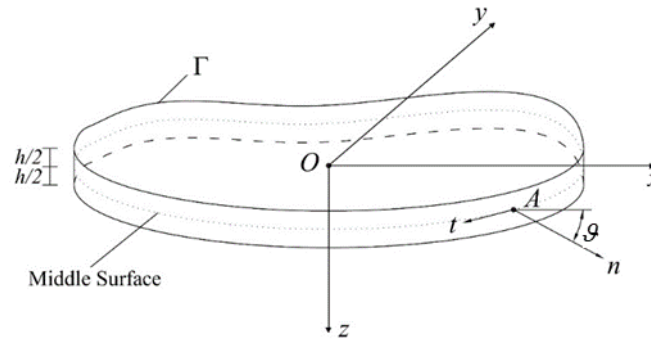


Figure 1.6 Arbitrarily shaped plate of contour  $\Gamma$ .

To derive the linear and elastic theories of bending of thin plates and membranes, some common fundamental assumptions can be given [1, 2, 4]:

- a) The plate is thin ( $h \ll a$ , where  $a$  is a characteristic length of the plate, at least ten times larger than the thickness); and, as stated above, the plate's *midplane* halves the plate into two equal parts  $z = \pm 1/2h$ ;
- b) The material of the plate is elastic and homogeneous;
- c) The plate is initially flat;
- d) The straight lines, initially normal to the midplane before the application of any loads, remain straight and normal to the midplane during deformation and their length is not altered. Thus, vertical shear strains ( $\gamma_{yz} = 0$  and  $\gamma_{zx} = 0$ ) and the normal strain can be omitted ( $\varepsilon_z = 0$ );

- e) The stress normal to the middle plane,  $\sigma_z$ , is small compared with the other stresses. This is due to the thin thickness of the plate. Consequently,  $\sigma_z$  can be neglected in the stress-strain relation.

In addition:

- In the case of thin plates under small deformations, two assumptions can be drawn:
    1. The deflection (the normal component of the displacement vector) of the *midplane* is small compared to the thickness of the plate. Thus, the slope of the deflected surface is very small and the square of the slope is much smaller than the unity;
    2. The middle surface of the plate remains unstrained during bending, since the displacements of the plate are small.
- Assumptions a-e combined with 1-2 are the fundamental assumptions of the *plate bending theory* commonly referred to as *Kirchhoff's plate theory of thin plates in small deflections*. All the above-mentioned assumptions allow the analysis of thin plates to be reduced from a three-dimensional to a two-dimensional problem.
- In the case of a large deflection, despite the membrane deflection ( $w(x, y)$ ) may be comparable to the plate thickness,  $w(x, y)$  is assumed to remain small compared to the other dimensions of the plate.

### **1.3.1) Kirchhoff's plate bending theory**

The mathematical description of thin plates dates back to the end of the 18th century, when Euler and Chladni experimentally investigated the modes of vibration of thin plates. Later, Bernoulli proposed a theoretical model of plates based on the Euler-Bernoulli beam bending theory, by considering the plate as a system of mutually perpendicular strips functioning as a beam. Some years later, Cauchy and Poisson also focused their studies on the behaviour of plates. However, the first satisfactory theory on the bending of plates was presented by Navier, who considered the rigidity of the plate as a function of the plate thickness, which was considered constant by Poisson.

Moreover, Navier proposed an “exact” solution for the bending problem of simply supported rectangular plates by employing Fourier trigonometric series. In 1850, Kirchhoff published a revised plate bending theory, based on the so called “Kirchhoff assumptions”, which allowed the reduction of the mathematical complexity of the plate study. At the end of the 19th century, shipbuilders began replacing wood with structural steel, thus plates and plate theory drew the attention of many researchers. Among them, Galerkin and Timoshenko contributed extensively to the development and refining of the plate bending theory proposed by Kirchhoff [4].

### 1.3.1.1) Strain expressions

As already discussed above, Kirchhoff’s assumptions allow the study of thin plates to be reduced from a three-dimensional to a two-dimensional problem, and thus the shear and normal strains with respect to the  $z$  axis can be neglected:

$$\gamma_{yz} = 0, \gamma_{zx} = 0 \text{ and } \varepsilon_z = 0 \quad (1.24)$$

Integrating Eqs. (1.11) and (1.12) over the plate thickness and taking into account Eqs. (1.24), one obtains:

$$u = u_0(x, y) - z \frac{\partial w}{\partial x}, \quad v = v_0(x, y) - z \frac{\partial w}{\partial y} \text{ and } w = w(x, y) \quad (1.25)$$

where the terms  $u_0(x, y)$  and  $v_0(x, y)$  represent the eventual initial extensions of the body due to a pre-stress loading of the midplane. As can be observed, the plate deflection  $w(x, y)$  does not vary along the plate thickness, while the displacements’ components  $u(x, y)$  and  $v(x, y)$  vary linearly over the plate thickness. It must be noted that, if the small deformation assumptions are taken into account,  $u_0(x, y)$  and  $v_0(x, y)$  vanish.

Considering Eqs. (1.25), the elements of the *Green’s symmetric strain tensor*, Eq. (1.6), can be expressed as follows [5]:

$$\varepsilon_x = \frac{\partial u}{\partial x} + \frac{1}{2} \left( \frac{\partial w}{\partial x} \right)^2 = \frac{\partial u_0}{\partial x} - z \frac{\partial^2 w}{\partial x^2} + \frac{1}{2} \left( \frac{\partial w}{\partial x} \right)^2$$

$$\varepsilon_y = \frac{\partial v}{\partial y} + \frac{1}{2} \left( \frac{\partial w}{\partial y} \right)^2 = \frac{\partial v_0}{\partial y} - z \frac{\partial^2 w}{\partial y^2} + \frac{1}{2} \left( \frac{\partial w}{\partial y} \right)^2$$

$$\varepsilon_z = \frac{\partial w}{\partial z} = 0 \quad (1.26 \text{ a, b, c})$$

$$\gamma_{xy} = 2\varepsilon_{xy} = \left( \frac{\partial u}{\partial y} + \frac{\partial v}{\partial x} \right) + \frac{\partial w}{\partial x} \frac{\partial w}{\partial y} = \left( \frac{\partial u_0}{\partial y} + \frac{\partial v_0}{\partial x} \right) - 2z \frac{\partial w^2}{\partial x \partial y} + \frac{\partial w}{\partial x} \frac{\partial w}{\partial y}$$

$$\gamma_{xz} = 2\varepsilon_{xz} = \left( \frac{\partial u}{\partial z} + \frac{\partial w}{\partial x} \right) = 0$$

$$\gamma_{yz} = 2\varepsilon_{yz} = \left( \frac{\partial v}{\partial z} + \frac{\partial w}{\partial y} \right) = 0 \quad (1.26 \text{ d, e, f})$$

Eqs. (1.26) take also into account both large deformations and pre-stress terms.

In the case of unstrained plates and small deflections, Eqs 1.26 become:

$$\varepsilon_x = -z \frac{\partial^2 w}{\partial x^2}, \quad \varepsilon_y = -z \frac{\partial^2 w}{\partial y^2} \quad \text{and} \quad \gamma_{xy} = -2z \frac{\partial w^2}{\partial x \partial y} \quad (1.27 \text{ a, b, c})$$

where,  $\frac{\partial^2 w}{\partial x^2}$  defines the curvature of the *midplane* along the x axis, commonly

indicated as  $\chi_x$ . Similarly,  $\frac{\partial^2 w}{\partial y^2}$  is the curvature of *midplane* along the y axis,

$\chi_y$ . Finally,  $\frac{\partial w^2}{\partial x \partial y}$  defines the cross-curvature generated by the plate torsion and

it is called *twisting curvature* with respect to the x and y axes,  $\chi_{xy}$ . Assuming the bending curvature to be positive if it is convex downward, i.e. in the positive direction of the z axis,  $\chi_x$ ,  $\chi_y$  and  $\chi_{xy}$  have a negative sign since the second derivative of the deflection for the convex downward curve is negative. Therefore, Eqs. (1.27 a-c) can be written as:

$$\varepsilon_x = z\chi_x, \quad \varepsilon_y = z\chi_y \quad \text{and} \quad \gamma_{xy} = 2z\chi_{xy} \quad (1.28 \text{ a, b, c})$$

### 1.3.1.2) Stress-strain relation for the case of small deformations

Based on Kirchhoff's assumptions the stress-strain relationship expressed by Eqs. (1.19), can be employed for the thin plate analysis. In particular, taking into account the definition of the plate curvatures ( i.e.,  $\chi_x$ ,  $\chi_y$  and  $\chi_{xy}$  ), Eqs. (1.19) can be written as follows:

$$\begin{aligned}\sigma_x &= \frac{E_x z}{1 - \nu_{xy} \nu_{yx}} (\chi_x + \nu_{yx} \chi_y) = -\frac{E_x z}{1 - \nu_{xy} \nu_{yx}} \left( \frac{\partial^2 w}{\partial x^2} + \nu_{yx} \frac{\partial^2 w}{\partial y^2} \right); \\ \sigma_y &= \frac{E_y z}{1 - \nu_{xy} \nu_{yx}} (\chi_y + \nu_{xy} \chi_x) = -\frac{E_y z}{1 - \nu_{xy} \nu_{yx}} \left( \frac{\partial^2 w}{\partial y^2} + \nu_{xy} \frac{\partial^2 w}{\partial x^2} \right); \\ \tau_{xy} &= 2G_{xy} z \chi_{xy} = -2G_{xy} z \frac{\partial^2 w}{\partial x \partial y}\end{aligned}\quad (1.29 \text{ a, b, c})$$

In the case of isotropic material, Eqs (1.29 a-c) simplify:

$$\begin{aligned}\sigma_x &= -\frac{Ez}{1 - \nu^2} \left( \frac{\partial^2 w}{\partial x^2} + \nu \frac{\partial^2 w}{\partial y^2} \right); \\ \sigma_y &= -\frac{Ez}{1 - \nu^2} \left( \frac{\partial^2 w}{\partial y^2} + \nu \frac{\partial^2 w}{\partial x^2} \right); \\ \tau_{xy} &= -\frac{Ez}{1 + \nu} \frac{\partial^2 w}{\partial x \partial y}\end{aligned}\quad (1.30 \text{ a, b, c})$$

Instead of working with stress components at a point in the body, it is convenient to introduce the shear forces  $V_x$  and  $V_y$ , and the bending and twisting moments  $M_x$ ,  $M_y$  and  $M_{xy}$ , which are the total statically equivalent forces and moments applied to the *midplane* of the plate:

$$\begin{Bmatrix} V_x \\ V_y \end{Bmatrix} = \int_{-h/2}^{h/2} \begin{Bmatrix} \tau_{xz} \\ \tau_{yz} \end{Bmatrix} z dz \quad (1.31)$$

and

$$\begin{Bmatrix} M_x \\ M_y \\ M_{xy} \end{Bmatrix} = \int_{-h/2}^{h/2} \begin{Bmatrix} \sigma_x \\ \sigma_y \\ \tau_{xy} \end{Bmatrix} z dz \quad (1.32)$$

It is worth noting that, although Kirchhoff's plate bending theory neglects the shear strain  $\tau_{xz}$  and  $\tau_{yz}$ , their corresponding shear forces are necessary for the plate element equilibrium.

Substituting Eqs. (1.29 a-c) into Eqs (1.31-32) and integrating over the plate thickness, the shear forces and the bending and twisting moments can be expressed as a function of the plate's deflection and curvature:

$$\begin{aligned} M_x &= -\frac{E_x h^3}{12(1-\nu_{xy}\nu_{yx})} \left( \frac{\partial^2 w}{\partial x^2} + \nu_{yx} \frac{\partial^2 w}{\partial y^2} \right) = -D_x \left( \frac{\partial^2 w}{\partial x^2} + \nu_{yx} \frac{\partial^2 w}{\partial y^2} \right) \\ M_y &= -\frac{E_y h^3}{12(1-\nu_{xy}\nu_{yx})} \left( \frac{\partial^2 w}{\partial y^2} + \nu_{xy} \frac{\partial^2 w}{\partial x^2} \right) = -D_y \left( \frac{\partial^2 w}{\partial y^2} + \nu_{xy} \frac{\partial^2 w}{\partial x^2} \right) \\ M_{xy} &= -2G_{xy} \frac{h^3}{12} \frac{\partial^2 w}{\partial x \partial y} = -2D_t \frac{\partial^2 w}{\partial x \partial y} \end{aligned} \quad (1.33-35)$$

where  $D_x$ ,  $D_y$ ,  $D_{xy}$  and  $D_t$  are the flexural and torsional rigidities of the plate [2]:

$$D_x = \frac{E_x h^3}{12(1-\nu_{xy}\nu_{yx})}, \quad D_y = \frac{E_y h^3}{12(1-\nu_{xy}\nu_{yx})} \quad (1.36-37)$$

$$D_t = (1 - \sqrt{\nu_{xy}\nu_{yx}}) \sqrt{D_x D_y} = (1 - \nu_{xy}) D_{xy} \quad \text{or} \quad D_t = G_{xy} \frac{h^3}{12},$$

$$D_{xy} = \frac{E_x h^3 \nu_{yx}}{12(1-\nu_{xy}\nu_{yx})}, \quad D_1 = \nu_{xy} D_y = \nu_{yx} D_x \quad (1.38-41)$$

In the case of isotropic materials Eqs. (1.33-35) becomes:

$$\begin{aligned} M_x &= -D \left( \frac{\partial^2 w}{\partial x^2} + \nu \frac{\partial^2 w}{\partial y^2} \right); \quad M_y = -D \left( \frac{\partial^2 w}{\partial y^2} + \nu \frac{\partial^2 w}{\partial x^2} \right); \\ M_{xy} &= M_{yx} = -D(1-\nu) \left( \frac{\partial^2 w}{\partial x \partial y} \right) \end{aligned} \quad (1.42-44)$$

and the flexural rigidity  $D$  of the plate is simply:

$$D = \frac{Eh^3}{12(1-\nu^2)} \quad (1.45)$$

### 1.3.1.3) The governing equation for the deflection of plates in Cartesian coordinates

The governing equation of the deflection of a thin plate can be presented by expressing the equilibrium condition of an infinitesimal portion of a plate subjected to an external vertically distributed load of intensity  $q(x, y)$ , as shown in Figure 1.7. Following the *midplane approach*, i.e. the load is assumed to be applied to the *midplane* surface of the plate, three equilibrium equations can be drawn [4]:

I. The force summation about the  $z$  axis

$$\left( V_x + \frac{\partial V_x}{\partial x} dx \right) dy + \left( V_y + \frac{\partial V_y}{\partial y} dy \right) dx + q(x, y) dx dy +$$

$$-V_x dy - V_y dx = 0$$

which leads to:

$$\frac{\partial V_x}{\partial x} + \frac{\partial V_y}{\partial y} + q(x, y) = 0 \quad (1.46 \text{ a, b})$$

II. The moment summation about the  $x$  axis:

$$\left( M_y + \frac{\partial M_y}{\partial x} dx \right) dy + \left( M_{xy} + \frac{\partial M_{xy}}{\partial x} dx \right) dy + \left( V_y + \frac{\partial V_y}{\partial y} dy \right) dx +$$

$$+ q(x, y) dx dy - M_y dx - M_{xy} dy - \left( V_y + \frac{\partial V_y}{\partial y} dy \right) dx = 0$$

Omitting the products of infinitesimal terms, having higher order of smallness, one obtains:

$$\frac{\partial M_{xy}}{\partial x} + \frac{\partial M_y}{\partial y} - V_y = 0 \quad (1.47 \text{ a, b})$$



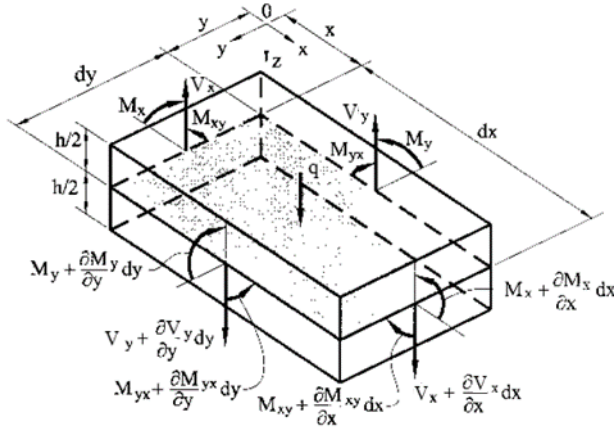


**Figure 1. 7** Equilibrium condition of an infinitesimal portion of a plate subjected to an external vertically distributed load of intensity  $q(x, y)$  [4].

Similarly, the moment summation about the  $y$  axis leads to:

$$\frac{\partial M_{yx}}{\partial y} + \frac{\partial M_x}{\partial x} - V_x = 0 \quad (1.48)$$

Combining Eqs. (1.47b-48) and Eqs. (1.33-35), the shear forces can be written as follows:

$$\begin{aligned} V_x &= \frac{\partial M_x}{\partial x} + \frac{\partial M_{yx}}{\partial y} = -\frac{\partial}{\partial x} \left( D_x \frac{\partial^2 w}{\partial x^2} + B \frac{\partial^2 w}{\partial y^2} \right) \\ V_y &= \frac{\partial M_y}{\partial y} + \frac{\partial M_{xy}}{\partial x} = -\frac{\partial}{\partial y} \left( B \frac{\partial^2 w}{\partial x^2} + D_y \frac{\partial^2 w}{\partial y^2} \right) \end{aligned} \quad (1.49-50)$$

Considering that  $M_{xy} = M_{yx}$ , substituting Eqs. (1.49-50) into Eq. (1.46b), one obtains:

$$\frac{\partial^2 M_x}{\partial x^2} + 2 \frac{\partial^2 M_{yx}}{\partial x \partial y} + \frac{\partial^2 M_y}{\partial y^2} = -q(x, y) \quad (1.51)$$

Or

$$D_x \frac{\partial^4 w}{\partial x^4} + 2B \frac{\partial^4 w}{\partial x^2 \partial y^2} + D_y \frac{\partial^4 w}{\partial y^4} = -q(x, y) \quad (1.52)$$

where  $B = 1/2(\nu_{yx}D_x + \nu_{xy}D_y + 4D_t)$  is the effective torsional rigidity of the orthotropic plate. Moreover, considering Eq. (1.17), the effective torsional rigidity can also be expressed as  $B \approx \nu_{xy}D_{xy} + 2D_t$ .

Eq. (1.52) is the governing differential equation for thin orthotropic plate bending analysis based on Kirchhoff's assumptions. Mathematically, Eq. (1.52) is a linear partial differential equation of the fourth order having constant coefficients. The equation describes the behaviour of both naturally and structurally orthotropic plates. Structurally orthotropic plates are plates where the addition of structural elements on their surface cause orthotropy.

As far as isotropic plates are concerned, Eq. (1.52) becomes:

$$\frac{\partial^4 w}{\partial x^4} + 2\frac{\partial^4 w}{\partial x^2 \partial y^2} + \frac{\partial^4 w}{\partial y^4} = -\frac{q(x, y)}{D} \quad (1.53)$$

Eq. (1.53) can also be presented as

$$\nabla^2(\nabla^2 w) = \nabla^4 w = -\frac{q(x, y)}{D} \quad (1.54)$$

where

$$\nabla^4 () = \frac{\partial^4}{\partial x^4} + 2\frac{\partial^4}{\partial x^2 \partial y^2} + \frac{\partial^4}{\partial y^4} \quad (1.55)$$

is the *biharmonic operator*.

In the case of isotropic plates, the sum of the bending moments (Eqs. (1.42-44)) is invariant, and thus the so-called moment sum can be defined as follows

$$M = \frac{M_x + M_y}{1 + \nu} = -D\nabla^2 w \quad (1.56)$$

Substituting Eq. (1.56) into Eqs. (1.49-50), the shear forces can be written as:

$$\begin{aligned} V_x &= \frac{\partial M}{\partial x} = -D \frac{\partial}{\partial x} \left( \frac{\partial^2 w}{\partial x^2} + \frac{\partial^2 w}{\partial y^2} \right) \\ V_y &= \frac{\partial M}{\partial y} = -D \frac{\partial}{\partial y} \left( \frac{\partial^2 w}{\partial x^2} + \frac{\partial^2 w}{\partial y^2} \right) \end{aligned} \quad (1.57-58)$$

Thus, the governing equation, Eq. (1.53), can be decomposed into two equivalent simultaneous Poisson's equations, as proposed by Marcus [9]:

$$\begin{aligned}\frac{\partial^2 M}{\partial x^2} + \frac{\partial^2 M}{\partial y^2} &= -q(x, y) \\ \frac{\partial^2 w}{\partial x^2} + \frac{\partial^2 w}{\partial y^2} &= -\frac{M(x, y)}{D}\end{aligned}\quad (1.59-60)$$

This is a system of two-second order partial differential equations, whose solutions can be simpler than that for Eq. (1.53) depending on the mathematical approach employed.

#### 1.3.1.4) The strain energy of plates

During the deformation, the work of the external forces,  $W_{ext}$ , is balanced by the work of the internal conservative forcercs,  $W_{int}$ . Thus, the law of conservation of energy holds [2]:

$$W_{ext} + W_{int} = 0 \quad (1.61)$$

In the case of thin plates, the strain energy of the plate, or the potential of the internal forces, can be defined as the opposite of the work done by the internal forces:

$$U_{Strain} = -W_{int} \quad (1.62)$$

The strain energy  $U_{Strain}$  is negative since the displacement of the body will always occur in the direction opposite to that of the internal forces. In particular, under the Kirchhoff's assumptions, the strain energy stored by an elastic body can be written as:

$$U_{Strain} = \frac{1}{2} \iiint (\sigma_x \varepsilon_x + \sigma_y \varepsilon_y + \tau_{xy} \gamma_{xy}) dV \quad (1.63)$$

where  $V$  is the whole body volume. Substituting the strain-stress relationships Eqs. (1.18) into Eq. (1.63), one has:

$$U_{Strain} = \frac{1}{2} \iiint \left( \frac{\sigma_x^2}{E_x} - 2\nu_{yx} \frac{\sigma_x \sigma_y}{E_y} + \frac{\sigma_y^2}{E_y} + \frac{\tau_{xy}^2}{G_{xy}} \right) dV \quad (1.64)$$

Substituting Eqs. (1.29) into Eq. (1.64) and integrating over the thickness the strain energy can be rewritten as:

$$U_{Strain} = \frac{1}{2} \iint \left[ \begin{aligned} &D_x \left( \frac{\partial^2 w}{\partial x^2} \right)^2 + 2D_{xy} \left( \frac{\partial^2 w}{\partial x^2} \frac{\partial^2 w}{\partial y^2} \right) + D_y \left( \frac{\partial^2 w}{\partial y^2} \right)^2 + \\ &+ 4D_t \left( \frac{\partial^2 w}{\partial x \partial y} \right)^2 \end{aligned} \right] dA \quad (1.65)$$

where  $D_x$ ,  $D_y$ ,  $D_{xy}$  and  $D_t$  are defined in Eqs. (1.36-41), and  $A$  is the area of the *midplane*.

In the case of an isotropic material Eq. (1.65) simplifies:

$$U_{Strain} = \frac{1}{2} \iint D \left[ \left( \frac{\partial^2 w}{\partial x^2} + \frac{\partial^2 w}{\partial y^2} \right)^2 - 2(1-\nu) \left[ \left( \frac{\partial^2 w}{\partial x^2} \frac{\partial^2 w}{\partial y^2} \right) - \left( \frac{\partial^2 w}{\partial x \partial y} \right)^2 \right] \right] dA \quad (1.66)$$

As was introduced for the internal forces, it is possible to define the potential of the external forces:

$$\Omega_{ext} = -W \quad (1.67)$$

In the case of static analysis, the potential of the external forces can be calculated as the product of the loads for the produced displacements [4]:

$$\Omega_{ext} = - \left[ \iint q(x, y) w(x, y) dA + \sum_i P_{c,ext} w_i + \sum_j M_j \theta_j \right] \quad (1.68)$$

where  $q(x, y)$  is a distributed load acting on the plate surface,  $w(x, y)$  is the corresponding surface deflection.  $P_{c,ext}$  and  $M_j$  are the concentrated forces and moments, and  $w_i$  and  $\theta_j$  the corresponding concentrated deflections and slopes of the surface at the point of application of the *ith* force and *jth* moment, respectively. The law of the conservation of energy states that the internal and external potential have to balance each other:

$$\Pi_{tot} = U_{Strain} + \Omega_{ext} = 0 \quad (1.69)$$

where  $\Pi_{tot}$  is the total potential energy of the plate.

### 1.3.1.5) Transverse vibrations of thin plates

So far, it was assumed that all external loads are applied slowly, and thus both the resulting stresses and deformations are independent of time. However, machines and many structures are subjected to loads which change with time or are applied suddenly i.e. seismic disturbances, wind gusts, etc. Two vibration states are commonly investigated:

- the free vibration of a body, which occurs in the absence of applied load, and can be initiated by applying an initial displacement to the body. The free vibration motion concerns the natural characteristics of the structure, and these natural vibrations occur at discrete frequencies, depending only on the geometry and material of the body.
- the forced vibration motion, which occurs if an external time-dependent force is applied to the body.

In these cases, the governing equation of plates can be adequately modified by using D’Alambert’s principle [4]. This principle introduces a new term concerning the inertia forces as reversed effective forces to the static governing equation. Considering an un-damped structure, i.e. a system where the effects of internal friction or surrounding media are neglected, and taking into account Eq. (1.52), a new term on the right hand side of Eq. (1.52) can be introduced to deal with the dependent variables as a function of time:

$$q(x, y, t) - \rho h \frac{\partial^2 w}{\partial t^2}(x, y, t) \quad (1.70)$$

where both  $p$  and  $w$  are now functions of time and space. In Eq. (1.70)  $\rho$  is the mass density of the material and  $h$  the plate thickness. As mentioned above, in the case of free vibration the term  $q(x, y, t)$  is null, since no external force is applied, whereas, in the case of forced vibrations, this term describes the external force acting on the body.

Introducing Eq. (1.70) into Eqs. (1.52) and (1.53), the governing equation of motion for the orthotropic and isotropic plates can be obtained:

$$D_x \frac{\partial^4 w}{\partial x^4} + 2B \frac{\partial^4 w}{\partial x^2 \partial y^2} + D_y \frac{\partial^4 w}{\partial y^4} = p(x, y, t) - \rho h \frac{\partial^2 w}{\partial t^2}(x, y, t) \quad (1.71)$$

and

$$D\nabla^2(\nabla^2 w(x, y, t)) = q(x, y, t) - \rho h \frac{\partial^2 w}{\partial t^2}(x, y, t) \quad (1.72)$$

Moreover, considering a plate in free vibrations, it is possible to define the kinetic energy of the plate correlated to its vibration, as follows:

$$T = \frac{1}{2} \iint \rho h \left[ \frac{\partial w(x, y, t)}{\partial t} \right]^2 dA \quad (1.73)$$

The kinetic energy of the plate must equal the strain potential energy of the body, therefore for vibrating plates, one has:

$$\Pi_{tot} = U_{Strain} - K = 0 \quad (1.74)$$

### 1.3.2) Membranes ( $a/h > 50$ )

Membranes are very thin plates, which do not have flexural rigidity and withstand to lateral loads by the action of in-plane forces. Membranes may be studied as thin plates with large deflections.

Therefore, the small deformation assumptions (1 and 2) are not valid, since the membrane deflection  $w(x, y)$  is comparable to the plate thickness.

Consequently, referring to Eq. (1.26), the terms  $\frac{\partial u}{\partial x}$  and  $\frac{\partial v}{\partial y}$  are of the same order

of smallness as  $\left(\frac{\partial w}{\partial x}\right)^2$  and  $\left(\frac{\partial w}{\partial y}\right)^2$ .

On the other hand, the terms linearly varying with respect to the thickness, i.e.  $-z \frac{\partial^2 w}{\partial x^2}$ ,  $z \frac{\partial^2 w}{\partial y^2}$  and  $-2z \frac{\partial w^2}{\partial x \partial y}$ , can be reasonably neglected as membranes have very small thicknesses. Consequently, the strain relations for the membrane case become:

$$\varepsilon_x = \frac{\partial u_0}{\partial x} + \frac{1}{2} \left( \frac{\partial w}{\partial x} \right)^2$$

$$\begin{aligned}\varepsilon_y &= \frac{\partial v_0}{\partial y} + \frac{1}{2} \left( \frac{\partial w}{\partial y} \right)^2 \\ \gamma_{xy} = 2\varepsilon_{xy} &= \left( \frac{\partial u_0}{\partial y} + \frac{\partial v_0}{\partial x} \right) + \frac{\partial w}{\partial x} \frac{\partial w}{\partial y}\end{aligned}\quad (1.75 \text{ a, b, c})$$

As far as stresses are concerned, the action of direct (or membrane) forces, i.e. forces acting in the plane of the plate, have to be considered. Considering an infinitesimal portion of a membrane subjected to the action of a lateral load  $q(x, y)$ , as shown in Figure 1. 8, the in-plane forces  $N_x$ ,  $N_y$  and  $N_{xy} = N_{yx}$  can be defined as [4]:

$$\begin{Bmatrix} N_x \\ N_y \\ N_{xy} \end{Bmatrix} = \int_{-h/2}^{h/2} \begin{Bmatrix} \sigma_x \\ \sigma_y \\ \tau_{xy} \end{Bmatrix} dz = \begin{Bmatrix} \sigma_x h \\ \sigma_y h \\ \tau_{xy} h \end{Bmatrix}\quad (1.76)$$

Membrane structures are often subjected to the action of initial in-plane forces, which can be called  $N_x^0$ ,  $N_y^0$  and  $N_{xy}^0 = N_{yx}^0$ .

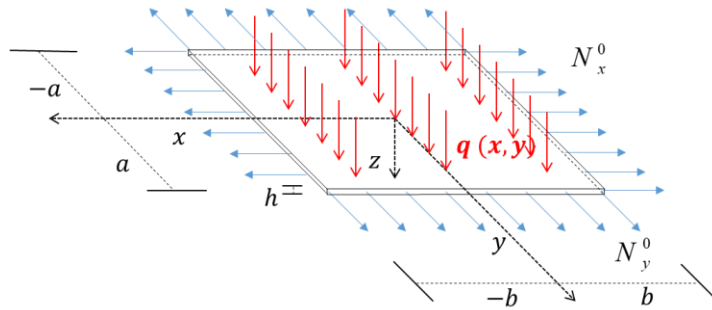


**Figure 1. 8** Membrane subjected to the action of a lateral external force  $q(x, y)$  and initial in-plane forces  $N_x^0$ ,  $N_y^0$  and  $N_{xy}^0 = N_{yx}^0$ .

For the sake of brevity, the accurate derivation of the governing equation of bending of membranes (the large deflection case of thin plates) is omitted. Thus, introducing the stress function  $\phi$  for the in-plane stress components:

$$N_x = \frac{\partial^2 \Phi}{\partial y^2}; \quad N_y = \frac{\partial^2 \Phi}{\partial x^2} \quad \text{and} \quad N_{xy} = -\frac{\partial^2 \Phi}{\partial x \partial y}\quad (1.77 \text{ a, b, c})$$

where  $\Phi = \phi h$ , the governing differential equations for large deflections of thin plates is:

$$\left\{ \begin{array}{l} \frac{1}{h} + \frac{1}{E_x} \frac{\partial^4 \Phi}{\partial x^4} + \frac{E_y - 2G_{xy}}{G_{xy} E_y} \frac{\partial^4 \Phi}{\partial x^2 \partial y^2} + \frac{1}{E_y} \frac{\partial^4 \Phi}{\partial y^4} = \left( \frac{\partial^2 w}{\partial x \partial y} \right)^2 - \frac{\partial^2 w}{\partial x^2} \frac{\partial^2 w}{\partial y^2} \\ D_x \frac{\partial^4 w}{\partial x^4} + 2B \frac{\partial^4 w}{\partial x^2 \partial y^2} + D_y \frac{\partial^4 w}{\partial y^4} = q(x, y) + \frac{\partial^2 \Phi}{\partial y^2} \frac{\partial^2 w}{\partial x^2} + \frac{\partial^2 \Phi}{\partial x^2} \frac{\partial^2 w}{\partial y^2} + \\ -2 \frac{\partial^2 \Phi}{\partial x \partial y} \frac{\partial^2 w}{\partial x \partial y} \end{array} \right. \quad (1.78a, b)$$

where  $D_x, D_y, D_{xy}$  and  $D_t$  are defined in Eqs. (1.36-41).

Eqs. (1.78 a, b) were first introduced by Von Karman in 1910. The resolution of these equations is a complex mathematical task. Consequently, numerical methods have been employed for solving the membrane problem in many different conditions [4].

### 1.3.2.1) The strain energy of membranes

In Section 1.3.1.4, the strain energy of a thin plate was defined as the opposite of the work done by the internal forces. Similarly, in the case of membranes, the internal potential energy can be defined as:

$$U_{Strain} = \frac{1}{2} \int_{-a/2}^{a/2} \int_{-a/2}^{a/2} (N_x \varepsilon_x + N_y \varepsilon_y + N_{xy} \gamma_{xy}) dx dy \quad (1.79)$$

Substituting Eqs. (1.75) and (1.76) into Eq. (1.79) and taking into account Eqs. (1.19 a-c), one has:



$$U_{Strain} = \frac{1}{2} \int_{-a/2}^{a/2} \int_{-b/2}^{b/2} \left[ \begin{aligned} & \left( \frac{E_x h}{(1-\nu_{xy}\nu_{yx})} \right) \left( \frac{\partial u}{\partial x} + \frac{1}{2} \left( \frac{\partial w}{\partial x} \right)^2 \right)^2 + \\ & + \left( \frac{E_y h}{(1-\nu_{xy}\nu_{yx})} \right) \left( \frac{\partial v}{\partial y} + \frac{1}{2} \left( \frac{\partial w}{\partial y} \right)^2 \right)^2 + \\ & + 2\nu_{yx} \left( \frac{E_x h}{(1-\nu_{xy}\nu_{yx})} \right) \left( \frac{\partial u}{\partial x} + \frac{1}{2} \left( \frac{\partial w}{\partial x} \right)^2 \right) \left( \frac{\partial v}{\partial y} + \frac{1}{2} \left( \frac{\partial w}{\partial y} \right)^2 \right) + \\ & G_{xy} \left( \left( \frac{\partial u}{\partial x} + \frac{\partial v}{\partial y} \right) + \frac{\partial w}{\partial x} \frac{\partial w}{\partial y} \right)^2 \end{aligned} \right] dx dy \quad (1.80)$$

Eq. (1.80) is the strain energy of membrane or thin plate with a large deflection. In the case of isotropic materials, Eq. (1.80) simplifies to:

$$U_{Strain} = \frac{Eh}{2(1-\nu^2)} \int_{-a/2}^{a/2} \int_{-b/2}^{b/2} \left[ \begin{aligned} & \left( \frac{\partial u}{\partial x} + \frac{1}{2} \left( \frac{\partial w}{\partial x} \right)^2 \right)^2 + \left( \frac{\partial v}{\partial y} + \frac{1}{2} \left( \frac{\partial w}{\partial y} \right)^2 \right)^2 + \\ & + 2\nu \left( \frac{\partial u}{\partial x} + \frac{1}{2} \left( \frac{\partial w}{\partial x} \right)^2 \right) \left( \frac{\partial v}{\partial y} + \frac{1}{2} \left( \frac{\partial w}{\partial y} \right)^2 \right) + \\ & + \frac{(1-\nu)}{2} \left( \left( \frac{\partial u}{\partial x} + \frac{\partial v}{\partial y} \right) + \frac{\partial w}{\partial x} \frac{\partial w}{\partial y} \right)^2 \end{aligned} \right] dx dy \quad (1.81)$$

As discussed above, membranes do not have bending stiffness. Thus, it is common to pretension these structural elements. The potential energy associated with initial pre-stress forces can be written as [5]:

$$U_{pre-stress} = \int_{-a/2}^{a/2} \int_{-b/2}^{b/2} \left[ \begin{aligned} & N_x^0 \frac{1}{2} \left( \frac{\partial w}{\partial x} \right)^2 + N_y^0 \frac{1}{2} \left( \frac{\partial w}{\partial y} \right)^2 + \\ & + 2N_{xy}^0 \left( \frac{\partial w}{\partial x} \frac{\partial w}{\partial y} \right) \end{aligned} \right] dx dy \quad (1.82)$$

where  $N_x^0$ ,  $N_y^0$  and  $N_{xy}^0 = N_{yx}^0$ , are the initial in-plane loads along the  $x$  and  $y$  axes. Please note that, only the terms of large out-of-plane rotations have been retained.

Finally, the total potential energy for a membrane subjected to an initial pre-stress and lateral load is:

$$\Pi_{tot} = U_{Strain} + U_{pre-stress} + \Omega_{ext} = 0 \quad (1.83)$$

Where  $\Pi_{tot}$  is the total potential energy.

### 1.3.3) Boundary conditions

Boundary conditions are a set of constraints which approximate the behaviour of a mechanical system in a specific circumstance. Precise boundary conditions have to be prescribed in advance to solve the governing equation of the system under study. In solid mechanics, boundary conditions can be classified as: *geometric* or *kinematic boundary conditions*, which impose restrictions on deflection or slope of a boundary; *static* or *natural boundary conditions* which concern both external loads or impose restrictions on the internal forces and moments at a boundary of the body. As far as thin plates and membranes are concerned, two kinematic boundary conditions have to be specified at each edge of the element under study. In the following section, the three most common *kinematic boundary conditions*, i.e. clamped edge, simply supported edge and free edge, are presented [4].

Consider an arbitrarily shaped plate, as shown in Figure 1. 6, let  $n$  and  $t$  be the outward unit normal and tangent vector at a point A of a generic curvilinear edge of the contour  $\Gamma$  and  $\varrho$  the angle between the normal  $n$  and the  $x$  axis. The moments on the plate boundary  $\Gamma$  can be called  $M_n$ ,  $M_t$  and  $M_{nt}$ , where  $M_n$  is the bending moment of the plane  $Oxz$ , oriented along the tangent to the contour;  $M_s$  is the bending moment in the perpendicular direction; and  $M_{nt}$  is the twisting moment about the normal [2].

Considering the equilibrium of a volume element on the plate boundary the frame transformations for the moments can be obtained as [4]:

$$\begin{aligned}
 M_n(x, y) &= n_x^2 M_x + n_y^2 M_y + 2n_x n_y M_{xy} \\
 M_t(x, y) &= n_x^2 M_y + n_y^2 M_x + 2n_x n_y M_{xy} \\
 M_{nt}(x, y) &= n_x n_y (M_y - M_x) + (n_x^2 - n_y^2) M_{xy}
 \end{aligned} \tag{1.84 a, b, c}$$

where  $n_x$  and  $n_y$  are the components of the unitary vector  $n$ .

Therefore, the boundary conditions can be expressed as:

1. *Clamped, or fixed edge:*

$$\begin{aligned}
 w(x, y) &= 0; \\
 \frac{\partial w(x, y)}{\partial n} &= n_x \frac{\partial w(x, y)}{\partial x} + n_y \frac{\partial w(x, y)}{\partial y} = 0
 \end{aligned} \tag{1.85 a, b}$$

The deflection and rotation (the slope) at the boundary must be null.

2. *Simply supported edge*

$$\begin{aligned}
 w(x, y) &= 0; \\
 M_n &= 0
 \end{aligned} \tag{1.86 a, b}$$

Note that, in the case of isotropic plates and small deformations, substituting Eqs. (1.42-44) into Eq. (1.84 a),  $M_n$  in Eq. (1.86 b) can be written as:

$$M_n = (n_x^2 + \nu n_y^2) \frac{\partial^2 w}{\partial x^2} + 2(1 - \nu) n_x n_y \frac{\partial^2 w}{\partial x \partial y} + (n_y^2 + \nu n_x^2) \frac{\partial^2 w}{\partial y^2} \tag{1.87}$$

Eq. (1.87) simplifies for a plate of straight edges oriented along the  $x$ ,  $y$  axes:

$$M_n = \frac{\partial^2 w}{\partial y^2} = 0 \text{ (for an edge along the } x \text{ axis)} \tag{1.88}$$

3. *Free edge*

$$\begin{aligned}
 \tilde{V}_n &= V_n + \frac{\partial M_{nt}}{\partial s} = 0; \\
 M_n &= 0
 \end{aligned} \tag{1.89 a, b}$$

where  $\tilde{V}_n$  is the so-called effective shear force, and  $V_n$  is the shearing force on the edge of the plate, given as:

$$V_n = n_x V_x + n_y V_y \tag{1.90}$$

The shearing forces were defined in Eqs. (1.49-50) and (1.57-58), for both orthotropic and isotropic plates.

The effective shear forces were first introduced by Kirchhoff to solve the *free edge* boundary condition. In fact, at a free edge no stresses are applied and thus all the moments and shear forces can be assumed to be zero. Therefore, three boundary conditions should be considered [1]:

$$M_y = 0; V_y = 0 \text{ and } M_{yx} = 0 \quad (1.91)$$

However, three boundary conditions are too many for the solution of the governing equation of the bending of plates. By introducing the concept of the effective shear forces, Kirchhoff proposed an appropriate approach to treat the free edge condition.

#### 1.4) Numerical methods

Mathematically the governing equation of thin plates and membranes are partial differential equations of the fourth order. An exact closed-form solution can be found only in a few specific geometries, load configurations and boundary support conditions, e.g. elliptical thin plate where all edges are clamped and subjected to a uniform constant load, or an equilateral plate with all edges simply-supported and subjected to uniformly distributed loads. Closed solutions can also be obtained by employing double trigonometric series and single series solutions. However, these methods can be applied only in a few cases. Consequently, many analytical and numerical methods have been developed to attain approximate solutions of arbitrarily shaped plates and membranes, with various type of boundary conditions and subjected to different load conditions. In the following section, a survey of the most common methods employed for the solution of the bending problem of plates and membranes are presented. For the sake of brevity, the methods are discussed for the application of isotropic materials and under the assumption of small deflections. Of course, the same methods can be extended to the solution of orthotropic materials, and to the large deflection of membranes both in static and dynamic analysis.

The most common methods can be subdivided depending on the main resolution approach [2, 4]:

- a) Methods based on Fourier series;
- b) Methods based on the Variational Method;
- c) Methods based on domain discretization.

#### 1.4.1) Methods based on Fourier series

Among the methods which employ the Fourier series, the Navier method and the Levy method are the oldest and most well-known.

##### 1.4.1.1) Navier methods (double series solution)

In 1820, Navier presented a paper to the French Academy of Sciences on the solution of bending of simply supported plates at all edges by double trigonometric series [2, 4]. Assuming a rectangular plate of sides  $a$ ,  $b$  and taking into account Eq. (1.87), the expression of the deflection surface  $w(x, y)$ , and the distributed load  $q(x, y)$ , can be sought in term of double sine series, as follows:

$$w(x, y) = \sum_{m=1}^{\infty} \sum_{n=1}^{\infty} W_{mn} \sin\left(\frac{m\pi x}{a}\right) \sin\left(\frac{n\pi y}{b}\right); \quad (1.92 \text{ a, b})$$

$$q(x, y) = \sum_{m=1}^{\infty} \sum_{n=1}^{\infty} Q_{mn} \sin\left(\frac{m\pi x}{a}\right) \sin\left(\frac{n\pi y}{b}\right) \text{ for } m, n = 1, 2, 3, \dots$$

where  $W_{mn}$  and  $Q_{mn}$  are coefficients to be determined. It must be noted that Eq. (1.92 a) satisfies the prescribed boundary conditions. Considering a generic load configuration, after some manipulations, the  $Q_{mn}$  coefficients can be expressed by:

$$Q_{mn} = \frac{4}{ab} \int_0^a \int_0^b q(x, y) \sin\left(\frac{m\pi x}{a}\right) \sin\left(\frac{n\pi y}{b}\right) dx dy \quad (1.93)$$

Substituting Eqs. (1.92 a, b) into the governing equation Eq. (1.53) and taking into account Eq. (1.93), an algebraic equation is obtained by which the

unknown coefficients  $W_{mn}$  can be calculated. Thus, substituting Eq. (1.92 a) into Eqs. (1.42-44) and Eqs. (1.57-58), the moments and shear forces can be found.

The infinite series solution for deflections  $w(x, y)$ , typically converges quickly and satisfactory solutions can be obtained by using a few terms. On the other hand, the convergence of the series becomes slow if moments and shear forces are sought. This is due to the fact that moments and shear forces are obtained from the second and third derivatives of the deflection, which makes the convergence slower and may be accompanied by some loss of accuracy; thus, a higher number of terms are preferred for their estimation. Convergence also becomes slow if concentrated and discontinuous loads are studied.

#### **1.4.1.2) Levy method (single series solution)**

In 1900 Levy proposed a method for solving rectangular plate bending problems by a single Fourier series for plates with two opposite simply-supported edges. This method is more practical compared to Navier's as it requires the evaluation of only single Fourier series [2, 4]. Moreover, the method can be employed for solving plates with various boundary conditions. In Levy's method, the deflection  $w(x, y)$  of the plate is composed of two terms:

$$w(x, y) = w_h + w_p \quad (1.94)$$

where  $w_h$  is the solution of the homogeneous form of Eq. (1.53) and  $w_p$  is the particular solution of Eq. (1.53). Each of these two terms can be expressed in terms of a single Fourier series and their unknown coefficients determined by satisfying the prescribed boundary conditions.

As an example, let a rectangular plate have opposite edges of coordinates  $x=0$  and  $x=a$ , simply supported, and the other opposite edges,  $y=0$  and  $y=b$ , which may have arbitrary supports. Taking into account Eq. (1.87) for simply supported edges,  $w_h$  can be expressed as:

$$w_h = \sum_{k=1}^{\infty} f_k(y) \sin\left(\frac{m\pi x}{a}\right) \quad (1.95)$$

where  $f_k(y)$  is a function of  $y$  only. Please note that Eq. (1.95) satisfies the prescribed boundary conditions.

Substituting Eq. (1.95) into the homogeneous form of the governing equation Eq. (1.53), after some manipulations,  $w_h$  can be given as:

$$w_h = \sum_{m=1}^{\infty} \left[ A_k \sinh\left(\frac{m\pi y}{a}\right) + B_k \cosh\left(\frac{m\pi y}{a}\right) + \frac{k\pi y}{a} \left( C_k \sinh\left(\frac{m\pi y}{a}\right) + D_k \cosh\left(\frac{m\pi y}{a}\right) \right) \right] \sin\left(\frac{k\pi y}{a}\right) \quad (1.96)$$

where the unknowns  $A_k, B_k, C_k$  and  $D_k$  are obtained from the boundary conditions on the edges  $y = 0$  and  $y = b$ .

Similarly, the particular solution of  $w_p$  and the distributed load can be expressed as:

$$\begin{aligned} w_h &= \sum_{k=1}^{\infty} g_k(y) \sin\left(\frac{k\pi x}{a}\right) \\ q(x, y) &= \sum_{k=1}^{\infty} q_k(y) \sin\left(\frac{k\pi x}{a}\right) \end{aligned} \quad (1.97 \text{ a, b})$$

where  $q_k(y)$  can be written as:

$$q_k(y) = \frac{2}{a} \int_0^a q(x, y) \sin\left(\frac{k\pi x}{a}\right) dx \quad (1.98)$$

Substituting Eqs. (1.97 a-b) into the governing equation Eq. (1.53),  $w_p$  can be found. Finally, the plate deflection  $w(x, y)$  is obtained by Eq. (1.94).

As for the Navier method, moments and forces can then be found by substituting Eq. (1.94) into Eqs. (1.42-44) and (1.57-58).

The convergence of Levy's method was proven to be very fast, even though it requires mathematical manipulations, which may be quite complex.

### 1.4.2 Variational methods

The variational methods, often defined as *energy methods*, use the Bernoulli's principle of virtual work and the Lagrange principle of minimum

potential energy for solving plate and membrane bending problems employing definite integrals of stresses, strains, and displacements functions called functionals. A functional is a scalar quantity depending on some function or several functions, as from independent variables. Energy methods are easier, both conceptually and mathematically, than the classical solutions and can be employed for the solution of arbitrarily shaped plates with arbitrary boundary conditions.

Assuming that a body is already in its equilibrium state of deformation due to the action of a force  $P_{int}$  and this equilibrium is disturbed by a small (infinitesimal or virtual), arbitrary, but compatible displacement, i.e. a displacement that satisfies the boundary conditions, the internal work produced can be written as:

$$\delta W_{int} = -P_{int} \delta x \quad (1.99)$$

Since the displacement is assumed to be very small, internal and external forces can be considered to be held constant, and the increment done by external forces can be expressed:

$$\delta W_{ext} = P_{ext} \delta x \quad (1.100)$$

The principle of virtual work states that an elastic body is in equilibrium if, and only if, the total work done by external forces and internal forces is zero for any admissible virtual displacements i.e.,

$$\delta W_{tot} = \delta W_{ext} + \delta W_{int} = 0 \quad (1.101)$$

Taking into account the definition of strain energy and the potential energy of external forces, see Section 1.3.1.4, Eq. (1.69) can be written in terms of infinitesimal variation:

$$\delta \Pi_{tot} = \delta U_{Strain} + \delta \Omega_{ext} = 0 \quad (1.102)$$

Eq. (1.102) can be solved by employing suitable functions  $f_i(x, y, z)$  of unknown coefficients  $c_i$  to approximate the shape of the plate displacements or the plate stress field. Specifically, substituting these equations in Eq. (1.102) and performing the minimization of the total potential energy  $\Pi_{tot}$ , with respect to the unknown coefficients  $c_i$ , an algebraic system of equations is attained.



Therefore, the analysis of the plates described by partial differential equations is reduced to a simpler algebraic system of equations, which can be easily solved.

Among the energy methods, the Rayleigh-Ritz and the Galerkin methods have been widely adopted.

#### 1.4.2.1) The Rayleigh-Ritz Method

The traditional Rayleigh-Ritz method applies the principle of minimum potential energy [2, 4]. In particular, the deflection function of the *midplane* surface  $w(x, y)$  is expressed in the form of a series of the type:

$$w(x, y) = \sum_{j=1}^N c_j \phi_j(x, y) \quad (1.103)$$

where  $N$  is the chosen truncation limit of the series expansion,  $c_j$  are unknown coefficients to be determined, and  $\phi_j(x, y)$  are the so-called Ritz functions, that satisfy individually at least, the geometrical boundary conditions. The unknown constants  $c_1, c_2, \dots, c_n$  can be found by applying the principle of the minimum potential energy, i.e.:

$$\frac{\partial \Pi_{tot}}{\partial c_1} = 0, \quad \frac{\partial \Pi_{tot}}{\partial c_2} = 0, \quad \dots, \quad \frac{\partial \Pi_{tot}}{\partial c_n} = 0 \quad (1.104)$$

The minimization procedure leads to a set of  $n$  algebraic equations in the unknown coefficients, which can be solved to find the unknown coefficients. Therefore, it is of paramount importance to select appropriate Ritz functions, which have to satisfy the boundary conditions and to approximate the shape of the deflection surface.

Many functions have been proposed for the Ritz method, i.e. trigonometric and hyperbolic series, polynomials, which were found to be effective, but their application to arbitrarily shaped plates with different combinations of edge supports may not be convenient. Liew et al. [10] proposed a set of two-dimensional orthogonal plate functions to apply the Rayleigh-Ritz method to arbitrarily shaped plates with different combinations of edge supports. A detailed explanation of this approach is reported in Section 3.2.

### 1.4.2.2) The Galerkin Method

Garlerkin proposed a further generalized and simplified formulation of the virtual work principle [2, 4].

Considering a structural body in equilibrium in a Cartesian coordinate system  $x, y, z$ , the equilibrium condition of an infinitesimal element can be described by the differential equation:

$$L_i(u, v, w) - q_i = 0 \quad (1.105)$$

where  $i=1,2,3$  and refers to the  $x, y, z$  quantities.  $L_i$  are either linear or non-linear differential operators operating on displacement functions of a body, and  $p_i$  are external loads. Referring to Eq. (1.54),  $L_i$  corresponds to  $\nabla^4(\bullet)$ .

The equilibrium of the structure can be obtained by integrating Eq. (1.105) over the whole structure. Assuming arbitrary infinitesimal variations of the displacement functions by  $\delta u, \delta v, \delta w$ , the virtual work of the external and internal forces of the body can be obtained directly from Eq. (1.105) as:

$$\begin{aligned} \iiint_{(V)} [L_1(u, v, w) - q_x](\delta u) dV &= 0, \\ \iiint_{(V)} [L_2(u, v, w) - q_y](\delta v) dV &= 0, \\ \iiint_{(V)} [L_3(u, v, w) - q_z](\delta w) dV &= 0, \end{aligned} \quad (1.106 \text{ a, b, c})$$

Eqs. (1.106 a-c) would be valid only if the displacement functions  $u(x, y)$ ,  $v(x, y)$ ,  $w(x, y)$  are the exact solution of the problem under study. Therefore, in order to get an approximate solution of Eqs. (1.106 a-c), displacement functions can be expressed in the form of series:

$$\begin{aligned} u(x, y) &= \sum_{k=1}^m a_k \xi_k(x, y), \\ v(x, y) &= \sum_{k=1}^n b_k \sigma_k(x, y), \\ w(x, y) &= \sum_{k=1}^r c_k \zeta_k(x, y) \end{aligned} \quad (1.107 \text{ a, b, c})$$

where  $\xi_k(x, y)$ ,  $o_k(x, y)$ ,  $\zeta_k(x, y)$  are functions that satisfy the prescribed boundary conditions,  $a_k, b_k$  and  $c_k$  are the unknown constants to be determined and  $m, n, r$  the truncation limits of the series expansion.  $\xi_k(x, y)$ ,  $o_k(x, y)$ ,  $\zeta_k(x, y)$  are functions should have at least the same order of derivatives as the differential operators  $L_i$ . Further, performing the variation of the displacements with respect to the unknown constants and taking into account equation Eqs. (1.106 a-c) a system of  $m+n+r$  equations in the unknown coefficient,  $a_k, b_k$  and  $c_k$  is provided. Thus, the unknown coefficients can be obtained and the displacement functions calculated by Eqs. (1.107 a-c).

The Galerkin method does not require the use of the strain energy. In this sense, the Galerkin method appears to be more general than the Ritz Method.

### **1.4.3) Domain Discretization methods**

Domain discretization methods employ computational algorithms for approximately solving problems of mathematical physics. They are often defined as discrete methods, since they require that a body or its boundaries have to be discretized either mathematically or physically. In the following section, among the several numerical methods, only the finite element method and the boundary element method are presented.

The Finite Element Method (FEM) [11] and the Boundary Element Method (BEM) [12, 13] unquestionably represent the most commonly employed and powerful numerical techniques for general structural analysis. Notably, the extensive research efforts in this field from the last few decades devoted to the development of these approaches have allowed the circumvention of most numerical problems associated to the domain or boundary discretization, thus making FEM and BEM the dominant approaches for most problems in computational mechanics.

#### **1.4.3.1) The Finite Element Method (FEM)**

Nowadays, the Finite Element Method (FEM) is the most dominant numerical method in structural analysis. The FEM is based on the concept that the continuum structure under investigation can be replaced by an assembly of discrete elements, i.e. finite elements having well defined displacement and material relationships. The three most common FEM approaches are: (a) FEM based on displacements, (b) mixed or hybrid FEM and (c) equilibrium-FEM. Among them, the most employed method is the displacement approach, wherein the governing set of algebraic equations is expressed in terms of unknown nodal displacements. In the FEM method the elements are connected at only certain points called *nodal points*. Mathematically, the FEM can be treated similarly to the Ritz method. However, the Ritz method is applied to the entire structure under investigation, while in the FEM the Ritz method is applied at each element, which forms the whole structure.

#### **1.4.3.2) The Boundary Element Method (BEM)**

The Boundary element method (BEM) is an emerging numerical solution technique, which has drawn much attention in the last few years. In contrast with the Finite Element Method, which requires the discretization of the entire body in finite elements, the BEM uses element discretization only at the boundaries of the plate. In particular, the governing equation of the system under study is transformed into a set of integral equations on the plate boundary and then these equations are discretized by a finite number of elements located on the boundary. At an interior point of the plate, the governing equation of the plate is satisfied and high accuracy is generally achieved with a relatively small number of boundary elements. This strongly reduces the computational effort of the calculus. Despite the advantages of the BEM, its implementation may be still tedious, since the solution of the system has to be expressed as the sum of a particular integral corresponding to a given loading applied to the plate and of a complementary solution. That solution satisfies the homogeneous partial differential equation corresponding to a load-free plate, subject to certain boundary condition.

## CHAPTER II

# AN INNOVATIVE PROCEDURE FOR THE ANALYSIS OF THIN PLATES OF ARBITRARY SHAPES UNDER STATIC LOADS

### 2.1) Introduction

Many structural problems in engineering mechanics are governed by partial differential equations (PDEs) whose exact solutions are known for a few restricted cases of practical interest.

As discussed in Chapter I, many numerical and analytical methods have been proposed for the solution of plate problems [14-16], since exact solutions are available only for certain shapes, boundary conditions and loading conditions [1].

In the last few decades the extensive research efforts devoted to the development of these approaches, and especially for FEM and BEM methods, have allowed engineers to circumvent most numerical problems associated with domain or boundary discretization.

Nevertheless, the possibility of obtaining numerical solutions for PDEs without resorting to any discretization, that is the so-called meshless approach, has recently gained the attention of scientists and engineers working in this field. As defined in ref [13] a meshless method, also referred to as meshfree method, is a method used to establish system equations for the whole problem domain without the use of a predefined mesh for the domain discretization. This approach has, therefore, become an alternative to the classical FEM and BEM due to some beneficial features such as its flexibility, wide applicability and the possibility of avoiding problems related to meshing and remeshing in the domain or boundary [13, 17].

In this regard, framed in the meshless approach, different procedures have been proposed to solve a variety of engineering problems [18], such as the

element free Galerkin Method [19, 20], the Petrov–Galerkin approach [21], the h-p clouds method [22], and the reproducing kernel element method [23] among others. Further, specifically referring to plate analysis, the works in [24-31] and references therein can be mentioned. Finally, note that other classes of methods, which are inherently meshless, exist for the plate bending problem, including the Trefftz method [32], the pb-2 Rayleigh-Ritz method [33], and the Galerkin method [34].

Additionally, a novel truly meshless procedure, namely the Line Element-less Method (LEM), has been introduced for the analysis of the De Saint Venant pure torsion and flexure-torsion problem for both isotropic and orthotropic materials [35-39]. Notably, this method does not require any discretization, neither in the domain nor in the boundary, and all the involved integrals are simple line integrals. Moreover, the efficiency and efficacy of the LEM has been proven by Barone et al. [40] demonstrating the competitiveness of the method with respect to the Complex Polynomial method (CPM) and the Complex Variable Boundary Element Method (CVBEM) especially when exact solutions exist.

Further, based on the analogy between plates bending under edge moments and beams in torsion [41-43], the aforementioned LEM has recently been employed for the bending problem of simply supported plates subjected to uniformly distributed edge moments [44].

In this Chapter, first, an overview of the LEM method developed for the analysis of the De Saint Venant pure torsion and flexure-torsion of beam problem is presented. Further, the analogy between plates bending under edge moments and beams in torsion is discussed. Finally, the LEM method for the solution of a simply supported plate bent by edge moments is extended for the analysis of arbitrarily shaped plates assuming various boundary conditions (BCs) and subject to transverse loads.

## **2.2) LEM for shear and torsion of beam**

The Line element-less method (LEM) was first presented by Di Paola et al. [35] in 2008 for solving torsion problems of beams. Framed in the complex

analysis context, the authors introduced a new potential function related with the shear stresses, involving the warping function and its harmonic conjugate, which satisfies the field equation in the whole domain without resorting any domain or boundary discretization.

Stresses were expressed by employing the double-ended Laurent series in terms of harmonic polynomials, and the coefficients of the Laurent expansion can be found by employing an element-free weak-form procedure. Specifically, the total square net flux across the border is imposed to be minimum, with respect to the parameters, together with the fulfilment of static equivalence.

The method has been shown to be robust, leading to exact analytical solutions, if these exist, or in the other cases, providing very accurate results using very few terms in the Laurent series.

For the sake of completeness, a brief overview of the classical theory of beam torsion is reported to elucidate the development of the LEM method.

Consider an elastic and isotropic De Saint-Venant bar of arbitrary cross-section, as shown in Figure 2. 1, subjected to the action of a moment  $M_z$ , applied at the end of the bar and causing the twisting of the bar.

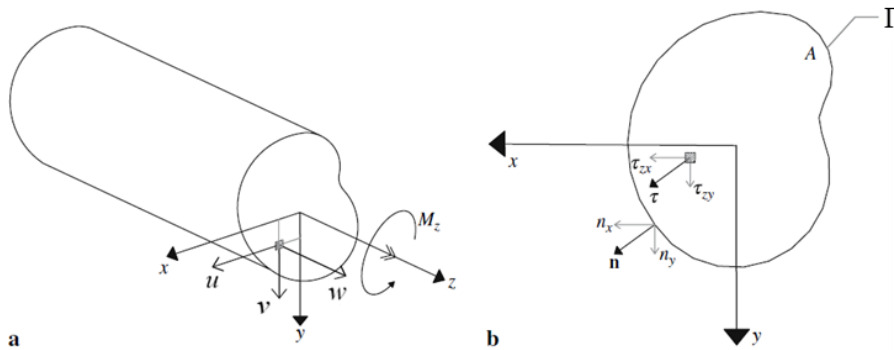


**Figure 2. 1** De Saint Venant cylinder under torsion: a) displacement field; b) stress field [35].

Consider a counter-clockwise coordinate system with  $x$  and  $y$  axes coincident with the principal axes of inertia of the beam's cross-section, and the cross-section being constant along the length. Referring to Figure 2. 1 the displacements  $u$ ,  $v$  and  $w$  of a point  $P(x, y, z)$  can be written as follows:

$$u = -\beta zy; v = \beta zx; w = \beta \omega(x, y); \quad (2.1 \text{ a-c})$$

where  $\beta$  is a constant accounting for the twist rotation of a cross-section per unit length, and where  $\omega(x, y)$  represents the warping function. It is worth noting that,  $\beta$  was assumed to be small. Assuming that the bar is free of stress between its ends, the resulting stress caused by the aforementioned displacement field can be expressed as:

$$\sigma_x = \sigma_y = \sigma_z = \tau_{xy} = 0; \tau_{zx} = G\beta \left( \frac{\partial \omega}{\partial x} - y \right); \tau_{zy} = G\beta \left( \frac{\partial \omega}{\partial y} + x \right); \quad (2.2\text{a-c})$$

where  $\boldsymbol{\tau}^T = [\tau_{zx} \tau_{zy}]$  is the shear stress vector of non-null values, and  $G$  is the shear modulus.

As far as boundary conditions are concerned, the free-traction boundary condition on the contour  $\Gamma$  of the cross-section should be satisfied, i.e.  $\tau_{zx}n_x + \tau_{zy}n_y = \boldsymbol{\tau}^T \mathbf{n} = 0$ , where  $\mathbf{n}^T = [n_x n_y]$  is the outward normal vector to the contour  $\Gamma$ . Further considering the three-dimensional equilibrium equations of elasticity, the warping function can be written as:

$$\frac{\partial}{\partial x} \left[ G\beta \left( \frac{\partial \omega}{\partial x} - y \right) \right] + \frac{\partial}{\partial y} \left[ G\beta \left( \frac{\partial \omega}{\partial y} + x \right) \right] = 0 \text{ in } A \quad (2.3)$$

which leads to the condition which must be satisfied by the warping function  $\omega(x, y)$ :

$$\nabla^2 \omega = \frac{\partial^2 \omega}{\partial x^2} + \frac{\partial^2 \omega}{\partial y^2} = 0 \text{ in } A \quad (2.4)$$

while the free-traction boundary condition in terms of warping function can be presented as:

$$\frac{\partial \omega}{\partial n} = \frac{\partial \omega}{\partial x} n_x + \frac{\partial \omega}{\partial y} n_y = yn_x + xn_y \text{ on } \Gamma \quad (2.5)$$

Therefore, the warping function may be found by solving the *Neumann* problem for the *Laplace* equation:



$$\begin{cases} \nabla^2 \omega = 0 & \text{in } A \\ \frac{\partial \omega}{\partial n} = yn_x - xn_y & \text{on } \Gamma \end{cases} \quad (2.6 \text{ a-b})$$

Since only the stresses  $\tau_{zx}$  and  $\tau_{zy}$  are not null in the case of the torsion problem, an equivalent solution can be achieved employing the Prandtl stress function  $\psi(x, y)$ , so that:

$$\tau_{zx} = \frac{\partial \psi}{\partial y}, \quad \tau_{zy} = -\frac{\partial \psi}{\partial x}, \quad (2.7 \text{ a-b})$$

which allows the torsion problem to be formulated in terms of the *Dirichlet* boundary value problem:

$$\begin{cases} \nabla^2 \psi(x, y) = -2G\beta & \text{in } A \\ \psi(x, y) = 0 & \text{on } \Gamma \end{cases} \quad (2.8 \text{ a-b})$$

A solution for the problem of torsion in terms of the *Dirichlet* boundary value problem can be found employing complex analytical torsion functions. In particular, the authors of [35] presented a novel potential function  $F(\hat{z})$  of the complex variable  $\hat{z} = x + iy$ , where  $i$  is the imaginary unit, for solving the torsion problem:

$$F(\hat{z}) = \tilde{\chi}_x(x, y) + i\tilde{\chi}_y(x, y) \quad (2.9)$$

where  $\tilde{\chi}_x(x, y)$  and  $\tilde{\chi}_y(x, y)$  are:

$$\begin{cases} \tilde{\chi}_x(x, y) = \text{Re}[F(\hat{z})] = \tau_{zx}(x, y) + G\beta y \\ \tilde{\chi}_y(x, y) = \text{Im}[F(\hat{z})] = -\tau_{zy}(x, y) + G\beta x \end{cases} \quad (2.10 \text{ a-b})$$

It is worth noting that  $\tilde{\chi}_x(x, y)$  and  $\tilde{\chi}_y(x, y)$  are harmonic in the domain:

$$\nabla^2 \tilde{\chi}_x(x, y) = 0, \quad \nabla^2 \tilde{\chi}_y(x, y) = 0 \quad \text{in } A \quad (2.11 \text{ a-b})$$

$$\partial \tilde{\chi}_x / \partial x = \partial \tilde{\chi}_y / \partial y, \quad \partial \tilde{\chi}_x / \partial y = -\partial \tilde{\chi}_y / \partial x \quad \text{in } A \quad (2.12 \text{ a-b})$$

Substituting Eqs. (2.10 a-b) into Eqs. (2.11 a-b), the compatibility equations for  $\tau_{zy}$  and  $\tau_{zx}$  can be obtained. Moreover, the Cauchy-Riemann conditions (Eqs. (2.12 a-b)) leads to the fulfilment of the equilibrium and compatibility conditions in the domain.

With regard to the potential  $F(\hat{z})$ ,  $F(\hat{z})$  is analytical in the entire domain and may be expanded in the double-ended Laurent series as:

$$F(\hat{z}) = \sum_{k=-\infty}^{+\infty} \alpha_k (\hat{z} - \hat{z}_0)^k, \quad \alpha_k, \hat{z}_0 \in \mathbb{C} \quad (2.13)$$

$\sum_{k=0}^{+\infty} \alpha_k (\hat{z} - \hat{z}_0)^k$  is called the *regular part* and it is capable of expressing any analytical function everywhere. The summation  $\sum_{k=-\infty}^{-2} \alpha_k (\hat{z} - \hat{z}_0)^k$  is called the *principal part* and it accounts for singularities in  $\hat{z}_0$ . As presented in [36] the term  $k = -1$  has to be neglected, because it returns multi-valued functions.

Powers  $(\hat{z})^k$  can be expressed as  $P_k = P_k + iQ_k$ , where  $P_k$  and  $Q_k$  are *harmonic polynomials* defined as follows:

$$P_k(x, y) = \text{Re}(x + iy)^k \quad (2.14 \text{ a})$$

$$Q_k(x, y) = \text{Im}(x + iy)^k \quad (2.14 \text{ b})$$

or, recursively as

$$P_k(x, y) = P_{k-1}x - Q_{k-1}y \quad (2.15 \text{ a})$$

$$Q_k(x, y) = Q_{k-1}x + P_{k-1}y \quad (2.15 \text{ b})$$

which are valid for  $k > 0$ , and with  $P_0 = 1$  and  $Q_0 = 0$ .

Further, the derivatives of the harmonic polynomials are

$$\frac{\partial P_k}{\partial x} = kP_{k-1}; \quad \frac{\partial P_k}{\partial y} = -kQ_{k-1} \quad (2.16 \text{ a-b})$$

$$\frac{\partial Q_k}{\partial x} = kQ_{k-1}; \quad \frac{\partial Q_k}{\partial y} = kP_{k-1} \quad (2.16 \text{ b-c})$$

$$\nabla^2 P_k = 0; \quad \nabla^2 Q_k = 0 \quad \forall k \quad (2.16 \text{ d-e})$$

Thus, the complex potential function  $F(\hat{z})$  and the shear stress field can be expressed in terms of harmonic polynomials. By letting  $\alpha_k = a_k + ib_k$  ( $a_k, b_k \in \mathbb{R}$ ), the unknown coefficients  $a_k, b_k$  of the harmonic polynomials can be found by

satisfying the free-stress boundary condition minimizing the squared value net flux of the shear stress vector  $\tau$  through the boundary of the domain

$$\mathfrak{J}(a_k, b_k, \beta) = \oint_{\Gamma} (\tau^T \mathbf{n})^2 d\Gamma \quad (2.17)$$

taking into account the static equivalence condition:

$$\int_A \tau^T \mathbf{g} dA = M_z \quad (2.18)$$

where  $\mathbf{g}^T = [-y \ x]$ .

Finally, considering the Green's lemma, surface integrals are converted into line integrals avoiding any discretization of the inner domain. The variational procedure of the potential function combined with the static equivalence condition and the use of line integrals leads to a system of algebraic equations from which the unknown constant can be found and the torsion problem of beam solved.

### 2.3) The analogy between the torsion beam problem and the plate bending problem

The harmonic partial differential equation, which describes the behaviour of an isotropic thin plate Eq. (1.54) can be decomposed in the two second order partial differential equations Eqs. (1.59-60). Many analogies between the Saint Venant-type torsion of beams and the bending of thin plates problems have been presented in literature [41-43]. In particular, a very useful analogy was presented by Murtha-Smith [41] for a studying simply supported Lagrange Kirchhoff type plate loaded by uniformly distributed edge moments.

Specifically, referring to Eqs. (1.59-60) and Eqs. (2.8 a-b), a relation between the Prandtl function and both the moment sum  $M(x, y)$  and the plate deflection  $w(x, y)$  can be noted:

$$\psi(x, y) = v_1 M(x, y) \quad (2.19a)$$

$$\psi(x, y) = v_2 w(x, y) \quad (2.19b)$$

where  $v_1$  and  $v_2$  are constants, thus

$$2G\beta = v_1 q \quad (2.20a)$$

$$2G\beta = v_2 \frac{M}{D} \quad (2.20b)$$

In the general case of a plate, the moment sum  $M$  varies along the plate surface and thus, appropriate analogous functions have to be defined. In the case of simply supported plate bent by moments  $M_n$  uniformly distributed along the plate edges and without any transversal loads ( $q=0$ ), the analogy between the beam and plate is easier to be carried out.

Specifically, in this case, where  $\Gamma$  is the contour of an arbitrarily shaped plate,  $M = M_n$  at all points of the contour. Therefore, Eq. (1.60) becomes:

$$\frac{\partial^2 w}{\partial x^2} + \frac{\partial^2 w}{\partial y^2} = -\frac{M_n}{D} \quad (2.21)$$

Therefore, Eq. (2.20 b) becomes:

$$2G\beta = v_2 \frac{M_n}{D} \quad (2.22)$$

and

$$\psi(x, y) = \left( \frac{2G\beta D}{M_n} \right) w(x, y) \quad (2.23)$$

Therefore, a solution of simply supported plates bent by uniformly distributed moments at all its edges can be found by means of similar numerical and analytical method employed in the case of beam torsion problem.

## **2.4) LEM for plates**

### **2.4.1) LEM for simply supported plates**

Based on the plate analogy discussed in Section 2.3, the LEM method introduced in 2.1 for the problem of Saint Venant beams in torsion has been successfully extended for the analysis of the plate bending problem [45]. Later, Pirrotta et al. [44] also applied a novel plate deflection function through series

expansion in terms of harmonic polynomials for the solution of a thin simply supported plate.

Considering a simply supported isotropic and elastic plate loaded by uniformly distributed edge moments  $M_n$ , recalling the harmonic polynomials  $P_k$  and  $Q_k$ , whose properties are expressed in Eqs. (2.14-16), the deflection functions can be written in terms of series of harmonic polynomials as follows:

$$w(x, y) = \sum_{k=0}^n a_k P_k(x, y) + \sum_{k=0}^n b_k Q_k(x, y) - \frac{M_n}{4D} (x^2 + y^2) \quad (2.24)$$

which requires the evaluation of  $(2n-1)$  coefficients  $a_k, b_k$ .

In the plate analysis, these constants can be found by fulfilling the boundary constrains. Specifically, for a plate which is simply supported at its edges, the closed path integral of the squared displacement function could be set to be null:

$$\mathfrak{I}(a_k, b_k) = \oint_C [w(x, y)]^2 d\Gamma = \min(a_k, b_k) \quad (2.25)$$

Finally, by performing the variations of the above functional with respect to the unknown coefficients, a linear algebraic system of equations is obtained, by which coefficients can be calculated and the problem solved.

#### **2.4.2) LEM extension for the analysis of arbitrarily shaped plates with different boundary conditions.**

As discussed above, the LEM represents a very powerful method to accurately solve problems in structural mechanics. Therefore, an extension of the LEM approach for the analysis of arbitrary shaped plates, without holes, with general boundary conditions (BCs), under a transverse load  $q(x, y)$  has been carried out. Specifically, considering a homogeneous isotropic thin plate, of arbitrary shape with contour  $\Gamma$  and domain  $\Omega$ , uniform thickness  $h$  and modulus of elasticity  $E$ , (Figure 2. 2), based on the classical applications of the LEM [35-37, 46] and taking into account Eqs. (1.59-60),  $M(x, y)$  and  $w(x, y)$  can be

expressed in terms of the aforementioned harmonic polynomials  $P_k$  and  $Q_k$ , defined in Eqs. (2.14-2.16).

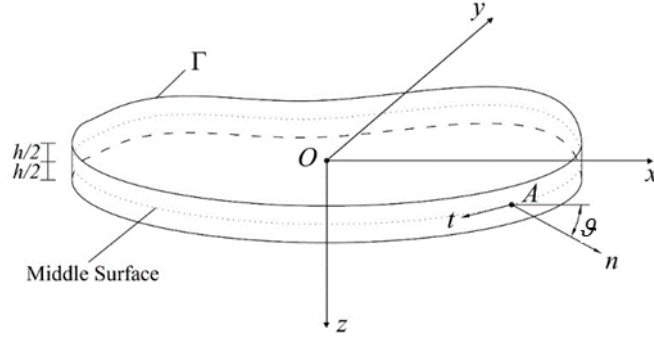


**Figure 2. 2** Plate with an arbitrary shape.

It can be argued that a solution of Eq. (1.59), can be obtained expressing the moment sum function as the sum of harmonic polynomials, which satisfy the Laplace equation as in Eq. (2.16 d-e), and a particular solution of Poisson's equation Eq. (1.59), namely  $M_p(x, y)$ ; that is

$$M(x, y) = \sum_{k=0}^n a_k P_k(x, y) + \sum_{k=1}^n b_k Q_k(x, y) + M_p(x, y) \quad (2.26)$$

where  $a_k$  and  $b_k$  are  $(2n+1)$  unknown coefficients to be determined, and  $n$  is an integer number which denotes the truncation limit of the series expansion.

Further, introducing the vectors

$$\mathbf{p}_n(x, y) = \begin{bmatrix} P_0(x, y) \\ \vdots \\ P_n(x, y) \end{bmatrix}; \quad \mathbf{q}_n(x, y) = \begin{bmatrix} Q_1(x, y) \\ \vdots \\ Q_n(x, y) \end{bmatrix}; \quad (2.27)$$

$$\mathbf{a} = \begin{bmatrix} a_0 \\ \vdots \\ a_n \end{bmatrix}; \quad \mathbf{b} = \begin{bmatrix} b_1 \\ \vdots \\ b_n \end{bmatrix}$$

Eq. (2.26) can conveniently be rewritten in compact form as

$$M(x, y) = \mathbf{r}_n \boldsymbol{\eta} + M_p(x, y) \quad (2.28)$$

where

$$\mathbf{r}_n = [\mathbf{p}_n^T \quad \mathbf{q}_n^T]; \quad \boldsymbol{\eta} = \begin{bmatrix} \mathbf{a} \\ \mathbf{b} \end{bmatrix} \quad (2.29)$$

are vectors containing the harmonic polynomials and the unknown coefficients, respectively.

Note that, as far as the particular solution to  $M_p(x, y)$  of Eq. (1.59) is concerned, this can be obtained in closed-form using the approach in [47], when the load function  $q(x, y)$  is represented by a homogeneous polynomial of degree  $N$ ; i.e.

$$q(x, y) = \sum_{k=0}^N A_k x^{N-k} y^k \quad (2.30)$$

where  $A_k$  are known coefficients which depend on the form of the assigned load.

Specifically, considering a Poisson's equation of the form

$$\nabla^2 f(x, y) = q(x, y) \quad (2.31)$$

where  $q(x, y)$  is a generic homogeneous polynomial of degree  $N$  given as Eq. (2.30), a closed form particular solution of Eq. (2.31):

$$f_p(x, y) = \sum_{k=0}^N \tilde{P}_k x^{N-k+2} y^k \quad (2.32)$$

which is a polynomial of degree  $N$ , where the coefficients  $\tilde{P}_k$  are

$$\tilde{P}_k = \sum_{m=0}^{\lfloor (N-k)/2 \rfloor} \frac{(-1)^m (k+2m)! (N-k-2m)!}{k! (N-k+2)!} A_{k+2m}; \quad 1 \leq k \leq N \quad (2.33)$$

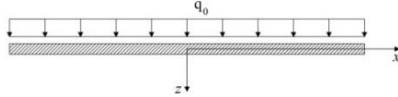
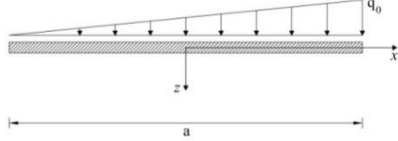
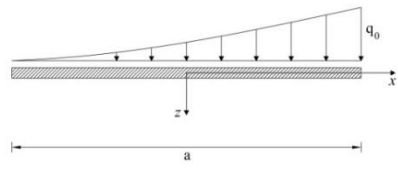
Note that, in Eq. (2.33) the term  $\lfloor (N-k)/2 \rfloor$  denotes the integer part of  $(N-k)/2$ .

It is worth mentioning that, when  $q(x, y)$  is not directly given, as in Eq. (2.30), the particular solution in Eq. (2.32) can still be used if  $q(x, y)$  is firstly appropriately approximated by a truncated series of Chebyshev polynomials [48, 49].

Clearly, this yields a quite versatile tool for expressing various shapes of load distributions, and even concentrated loads. For completeness' sake, expressions of  $M_p(x, y)$  are reported in Table 2. 1 for some common cases of transverse distributed loads  $q(x, y)$ .

As far as the unknown coefficients in Eq. (2.26) or (2.28) are concerned, the  $(2n + 1)$  values of  $a_k$  and  $b_k$  in the vector  $\boldsymbol{\eta}$  can be determined appropriately imposing the specified BCs of the plate. In this context, it is convenient to firstly consider the simplified case of polygonal plate with simply-supported edges, which will be then further generalized to arbitrary shaped plates with any boundary conditions.

**Table 2. 1** Particular solution of Eq. (1.59) for different distributed loads.

Type of load	Load function	Particular solution
<p><i>Uniform</i></p> 	$q(x, y) = q_0$	$M_p(x, y) = -\frac{q_0}{4}(x^2 + y^2)$
<p><i>Triangular</i></p> 	$q(x, y) = q_0 \left( \frac{1}{2} + \frac{x}{a} \right)$	$M_p(x, y) = -\frac{q_0}{2} \left( \frac{x^2}{2} + \frac{x^3}{3a} \right)$
<p><i>Parabolic</i></p> 	$q(x, y) = \frac{q_0}{a^2} \left( x^2 + ax + \frac{a^2}{4} \right)$	$M_p(x, y) = -\frac{q_0}{2} \left( \frac{x^2}{4} + \frac{x^3}{3a} + \frac{x^4}{6a^2} \right)$



### 2.4.2.1) Simply-supported polygonal plate

Let the plate be of a polygonal shape and with all the edges simply-supported, transversely loaded and free of moments at the edges. As discussed in Section 2.3, since in this case the moment sum function must be zero along the entire contour of the polygonal plate, the following relation holds

$$M_n(x, y) = M(x, y) = 0, \quad \text{in } \Gamma \quad (2.34)$$

Taking into account Eq. (2.34), it is feasible to evaluate these unknown coefficients  $\boldsymbol{\eta}$  in Eq. (2.28) applying a minimization procedure on the closed contour path integral of the squared moment sum function:

$$\Psi(\boldsymbol{\eta}) = \oint_{\Gamma} [M(x, y)]^2 d\gamma \quad (2.35)$$

Thus, introducing Eq. (2.28) into Eq. (2.35), the functional can be recast as

$$\Psi(\boldsymbol{\eta}) = \oint_{\Gamma} [(\mathbf{r}_n \boldsymbol{\eta})^2 + M_p^2(x, y) + 2\mathbf{r}_n \boldsymbol{\eta} M_p(x, y)] d\gamma \quad (2.36)$$

Further, performing variations of the above functional with respect to  $\boldsymbol{\eta}$ , yields:

$$\frac{\partial \Psi(\boldsymbol{\eta})}{\partial \boldsymbol{\eta}} = \mathbf{Q}_n \boldsymbol{\eta} + \boldsymbol{\tau} = \mathbf{0} \quad (2.37)$$

which is a linear algebraic system in the unknowns  $\boldsymbol{\eta}$ , where

$$\mathbf{Q}_n = 2 \oint_{\Gamma} \mathbf{r}_n^T \mathbf{r}_n d\gamma \quad (2.38)$$

$$\boldsymbol{\tau} = 2 \oint_{\Gamma} \mathbf{r}_n^T M_p(x, y) d\gamma \quad (2.39)$$

In this manner the vector  $\boldsymbol{\eta}$  can be directly evaluated as:

$$\boldsymbol{\eta} = -\mathbf{Q}_n^{-1} \boldsymbol{\tau} \quad (2.40)$$

and, taking into account Eq. (2.28), the moment sum function can be expressed as

$$M(x, y) = -\mathbf{r}_n \mathbf{Q}_n^{-1} \boldsymbol{\tau} + M_p(x, y) \quad (2.41)$$

Once  $M(x, y)$  is determined, the deflection function  $w(x, y)$  can be obtained solving Eq. (1.60). Specifically, as is performed similarly for the

moment sum function, a solution of Eq. (1.60) can be found by assuming  $w(x, y)$  as the sum of harmonic polynomials, and a particular solution of the Poisson's equation Eq. (1.60), namely  $w_p(x, y)$ ; that is

$$w(x, y) = \sum_{k=0}^m c_k P_k(x, y) + \sum_{k=1}^m d_k Q_k(x, y) + w_p(x, y) \quad (2.42)$$

where  $c_k$  and  $d_k$  are  $(2m+1)$  unknown coefficients to be determined, and  $m$  is an integer number which denotes the truncation limit of the series expansion.

Again, note that the particular solution  $w_p(x, y)$  can be evaluated by applying the procedure in [47] considering the obtained moment sum function  $M(x, y)$  in Eq. (2.41).

As far as the unknown coefficients in Eq. (2.42) are concerned, the  $(2m+1)$  values of  $c_k$  and  $d_k$  are determined appropriately by imposing the BCs. In this regard, Eq. (2.42) can conveniently be rewritten in compact form as

$$w(x, y) = \mathbf{r}_m \boldsymbol{\xi} + w_p(x, y) \quad (2.43)$$

where  $\boldsymbol{\xi}^T = [\mathbf{c}^T \quad \mathbf{d}^T]$  is the vector containing the unknown coefficients, and:

$$\begin{aligned} \mathbf{r}_m = [\mathbf{p}_m^T \quad \mathbf{q}_m^T]; \quad \mathbf{p}_m(x, y) = \begin{bmatrix} P_0(x, y) \\ \vdots \\ P_m(x, y) \end{bmatrix}; \quad \mathbf{q}_m(x, y) = \begin{bmatrix} Q_1(x, y) \\ \vdots \\ Q_m(x, y) \end{bmatrix}; \\ \mathbf{c} = \begin{bmatrix} c_0 \\ \vdots \\ c_m \end{bmatrix}; \quad \mathbf{d} = \begin{bmatrix} d_1 \\ \vdots \\ d_m \end{bmatrix} \end{aligned} \quad (2.44)$$

Therefore, considering that for a simply-supported plate Eq. (1.86 a) holds, the vector  $\boldsymbol{\xi}$  can be found by minimising the closed contour path integral of the squared deflection function; that is

$$\Theta(\boldsymbol{\xi}) = \oint_{\Gamma} [w(x, y)]^2 d\gamma \quad (2.45)$$

Introducing Eq. (2.43) into Eq. (2.45), and performing variation with respect to the unknown coefficients leads to an algebraic linear system in terms of the unknowns  $\xi$ , as:

$$\frac{\partial \Theta(\xi)}{\partial \xi} = \mathbf{Q}_m \xi + \lambda = \mathbf{0} \quad (2.46)$$

where

$$\mathbf{Q}_m = 2 \oint_{\Gamma} \mathbf{r}_m^T \mathbf{r}_m \, d\gamma \quad (2.47)$$

$$\lambda = 2 \oint_{\Gamma} \mathbf{r}_m^T w_p(x, y) \, d\gamma \quad (2.48)$$

Finally, obtaining the vector  $\xi$  from Eq. (2.46) as

$$\xi = -\mathbf{Q}_m^{-1} \lambda \quad (2.49)$$

and substituting into Eq. (2.43), yields the deflection function of the plate  $w(x, y)$  as:

$$w(x, y) = -\mathbf{r}_m \mathbf{Q}_m^{-1} \lambda + w_p(x, y) \quad (2.50)$$

Note that if the number of terms in Eq. (2.42) corresponds to that of Eq. (2.26), that is if  $n = m$ , then  $\mathbf{r}_m = \mathbf{r}_n$  and  $\mathbf{Q}_m = \mathbf{Q}_n$ ; thus, in this case it is only necessary to compute  $\mathbf{Q}_n$  via Eq. (2.38) once beforehand.

#### 2.4.2.2) General plate analysis

As previously mentioned, the above discussed procedure is strictly valid for polygonal plates with all edges simply-supported. In this case, in fact, both the moment sum and the deflection functions must be null on the contour, that is  $M(x, y) = 0$  and  $w(x, y) = 0$  in  $\Gamma$ . Notably, these properties allow the functionals  $\Psi(\boldsymbol{\eta})$  and  $\Theta(\xi)$  to be expressed as in Eqs. (2.35) and (2.45), respectively.

Clearly, in the generic case of arbitrarily shaped plates with any BCs, neither  $M(x, y)$  nor  $w(x, y)$  will equal zero on the entire contour, and hence Eqs. (2.40, 2.49) cannot be directly used to find the unknown coefficients. This is, for

instance, the case of a plate with curved boundaries ( $M(x, y) \neq 0$  in  $\Gamma$ ), in which at least one edge can undergo vertical deflections ( $w(x, y) \neq 0$  in  $\Gamma$ ). Therefore, the possibility of the moment sum or the deflection functions being present in  $\Gamma$  should be appropriately accounted for in the evaluation of the unknown coefficients.

In this regard, assuming that the plate boundary conditions are the same on the entire contour  $\Gamma$ , the functional in Eq. (2.35) can be properly modified as

$$\tilde{\Psi}(\boldsymbol{\eta}) = \oint_{\Gamma} [M(x, y) - \tilde{M}(x, y)]^2 d\gamma \quad (2.51)$$

where  $M(x, y)$  is given in Eq. (2.26) and  $\tilde{M}(x, y)$  is an additional function, conventionally introduced to take into account the generic plate boundary conditions. As is apparent from Eq. (2.51), this function represents the pertinent moment sum function evaluated on the boundary. For consistency,  $\tilde{M}(x, y)$  can be expressed in terms of harmonic polynomials as

$$\tilde{M}(x, y) = \sum_{k=0}^{\tilde{n}} \tilde{a}_k P_k(x, y) + \sum_{k=1}^{\tilde{n}} \tilde{b}_k Q_k(x, y) \quad (2.52)$$

in which  $\tilde{a}_k$  and  $\tilde{b}_k$  are unknown coefficients to be determined, while  $\tilde{n}$  is an integer number denoting the truncation limit of the series expansion, with  $\tilde{n} < n$  and it is generally small.

Denoting these as:

$$\begin{aligned} \mathbf{p}_{\tilde{n}}(x, y) &= \begin{bmatrix} P_0(x, y) \\ \vdots \\ P_{\tilde{n}}(x, y) \end{bmatrix}; \quad \mathbf{q}_{\tilde{n}}(x, y) = \begin{bmatrix} Q_1(x, y) \\ \vdots \\ Q_{\tilde{n}}(x, y) \end{bmatrix}; \\ \tilde{\mathbf{a}} &= \begin{bmatrix} \tilde{a}_0 \\ \vdots \\ \tilde{a}_{\tilde{n}} \end{bmatrix}; \quad \tilde{\mathbf{b}} = \begin{bmatrix} \tilde{b}_1 \\ \vdots \\ \tilde{b}_{\tilde{n}} \end{bmatrix} \end{aligned} \quad (2.53)$$

Eq. (2.52) can conveniently be rewritten in compact form as

$$\tilde{M}(x, y) = \mathbf{s}_{\tilde{n}} \tilde{\boldsymbol{\eta}} \quad (2.54)$$

where

$$\mathbf{s}_{\tilde{n}} = [\mathbf{p}_{\tilde{n}}^T \quad \mathbf{q}_{\tilde{n}}^T]; \quad \tilde{\boldsymbol{\eta}} = \begin{bmatrix} \tilde{\mathbf{a}} \\ \tilde{\mathbf{b}} \end{bmatrix} \quad (2.55)$$

Clearly, as shown in Figure 2. 3, if the plate's BCs vary on the contour  $\Gamma$ , it is feasible to appropriately subdivide  $\Gamma$  in the  $N_\gamma$  edges  $\Gamma_i$  on which the BCs remain constant, that is  $\Gamma = \bigcup_{i=1}^{N_\gamma} \Gamma_i$ .

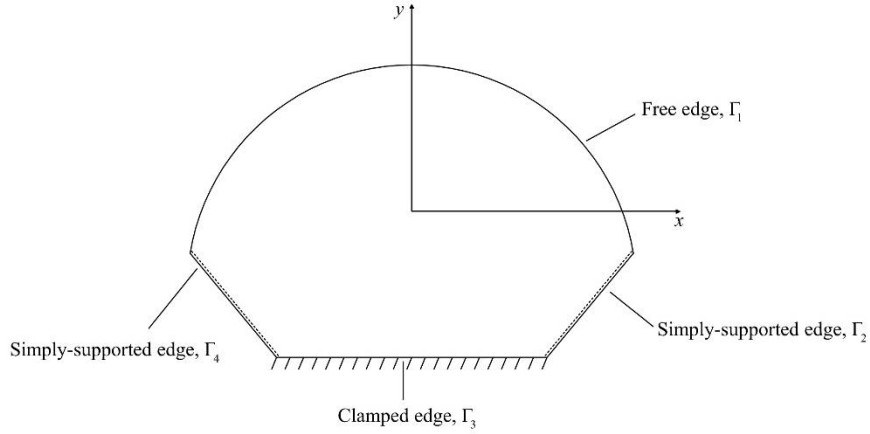


**Figure 2. 3** Arbitrary shaped plate with mixed BCs and  $N_\gamma = 4$ .

Therefore, the functional in Eq. (2.51) becomes:

$$\tilde{\Psi}(\boldsymbol{\eta}) = \sum_{i=1}^{N_\gamma} \int_{\Gamma_i} [M(x, y) - \tilde{M}_i(x, y)]^2 d\gamma \quad (2.56)$$

where the symbol  $\int_{\Gamma_i} (\cdot) d\gamma$  denotes the classical line integration and, similarly to

Eq. (2.54), the function  $\tilde{M}_i(x, y)$ , representing the moment sum function on the corresponding edge, is given by:

$$\tilde{M}_i(x, y) = \mathbf{s}_{\tilde{n}} \tilde{\boldsymbol{\eta}}_i; \quad i = 1, \dots, N_\gamma \quad (2.57)$$

where the subscript  $i$  refers to the  $i$ -th edge  $\Gamma_i$ . It is worth stressing that, as previously mentioned,  $\tilde{M}_i(x, y)$  equals zero only for simply-supported straight edges.

Taking into account Eqs. (2.28) and (2.57) and substituting into Eq. (2.56), yields

$$\tilde{\Psi}(\boldsymbol{\eta}) = \sum_{i=1}^{N_y} \int_{\Gamma_i} \left[ \mathbf{r}_n \boldsymbol{\eta} + M_p(x, y) - \mathbf{s}_n \tilde{\boldsymbol{\eta}}_i \right]^2 d\gamma \quad (2.58)$$

Analogously, to allow for the possibility of vertical deflections on the contour, the functional in Eq. (2.45) can be properly modified as:

$$\tilde{\Theta}(\boldsymbol{\xi}) = \sum_{i=1}^{N_y} \int_{\Gamma_i} \left[ w(x, y) - \tilde{w}_i(x, y) \right]^2 d\gamma \quad (2.59)$$

where  $w(x, y)$  is given in Eq. (2.42) and  $\tilde{w}_i(x, y)$  is an additional function, conveniently introduced to take into account the possibility of boundary deflections. Similarly to  $\tilde{M}(x, y)$  in Eq. (2.51),  $\tilde{w}_i(x, y)$  represents the pertinent deflection function evaluated on the boundary. Expressing  $\tilde{w}_i(x, y)$  in terms of harmonic polynomials, yields

$$\tilde{w}_i(x, y) = \sum_{k=0}^{\tilde{m}} \tilde{c}_{k,i} P_k(x, y) + \sum_{k=1}^{\tilde{m}} \tilde{d}_{k,i} Q_k(x, y); \quad i = 1, \dots, N_y \quad (2.60)$$

in which  $\tilde{c}_{k,i}$  and  $\tilde{d}_{k,i}$  are unknown coefficients to be determined, while  $\tilde{m}$  is the chosen truncation limit of the series expansion, with  $\tilde{m} < m$  and it is generally small.

Denoting these as:

$$\mathbf{p}_{\tilde{m}}(x, y) = \begin{bmatrix} P_0(x, y) \\ \vdots \\ P_{\tilde{m}}(x, y) \end{bmatrix}; \quad \mathbf{q}_{\tilde{m}}(x, y) = \begin{bmatrix} Q_1(x, y) \\ \vdots \\ Q_{\tilde{m}}(x, y) \end{bmatrix};$$

$$\tilde{\mathbf{c}}_i = \begin{bmatrix} \tilde{c}_{0,i} \\ \vdots \\ \tilde{c}_{\tilde{m},i} \end{bmatrix}; \quad \tilde{\mathbf{d}}_i = \begin{bmatrix} d_{1,i} \\ \vdots \\ \tilde{b}_{\tilde{m},i} \end{bmatrix} \quad (2.61)$$

Eq. (2.60) can conveniently be rewritten in compact form as

$$\tilde{w}_i(x, y) = \mathbf{s}_{\tilde{m}} \tilde{\xi}_i; \quad i = 1, \dots, N_\gamma \quad (2.62)$$

where

$$\mathbf{s}_{\tilde{m}} = \begin{bmatrix} \mathbf{p}_{\tilde{m}}^T & \mathbf{q}_{\tilde{m}}^T \end{bmatrix}; \quad \tilde{\xi}_i = \begin{bmatrix} \tilde{\mathbf{c}}_i \\ \tilde{\mathbf{d}}_i \end{bmatrix} \quad (2.63)$$

Further, taking into account Eqs. (2.43) and (2.62) and substituting them into Eq. (2.59), the functional is obtained in the form:

$$\tilde{\Theta}(\xi) = \sum_{i=1}^{N_\gamma} \int_{\Gamma_i} \left[ \mathbf{r}_m \xi + w_p(x, y) - \mathbf{s}_{\tilde{m}} \tilde{\xi}_i \right]^2 d\gamma \quad (2.64)$$

Note that, the additional function  $\tilde{w}_i(x, y)$  in Eq. (2.59) must be taken into account only for the plate edges  $\Gamma_i$  which can undergo vertical deflections (such as for a free edge). Therefore, unless at least one edge is allowed to move vertically,  $\tilde{w}_i(x, y) = 0 \forall i$ , that is  $\tilde{\xi}_i = 0$ , and the functional in Eq. (2.59) reverts to the more simple one in Eq. (2.45).

As far as the solution procedure is concerned, a three steps scheme can be followed.

The first step is associated with the solution of Eq. (1.59), which leads to the momentum sum function  $M(x, y)$ . In this regard, minimising the functional in Eq. (2.58), that is performing the variation of the functional with respect to the unknown coefficients  $\boldsymbol{\eta}$ , yields:

$$\frac{\partial \tilde{\Psi}(\boldsymbol{\eta})}{\partial \boldsymbol{\eta}} = \mathbf{Q}_n \boldsymbol{\eta} + \boldsymbol{\tau} - \sum_{i=1}^{N_\gamma} \tilde{\mathbf{Q}}_{n,i} \tilde{\boldsymbol{\eta}}_i = \mathbf{0} \quad (2.65)$$

which is an algebraic linear system of equations, where:

$$\tilde{\mathbf{Q}}_{n,i} = 2 \int_{\Gamma_i} \mathbf{r}_n^T \mathbf{s}_{\tilde{m}} d\gamma; \quad i = 1, \dots, N_\gamma \quad (2.66)$$

Equation (2.65) can equivalently be rewritten as:

$$\boldsymbol{\eta} = -\mathbf{Q}_n^{-1} \boldsymbol{\tau} + \sum_{i=1}^{N_\gamma} \mathbf{Q}_n^{-1} \tilde{\mathbf{Q}}_{n,i} \tilde{\boldsymbol{\eta}}_i \quad (2.67)$$

to express the coefficients  $\boldsymbol{\eta}$  in terms of the vectors  $\tilde{\boldsymbol{\eta}}_i$ .

Note that, as previously stated, if the plate's BCs do not vary on the contour  $\Gamma$ , the functional in Eq. (2.51) should be used instead of the one in Eq. (2.58); thus, in this case,  $N_\gamma = 1$  and the line integral in Eq. (2.66) simply reverts to a contour integral in  $\Gamma$ .

In this manner, considering Eq. (2.28) the moment sum function  $M(x, y)$  can be directly expressed as:

$$M(x, y) = -\mathbf{r}_n \mathbf{Q}_n^{-1} \boldsymbol{\tau} + \sum_{i=1}^{N_\gamma} \mathbf{r}_n \mathbf{Q}_n^{-1} \tilde{\mathbf{Q}}_{n,i} \tilde{\boldsymbol{\eta}}_i + M_p(x, y) \quad (2.68)$$

and a particular solution of Eq. (1.60)  $w_p(x, y)$ , which is required for the definition of the functional in Eq. (2.64), can be evaluated following the approach in [47]. It is worth stressing that, since  $M(x, y)$  depends on  $\tilde{\boldsymbol{\eta}}_i$  as shown in Eq. (2.68), also  $w_p(x, y)$  will be a function of the unknown  $\tilde{\boldsymbol{\eta}}_i$ . To directly express this dependence, hereinafter the particular solution will be denoted as  $w_p(x, y, \tilde{\boldsymbol{\eta}}_i)$ .

The second step is associated with the solution of Eq. (1.60), which yields the deflection function  $w(x, y)$ . In this regard, the variation of the functional in Eq. (2.64), with respect to the unknown coefficients  $\boldsymbol{\xi}$ , can be performed as:

$$\frac{\partial \tilde{\Psi}(\boldsymbol{\xi})}{\partial \boldsymbol{\xi}} = \mathbf{Q}_m \boldsymbol{\xi} + \boldsymbol{\lambda} - \sum_{i=1}^{N_\gamma} \tilde{\mathbf{Q}}_{m,i} \tilde{\boldsymbol{\xi}}_i = \mathbf{0} \quad (2.69)$$

Where:

$$\tilde{\mathbf{Q}}_{m,i} = 2 \int_{\Gamma_i} \mathbf{r}_m^T \mathbf{s}_{\tilde{m}} d\gamma; \quad i = 1, \dots, N_\gamma \quad (2.70)$$

this solution leads to the coefficients  $\boldsymbol{\xi}$  in terms of the unknowns  $\tilde{\boldsymbol{\xi}}_i$ , that is

$$\boldsymbol{\xi} = -\mathbf{Q}_m^{-1} \boldsymbol{\lambda} + \sum_{i=1}^{N_\gamma} \mathbf{Q}_m^{-1} \tilde{\mathbf{Q}}_{m,i} \tilde{\boldsymbol{\xi}}_i \quad (2.71)$$



Once these coefficients are found, the deflection function  $w(x, y)$  can be evaluated through the substitution of Eq. (2.71) into Eq. (2.43):

$$w(x, y) = -\mathbf{r}_m \mathbf{Q}_m^{-1} \boldsymbol{\lambda} + \sum_{i=1}^{N_y} \mathbf{r}_m \mathbf{Q}_m^{-1} \tilde{\mathbf{Q}}_{m,i} \tilde{\boldsymbol{\xi}}_i + w_p(x, y, \tilde{\boldsymbol{\eta}}_i) \quad (2.72)$$

Finally, the unknown terms  $\tilde{\boldsymbol{\eta}}_i$  and  $\tilde{\boldsymbol{\xi}}_i$  can be obtained by imposing the appropriately specified BCs on the edges  $\Gamma_i$  for which the additional functions  $\tilde{M}_i(x, y)$  and  $\tilde{w}_i(x, y)$  have been introduced. Specifically, for the most common cases, taking into account Eqs. (1.85 a, b, 1.86 a, b) and (1.89 a, b), the following functionals can be defined for each edge  $\Gamma_i$  of the whole plate contour  $\Gamma$

- i. Simply-supported curved edge

$$\Xi_i(\tilde{\boldsymbol{\eta}}_i) = \int_{\Gamma_i} [M_n(x, y)]^2 d\gamma \quad (2.73)$$

- ii. Clamped edge

$$\Xi_i(\tilde{\boldsymbol{\eta}}_i) = \int_{\Gamma_i} \left[ \frac{\partial w(x, y)}{\partial n} \right]^2 d\gamma \quad (2.74)$$

- iii. Free edge

$$\Xi_i(\tilde{\boldsymbol{\eta}}_i) = \int_{\Gamma_i} [M_n(x, y)]^2 d\gamma \quad (2.75)$$

$$\Lambda_i(\tilde{\boldsymbol{\xi}}_i) = \int_{\Gamma_i} [\tilde{V}_n(x, y)]^2 d\gamma \quad (2.76)$$

Note that, taking advantage of the properties of the harmonic polynomials, and considering the general expression of the deflection function in Eq. (2.72), all the aforementioned BCs in Eqs. (2.73) and (2.74-2.76) can be appropriately represented in compact matrix form. In this regard, for simplicity's sake, the resulting expressions are reported in Appendix A.

In this context, observe that even more complex BCs, such as guided-end conditions, elastically restrained edges or imposed deflections, can be taken into account in a similar manner. Further, variations of the BCs on the same edge  $\Gamma_i$

can be considered as well, appropriately subdividing the pertinent edge  $\Gamma_i$  in the corresponding part on which the BCs remain constant.

Clearly, minimising the above defined functionals, that is performing the variation with respect to the unknown coefficients  $\tilde{\eta}_i$  and  $\tilde{\xi}_i$ , as

$$\frac{\partial \Xi_i(\tilde{\eta}_i)}{\partial \tilde{\eta}_i} = \mathbf{0} \quad (2.77a)$$

$$\frac{\partial \Lambda_i(\tilde{\xi}_i)}{\partial \tilde{\xi}_i} = \mathbf{0} \quad (2.77b)$$

yields an algebraic linear system of equations in terms of  $\tilde{\eta}_i$  and  $\tilde{\xi}_i$ , which can be easily solved for the coefficients. Further substitution in Eq. (2.72) leads to the complete definition of deflection function  $w(x, y)$ .

To further elucidate the mechanics of the technique, Figure 2. 4 provides a step-by-step flowchart for the method.

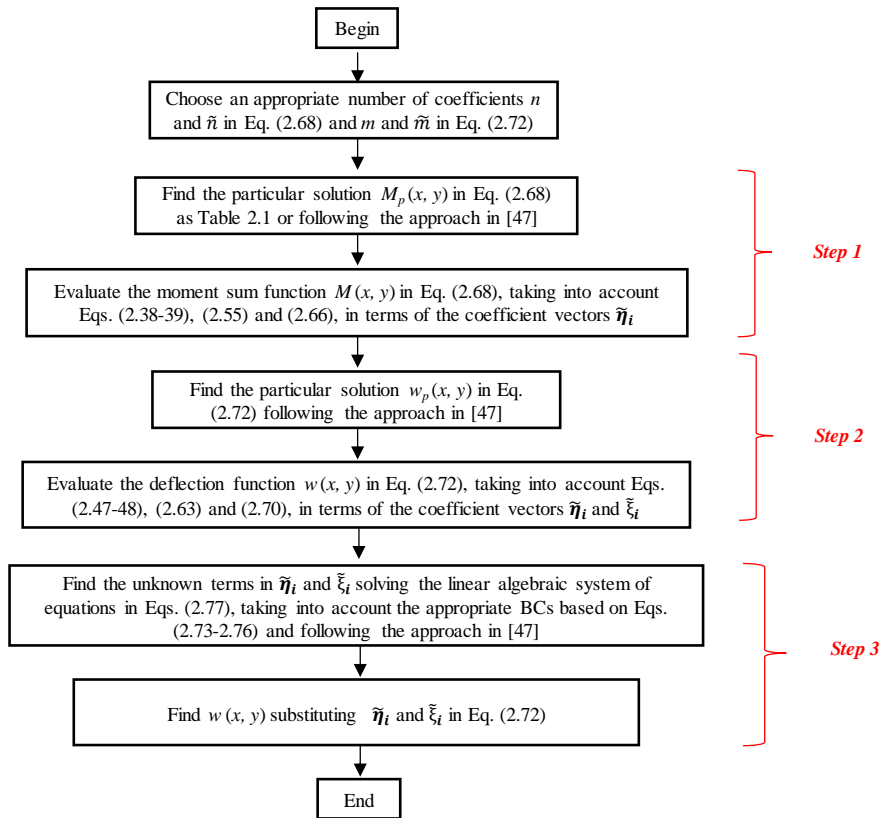


Figure 2. 4 Flowchart of the method.

### 2.4.3) Numerical applications

Firstly, as benchmark cases, the extended LEM method is employed for three different well-known examples, namely a triangular, simply-supported plate; a circular, clamped plate; and an elliptical clamped plate, demonstrating the ability of the method to directly yield the exact solutions. Further, as approximate solutions, a rectangular shaped plate with mixed boundary conditions, a triangular simply-supported plate under a concentrated load and a plate with a complex shape are investigated to show the potential of the method. Finally, to assess the accuracy of the procedure, the LEM based deflection functions are compared with the results of classical Finite Element analyses for all the above mentioned

configurations. As far as the selection of the number of terms in Eqs. (2.26), (2.42), (2.52) and (2.60) is concerned for these numerical applications, it is noted that these values strongly depend on the specific problem under consideration. In this regard, in general, greater values might be required for determining the deflection of plates with complex shapes or BCs, and in the case of complex load functions. Further, a higher number of terms is generally necessary if stress distributions on the boundaries must be found. Obviously, a higher number of terms leads to enhanced accuracy, at the expense, however, of higher computational cost. Further, as a rule of thumb for choosing an appropriate number of terms, the procedure in Figure 2. 4 can be performed for few different values of  $n$  and  $m$ , since the approach generally requires a few seconds in terms of computational cost.

### 2.4.3.1) Exact solutions

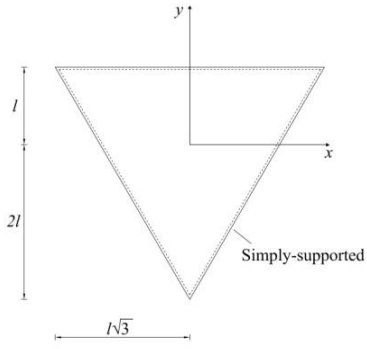
Consider the case of a triangular shaped plate (see Table 2. 2) under a uniformly distributed load  $q(x, y) = q_0$  and with all the edges simply-supported. Applying the previously described procedure yields the non-null series coefficients for the deflection function Eq. (2.43) of the vector  $\xi$ , as reported in Table 2. 2.

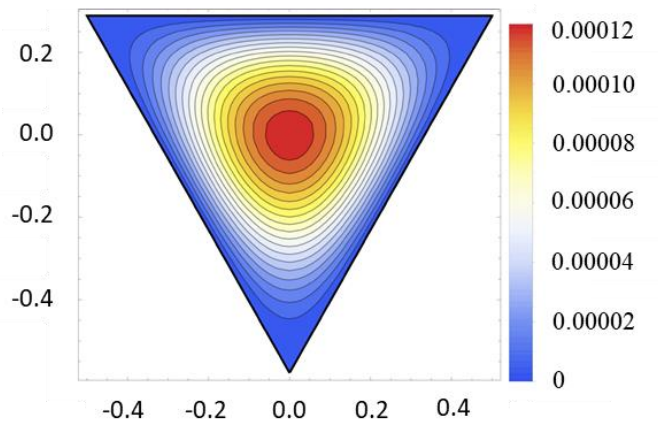
Substituting this in Eq. (2.43) leads to

$$w(x, y) = \left( \frac{q_0}{192lD} \right) \left[ -y^3 + 3x^2y - 3l(x^2 + y^2) + 4l^3 \right] (l^2 - x^2 - y^2) \quad (2.78)$$

which is the exact solution of the considered problem [1]. In this regard, the contours of the above obtained deflection function are shown in Figure 2. 5 for  $l = \sqrt{3}/6 \text{ m}$ .

**Table 2. 2** Triangular shaped plate and corresponding coefficients of the deflection function.

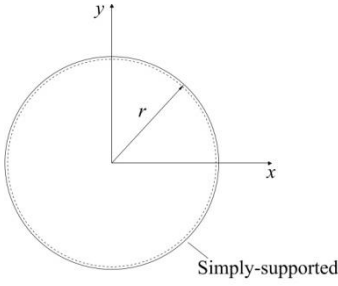
Plate Shape and BCs	Non-null coefficients of $w(x,y)$
	$c_0 = \frac{q_0 l^4}{12D}; \quad c_2 = \frac{q_0 l^2}{12D}; \quad c_4 = \frac{q_0}{64D};$ $d_3 = \frac{q_0 l}{48D}; \quad d_5 = \frac{q_0}{192lD};$



**Figure 2. 5** Deflection functions for  $q_0 = 500\text{N}/\text{m}^2; h = 5\text{mm}; E = 210\text{GPa}; \nu = 0.3$  for the triangular simply-supported plate of Table 2. 2.

Moreover, consider the case of a circular plate (see Table 2. 3) of radius  $r$  under a uniformly distributed load  $q_0$  and simply-supported along the entire contour ( $N_\gamma = 1$ ).

**Table 2. 3** Circular shaped plate and corresponding coefficients of the deflection function.

Plate Shape and BCs	Non-null coefficients of $w(x, y)$
 <p>The diagram shows a circular plate of radius <math>r</math> in a Cartesian coordinate system with <math>x</math> and <math>y</math> axes. The center of the circle is at the origin. A radius <math>r</math> is drawn from the origin to the edge of the circle. The boundary is labeled 'Simply-supported'.</p>	$c_0 = \frac{q_0 r^4 (5 + \nu)}{64D(1 + \nu)}; \quad c_2 = \frac{q_0 r^2 (3 + \nu)}{32D(1 + \nu)};$ $c_4 = \frac{q_0}{64D}$

The plate boundary  $\Gamma$  is defined by the curve in parametric form

$$\begin{cases} x = r \cos \zeta \\ y = r \sin \zeta \end{cases}, \quad 0 \leq \zeta \leq 2\pi \quad (2.79)$$

Since the boundary is curvilinear, the additional moment sum function  $\tilde{M}_1(x, y)$  should be taken into account, while  $\tilde{w}_1(x, y)$  is equal to zero, that is  $\tilde{\xi}_1 = 0$ , because of the chosen BCs. Applying the previously defined procedure, coefficients  $\eta$  and  $\xi$  are found via Eq. (2.67) and (2.71), respectively, in terms of the unknowns  $\tilde{\eta}_1$ . Finally, considering Eq. (2.72), the remaining coefficients  $\tilde{a}_k$  and  $\tilde{b}_k$  in  $\tilde{\eta}_1$  are found using Eq. (2.73). In this regard, a value of  $\tilde{a}_0 = -\frac{q_0 r^2 (\nu - 1)}{8(1 + \nu)}$  is obtained, while all the other terms are equal to zero.

Therefore, substituting in Eq. (2.72) yields the well-known exact solution of the deflection function as

$$w(x, y) = \frac{q_0 (r^2 - x^2 - y^2) [-(x^2 + y^2)(1 + \nu) + r^2 (5 + \nu)]}{64D(1 + \nu)} \quad (2.80)$$

In this regard, the contours of the function into Eq. (2.80) are shown in Figure 2. 6 for  $r = 1m$ .

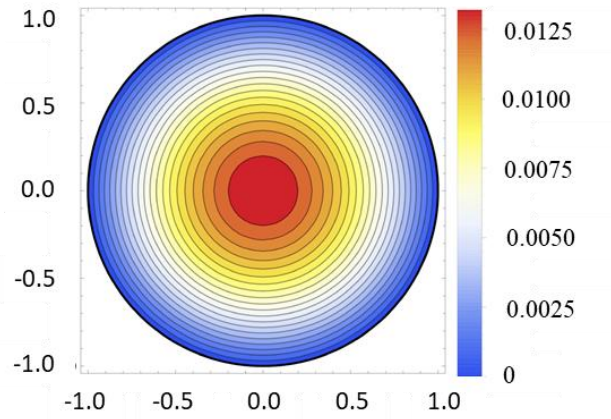


**Figure 2. 6** Deflection functions for  $q_0 = 500\text{N}/\text{m}^2$ ;  $h = 5\text{mm}$ ;  $E = 210\text{GPa}$ ;  $\nu = 0.3$  for the circular simply-supported plate of Table 2. 3.

Finally, consider the case of a clamped elliptical plate of axes  $a$  and  $b$  (see Table 2. 4), under a uniformly distributed load  $q_0$ .

**Table 2. 4** Elliptical shaped plate and corresponding coefficients of the deflection function.

Plate Shape and BCs	Non-null coefficients of $w(x,y)$
	$c_0 = \frac{q_0 a^4 b^4}{8tD}; \quad c_2 = \frac{q_0 a^2 b^2}{4tD}; \quad c_4 = \frac{q_0 a^4}{8tD}$ $t = (3a^4 + 2a^2 b^2 + 3b^4)$

The plate boundary  $\Gamma$  is defined by the curve in parametric form

$$\begin{cases} x = a \cos \zeta \\ y = b \sin \zeta \end{cases}, \quad 0 \leq \zeta \leq 2\pi \quad (2.81)$$

As in the previous case, taking into account the BCs and the plate shape,  $N_\gamma = 1$ ,  $\tilde{M}_1(x,y) \neq 0$  and  $\tilde{w}_1(x,y) = 0$ . Following the previously described

procedure, all the pertinent coefficients are found minimizing the functional in Eq. (2.73) considering Eqs. (2.67) and (2.71), leading to the deflection function

$$w(x, y) = \frac{q_0 \left[ b^2 x^2 + a^2 (-b^2 + y^2) \right]^2}{8(3a^4 + 2a^2 b^2 + 3b^4) D} \quad (2.82)$$

which is the exact solution of the problem in [1]. In this regard, the contours of Eq. (2.82) are shown in Figure 2. 7 for  $a = 1.5m$  and  $b = 1m$ .

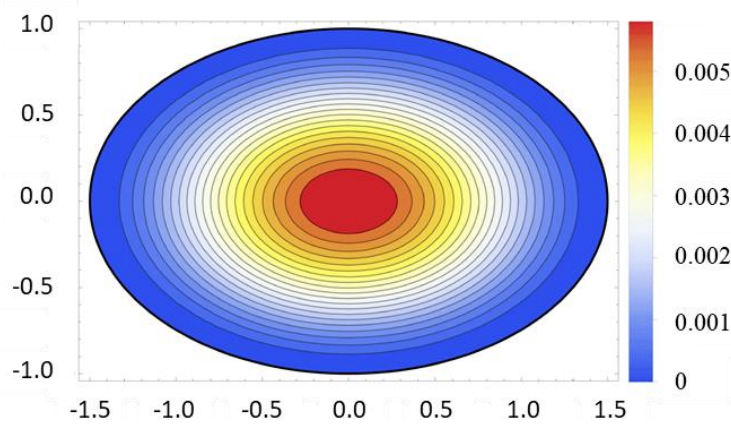


**Figure 2. 7** Deflection functions for  $q_0 = 500N/m^2$ ;  $h = 5mm$ ;  $E = 210GPa$ ;  $\nu = 0.3$  for the elliptical simply-supported plate of Table 2. 4.

As far as the convergence rates of the proposed approach is concerned, analyses can be performed in terms of the  $L_2$  displacement and energy norm, which can be defined respectively as [27]

$$\|w\| = \left[ \int_{\Omega} w(x, y)^2 d\Omega \right]^{\frac{1}{2}} \quad (2.83)$$

and:

$$\|e\| = \frac{D}{2} \left[ \int_{\Omega} \nabla^2 w(x, y)^2 d\Omega \right]^{\frac{1}{2}} \quad (2.84)$$

In Table 2. 5 the relative error between the  $L_2$  displacement and energy norm of the exact solution and the proposed approach, for different values of the



number of coefficients  $m$  in Eq. (2.42) is reported. As can be seen, the relative error is exactly equal to zero for the highest number of terms in the series expansion since, as previously mentioned, the proposed method leads to the analytical solutions.

**Table 2. 5** Relative errors in terms of  $L_2$  displacement and energy norm.

<i>Plate Shape and BCs</i>	<i>Number of coefficients <math>m</math></i>	<i>Relative error for the <math>L_2</math> displacement norm</i>	<i>Relative error for the <math>L_2</math> energy norm</i>
<i>Triangular simply-supported plate</i>	$m=5$	0	0
	$m=4$	$3.42 \cdot 10^{-2}$	$3.33 \cdot 10^{-1}$
	$m=3$	$1.27 \cdot 10^{-1}$	$7.11 \cdot 10^{-1}$
<i>Circular simply-supported plate</i>	$m=4$	0	0
	$m=3$	$4.93 \cdot 10^{-3}$	$5.37 \cdot 10^{-3}$
	$m=2$	$4.93 \cdot 10^{-3}$	$5.37 \cdot 10^{-3}$
<i>Elliptical clamped plate</i>	$m=4$	0	0
	$m=3$	1.89	1.13
	$m=2$	1.89	1.13

Note that, classically to obtain the above reported exact solutions in Eqs. (2.78), (2.80) and (2.82) different approaches are required for each plate shape [1]. For instance, the solution of circular and elliptical plates is generally obtained considering polar and elliptical coordinates. On the other hand, as shown, the proposed method yields the exact solutions, if available, regardless the chosen plate geometry.

### 2.4.3.2) Concentrated load

To show how the proposed procedure can also be applied for plate under generic load conditions, consider the case of a simply-supported triangular plate under a concentrated load  $\bar{Q}$  applied at the origin.

Since in this case  $\bar{Q}$  cannot be directly expressed as in Eq. (2.30), the concentrated load can be assumed as a distributed load  $q(x, y)$  shaped as a Dirac's delta  $\delta(x, y)$  of amplitude equal to  $\bar{Q}$ , which can be conveniently approximated in terms of Chebyshev polynomials as:

$$q(x, y) \approx \bar{Q} \left( \frac{1}{\pi} T_0(x) + \frac{2}{\pi} \sum_{m=1}^N (-1)^i T_{2m}(x) \right) \left( \frac{1}{\pi} T_0(y) + \frac{2}{\pi} \sum_{m=1}^N (-1)^i T_{2m}(y) \right) \quad (2.85)$$

where  $N$  is the truncation limit of the series expansion, while  $T_m(\cdot)$  is the Chebyshev polynomial of order  $m$ , defined by the recurrence relation [49]

$$T_{m+1}(x) = 2xT_m(x) - T_{m-1}(x) \quad (2.86)$$

in which  $T_0(x) = 1$  and  $T_1(x) = x$ .

Once the concentrated load has been expressed as in Eq. (2.85), the particular solution  $M_p(x, y)$  of Eq. (1.59) can be obtained in a closed-form using the approach in [47].

In this manner, the LEM procedure can be easily applied. Thus, firstly the moment sum function  $M(x, y)$  is directly determined via Eq. (2.41) and secondly the deflection function  $w(x, y)$  is immediately retrieved using Eq. (2.50).

In this regard, Figure 2. 8 (a) shows the contour plot of the aforementioned function, assuming  $l = \sqrt{3}/6m$ . Note that in this case 22 terms have been used in the vector  $\xi$  in Eq. (2.49), considering only even coefficients  $c_{2k}$  and odd coefficients  $d_{2k+1}$  (thus also  $m = 22$  in Eq. 2.42). Further, in Figure 2. 8 (b) LEM results of the deflection profile at  $x = 0$  are compared with pertinent FEM data obtained employing the commercial code Ansys.

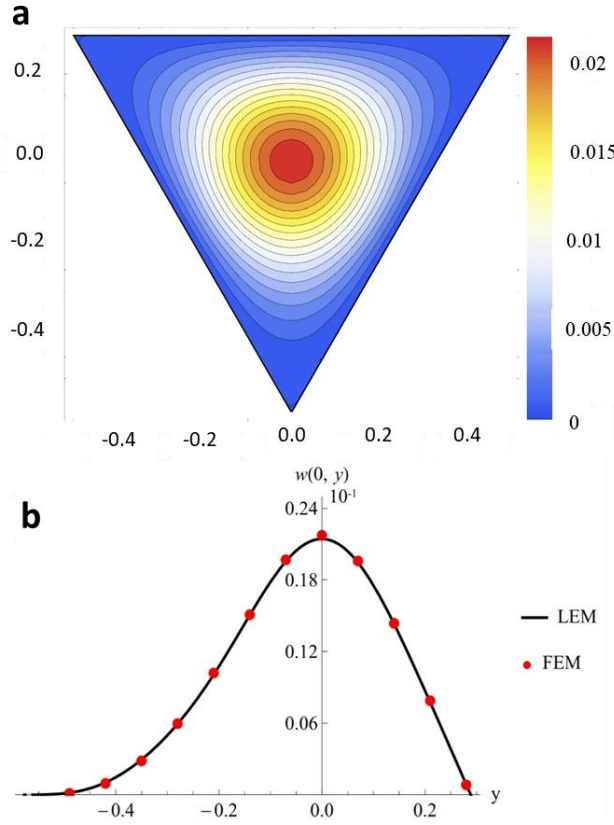


**Figure 2. 8** Deflection functions for  $\bar{Q} = 100\text{ N}$ ;  $h = 1\text{ mm}$ ;  $E = 210\text{ GPa}$ ;  $\nu = 0.3$ : (a) Contours plot with LEM; (b) Deflection profile.

As can be observed, classical FEM data are in very good agreement with the results of the proposed LEM approach, attesting to the accuracy of the considered procedure.

To further assess the reliability of the procedure, the average relative discrepancy index  $\bar{\varepsilon}_r$  between the proposed method results and the FEM data has been computed.

Specifically,  $\bar{\varepsilon}_r$  can be defined as:

$$\bar{\varepsilon}_r = \frac{1}{N_p} \sqrt{\frac{(w_{LEM} - w_{FEM})^2}{w_{FEM}^2}} \cdot 100 \quad (2.87)$$

where  $w_{LEM}$  and  $w_{FEM}$  are the values of the deflection obtained using the LEM and FEM approach respectively, while  $N_p$  is the considered number of points of the deflection functions.

In this regard, taking into account the points in Figure 2. 8 (b),  $\bar{\varepsilon}_r = 1.75\%$ , thus showing the accuracy of the proposed approach.

### 2.4.3.3) Mixed BCs

Aiming at demonstrating the capability of the proposed procedure to treat plates with mixed BCs., consider the case of a rectangular plate under a uniformly distributed load  $q_0$ , assuming that two opposite plate edges are simply-supported, one edge is clamped and one free, as shown in Figure 2. 9 (a).

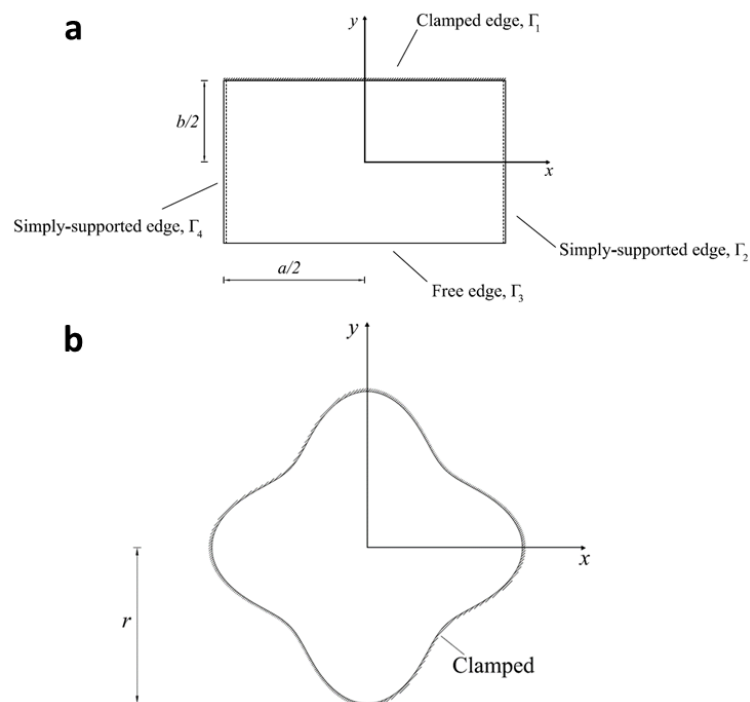


**Figure 2. 9** Plate geometries: (a) Rectangular plate with mixed BCs; (b) Clamped plate of complex shape.

Applying the proposed method, the plate boundary  $\Gamma$  can be conveniently subdivided into four edges  $\Gamma_i$ , that is  $N_\gamma = 4$ . Note that, since the two edges  $\Gamma_2$  and  $\Gamma_4$  are simply-supported, as previously mentioned the corresponding function  $\tilde{M}_2(x, y)$  and  $\tilde{M}_4(x, y)$  in Eq. (2.56) can be assumed equal to zero and only the remaining functions  $\tilde{M}_1(x, y)$  and  $\tilde{M}_3(x, y)$  must be taken into account. Further, since just the boundary  $\Gamma_3$  can undergo vertical deflections,  $\tilde{w}_3(x, y) \neq 0$  while  $\tilde{w}_i(x, y) = 0, i = 1, 2, 3$  in Eq. (2.59).

In this manner, the vector  $\boldsymbol{\eta}$  in Eq. (2.67) can be specified as:

$$\boldsymbol{\eta} = -\mathbf{Q}_n^{-1} \boldsymbol{\tau} + \mathbf{Q}_n^{-1} \tilde{\mathbf{Q}}_{n,1} \tilde{\boldsymbol{\eta}}_1 + \mathbf{Q}_n^{-1} \tilde{\mathbf{Q}}_{n,3} \tilde{\boldsymbol{\eta}}_3 \quad (2.88)$$

and the moment sum function  $M(x, y)$  can be obtained via Eq. (2.29).

Further, the vector  $\boldsymbol{\xi}$  in Eq. (2.71) becomes:

$$\boldsymbol{\xi} = -\mathbf{Q}_m^{-1} \boldsymbol{\lambda} + \mathbf{Q}_m^{-1} \tilde{\mathbf{Q}}_{m,3} \tilde{\boldsymbol{\xi}}_3 \quad (2.89)$$

and the deflection function can be evaluated substituting in Eq. (2.43) as

$$w(x, y) = -\mathbf{r}_m \mathbf{Q}_m^{-1} \boldsymbol{\lambda} + \mathbf{r}_m \mathbf{Q}_m^{-1} \tilde{\mathbf{Q}}_{m,3} \tilde{\boldsymbol{\xi}}_3 + w_p(x, y, \tilde{\boldsymbol{\eta}}_1, \tilde{\boldsymbol{\eta}}_3) \quad (2.90)$$

Finally, the unknown terms  $\tilde{\boldsymbol{\eta}}_1$ ,  $\tilde{\boldsymbol{\eta}}_3$  and  $\tilde{\boldsymbol{\xi}}_3$  can be obtained by imposing the specified BCs on the edges  $\Gamma_1$  and  $\Gamma_3$  for which the additional functions  $\tilde{M}_i(x, y)$  and  $\tilde{w}_i(x, y)$  have been introduced.

Specifically, minimizing the functional in Eqs. (2.75-2.76) specified for  $\Gamma_3$ , namely  $\Xi_3(\tilde{\boldsymbol{\eta}}_3)$  and  $\Lambda_3(\tilde{\boldsymbol{\xi}}_3)$ , as in Eq. (2.77), the vectors  $\tilde{\boldsymbol{\eta}}_3$  and  $\tilde{\boldsymbol{\xi}}_3$  can be obtained in terms of  $\tilde{\boldsymbol{\eta}}_1$ . Finally, minimization of the functional in Eq. (2.74) for  $\Gamma_1$ , that is  $\Xi_1(\tilde{\boldsymbol{\eta}}_1)$ , yields the vector  $\tilde{\boldsymbol{\eta}}_1$ . Clearly, further substitution in Eq. (2.90) leads to the complete definition of deflection function  $w(x, y)$ .

In this regard in Figure 2. 10 (a) the contour plot of the deflection function is shown, assuming  $a = 1m$  and  $b = 0.5m$ . Note that in this case 12 coefficients  $c_k$  and 10 coefficients  $d_k$  have been used in the vector  $\xi$ . Further, the proposed method results vis-à-vis FEM data are shown in Figure 2. 10 (b) for the deflection profile at  $x = 0$ .

As can be seen, an excellent agreement is achieved between classical FEM data and the proposed LEM approach, showing the accuracy of the considered procedure.

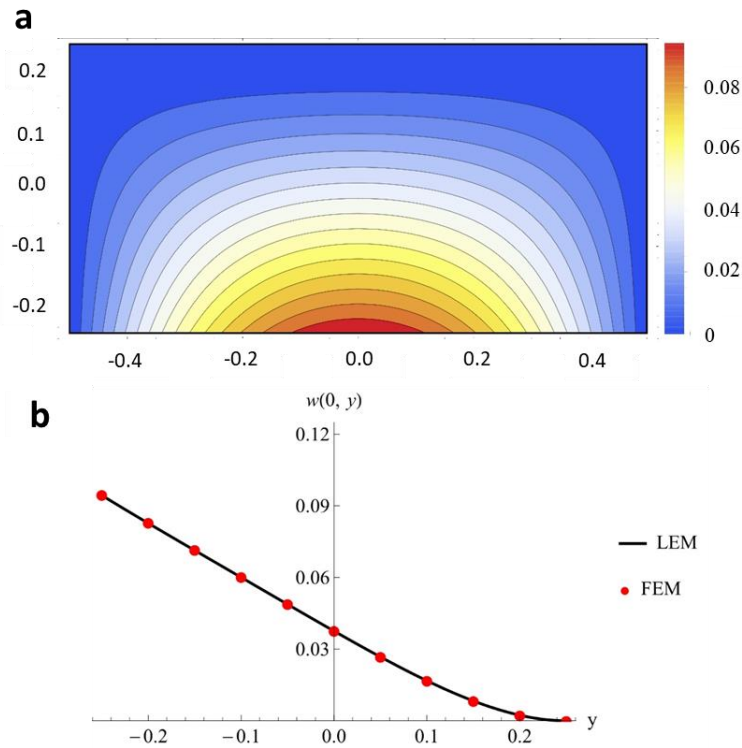


**Figure 2. 10** Deflection functions for  $q_0 = 500N/m^2$ ;  $h = 1mm$ ;  $E = 210GPa$ ;  $\nu = 0.3$ : (a) Contours plot with LEM; (b) Deflection profile.

To further show the reliability of the approach, the average relative discrepancy index in Eq. (2.87) has been computed, considering the points in Figure 2. 10 (b), leading to the very low value of  $\bar{\varepsilon}_r = 0.28\%$ .

#### 2.4.3.4) Arbitrarily shaped plate

Finally, to demonstrate the capability of the method to treat plates with arbitrary geometries, a clamped plate with a complex shape (see Figure 2. 9(b)) under a uniformly distributed load  $q_0$  has been analyzed. The boundary  $\Gamma$  of the plate is defined by the curve in parametric form

$$\begin{cases} x = r \left( |\sin \zeta|^3 + |\cos \zeta|^3 \right) \cos \zeta \\ y = r \left( |\sin \zeta|^3 + |\cos \zeta|^3 \right) \sin \zeta \end{cases}, \quad 0 \leq \zeta \leq 2\pi \quad (2.91)$$

Applying the proposed procedure, considering the specified BCs, the moment sum function can be expressed as:

$$M(x, y) = -\mathbf{r}_n \mathbf{Q}_n^{-1} \boldsymbol{\tau} + \mathbf{r}_n \mathbf{Q}_n^{-1} \tilde{\mathbf{Q}}_{n,1} \tilde{\boldsymbol{\eta}}_1 + M_p(x, y) \quad (2.92)$$

where  $\tilde{\boldsymbol{\eta}}_1$  is a vector of unknowns due to the additional function  $\tilde{M}_1(x, y)$  which takes into account the clamped BCs, while  $M_p(x, y)$  is given in Table 2. 1 for the uniform load distribution.

Further, since no deflection occurs on  $\Gamma$ ,  $\tilde{\xi}_i = 0$  and the deflection function in Eq. (2.72) can be simplified as

$$w(x, y) = -\mathbf{r}_m \mathbf{Q}_m^{-1} \boldsymbol{\lambda} + w_p(x, y, \tilde{\boldsymbol{\eta}}_1) \quad (2.93)$$

where the particular solution  $w_p(x, y, \tilde{\boldsymbol{\eta}}_1)$  can be obtained as in [47].

Finally, the unknown term  $\tilde{\boldsymbol{\eta}}_1$  can be evaluated through imposing the specified BCs on  $\Gamma$ . Specifically, performing variation of the functional in Eq. (2.74) with respect to  $\tilde{\boldsymbol{\eta}}_1$  yields a linear system of algebraic equation, whose solution leads to the unknowns coefficients  $\tilde{\boldsymbol{\eta}}_1$ .

In this regard, the contours of the deflected surface for  $r = 1m$  is depicted in Figure 2. 11 (a), while in Figure 2. 11 (b) the deflection profile at  $x = 0$  is reported vis-à-vis pertinent FEM data. Note that, in this case just 9 terms of the

even coefficients  $c_{2k}$  are required in the vector  $\xi$  in Eq. (2.71) (that is  $m=16$ ), given that all the coefficients  $c_{2k+1}$  and  $d_k$  equal zero. As can be observed, also in this case an excellent agreement is achieved between proposed and FEM data, further assessing the reliability of the proposed procedure. Moreover, the average relative discrepancy index in Eq. (2.87) has been computed, considering the points in Figure 2. 11 (b), leading to the satisfactorily low value  $\bar{\varepsilon}_r = 1.83\%$ .

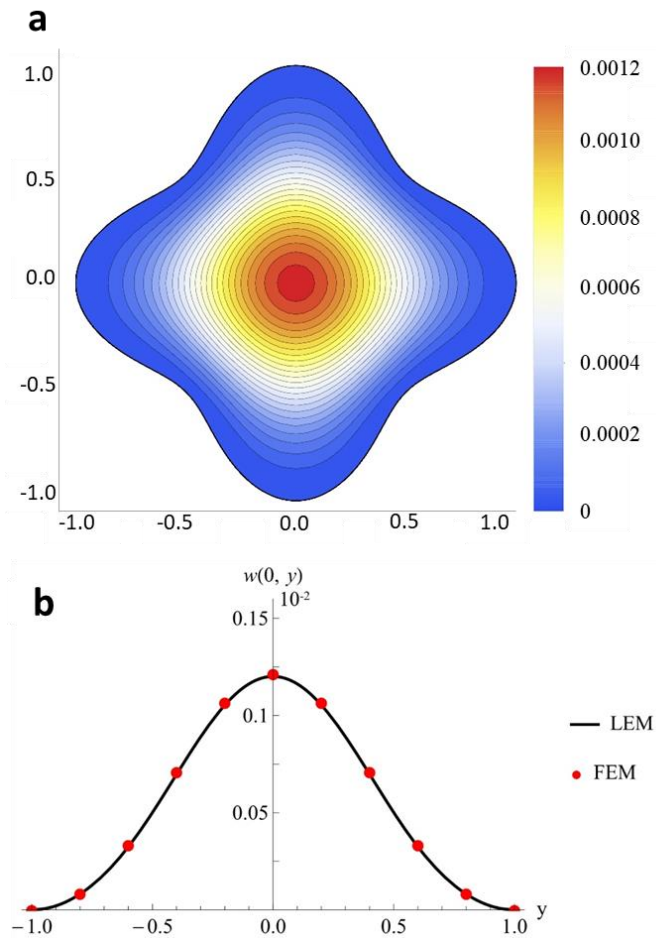


**Figure 2. 11** Deflection functions for  $q_0 = 500 \text{ N/m}^2$ ;  $h = 5 \text{ mm}$ ;  $E = 210 \text{ GPa}$ ;  $\nu = 0.3$ : (a) Contours plot with LEM; (b) Deflection profile.



## CHAPTER III

# AN INNOVATIVE PROCEDURE FOR THE ANALYSIS OF THIN PLATES OF ARBITRARY SHAPES UNDER DYNAMICS LOADS

### 3.1) Introduction

In the previous chapter, attention has been focused on the analysis of the static response of isotropic thin plates. However, in many practical cases, structural properties of thin plates differ in two mutually perpendicular directions, so that the plate is described as orthogonally anisotropic or, in short, orthotropic [50]. Such anisotropy can be due to the inherent orthotropic characteristic of the material, or it can be introduced by ribs, corrugation or stiffeners. Examples include reinforced plates with a set of equidistant stiffeners in one or two directions, open gridworks and corrugated plates [51]. Further, even isotropic plates altered by metallurgical process along perpendicular directions exhibit orthotropic characteristics [52, 53], thus requiring an orthotropic plate model.

Therefore, considerable attention has been devoted by researchers to develop efficient and accurate methods for the investigation of orthotropic thin plates. In this context, the problem of the dynamic response determination of orthotropic plates under various boundary conditions (BCs) has been addressed. Existing approaches pertain generally rectangular shaped plates and resort either to Rayleigh-Ritz procedures [54, 55] or classical Finite Elements (FE) methods [56]. A recent contribution can be found in [52], where exact solutions have been obtained for the free-vibration response of rectangular plates with simply supported or clamped edges, while other numerical approaches can be found in [57-59]. On the other hand, the free-vibration analysis of orthotropic generally shaped plates has been much less addressed. Specifically, few common cases

have been studied in the literature, such as elliptical or circular plates [60], general triangular plates [61], skew plates [62], and trapezoidal plates [63].

In this chapter, the so-called pb-2 Rayleigh-Ritz procedure [33, 64-66], commonly used to treat isotropic plates of general shape, is extended to deal with arbitrarily shaped orthotropic plates. In particular, first, the pb-2 Rayleigh-Ritz procedure is extended for the analysis of orthotropic plates. Then, the Green's lemma is employed to convert involved computationally demanding double integrals in the plate domain to more simple line integrals over the contour of the plate. Finally, the accuracy of the proposed method is investigated by determining the dynamic response of two orthotropic plates with different shapes and boundary conditions.

### 3.2) Pb-2 Rayleigh-Ritz method for general orthotropic plate analysis.

The classical Rayleigh-Ritz method employs the principle of minimum potential energy in order to solve structural engineering problems. Specifically, in the case of thin plate, the deflection function of middle plane surface  $w(x, y)$  can be expressed in the form of series of the type:

$$w(x, y) = \sum_{j=1}^N c_j \phi_j(x, y) \quad (3.1)$$

where  $N$  is the chosen truncation limit of the series expansion,  $c_j$  are unknown coefficients to be determined, and  $\phi_j(x, y)$  are the so-called Ritz functions, that satisfy individually at least the geometrical boundary conditions. As discussed in section 1.4.2.1, the main concern of applying the Rayleigh-Ritz method lies in the use of the most suitable Ritz function, which approximate the deflection function of the plate. A set of two-dimensional orthogonal plate functions have been proposed for the free vibration analysis of rectangular plates [10] and later applied for the analysis of isotropic plates of general shape [33, 64-66]. The method is referred as pb-2 Rayleigh-Ritz, where p, b and 2 denote polynomials, boundary expressions, and dimension, respectively. Specifically, in

this procedure, Ritz functions,  $\phi_j(x, y)$ , are defined as the product of a boundary function  $\phi_1(x, y)$ , and polynomial functions  $f_j(x, y)$ , thus

$$\phi_j(x, y) = f_j(x, y) \phi_1(x, y), \quad j \geq 2 \quad (3.2)$$

Considering a thin homogeneous plates of arbitrarily shape, contour  $\Gamma$  and thickness  $h$ , as shown in Figure 3. 1, if the plate BCs vary on the contour, it is feasible to appropriately subdivide  $\Gamma$  in the  $N_\gamma$  edges, described by the equation

$$\Gamma_k(x, y), \text{ on which the BCs remain constant, that is } \Gamma = \bigcup_{k=1}^{N_\gamma} \Gamma_k(x, y).$$

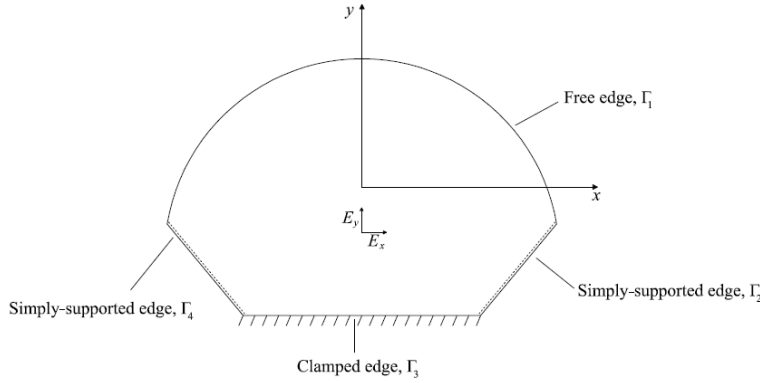


Figure 3. 1 Arbitrary shaped plate with mixed BCs.

In this case, the boundary function  $\phi_1(x, y)$  can be expressed as

$$\phi_1(x, y) = \prod_{k=1}^{N_\gamma} \Gamma_k(x, y)^{\beta_k} \quad (3.3)$$

where the exponents  $\beta_k$  depend on the support edge condition, as

$$\begin{aligned} \beta_k &= 0, & \text{if the } k\text{-th edge is free} \\ \beta_k &= 1, & \text{if the } k\text{-th edge is simply supported} \\ \beta_k &= 2, & \text{if the } k\text{-th edge is clamped} \end{aligned} \quad (3.4)$$

Further, the polynomial function  $f_j(x, y)$  in Eq. (3.2) may be generated as

$$f_j(x, y) = x^{r_R} y^{s_R} \cos^2 \frac{\pi(j - r_R^2 - 1)}{2} + x^s y^r \sin^2 \frac{\pi(j - r_R^2 - 1)}{2}, \quad j \geq 2 \quad (3.5)$$

where

$$r_R = \lceil \sqrt{j-1} \rceil \quad (3.6)$$

and

$$s_R = \left( \frac{j - r_R^2 - 1}{2} \right) \cos^2 \frac{\pi(j - r_R^2 - 1)}{2} + \left( \frac{j - r_R^2 - 2}{2} \right) \sin^2 \frac{\pi(j - r_R^2 - 1)}{2} \quad (3.7)$$

in which the symbol  $\lceil \cdot \rceil$  denotes the so-called maximum integer function.

It is worth mentioning that, through the chosen boundary function in Eq. (3.3), the Ritz functions  $\phi_j(x, y)$  in Eq. (3.2) automatically satisfy the kinematic BCs.

Introducing the energy functional of the plate

$$\Pi_{tot} = U_{Strain} - \beta_1 \Omega_{ext} - \beta_2 U_{pre-stress} - \beta_3 T \quad (3.8)$$

where  $\Pi_{tot}$  is the total potential energy of the plate,  $U_{Strain}$  is the potential energy of the plate,  $\Omega_{ext}$  is the potential energy of external forces acting on the body,  $U_{pre-stress}$  is the potential energy of external pre-stretching force on the plate and  $T$  is the kinetic energy. In the case of  $\beta_1 = 1, \beta_2 = \beta_3 = 0$  Eq. (3.8) can be applied to deal with the solution of the bending of plates under transversal loads. The Ritz method can also be used for the analysis of plates under combined transversal and in-plane loads and lateral loads  $\beta_1 = \beta_2 = 1, \beta_3 = 0$ . Further, the method can be employed for both the free vibration analysis of plates with ( $\beta_1 = 0, \beta_2 = \beta_3 = 1$ ) and without ( $\beta_1 = \beta_2 = 0, \beta_3 = 1$ ) the influence of in-plane loads.

In the following, the pb-2 Rayleigh-Ritz method, introduced in [33, 64, 65] for general isotropic plate, is appropriately extended to deal with thin plates made of orthotropic material. In particular, the attention is focused for the free vibration analysis of orthotropic plates without the influence of in-plane loads ( $\beta_1 = \beta_2 = 0, \beta_3 = 1$ ).

In this case, Eq. (3.8) becomes:

$$\Pi_{tot} = U_{Strain} - T \quad (3.9)$$

Substituting Eqs. (1.65) and (1.73) into Eq. (3.9), taking into account Eqs. (3.1-7) leads to

$$\begin{aligned} U_{Strain} = & \frac{1}{2} \iint_{\Omega} \left[ D_x \left( \sum_{j=1}^N c_j \frac{\partial^2 \phi_j}{\partial x^2} \right) \left( \sum_{i=1}^N c_i \frac{\partial^2 \phi_i}{\partial x^2} \right) + \right. \\ & + 2\nu_{xy} D_y \left( \sum_{j=1}^N c_j \frac{\partial^2 \phi_j}{\partial x^2} \right) \left( \sum_{i=1}^N c_i \frac{\partial^2 \phi_i}{\partial y^2} \right) + \\ & + D_y \left( \sum_{j=1}^N c_j \frac{\partial^2 \phi_j}{\partial y^2} \right) \left( \sum_{i=1}^N c_i \frac{\partial^2 \phi_i}{\partial y^2} \right) \\ & \left. + 4D_t \left( \sum_{j=1}^N c_j \frac{\partial^2 \phi_j}{\partial x \partial y} \right) \left( \sum_{i=1}^N c_i \frac{\partial^2 \phi_i}{\partial x \partial y} \right) \right] dx dy \end{aligned} \quad (3.10)$$

and

$$T = \frac{1}{2} \rho h \tilde{\omega}^2 \iint_{\Omega} \left( \sum_{j=1}^N c_j \phi_j \right) \left( \sum_{i=1}^N c_i \phi_i \right) dx dy \quad (3.11)$$

Taking into account Eq. (3.9) and performing variation with respect to the unknown coefficients  $c_j$  yields

$$\begin{aligned}
 & 2D_x \sum_{i,j=1}^N c_i \left( \iint_{\Omega} \frac{\partial^2 \phi_i}{\partial x^2} \frac{\partial^2 \phi_j}{\partial x^2} dx dy \right) + \\
 & + 2v_{xy} D_y \sum_{i,j=1}^N c_i \left( \iint_{\Omega} \frac{\partial^2 \phi_i}{\partial x^2} \frac{\partial^2 \phi_j}{\partial y^2} dx dy + \iint_{\Omega} \frac{\partial^2 \phi_i}{\partial y^2} \frac{\partial^2 \phi_j}{\partial x^2} dx dy \right) + \\
 & 2D_y \sum_{i,j=1}^N c_i \left( \iint_{\Omega} \frac{\partial^2 \phi_i}{\partial y^2} \frac{\partial^2 \phi_j}{\partial y^2} dx dy \right) + 8D_t \sum_{i,j=1}^N c_i \left( \iint_{\Omega} \frac{\partial^2 \phi_i}{\partial x \partial y} \frac{\partial^2 \phi_j}{\partial x \partial y} dx dy \right) + \\
 & - 2\rho h \omega^2 \sum_{i,j=1}^N c_i \left( \iint_{\Omega} \phi_i \phi_j dx dy \right) = 0
 \end{aligned} \tag{3.12}$$

Introducing the matrices  $\mathbf{R}^{(de,pq)}$  whose elements are given as

$$\begin{aligned}
 R_{ij}^{(de,pq)} &= \iint_{\Omega} \left[ \frac{\partial^{d+e} \phi_i(x,y)}{\partial x^d \partial y^e} \right] \left[ \frac{\partial^{p+q} \phi_j(x,y)}{\partial x^p \partial y^q} \right] dx dy, \\
 & i=1, \dots, N; j=1, \dots, N
 \end{aligned} \tag{3.13}$$

where the generic superscript  $(de,pq)$  of the term  $R_{ij}^{(de,pq)}$  refers to the order of the partial derivatives of the functions  $\phi_i(x,y)$  and  $\phi_j(x,y)$  at the right-hand side of Eq. (3.13).

In this manner, the integrals in Eq. (3.12) can be specified as

$$\begin{aligned}
 R_{ij}^{(20,20)} &= \iint_{\Omega} \left[ \frac{\partial^{2+0} \phi_i}{\partial x^2 \partial y^0} \right] \left[ \frac{\partial^{2+0} \phi_j}{\partial x^2 \partial y^0} \right] dx dy = \iint_{\Omega} \frac{\partial^2 \phi_i}{\partial x^2} \frac{\partial^2 \phi_j}{\partial x^2} dx dy; \\
 R_{ij}^{(20,02)} &= \iint_{\Omega} \left[ \frac{\partial^{2+0} \phi_i}{\partial x^2 \partial y^0} \right] \left[ \frac{\partial^{0+2} \phi_j}{\partial x^0 \partial y^2} \right] dx dy = \iint_{\Omega} \frac{\partial^2 \phi_i}{\partial x^2} \frac{\partial^2 \phi_j}{\partial y^2} dx dy; \\
 R_{ij}^{(02,20)} &= \iint_{\Omega} \left[ \frac{\partial^{0+2} \phi_i}{\partial x^0 \partial y^2} \right] \left[ \frac{\partial^{2+0} \phi_j}{\partial x^2 \partial y^0} \right] dx dy = \iint_{\Omega} \frac{\partial^2 \phi_i}{\partial y^2} \frac{\partial^2 \phi_j}{\partial x^2} dx dy; \\
 R_{ij}^{(02,02)} &= \iint_{\Omega} \left[ \frac{\partial^{0+2} \phi_i}{\partial x^0 \partial y^2} \right] \left[ \frac{\partial^{0+2} \phi_j}{\partial x^0 \partial y^2} \right] dx dy = \iint_{\Omega} \frac{\partial^2 \phi_i}{\partial y^2} \frac{\partial^2 \phi_j}{\partial y^2} dx dy; \\
 R_{ij}^{(11,11)} &= \iint_{\Omega} \left[ \frac{\partial^{1+1} \phi_i}{\partial x^1 \partial y^1} \right] \left[ \frac{\partial^{1+1} \phi_j}{\partial x^1 \partial y^1} \right] dx dy = \iint_{\Omega} \frac{\partial^2 \phi_i}{\partial x \partial y} \frac{\partial^2 \phi_j}{\partial x \partial y} dx dy; \\
 R_{ij}^{(00,00)} &= \iint_{\Omega} \left[ \frac{\partial^{0+0} \phi_i}{\partial x^0 \partial y^0} \right] \left[ \frac{\partial^{0+0} \phi_j}{\partial x^0 \partial y^0} \right] dx dy = \iint_{\Omega} \phi_i \phi_j dx dy;
 \end{aligned} \tag{3.14a-f}$$

and Eq. (3.12) can be rewritten in more compact form as

$$\begin{aligned}
 & D_x \sum_{i,j=1}^N c_i R_{ij}^{(20,20)} + \nu_{xy} D_y \sum_{i,j=1}^N c_i \left( R_{ij}^{(20,02)} + R_{ij}^{(02,20)} \right) + D_y \sum_{i,j=1}^N c_i R_{ij}^{(02,02)} + \\
 & 4D_t \sum_{i,j=1}^N c_i R_{ij}^{(11,11)} - \rho h \tilde{\omega}^2 \sum_{i,j=1}^N c_i R_{ij}^{(00,00)} = 0
 \end{aligned} \tag{3.15}$$

Let  $\mathbf{c}$  be the vector containing the unknown coefficients, that is  $\mathbf{c}^T = [c_1 \dots c_N]$ , and  $\mathbf{R}^{(20,20)}$ ,  $\mathbf{R}^{(20,02)}$ ,  $\mathbf{R}^{(02,20)}$ ,  $\mathbf{R}^{(02,02)}$ ,  $\mathbf{R}^{(11,11)}$ , and  $\mathbf{R}^{(00,00)}$ , the matrices containing as elements those in Eqs. (3.14 a) – (3.14 f) respectively. Then, Eq. (3.15) can be rewritten in compact matrix form as

$$\begin{bmatrix} \frac{D_x}{\nu_{xy}} \mathbf{R}^{(20,20)} + \frac{D_y}{\nu_{xy}} \mathbf{R}^{(02,02)} + D_y [\mathbf{R}^{(20,02)} + \mathbf{R}^{(02,20)}] \\ + 4 \frac{D_t}{\nu_{xy}} \mathbf{R}^{(11,11)} - \lambda \mathbf{R}^{(00,00)} \end{bmatrix} \mathbf{c} = \mathbf{0} \tag{3.16}$$

where  $\lambda = \rho h \tilde{\omega}^2 / \nu_{xy}$ .

Finally, defining the stiffness ( $\mathbf{K}$ ) and mass matrices ( $\mathbf{M}$ ) as

$$\mathbf{K} = \frac{D_x}{\nu_{xy}} \mathbf{R}^{(20,20)} + \frac{D_y}{\nu_{xy}} \mathbf{R}^{(02,02)} + D_y [\mathbf{R}^{(20,02)} + \mathbf{R}^{(02,20)}] + 4 \frac{D_t}{\nu_{xy}} \mathbf{R}^{(11,11)} \tag{3.17}$$

and

$$\mathbf{M} = \mathbf{R}^{(00,00)} \tag{3.18}$$

The Ritz method leads to a generalized eigenvalue problem

$$(\mathbf{K} - \lambda \mathbf{M}) \mathbf{c} = \mathbf{0} \tag{3.19}$$

Therefore, the natural frequencies  $\tilde{\omega}$  and the corresponding coefficients vector  $\mathbf{c}$  of an orthotropic thin plate can be found.

### 3.3) Extension of the Pb-2 Rayleigh-Ritz method to arbitrary shaped plates

In Section 3.2, the pb-2 Rayleigh-Ritz was extended for the analysis of orthotropic thin plates. The procedure represents a simple and effective method

to determine natural frequencies and mode shapes of orthotropic plates under most common BCs. However, double integrals in Eq. (3.14 a-f) can be particularly cumbersome to be evaluated for plates of arbitrary shape. For this reason, application of the pb-2 Rayleigh-Ritz procedure is generally limited to the case of rectangular plate, for which integrals can be simply obtained numerically.

In this context, taking into account Green's theorem, double integrals in Eq. (3.14 a-f) can be converted into much simpler line integrals, which allow for an elegant and straightforward application of the proposed procedure to orthotropic plates of arbitrary shape.

Specifically, considering Eq. (3.13), a function  $G_{i,j}^{de,pq}$  can be defined as:

$$G_{i,j}^{de,pq}(x,y) = \left[ \frac{\partial^{d+e} \phi_i(x,y)}{\partial x^d \partial y^e} \right] \left[ \frac{\partial^{p+q} \phi_j(x,y)}{\partial x^p \partial y^q} \right]; \quad (3.20)$$

$$i = 1, \dots, N; j = 1, \dots, N$$

where the generic superscript  $(de, pq)$  refers to the order of the partial derivatives of the functions  $\phi_i(x,y)$  and  $\phi_j(x,y)$ . Consequently, the functions  $A_{ij}^{(de,pq)}(x,y)$  and  $B_{ij}^{(de,pq)}(x,y)$  can be introduced as

$$A_{ij}^{(de,pq)}(x,y) = \int G_{i,j}^{(de,pq)} dx = \int \left[ \frac{\partial^{d+e} \phi_i(x,y)}{\partial x^d \partial y^e} \right] \left[ \frac{\partial^{p+q} \phi_j(x,y)}{\partial x^p \partial y^q} \right] dx, \quad (3.21)$$

$$i = 1, \dots, N; j = 1, \dots, N$$

and

$$B_{ij}^{(de,pq)}(x,y) = \int G_{i,j}^{(de,pq)} dy = \int \left[ \frac{\partial^{d+e} \phi_i(x,y)}{\partial x^d \partial y^e} \right] \left[ \frac{\partial^{p+q} \phi_j(x,y)}{\partial x^p \partial y^q} \right] dy, \quad (3.22)$$

$$i = 1, \dots, N; j = 1, \dots, N$$

Note that the above defined indefinite integrals can be generally obtained in closed form since they involve integrations of polynomial functions.

Further, referring to Figure 3. 1, let the equation of the k-th edge  $\Gamma_k(x,y)$  of the plate be given in parametric form as  $\Gamma_k(\gamma) = [x_k(\gamma), y_k(\gamma)]$ . Thus,



functions in Eqs. (3.21) and (3.22) can be expressed in terms of the generic parameter  $\gamma$  as well, that is  $A_{ij}^{(de,pq)}(\gamma)$  and  $B_{ij}^{(de,pq)}(\gamma)$ .

Taking into account Eqs (3.21) and (3.22), application of the Green's theorem yields the terms  $R_{ij}^{(de,pq)}$  in Eq. (3.13) as

$$R_{ij}^{(de,pq)} = \frac{1}{2} \sum_{k=1}^{N_\gamma} \int_{\Gamma_k} H_{ij,k}^{(de,pq)}(\gamma) d\gamma \quad (3.23)$$

where the symbol  $\int_{\Gamma_k}(\cdot)d\gamma$  denotes the classical line integration, and the function  $H_{ij,k}^{(de,pq)}(\gamma)$  is given as

$$H_{ij,k}^{(de,pq)}(\gamma) = -A_{ij}^{(de,pq)}(\gamma) \frac{dy_k(\gamma)}{d\gamma} + B_{ij}^{(de,pq)}(\gamma) \frac{dx_k(\gamma)}{d\gamma} \quad (3.24)$$

In this manner, Eq. (3.23) allows for a simpler evaluation of the terms  $R_{ij}^{(de,pq)}$  of Eqs (3.14 a-f). Therefore, the method can be used even for plates of more complex shape.

In passing, it is noted that if the plate BCs do not vary on the contour  $\Gamma$ , and the entire plate boundary can be described by a single equation  $\Gamma(\gamma)$ , then the line integral in Eq. (3.23) simply reverts to a contour path integral in  $\Gamma$ , that is

$$R_{ij}^{(de,pq)} = \frac{1}{2} \oint_{\Gamma} H_{ij}^{(de,pq)}(\gamma) d\gamma \quad (3.25)$$

### 3.4) Numerical applications

To assess the accuracy of the proposed procedure to orthotropic plates of arbitrary shape, the frequencies of two plates were determined and compared with experimental and numerical values from the literature.

In particular, a clamped elliptical plate and a triangular cantilever plate have been analyzed (see Figure 3. 2). Two material properties have been taken into account for each configuration, see Table 3. 1.

**Table 3. 1** Material properties [67].

Material	$E_x$ [GPa]	$E_y$ [GPa]	$G_{xy}$ [GPa]	$\nu_{xy}$	$\rho$ [Kg/m <sup>3</sup> ]
Graphite/Epoxy	181	10.30	7.17	0.28	1600
Carbon/Epoxy	229	13.35	5.25	0.315	1600

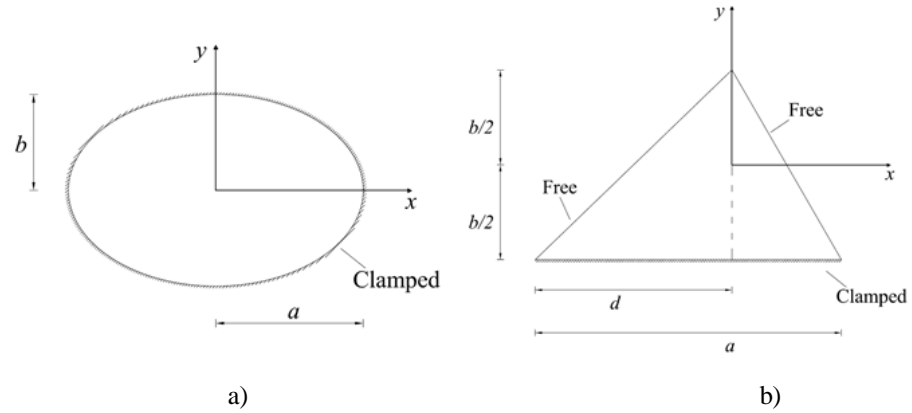


**Figure 3. 2** Analysed configurations: a) Elliptical clamped plate; b) Triangular cantilever plate.

Please note that,  $N = 20$  terms in Eq. (3.1) have been used for the pb-2 Rayleigh-Ritz procedure.

### 3.4.1) Elliptical plate

Consider the case of an elliptical shaped plate, made of orthotropic material, clamped along the whole boundary, as shown in Figure 3. 2 (a). The boundary equation  $\Gamma(x, y)$  is given as

$$\Gamma(x, y) = \left(\frac{x}{a}\right)^2 + \left(\frac{y}{b}\right)^2 - 1 \quad (3.26)$$

and, considering the chosen BCs, the boundary function  $\phi_1(x, y)$  in Eq. (3.3) can be expressed as  $\phi_1(x, y) = \Gamma(x, y)^2$ . Further, taking into account that the boundary of the plate is defined by the curve in parametric form

$$\begin{cases} x = a \cos \gamma \\ y = b \sin \gamma \end{cases}, \quad 0 \leq \gamma \leq 2\pi \quad (3.27)$$

Eq. (3.25) can be used to obtain the element of the matrices  $\mathbf{R}^{(de,pq)}$  in Eqs. (3.17) and (3.18).

The pb-2 Rayleigh-Ritz procedure has then been applied to identify the first five frequencies of elliptical plates considering the two materials in Table 3. 1. Results are reported in Tables 3. 2 and 3. 3, considering  $a = 1m$ ,  $b = 0.5m$  and  $h = 5mm$ , for *Graphite/Epoxy* and *Carbon/Epoxy* materials, respectively. Note that, for each frequency, relative percent error is reported.

**Table 3. 2** Frequencies  $\tilde{f}_k = \tilde{\omega}_k / 2\pi$  [Hz] for elliptical plate of *Graphite/Epoxy* material.

<i>Graphite/Epoxy</i>	1 <sup>st</sup>	2 <sup>nd</sup>	3 <sup>rd</sup>	4 <sup>th</sup>	5 <sup>th</sup>
Frequency in [60]	22.53	46.23	47.51	73.42	79.94
Calculated frequency	22.53	46.25	47.53	73.52	80.10
Error %	0	-0.04	-0.04	-0.14	-0.20

**Table 3. 3** Frequencies  $\tilde{f}_k = \tilde{\omega}_k / 2\pi$  [Hz] for elliptical plate of *Carbon/Epoxy* material.

<i>Carbon/Epoxy</i>	1 <sup>st</sup>	2 <sup>nd</sup>	3 <sup>rd</sup>	4 <sup>th</sup>	5 <sup>th</sup>
Frequency in [60]	25.00	51.46	52.55	80.41	89.81
Calculated frequency	25.00	51.49	52.58	80.52	89.99
Error %	0	0.06	0.06	-0.14	-0.20

Results show an excellent agreement between identified and reference frequencies with errors lower than 1% for all the frequencies investigated.

### 3.4.2) Triangular plate

Consider a general orthotropic triangular plate, bounded by the sides (1)  $y = bx/d + b/2$ , (2)  $y = -b/2$  and (3)  $y = -bx/(a-d) + b/2$ , where the quantities  $a$ ,  $b$  and  $d$  are shown in Figure 3. 2 (b). Assuming the plate to be

clamped only along the second edge, while the other two are free, the boundary function  $\phi_1(x, y)$  in Eq. (3.3) can be expressed as

$$\phi_1(x, y) = \left(y + \frac{b}{2}\right)^2 \quad (3.28)$$

Representing the aforementioned boundary equations in parametric form, the element of the matrices  $\mathbf{R}^{(de,pq)}$  in Eqs. (3.17) and (3.18) can be determined using Eq. (3.25).

The first five frequencies of the triangular plate have been then identified for the two materials in Table 3. 1 and compared with those numerically calculated in [61], considering  $a=0.25m$ ,  $b=3a/2$ ,  $d=a/2$  and  $h=5mm$ . Results are reported in Tables 3. 4 and 3. 5 for *Graphite/Epoxy* and *Carbon/Epoxy* materials, respectively.

Note that, for each frequency, relative percent error is reported.

**Table 3. 4** Frequencies  $\tilde{f}_k = \tilde{\omega}_k/2\pi$  [Hz] for triangular plate of *Graphite/Epoxy* material.

<i>Graphite/Epoxy</i>	1 <sup>st</sup>	2 <sup>nd</sup>	3 <sup>rd</sup>	4 <sup>th</sup>	5 <sup>th</sup>
Frequency in [61]	29.60	128.36	218.24	311.85	536.72
Calculated frequency	29.62	128.43	218.38	317.19	540.37
Error %	-0.04	-0.05	-0.66	-1.71	-0.68

**Table 3. 5** Frequencies  $\tilde{f}_k = \tilde{\omega}_k/2\pi$  [Hz] for triangular plate of *Carbon/Epoxy* material.

<i>Carbon /Epoxy</i>	1 <sup>st</sup>	2 <sup>nd</sup>	3 <sup>rd</sup>	4 <sup>th</sup>	5 <sup>th</sup>
Frequency in [61]	33.70	146.09	201.29	354.86	507.08
Calculated frequency	33.71	146.18	201.46	361.09	509.79
Error %	-0.03	-0.06	-0.08	-1.75	-0.54

Again, as for the elliptical case, an excellent agreement between calculated and reference frequencies have been obtained. Only the 4th frequencies show a percent error higher than 1%, but still lower than 2%. Results show the ability of the method to detect modal parameters of orthotropic arbitrarily shaped thin plates regardless the orthotropic material considered.

## CHAPTER IV

# IDENTIFICATION OF THE MECHANICAL PROPERTIES OF ORTHOTROPIC PLATES AND MEMBRANES

### 4.1) Introduction

The accurate identification of the mechanical properties of materials is a crucial aspect for any structural analysis, optimum design and quality control. Besides classical static testing [68], which require time and can damage the tested materials, alternative approaches combine non-destructive tests and the use of numerical methods.

Specifically, the natural frequencies and corresponding mode shapes of a structure can be detected by means of dynamic tests. Similarly, the static response of a system can be obtained performing non-destructive load-deflection tests, e.g. bulge tests.

The experimentally determined characteristics can be employed in optimization models, which update the elastic constants of a material until the predicted properties fit the experimental data within a certain tolerance.

Notably, this procedure represents a fast and non-destructive method for the identification of the mechanical properties of structural elements.

In this Chapter, two mixed numerical/experimental procedures are presented to identify the mechanical parameters of both orthotropic thin plates and membranes. In particular, first, the extended pb-2 Rayleigh-Ritz method, introduced in Chapter III, is combined with the Particle Swarm Optimization algorithm to yield the mechanical characteristic of orthotropic plates based on free-vibration data. The procedure is validated by identifying the mechanical properties of structurally thin plates, whose modal characteristics were detected by performing an extensive Experimental campaign at the Laboratory of

Experimental Dynamics of the University of Palermo. Second, the principle of the minimum energy is combined with a genetic optimization algorithm in order to identify the mechanical parameters of orthotropic membranes based on static bulge test data.

#### **4.2) Mechanical properties identification of orthotropic plates**

Several research efforts have focused in past decades on the development of numerical methods which would be able to determine mechanical properties of plates by vibration based experiments [69-72]. Initial approaches commonly employed a Rayleigh-Ritz technique to model the dynamic behavior of a plate, comprising of a least-squares method for estimating the elastic constants [69, 70]. Recent studies, which generally pertain to the application of FE method and novel optimization procedures, such as Genetic Algorithm, may be found in [73-80]. Although being very accurate, these latter approaches can be quite cumbersome and computationally demanding to implement, since they require a time consuming number of iterations in the FE simulations.

As previously discussed in Chapter III, the pb-2 Rayleigh-Ritz approach leads to an eigenvalue problem which can be easily solved to determine natural frequencies, as well as mode shapes, of arbitrarily shaped plates under several BCs and made of orthotropic material.

Notably, one of the beneficial features of this procedure lies in the fact that plate flexural and torsional rigidities directly appear in the mass and stiffness matrices in Eqs. (3.17) and (3.18). Thus, it can be argued that the aforementioned approach could be appropriately exploited, as an inverse problem, for the identification of the orthotropic material parameters. In passing, it is noted that existing approaches to this problem [69, 80] concern rectangular shaped plates, due to their widespread diffusion and the required lower computational cost. On the other hand, the case of arbitrary plate shapes, and their influence on the identification of mechanical properties, has not been investigated yet. Remarkably, such cases may not be uncommon, since, for instance, they occur whenever plate edges are not perfectly parallel to the orthotropy axes, assumed to be aligned to the  $x$  and  $y$  axes of the chosen coordinate system. Specifically,

based on some known values of the natural frequencies  $\tilde{\omega}_k$ , for instance those which are experimentally identified, an inverse procedure can be implemented leading to an estimate of the four involved mechanical parameters  $E_x$ ,  $E_y$ ,  $G_{xy}$  and  $\nu_{xy}$ . Note that, such a procedure can be easily pursued properly defining an objective function, to be minimized, related to the aforementioned elastic constants.

Specifically, in the present procedure, assuming dimensions and density of the plate to be known, the objective function is expressed by the functional

$$\Phi(D_x, D_y, D_t, \nu_{xy}) = \frac{1}{n_f} \sum_{k=1}^{n_f} \sqrt{\frac{|\tilde{\omega}_k - \omega_k|}{\tilde{\omega}_k}} \quad (4.1)$$

subject to the constraints

$$\begin{aligned} D_x &\in [D_{x,lower}, D_{x,upper}]; D_y \in [D_{y,lower}, D_{y,upper}]; \\ D_t &\in [D_{t,lower}, D_{t,upper}]; \nu_{xy} \in [\nu_{xy,lower}, \nu_{xy,upper}] \end{aligned} \quad (4.2)$$

where  $n_f$  is a chosen number of considered frequencies,  $\tilde{\omega}_k$  is the k-th natural frequency determined solving the eigenvalue problem in Eq. (3.19) and the terms in square brackets in Eq. (4.2) denote lower and upper bounds, respectively. Therefore, the functional to be minimized gives an account of the deviation between the measured  $\tilde{\omega}_k$  and numerically calculated  $\tilde{\omega}_k$  frequencies. Clearly, minimization of the functional in Eq. (4.1) leads to estimates of the flexural and torsional rigidities in Eqs. (1.36-37) and Eqs. (1.39-41), since the  $n_f$  natural frequencies  $\tilde{\omega}_k$  depend on these parameters via Eq. (3.19).

As far as the minimization of the functional  $\Phi(D_x, D_y, D_t, \nu_{xy})$  is concerned, the Particle-Swarm Optimization (PSO) method [81] has been used. This is a population-based approach, inspired by a mathematical description of the swarming of birds, with some useful characteristics [82] as simple implementation and execution, avoided evaluation of the objective function derivatives, and ability of finding regions in which a global minimum is attained even in presence of non-smooth objective functions (as in the case in which

experimental data are used). This method has proven particularly suitable for optimization procedures pertaining to structural mechanics problems [82-85]. Further, the method is based on few parameters (see [82] for details), among which the maximum number of iterations and the population size are particularly important. In fact, to avoid possible premature convergence of the PSO method, appropriate values of these two parameters can be chosen.

In this context, it is worth mentioning that other optimization procedures could be used to minimize the functional in Eq. (4.1) with respect to the coefficients  $(D_x, D_y, D_t, \nu_{xy})$ , such as ant colony optimization [86, 87], genetic algorithms [76, 78], and hybrid optimization techniques exploiting combination of the above mentioned procedures and classical gradient-based minimization routines [84]. Moreover, objective functions different from the one in Eq. (4.1) could also be considered, as those reported in [71] and [73], and even some based on the joint use of experimentally determined natural frequencies and mode shapes [88].

As far as the numerical implementation of the identification procedure is concerned, a three step scheme can be followed:

- i) Based on known plate dimensions, geometry and BCs, matrices  $\mathbf{R}^{(de,pq)}$  in Eqs. (3.17) and (3.18) are determined using Eq. (3.23).
- ii) PSO, implemented for instance in the MATLAB environment, is used to minimize the functional in Eq. (4.1) with respect to the coefficients  $(D_x, D_y, D_t, \nu_{xy})$ . At each iteration of the optimization procedure, values of the aforementioned coefficients are assumed and corresponding natural frequencies  $\omega_k$  are obtained solving the eigenvalue problem in Eq. (3.19).
- iii) Once the optimal values of the coefficients  $(D_x, D_y, D_t, \nu_{xy})$  which minimize Eq. (4.1) have been obtained, pertinent values of the mechanical parameters can be determined taking into account Eqs. (1.36-37) and Eqs. (1.39-41) as



$$\begin{aligned}
 E_x &= \frac{12}{h^3} (D_x - D_y \nu_{xy}^2); E_y = \frac{D_y}{D_x} E_x \\
 G_{xy} &= \frac{12 D_t}{h^3}; \nu_{yx} = \frac{D_y}{D_x} \nu_{xy}
 \end{aligned}
 \tag{4.3}$$

Observe that the evaluation of the matrices  $\mathbf{R}^{(de,pq)}$ , which represents the most computationally demanding step, can be carried out once beforehand. In this manner, since second and third steps do not depend on the plate shape or BCs, the identification procedure is completely generic and can be implemented independently on the first step.

#### 4.2.1) Literature comparison

To primarily assess the accuracy of the proposed procedure, the mechanical properties of the two plate configurations investigated in Section 3.4 were identified.

Again, properties of the two materials in Table 3. 1 have been taken into account for each configuration, demonstrating the ability of the method to detect mechanical properties regardless the orthotropic material considered.

Note that, for the following applications upper and lower bounds in Eq. (4.2) for the mechanical properties have been determined using Eqs. (1.36-37) and Eqs. (1.39-41) and assuming a  $\pm 60\%$  of variation with respect to the reference values in Table 3. 1. Further,  $N = 20$  terms in Eq. (3.1) have been used for the pb-2 Rayleigh-Ritz procedure.

##### 4.2.1.1) Elliptical plate

Consider the case of an elliptical shaped plate, made of orthotropic material, clamped along the whole boundary, as shown in Figure 3. 2 (a), and discussed in 3.3.1.

The proposed procedure has then been applied to identify the mechanical characteristics of the two materials in Table 3. 1, assuming as measured frequencies  $\tilde{\omega}_k$  in Eq. (4.1) those numerically calculated in [60], considering  $a = 1m$ ,  $b = 0.5m$  and  $h = 5mm$ . Please note that to investigate the accuracy of

the approach, two different numbers of considered natural frequencies  $n_f$  in Eq. (4.1) have been used, namely  $n_f = 5$  and  $n_f = 10$ . Thus frequencies in Tables 3.2 and 3.3 were extended up to ten frequencies, see Table 4. 1.

**Table 4. 1** Frequencies  $\tilde{f}_k = \tilde{\omega}_k/2\pi$  [Hz] for elliptical plate [60].

Material	Mode sequence number									
	1 <sup>st</sup>	2 <sup>nd</sup>	3 <sup>rd</sup>	4 <sup>th</sup>	5 <sup>th</sup>	6 <sup>th</sup>	7 <sup>th</sup>	8 <sup>th</sup>	9 <sup>th</sup>	10 <sup>th</sup>
<i>Graphite/ Epoxy</i>	22.5	46.2	47.5	73.4	79.9	87.8	110.5	111.8	145.9	151.4
<i>Carbon /Epoxy</i>	25.0	51.5	52.5	80.4	89.8	97.2	121.9	123.2	163.5	168.2

Identified mechanical parameters, for each value of  $n_f$  and material, are reported in Table 4. 2. Note that, for each identified parameter, the pertinent relative error is reported in square brackets.

**Table 4. 2** Identified mechanical parameters for elliptical clamped plate.

Material	$n_f$	$E_x$ [GPa]	$E_y$ [GPa]	$G_{xy}$ [GPa]	$\nu_{xy}$
<i>Graphite/ Epoxy</i>	5	181.7 [0.4 %]	10.34 [0.4 %]	7.39 [3.1 %]	0.201 [28.3 %]
	10	180.8 [0.1 %]	10.23 [0.1%]	7.05 [1.7 %]	0.303 [8.3 %]
<i>Carbon/ Epoxy</i>	5	228.5 [0.2 %]	13.32 [0.2 %]	4.36 [16.8 %]	0.411 [30.4 %]
	10	228.8 [0.1 %]	13.34 [0.1 %]	5.12 [2.4 %]	0.336 [5.9 %]

As can be observed in Table 4. 2, a satisfactory agreement between identified and reference Young's moduli in the x and y directions have been obtained, even for a low number of natural frequencies  $n_f$ . However, generally a higher value of  $n_f$  must be taken into account to more accurately identify the Poisson's ratio

and the shear modulus, for both materials considered. This may be due to the fact that natural frequencies are not particularly influenced by variations of  $\nu_{xy}$ .

#### 4.2.1.2) Triangular plate

Consider the case of an orthotropic triangular plate presented in Section 3.4.2, clamped only along the second edge, while the other two are free as shown in Figure 3.2 (b).

The mechanical characteristics of the two materials in Table 3.1 have then been identified, assuming as measured frequencies  $\tilde{\omega}_k$  in Eq. (4.1) those numerically calculated in [61], considering  $a = 0.25m$ ,  $b = 3a/2$ ,  $d = a/2$  and  $h = 5mm$ . Again, to investigate the accuracy of the approach, frequencies in Table 3.4 and Table 3.5 were extended up to the tenth, see Table 4.3.

**Table 4.3** Frequencies  $\tilde{f}_k = \tilde{\omega}_k/2\pi$  [Hz] for triangular plate.

Material	Mode sequence number									
	1 <sup>st</sup>	2 <sup>nd</sup>	3 <sup>rd</sup>	4 <sup>th</sup>	5 <sup>th</sup>	6 <sup>th</sup>	7 <sup>th</sup>	8 <sup>th</sup>	9 <sup>th</sup>	10 <sup>th</sup>
<i>Graphite/ Epoxy</i>	29.6	128.4	218.2	311.8	536.7	572.6	957.9	1606.4	1801.0	1818.2
<i>Carbon/ Epoxy</i>	33.7	146.1	1264.8	201.3	507.1	655.4	942.1	1654.1	1817.7	2002.8

In this regard, identified material parameters are reported in Table 4.4, for the two chosen values of  $n_f$ . Note that, for each identified parameter, the pertinent relative error is reported in square brackets.

**Table 4.4:** Identified mechanical parameters for triangular cantilever plate.

Material	$n_f$	$E_x$ [GPa]	$E_y$ [GPa]	$G_{xy}$ [GPa]	$\nu_{xy}$
<i>Graphite/ Epoxy</i>	5	163.8 [9.5 %]	10.29 [0.1 %]	7.17 [0 %]	0.226 [19.1 %]
<i>Carbon/ Epoxy</i>	10	181.0 [0 %]	10.30 [0 %]	7.17 [0 %]	0.279 [0 %]
<i>Graphite/ Epoxy</i>	5	216.2 [5.6 %]	13.34 [0.1 %]	5.24 [0.1 %]	0.212 [32.7 %]
<i>Carbon/ Epoxy</i>	10	229.0 [0 %]	13.35 [0 %]	5.25 [0 %]	0.315 [0 %]

Again, as can be observed in Table 4. 4, a good agreement between identified and reference Young's moduli in the x and y directions have been obtained, even for a low number of natural frequencies  $n_f$ . However, in this case a very low value of relative error has also been achieved for the shear modulus  $G_{xy}$  for both materials, while higher discrepancies are obtained for the Young's modulus  $E_x$ . This could be due to both the shape of the plate and the adopted BCs. Further, it can be observed that considering a higher number of natural frequencies  $n_f$  allow a very accurate estimation of all the mechanical characteristics.

#### 4.2.2) Vibration based frequency identification of stiffened plates

To further assess the reliability of the procedure, an extensive experimental campaign was conducted at the Laboratory of Experimental Dynamics at the University of Palermo. Specifically, free-vibration tests were performed for several rectangular 3D printed plates reinforced by equidistant stiffeners in one direction. Plates were made by means of a 3D printer in order to avoid any possible detrimental effect due to bad connections between the plate and the stiffeners. Experimentally measured frequencies and mode shapes were obtained using both laser scanning vibrometer and impulsive tests.

##### 4.2.2.1) Experimental campaigns

Three different plate configurations have been considered, as shown in Figure 4. 1(a): a homogeneous flat rectangular plate (Configuration #1), a rectangular plate with 6 equidistant stiffeners in one direction (Configuration #2) and a rectangular plate with 9 equidistant stiffeners in one direction (Configuration #3). A sketch of the plates geometry is shown in Figure 4. 1 (b), while dimensions of each Configuration is reported in Table 4. 5.

Plates have been realized through a 3D printer Model PRUSA i3 MK2S, as shown in Figure 4. 1 (c), which is a fuse deposition modeling printer, employing common polylactic acid (PLA) filaments. Remarkably, thanks to the 3D printing

manufacturing process, any mechanical or adhesive bonding between the plate and the stiffeners have been avoided.

**Table 4. 5** Plate configurations parameters.

Configurations	$\tilde{a}$ [mm]	$\tilde{b}$ [mm]	$h$ [mm]	$\tilde{h}$ [mm]	$\tilde{L}$ [mm]	$\tilde{p}$ [mm]	$\rho$ [kg/m <sup>3</sup> ]
<i>Configuration #1</i>	190	210	4	-	-	-	1240
<i>Configuration #2</i>	190	210	4	2	7.6	22.8	1240
<i>Configuration #3</i>	190	210	4	2	7.6	15.2	1240

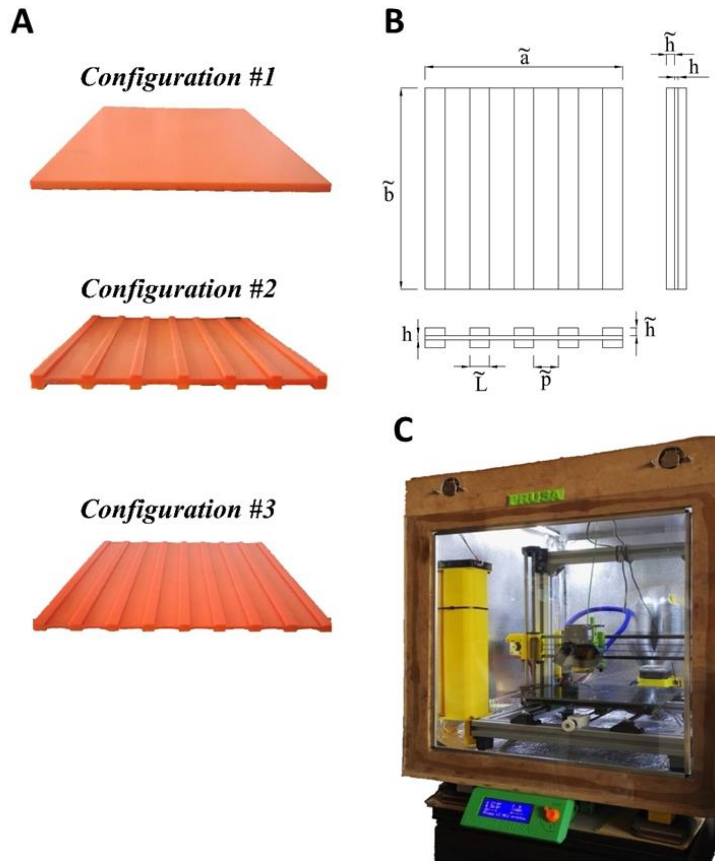


**Figure 4. 1** (a) Plate Configurations; (b) Plate geometry; (c) 3D Printer.

As far as the experimental set-up is concerned, cantilever plate conditions have been employed for the tests for each Configuration, since these BCs are

particularly suitable for experiments compared to other common cases. In this regard, Figure 4. 2 shows the adopted experimental set-up, while in Figure 4. 3 pictures of the experimental equipment are reported.

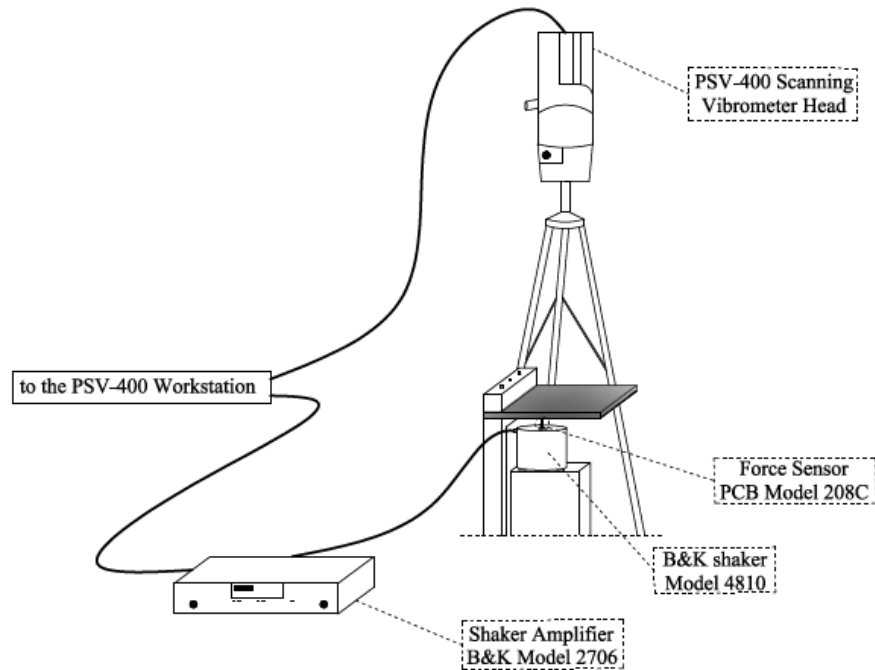


**Figure 4. 2** Experimental set-up.

As can be seen, each plate configuration has been fixed on one side of a rigid frame (Figure 4. 3 (b)) and excitation has been provided through a B&K shaker type 4810 (Figure 4. 3 (c)) connected with a stinger close to the clamped side of the plate. Further, the input force signal has been acquired through a PCB ICP Force Sensor model 208C, directly positioned between the shaker and the plate (Figure 4. 3 (d)). The Frequency Response Functions (FRFs) and the mode shapes of the plates have been measured with a Polytec laser scanning vibrometer model PSV-400 (Figure 4. 3 (e)) which allows the measurement of both velocity and displacements over a chosen grid of points of the plate without any contact through the laser signal. Note that the forcing signal, provided by the shaker

connected to the B&K amplifier model 2706 Figure 4. 3 (f) is generated by the Polytec workstation Figure 4. 3 (g), to which the laser head is also connected.



**Figure 4. 3** Devices employed for the experimental tests.

A sweep sine, of frequency range between 0.1 and 2000 Hz, has been used as forcing signal and repeated for each point of the grid, while the chosen sample rate was 2000 Hz. Finally, the mode shapes and corresponding natural frequencies have been identified by means of the vibrometer software version 9.2.

To obtain more precise data especially at the lowest frequency, impulsive tests have been also performed for all the three Configurations. Specifically, a small impact hammer model PCB 086E80 Figure 4. 4(a) has been used to provide the impulse, while four miniature PCB piezoelectric accelerometers Model 352C23 Figure 4. 4 (b) have been employed to measure the acceleration responses on different points of the plates. Note that, considering the small

dimensions and mass of each of these accelerometers, the influence of these sensors on the plate frequency response can be neglected. Further, signals have been then digitalized and acquired by means of a National Instruments NI 4497 PXI Acquisition Board provided inside the chassis of a National Instruments PXIe model 1082, and then processed in self-developed LabView and MATLAB environments programs (Figure 4. 4 (c)).

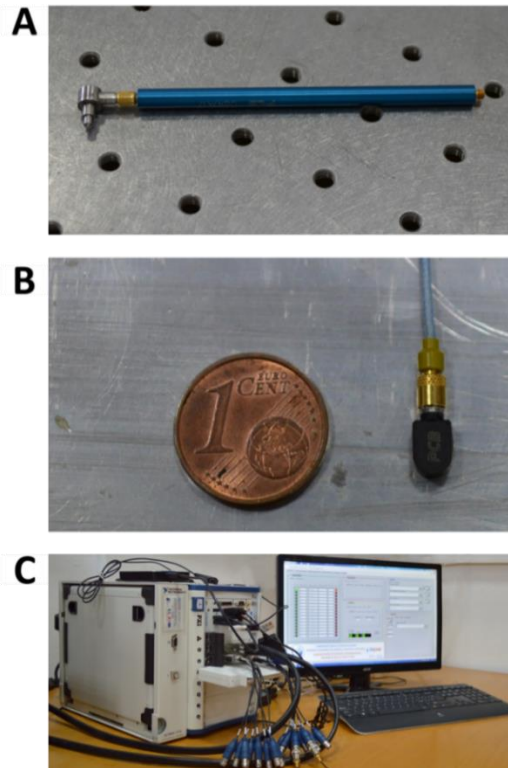


**Figure 4. 4** Devices employed for the impulsive tests: (a) PCB impact hammer model 086E80; (b) miniature PCB accelerometers Model 352C23; (c) NI PXIe model 1082.

For each plate Configuration five tests have been performed, both with shaker and the impact hammer, and pertinent average FRFs has been determined. The corresponding identified natural frequencies are reported in Table 4. 6.



**Table 4. 6** Experimentally identified frequencies  $\tilde{f}_k = \tilde{\omega}_k/2\pi$  [Hz].

Configurations	Mode sequence number									
	1 <sup>st</sup>	2 <sup>nd</sup>	3 <sup>rd</sup>	4 <sup>th</sup>	5 <sup>th</sup>	6 <sup>th</sup>	7 <sup>th</sup>	8 <sup>th</sup>	9 <sup>th</sup>	10 <sup>th</sup>
<b>Configuration #1</b>	22.4	60.3	138.7	216	219	388	412	476	545	661
<b>Configuration #2</b>	34.5	76	201	221	292	474	482	586	650	684
<b>Configuration #3</b>	37.4	88.4	218.5	236.2	317.5	506	511	646	700	745

**4.2.2.2) Mechanical properties identification of 3D printed plates**

The mechanical parameters of the three printed plates were identified based on the vibration data obtained. Moreover, to verify the reliability of the approach, a comparison among experimental data, FE simulations and numerical results of the proposed procedure has been performed.

Firstly, material parameters (Young’s modulus  $E$  and Poisson's ratio  $\nu$ ) of the homogeneous flat plate (Configuration #1, see Figure 4. 1(a)), assumed to be isotropic, have been identified minimizing the mean squared error between the first two experimentally obtained natural frequencies, and the corresponding analytical ones reported in [3]. In this regard, the identified values are reported in first line of Table 4. 7. Clearly, since the material is isotropic  $E = E_x = E_y$  and  $\nu = \nu_{xy} = \nu_{yx}$ .

**Table 4. 7** Identified material parameters.

Configurations	$E_x$ [GPa]	$E_y$ [GPa]	$G_{xy}$ [GPa]	$\nu_{xy}$
<b>Configuration #1</b>	2.77	2.77	1.09	0.263
<b>Configuration #2</b>	3.95	1.44	0.94	0.383
<b>Configuration #3</b>	4.17	1.44	1.01	0.307

To verify the validity of the identified parameters, the natural frequencies of the plate have been determined also by FE analysis on ANSYS environment using these aforementioned values. Specifically, for the FE analysis a hexahedral mesh with 395 nodes and 67.000 elements has been used. Pertinent results are shown in Figure 4. 5 where experimental natural frequencies (black circles) are reported vis-à-vis analytical ones [3] (dashed blue line) and those from the numerical FE simulation (magenta squares). In this figure the modes are labelled by two mode indices, namely  $m$  and  $n$ , indicating the number of nodal lines approximately parallel to  $y$ - and  $x$ -axis, respectively, including the boundaries as nodal lines, except when the boundary is free [3]. The frequencies are plotted over the mode index  $m$ . Lines connecting the symbols are guides to the eyes only.

As can be seen, a very good match between experimental and numerical natural frequencies is achieved, thus proving the validity of the identified parameters. In this regard, a low average relative error between FE results and experimental data, of approximately 2.5%, has been obtained.

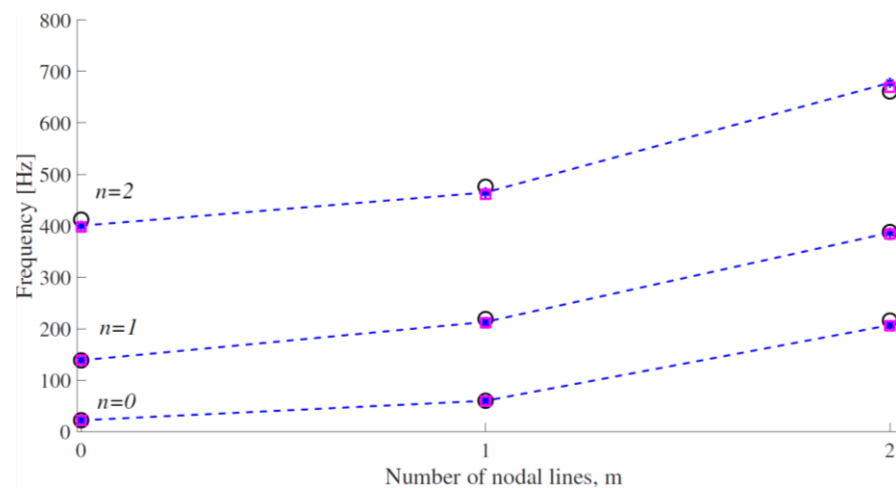


**Figure 4. 5** Comparison of experimental vis-à-vis numerical data in terms of natural frequencies for Configuration #1. Dashed blue lines –Analytical results; Magenta squares – FE results; Black circles – Experimental data.

Once the material parameters of the flat plate (Configuration #1) have been determined and verified, attention has been focused on the two stiffened plates (Configurations #2 and #3, Figure 4. 1(a)).

Specifically, assuming an orthotropic behavior of these plates, firstly the proposed identification procedure has been applied. On this base, equivalent orthotropic parameters of the two Configurations have been retrieved minimizing the functional in Eq. (4.1) considering the  $n_f = 10$  experimentally determined natural frequencies  $\tilde{\omega}_k$  in Table 4. 6. The pertinent identified mechanical parameters are reported in Table 4. 7 (second and third lines). Further, numerical results in terms of mode shapes and natural frequencies for Configurations #2 and #3 have also been obtained applying the pb-2 Rayleigh-Ritz procedure described in Chapter III. Again, to verify the validity of these identified parameters, natural frequencies and mode shapes of the actual stiffened plate have been determined also via FE analyses in the ANSYS environment using the actual geometry of the plate (Table 4. 5 and Figure 4. 1 (b)). Specifically, the real plates shapes (flat plates with stiffeners) have been modelled with 3D elements, assuming the isotropic material with the previously obtained Configuration #1 Young's modulus and Poisson's ratio (see Table 4. 4).

It has to be noted that corrugated and stiffened plates have been deeply investigated in the past decades. Stiffened plates, in fact, show some economical and mechanical advantages, but their analysis and optimization may be a daunting task, thus requiring computationally demanding FE analyses. In some cases, however, mechanical behavior of stiffened or corrugated plates can be also studied considering an equivalent flat plate made of orthotropic material, generally referred to as Equivalent Plate Model (EPM). Previously obtained experimental data indicate good accuracy of such idealization, provided that relatively small, and closely spaced, stiffeners are employed. Clearly, this approach yields various advantages, such as reducing the computational effort that FE method would have demanded, especially in preliminary design. Therefore, several research efforts have been devoted to determining the required equivalent orthotropic plate parameters. It is worth noting that, the majority of studies have dealt with the cases of corrugated plates, introducing several

different approximate relations, which have also been experimentally analyzed [89]. On the other hand, the case of longitudinally stiffened plates has been less investigated, many studies date back to the '50s [90-93] and few other have been more recently presented [94, 95] on this topic. Further, experimental analyses in literature generally comprise only the first fundamental natural frequency, while the accuracy of such EPM pertaining to higher natural frequencies and mode shapes has been much less addressed [93]. Thus, to further assess the reliability of the approach, equivalent orthotropic plate rigidities have been estimated applying the relations of the so-called EPM for stiffened plates, given in [1, 2]. In this regard, according to the EPM, the orthogonally stiffened plate can be treated as an equivalent flat plate made of orthotropic material. Specifically, for a rectangular plate reinforced by equidistant stiffeners in one direction of thickness  $\tilde{h}$ , disposed symmetrically with respect to the middle plane of the plate (Figure 4. 1(b)), and assuming that both the plate and the stiffeners are made of the same isotropic material, EPM yields the equivalent rigidities as

$$D_x = \frac{E h^3}{12(1-\nu^2)} + \frac{E I}{(\tilde{p} + \tilde{L})}; \quad D_y = \frac{E h^3}{12(1-\nu^2)}; \quad D_1 = \nu D_y; \quad (4.4)$$

$$\nu_{xy} = \frac{D_1}{D_y}; \quad \nu_{yx} = \frac{D_1}{D_x}; \quad D_t \approx \frac{(1 - \sqrt{\nu_{xy}\nu_{yx}})\sqrt{D_x D_y}}{2}$$

where  $E$  and  $\nu$  are the elastic constant of Configuration #1 given in Table 4. 7,  $I$  the moment of inertia of the stiffener taken with respect to the middle axis of the cross section of the plate, while  $\tilde{p}$  and  $\tilde{L}$  are reported in Figure 4. 1(b). In this manner, based on Eq. (4.4), Eq. (3.19) yields the corresponding natural frequencies of Configurations #2 and #3 for the EPM.

Comparisons of the different adopted procedures are shown in Figure 4. 6. In this figure natural frequencies obtained by applying the proposed procedure (red dotted line) are compared with the experimentally determined natural frequencies (black circles), the EPM numerical data (dashed blue line) and the numerical FE simulation results (magenta squares).

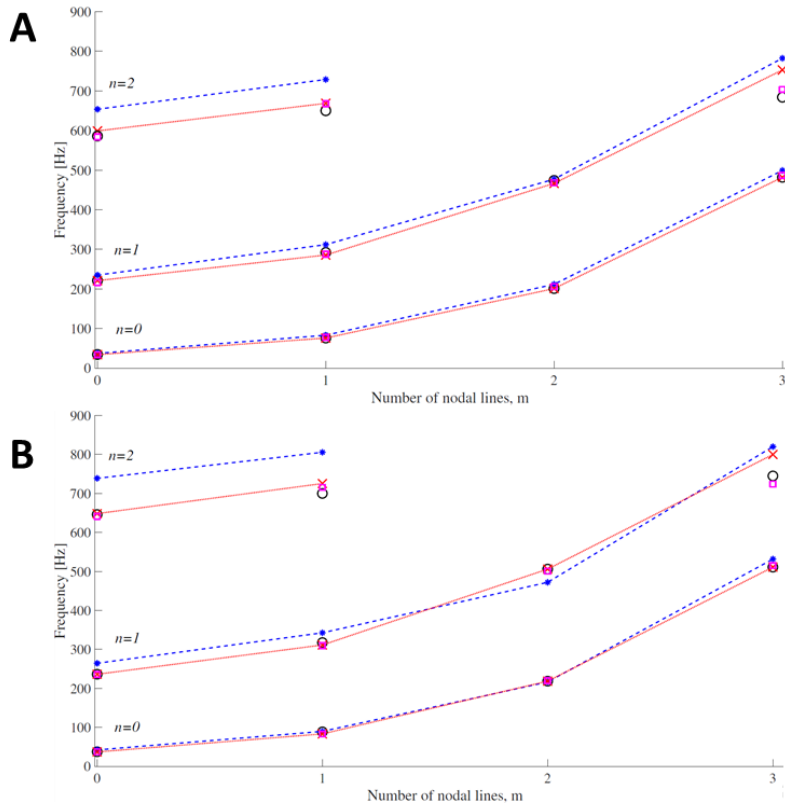


**Figure 4. 6** Comparison of experimental vis-à-vis numerical data in terms of natural frequencies: a) Configuration #2; b) Configuration #3. Red dotted lines - Proposed procedure results; Blue dashed lines –EPM results; Magenta squares – FE results; Black circles – Experimental data.

As is apparent, the proposed method results excellently agree with both pertinent experimental data and FE simulations, thus proving the reliability of the proposed identification procedure. Specifically, the average relative errors between the proposed method results and experimental data are 2.1% for Configuration #2 and 2.2% for Configuration #3. Moreover, considering that FE analyses have been carried out on the actual plate's geometry, i.e. no assumptions have been made for these simulations, the validity of the applied experimental procedure has been further assessed.

As far as the EPM results are concerned, Figure 4. 6 shows that EPM leads to a satisfactory agreement with the experimental data at lower frequencies, while, as expected, the accuracy of the EPM results decrease drastically at higher

frequencies. It can be therefore argued that EPM could be adopted to estimate the first few natural frequencies of stiffened plates.

In addition, as shown in Figure 4. 7, analogous analyses have been also performed in terms of mode shapes. Specifically, in this figure, the first three mode shapes obtained experimentally are compared with those which are numerically determined with the proposed procedure and FE analyses with ANSYS on the actual stiffened plate geometry. As it can be observed, these numerical methods lead to satisfactory agreement with the experimental data. Similar results have also been obtained for higher modes, omitted for brevity's sake.

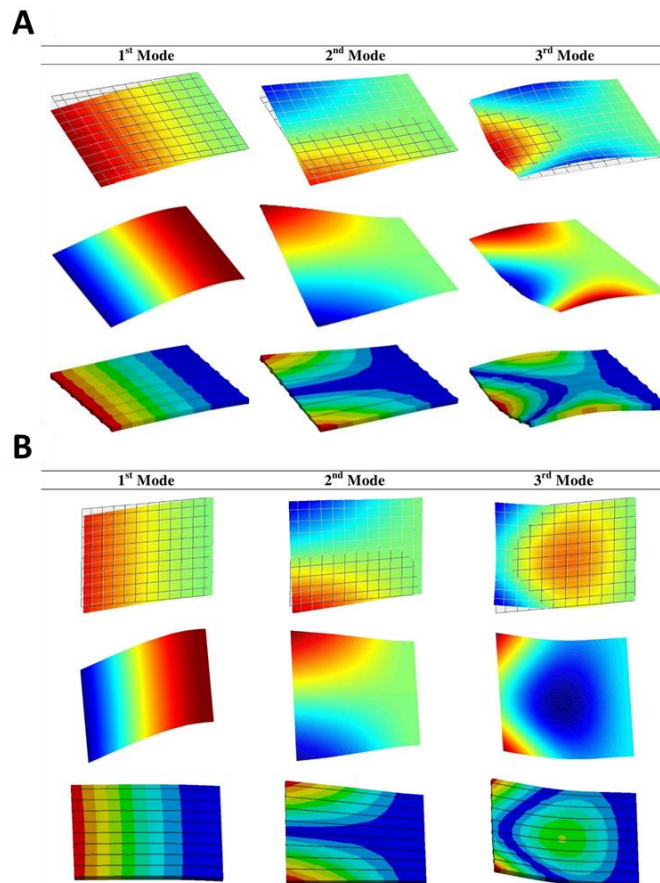


**Figure 4. 7** Comparison of experimental vis-à-vis numerical results in terms of mode shapes for the stiffened plate a) Configuration #2; b) Configuration #3. First row- Experimental data; Second row – Numerical results with proposed procedure; Third row – FE results with ANSYS.

### **4.3) Mechanical properties identification of orthotropic membranes**

Mixed numerical-experimental procedures have also been proposed for the analysis of orthotropic thin films and membranes in order to establish a reliable test method to determine the mechanical properties of these structural elements.

To date, the mechanical characterization of orthotropic membranes presents many difficulties, which hinder the accuracy of the results. Their very thin thickness complicates the measurement of both longitudinal and transversal elongations using classical strain-gage extensometers [96]. Consequently, the longitudinal elongation is often measured by the crosshead movement of the testing machine, which is influenced by errors in measurements and by the slippage of the specimen.

To overcome these limitations, several alternative methods have been proposed: ultrasonic based techniques have been used for the mechanical characterization of papers [97, 98]; and optic methods have been employed for the strain field analysis of papers under different orientation [99, 100]. A promising procedure, which combines a theoretical model of the response of thin films and experimentally determined load-deflection curves has garnered much attention. The procedure is based on recording the load-deflection response of thin films in bulge test apparatus. The bulge test system consists of a sample holder with a square or circular window, which allows the sample to deform under the action of a load. Samples are clamped at the edges of the window and both the load and the sample's deflection are measured during the test. Since the determined load-deflection curve depends on the mechanical characteristics of the material under investigation, a mathematical model can be employed to extract the material's mechanical properties.

This method has been widely applied to the study of thin films [101, 102], biological tissues [103, 104], MEMS [105, 106] and membranes [107].

Many studies have been focused on the development of theoretical models for the analysis of isotropic membranes. Tabata et al. [108] proposed an analytical formulation to describe the load-deflection relation of rectangular membranes. A functional form of the membrane's displacements was assumed and the total

membrane potential energy was minimized. Functionals of the type of the Fourier expansion, presented by Timoshenko in early studies [1], were employed. Then, the material's mechanical characteristics can be found by the least-square fitting between the experimentally measured load-deflection curve and that which was mathematically obtained.

Later, Pan. et al. [109] investigated the accuracy of Tabata's equation via numerical and experimental analysis. They developed an ad-hoc FEM model, which was validated by experimental measurements. The FEM model was in excellent agreement with the experimental results, while the analytical equation proposed by Tabata showed errors greater than 10%. Moreover, Tabata's equation did not very accurately match the experimentally measured bending lines along the diagonals of the thin material.

Some years later, Maier et al. [102] introduced a novel functional form for the membrane deflection to improve the accuracy of Tabata's analytical equation. Results showed a very good agreement with Pan's FEM results and membrane bending shapes.

As far as orthotropic thin membranes are concerned, some authors have proposed theoretical models for the analysis of orthotropic membranes. Among them, Chucheepsakul [110] presented a solution for the large deflection analysis of orthotropic elliptic membranes based on the Rayleigh-Ritz method. Moreover, Bouzidi et al. [111] introduced a semi-analytical solution for the deflection of orthotropic rectangular membranes by directly minimizing the total potential energy. The authors indicated that the approach may be used as an inverse problem to determine the mechanical characteristics of membranes based on experimental bulge tests.

In this context, in the following section, the energy minimization method is applied for the analysis of the deflection of rectangular orthotropic membranes and combined with an optimization procedure in order to propose a novel procedure for the characterization of the properties of orthotropic membranes by means of experimental bulge tests.



### 4.3.1) The energy minimization principle for orthotropic membranes

As mentioned above, the energy minimization method has previously been employed [101, 102, 108] to describe the load-deflection behaviour of isotropic thin films. The method can be adequately applied also for the analysis of orthotropic membranes.

Specifically, considering a rectangular membrane, as shown in Figure 1. 8, functional forms of the displacement functions  $u(x, y)$ ,  $v(x, y)$  and  $w(x, y)$  can be expressed as:

$$\begin{cases} u(x, y) = (c_1 + c_2x^2 + c_3y^2 + c_4x^2y^2) \sin\left(\frac{\pi x}{a}\right) \cos\left(\frac{\pi y}{2b}\right) \\ v(x, y) = (c_5 + c_6x^2 + c_7y^2 + c_8x^2y^2) \cos\left(\frac{\pi x}{2a}\right) \sin\left(\frac{\pi y}{b}\right) \\ w(x, y) = (c_9 + c_{10}x^2 + c_{11}y^2 + c_{12}x^2y^2) \cos\left(\frac{\pi x}{2a}\right) \cos\left(\frac{\pi y}{2b}\right) \end{cases} \quad (4.5-7)$$

where  $a$  and  $b$  are the membrane half-edge length along the  $x$  and  $y$  axes, respectively;  $c_i$  are the unknown coefficients to be determined. Eqs. (4.5-7) are of the form of those proposed by Maier et al. [102] adequately modified to be used for the analysis of both orthotropic and rectangular membranes.

As far as boundary conditions are concerned, Eqs. (4.5-7) satisfy the zero displacement condition at the boundaries. It should be noted that in the case of membranes, the tangent of the deflection function at the clamped edges is not horizontal, since thin films do not have flexural rigidity.

According to the principle of minimum potential energy, the unknown coefficients  $c_i$  can be obtained by performing the variation of the total potential energy of the membrane with respect to the unknown coefficients.

Thus, recalling the total potential energy for a membrane subjected to an initial pre-stress and lateral loading (Eq. (1.83)) and performing the variation with respect to the unknown coefficients  $c_i$ , one has:

$$\frac{\partial \Pi_{tot}}{\partial c_i} = 0 \quad i = 0, 1, 2, \dots, 12 \quad (4.8)$$

Consequently, a set of non-linear equations in terms of the unknown coefficients  $c_i$  is obtained. Substituting, Eqs. (1.68), (1.80) and (1.82) into Eq. (4.8) and taking into account Eqs. (4.5-7), the coefficients can be retrieved and the displacement field obtained.

### 4.3.2) Mechanical properties identification

The principle of minimum energy can be employed to determine the displacement field of a membrane subjected to an external load and pre-stress loading. It is worth noting that the material properties ( i.e.,  $E_x$ ,  $E_y$ ,  $G_{xy}$  and  $\nu_{xy}$ ) directly appear in the strain energy of the membrane (Eq. (1.80)).

Therefore, the procedure could also be used as an inverse problem for evaluating the mechanical properties of a membrane, if the membrane deflection-load relation of a bulge test is known.

Specifically, an objective function, related to the material elastic parameters, can be defined and minimized. In particular, the absolute percentage error between experimental membrane deflection and that calculated by using the energy minimization method can be used:

$$\Upsilon(E_x, E_y, \nu_{xy}, G_{xy}) = \frac{|\tilde{w} - w|}{\tilde{w}} \times 100 \quad (4.9)$$

Subject to constraints:

$$\begin{aligned} E_x &\in [E_{x,lower}, E_{x,upper}]; E_y \in [E_{y,lower}, E_{y,upper}]; \\ \nu_{xy} &\in [\nu_{xy,lower}, \nu_{xy,upper}]; G_{xy} \in [G_{xy,lower}, G_{xy,upper}] \end{aligned} \quad (4.10-4.13)$$

where  $\tilde{w}$  is the experimentally measured deflection of the membrane at a certain point over the surface and for a certain loading value, and  $w$  is the surface deflection value calculated numerically. Subscripts in Eqs. (4.10-4.13) indicate the lower and upper values limiting the intervals where the variables can be modified in the optimization procedure.

As far as the minimization of the functional  $\Upsilon(E_x, E_y, \nu_{xy}, G_{xy})$  is concerned, a genetic algorithm has been used.

To identify the material properties, a two steps scheme can be followed:

- First, Eqs. (4.5-7) can be substituted into Eqs. (1.68), (1.80) and (1.82), thus expressing the total potential energy as a function of the unknown coefficients  $c_i$ . Then, the total potential energy is integrated with respect to the membrane geometry characteristics (i.e. membrane thickness, width and length). Finally, by performing the variation of the total potential energy (Eq. (4.8)) an algebraic system of equations is attained and membrane deflection can be found.
- Second, a genetic algorithm, implemented for instance in the MATLAB environment, is used to minimize the functional, Eq. (4.9), by identifying the best set of the mechanical parameters  $E_x, E_y, \nu_{xy}, G_{xy}$ .

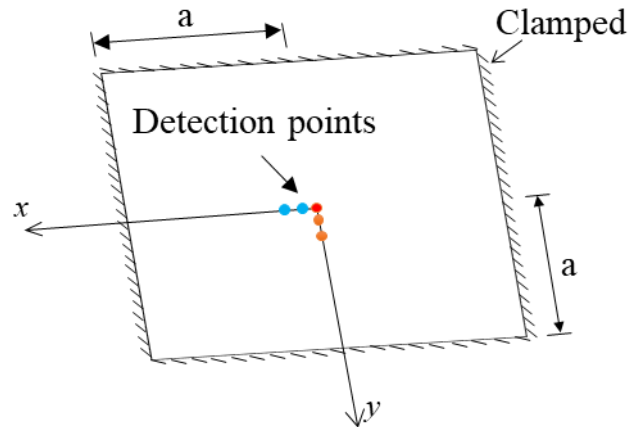
Please note that, the first step requires high computing time due to the calculation of the integrals and then of the derivatives of the total potential energy. Therefore, an analytical expression of the derivatives of the total potential energy as a function of the material's mechanical properties, unknown coefficients, the membrane's geometrical characteristics (thickness, width and length) and of the loads was determined by employing the Mathematica software. Thus, the first step can be solved only one time, drastically reducing the computing time for the optimization procedure.

#### 4.3.2.1) Membrane properties from virtual bulge tests

To assess the accuracy of the procedure, the mechanical properties of two square orthotropic membranes of 4 cm side (see Figure 4. 8) were identified using virtual experimental data. Specifically, the deflection-loading relation of the two membranes was obtained using the Finite Element software COMSOL Multiphysics. The membranes were simulated as a 2D surface with all edges clamped. A structured square mesh was used with 4489 square elements. The mechanical properties of the membrane investigated are reported in Table 4. 8.

**Table 4. 8** Material properties of the two investigated thin films.

Material	$E_x$ [MPa]	$E_y$ [MPa]	$G_{xy}$ [MPa]	$\nu_{xy}$	$h$ [mm]
<i>Spinnaker</i> [112]	1110	385	220	0.35	0.1
<i>UKP</i> [113]	7320	2680	1890	0.164	0.125

**Figure 4. 8** Configuration of the square orthotropic membrane analysed and detection points for the evaluation of membrane deflection.

Membrane deflection was investigated for a transversal load varying from 0 to 0.2 MPa, for in-plane pretension of 2.06 MPa and 1.90 MPa along the  $x$ -axis for the UKP and the Spinnaker membranes, and in-plane pretension of 0.83 MPa and 0.79 MPa along the  $y$ -axis for the UKP and the Spinnaker membranes, respectively. The functional  $\Upsilon(E_x, E_y, \nu_{xy}, G_{xy})$  Eq. (4.9) was evaluated for five detection points along the  $x$  and  $y$  axes at three loads of 0.1, 0.15 and 0.2 MPa. Specifically, the surface's middle point and two points placed respectively at a distance of 1 mm from each other were considered, as shown in Figure 4. 8. Therefore, Eq. (4.9) was computed fifteen times for each set of mechanical parameters  $E_x, E_y, \nu_{xy}, G_{xy}$ . Then, the largest discrepancy between calculated and experimental deflections is minimized to find the best set of mechanical

parameters. Further, to increase the accuracy of the identified mechanical parameters, the procedure was carried out following two steps:

- First, the lower and upper values of  $E_x$  and  $E_y$  in Eqs. (4.10-4.11) were set to be  $\pm 30\%$  of their reference values (Table 4. 8), whereas,  $G_{xy}$  and  $\nu_{xy}$  in Eqs. (4.12-4.13) were let to vary between  $\pm 50\%$  of their reference values (Table 4. 8).
- In the second step,  $E_x$  and  $E_y$  were let to vary between  $\pm 10\%$  and  $G_{xy}$  and  $\nu_{xy}$  of  $\pm 15\%$  with respect to the identified values in step 1.

Each step is run 20 times and the resulting mechanical parameters are calculated as the mean value of those calculated for the each run.

Tables 4. 9 and 4. 10 report the identified values for the Spinnaker [112] membrane characteristics for the first step and second step of the proposed procedure. Discrepancies are calculated with respect to values from literature (Table 4. 8). Standard deviation is also reported.

**Table 4. 9:** Identified material parameters for the Spinnaker membrane material [112] at the 1<sup>o</sup>Step. Discrepancies with respect to literature values and standard deviation are also reported.

Quantities	Identified values		
	1 <sup>o</sup> Step	Discrepancy %	St. Dev
$E_x$ [MPa]	1133.2	<b>-2.1</b>	38.48
$E_y$ [MPa]	386.65	<b>-0.43</b>	19.67
$G_{xy}$ [MPa]	207.8	<b>5.54</b>	56.25
$\nu_{xy}$	0.3175	<b>9.28</b>	0.072

**Table 4. 10** Identified material parameters for the Spinnaker membrane material [112] at the 2<sup>o</sup>Step. Discrepancies with respect to literature values and standard deviation are also reported.

Quantities	Identified values		St. Dev
	2 <sup>nd</sup> Step	Discrepancy %	
$E_x$ [MPa]	1130.85	<b>-1.88</b>	10.43
$E_y$ [MPa]	385.2	<b>-0.05</b>	6.88
$G_{xy}$ [MPa]	205.2	<b>6.6</b>	13.96
$\nu_{xy}$	0.3235	<b>7.57</b>	0.02

The highest discrepancy value is found to be 9.28% for the Poisson ratio identified at the 1<sup>st</sup> Step. Performing the 2<sup>nd</sup> Step, the value decreases to 7.57%, thus improving the accuracy of the identified value. As far as the Young's moduli ( $E_x$  and  $E_y$ ) are concerned, they are accurately detected, where the highest discrepancy found during the 2<sup>nd</sup> Step is only -1.88% for  $E_x$ .

With regard to the UKP membrane [113] investigation, results are reported in Tables 4. 11 and 4. 12.

**Table 4. 11** Identified material parameters for the UKP membrane material [113] at the 1<sup>o</sup>Step. Discrepancies with respect to literature values and standard deviation are also reported.

Quantities	Identified values		St. Dev
	1 <sup>o</sup> Step	Discrepancy %	
$E_x$ [MPa]	7540	<b>-3</b>	130.84
$E_y$ [MPa]	2520	<b>5.97</b>	60.3
$G_{xy}$ [MPa]	1818.95	<b>3.76</b>	294.66
$\nu_{xy}$	0.176	<b>-7.59</b>	0.0309

**Table 4. 12** Identified material parameters for the UKP membrane material [113] at the 2<sup>o</sup>Step. Discrepancies with respect to literature values and standard deviation are also reported.

Quantities	Identified values		St. Dev
	2 <sup>nd</sup> Step	Discrepancy %	
$E_x$ [MPa]	7555.8	<b>-3.22</b>	56.82
$E_y$ [MPa]	2530	<b>5.59</b>	40.49
$G_{xy}$ [MPa]	1812	<b>-4.13</b>	118.23
$\nu_{xy}$	0.170	<b>-3.84</b>	0.0129

In this case, the highest discrepancy of -7.59% is detected for the Poisson ratio at the 1<sup>st</sup> Step. The value is almost halved by performing the 2<sup>nd</sup> Step. At the 2<sup>nd</sup> Step, the highest discrepancy of 5.59% is calculated for the  $E_y$ . Overall, all the parameters identified in the 2<sup>nd</sup> Step have discrepancy values lower than 6%.

Results obtained for both Spinnaker and UKP membranes show the reliability of the proposed method for identifying orthotropic parameters of membranes by means of deflection-load relations from the bulge tests.

## CHAPTER V

# **ANALYSIS OF THE MECHANICAL BEHAVIOUR OF ION EXCHANGE MEMBRANES IN MEMBRANE BASED TECHNOLOGIES**

### **5.1) Introduction**

In the previous chapters, the studies conducted on the mechanical behaviour of thin plates and membranes provide the necessary background to better understand membrane response in many possible scenarios. In the following chapters, the attention is focused on the investigation on the effects of membrane deformation in the specific application of the membrane-based Electrodialysis and Reverse Electrodialysis processes.

#### **5.1.1) Electrodialysis and Reverse Electrodialysis processes**

Membrane based processes have drawn much attention in water treatment [114], food processing [115] and energy harvesting [116], as both environmentally friendly and economically attractive. Among them, Electrodialysis and Reverse Electrodialysis have proved their reliability in water desalination and energy production, respectively. Specifically, in Electrodialysis (ED) [117], ions are driven by an imposed electric field from a dilute electrolyte solution to a concentrate one. Conversely, Reverse Electrodialysis (RED) [118] harvests electrical energy from the controlled mixing of two solutions at different salt concentration. ED and RED units are built by alternately stacking anion- and cation- exchange membranes, separated by net spacers or built-in profiles creating the fluid channels where the two solutions (concentrate and diluate) flow. The two membranes and the two solutions form the repeating unit, referred to as



cell pair. For the sake of brevity, in Figure 5. 1 is reported only a schematic representation of an ED stack.

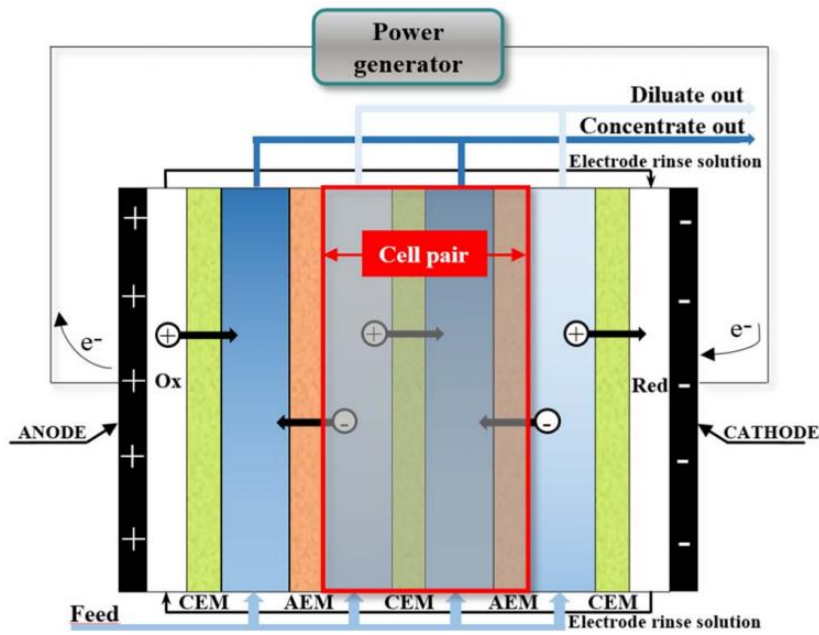


**Figure 5. 1** Schematic representation of an Electrodeionization system. The repeating unit (cell pair) of the system is highlighted by a red rectangle [114].

Spacers cover part of the membrane surface, thus reducing the actual active area, and increase the electrical resistance, as they are electrically non-conductive. Therefore, profiled membranes have recently been presented as an innovative solution to overcome net spacers drawbacks [117, 119, 120]. Profiled membranes simplify the stack assembly avoiding the use of spacers, and may improve the process performance. Numerical simulations [121-123] and experimental lab scale tests [117, 124-128] have confirmed their potential benefits. However, the actual performance of profiled membranes stacks depends on the specific profile geometry. Simple geometries (e.g., pillar or ridges profiles) are characterized by reduced hydraulic friction, but may exhibit lesser mixing properties than spacers [123, 125, 127-129]; on the other hand, improved profile shapes may provide better trade-off solutions among pressure drops, mixing and

Ohmic resistance, thus improving the stack performance [121, 128, 129]. In this context, two profiled membranes with Overlapped Cross Filaments (OCF) and Round Pillars (RP) are investigated in this Chapter.

### **5.1.2) Trans-membrane pressure in membrane-based processes**

In membrane-based processes, a trans-membrane pressure (TMP) between the different solutions flowing through a module may be a design feature or may arise for various reasons (e.g., flow arrangement or differences in geometry, flow rate or physical properties). This may lead to local deformations of membranes and membrane-bounded channels. As a result, the channel geometry (shape and average size) may be modified with respect to the nominal one, affecting fluid dynamics and transport mechanisms (of mass, heat, ions) and, thus, the process performance.

The effects of membrane/channel deformation have been studied in the context of different processes. She et al. [130] tested pressure retarded osmosis (PRO) modules at pressures up to 16 bar. Experimental performance became worse than theoretical predictions as the hydrostatic pressure increased; this difference was attributed to a more severe membrane deformation at high pressures. Later, She et al. [131] studied in detail the influence of spacer geometry on PRO efficiency under pressure loads up to 20 bar. The spacer with the largest mesh pitch gave the poorest performance in terms both of power density and of pressure drop.

Karabelas et al. [132] investigated the influence of the compressive stresses that arise in reverse osmosis (RO) spiral wound membrane modules, provided with spacers, during the assembly stage. Interestingly, mild applied pressures (1–2 bar) were sufficient to cause significant effects.

Huang [133] simulated flow and heat transfer in deformed channels for liquid-to-air membrane energy exchanger (LAMEE) units. Membrane deformation was not actually computed, and the deformed membrane was modelled as a spherical surface. As membrane deformation increased, the friction coefficient was found to increase in the compressed (air) channel and to decrease

in the expanded (liquid) channel. Heat transfer was affected by deformation in a complex way.

The influence of channel deformation on the performance of proton exchange membrane fuel cells (PEMFC) was assessed in several studies following similar approaches. Shi and Wang [134] predicted the compression of the porous gas diffusion layer due to the clamping (assembly) force, and simulated fluid dynamics, mass transport and electrochemical phenomena in the deformed geometries. The authors considered a serpentine channel and found that the assembly compression of the units enhanced pressure drop in the fluid channels, and that the process performance was particularly affected by deformation at high current densities. Zhou et al. [135] simulated a unit with a single straight channel including the membrane. As expected, most of the deformation was found to occur in the porous gas diffusion layer due to its lower mechanical stiffness.

Hereijgers et al. [136] measured membrane deflection and mass transfer coefficients in membrane microcontactors using round and diamond-shaped pillar spacers of different pitch. They found that trans-membrane pressure exhibited a minimum as the spacer pitch was made to vary, and that membrane deflection had a positive or negative impact on mass transfer depending on the diffusion coefficients in the two immiscible phases.

Time-dependent membrane deformation has recently been considered as a possible means to improve process performance. Moreno et al. [137] introduced the concept of “breathing cell” for reverse electrodialysis systems. In the breathing cell, the channels thickness changes dynamically due to the intermittent (5–15 cycles per minute) closure of an outlet valve in the concentrate channels. As a result, the Ohmic resistance of the diluate compartment (which is the predominant one) decreases. This cyclic operation was shown to yield higher net power densities in a range of flow rates.

### 5.1.3) Trans-membrane pressure in ED and RED cases

In some ED/RED practical applications TMP values are almost null ( $TMP \approx 0$ ). However, in prototype and industrial size stacks with non-parallel flow layouts (cross flow, counter flow) and/or with asymmetric channels (different geometries, fluid properties, flow rates), where the pressure distribution in the two compartments is different, appreciable values of TMP may arise. In particular, when some factors enhancing pressure drop are present, TMP values amounting to some tenths of a bar can be exhibited (higher TMP levels can cause severe risks of leakages [138-140]).

In the cross-flow RED prototype units ( $44 \times 44 \text{ cm}^2$ ) installed within the REAPower project [141], pressure drops from  $\sim 0.2$  to  $\sim 0.9$  bar were measured at flow velocities up to 1 cm/s [142]. Despite some of the pressure drop can be supposed to occur in the manifolds, a significant part of it is expected to occur in the channels, thus causing the onset of non-negligible TMP values. Moreover, the compartments were asymmetric, because the viscosity of the concentrated solution (brine) was almost twice that of the dilute feed, thus causing an unbalanced pressure distribution in the two solutions. Larger TMP values (up to  $\sim 1.5$  bar) were measured by Hong et al. [140] in a cross-flow RED stack ( $35.5 \times 35.5 \text{ cm}^2$ ) fed with inlet velocities up to  $\sim 5$  cm/s, which provided a significantly lower electrical power (less than half) compared to an equivalent parallel-flow stack. Although the authors attributed this decline in performance to issues of internal leakage, an important effect of deformation can be supposed.

ED units operate with fluid velocities higher than those typical of RED (in order to increase the limiting current density) and, despite the usually higher channel thickness, exhibit large pressure drops [114]. For example, Wright et al. [143] performed ED tests in a bench-scale unit and in a commercial-scale unit with parallel flow, measuring pressure drops up to  $\sim 0.65$  bar and  $\sim 1.30$  bar, respectively, at fluid velocities up to  $\sim 9$  cm/s. If such operating conditions were adopted in non-parallel flow arrangements, they would lead to significant levels of TMP.

Recent studies showed that asymmetric channels are optimal for RED applications [144, 145]. However, they can be affected by TMP-related issues.

For example, in ref [145] it was shown that for the couple of NaCl solutions 15–500 mol/m<sup>3</sup> fed with parallel flow in a stack 50 cm long, the optimum thickness and fluid velocity are ~400 μm and ~1.4 cm/s for the concentrate and ~217 μm and ~2.6 cm/s for the diluate. The pressure drop predicted by CFD correlations is 0.07 bar for the concentrate and 0.46 bar for the diluate, thus giving a maximum TMP located at the inlet equal to ~0.39 bar.

It must also be added that ion exchange membranes may have very different mechanical features. The Young's modulus ( $E$ ) may vary within a broad range from 10 MPa to 1 GPa [146-156] or even to higher values in some cases [157, 158], but decreases with ageing due to membrane usage [147-149, 157]. Moreover, the new generation membranes are manufactured with low thickness, e.g., from 80 to 250 μm [159, 160]; even lower values can be found among commercial membranes and experimental membranes prepared in laboratory [161]. A theoretical study [162] has recently found optimal thicknesses of 15–20 and 50–70 μm for ED and RED applications, respectively. Therefore, it is quite common that ion exchange membranes exhibit a low stiffness, due to the combined effects of a low  $E$  and a low thickness. This feature makes the membranes susceptible to large deformations in stacks with a non-negligible TMP, depending also on the spacer features.

The presence of negligible TMP values may trigger a fluid-membrane mechanical interaction, which will find an equilibrium state characterized by some distribution of pressure, geometry, flow rate, hydraulic friction, mass transfer coefficient, current density, Ohmic and non-Ohmic resistances in both solution compartments. Compared to the nominal conditions, the values of any of the above quantities under deformed conditions may be: (i) either higher or lower in the whole channel (e.g., in asymmetric configurations); (ii) higher in some parts of the channel and lower in other ones (e.g., in non-parallel flow arrangements). In both cases, these deviations from the undeformed conditions may impair the process performance due to the lack of compensation of effects between compressed zones and expanded zones (in the same or in different channels). For instance, an increase in the thickness of the diluate (which often provides the predominant resistance), in the whole channel or in a part of it,

especially where the solution is less conductive, causes an increase in the average Ohmic resistance. Imbalances may also affect hydraulic friction, increasing the overall pressure drop. A significant increment of non-Ohmic resistance, is another well-known detrimental effect due to uneven flow rate distributions [126].

In the present Chapter the unexplored field of the mechanical response of membranes in ED and RED units is addressed. First, the results of an experimental campaign carried out to characterize the mechanical properties of cation and anion exchange membranes by uniaxial tensile tests are presented. These properties were used in a finite element model to determine the membrane deformation of a couple of profiled membranes, belonging to a cell pair, at different TMP values. The investigation was conducted at the small scale of a periodic portion of the membranes themselves.

## **5.2) Experimental characterization of Ion Exchange Membranes**

The mechanical properties of anion and cation exchange membranes, currently employed in ED and RED applications, have been investigated by conducting uniaxial tensile tests. Specifically, flat ion exchange membranes produced by FujiFilm Manufacturing Europe B.V. with the name “Type 10” were studied. According to information provided by the manufacturer, Type 10 is a homogeneous reinforced membrane and is based on an amide polymer as backbone. The membrane is produced by roll to roll.

The tensile machine (Zwick Roell z010) equipped with 10kN load cell was used for all measurements. Further, an ad hoc system was developed to keep the membrane wet during tests. To do so a small bag was filled with water or salt solution and a pair of customized clamps were built. Figure 5. 2 presents the equipment used. It is worth noting that, the bag was carefully designed to prevent the clamps from exiting the bag throughout the entire duration of the tests. Moreover, attention was paid to avoid any slippage of the sample and the bag.

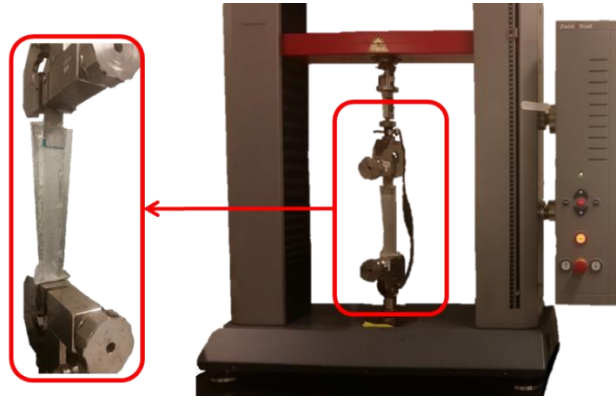


**Figure 5. 2** Zwick Roell z010 uniaxial tensile machine and details of the customized system used for the membrane characterization: a plastic small bag and a pair of appropriately designed clamps.

The membrane was cut into rectangular strips of 30 cm ( $L$ )  $\times$  1.5 cm ( $W$ ) and the wet membrane thickness, measured by a micrometer at four points along the sample length, were  $\sim 145 \pm 5 \mu\text{m}$  and  $\sim 154 \pm 5 \mu\text{m}$  for AEM and CEM membranes respectively. Tests were carried out at room temperature of  $22^\circ\text{C}$  and run five times for reproducibility.

Uniaxial tensile tests and loading and un-loading tests were performed.

Tensile tests were conducted following the ASTM D882 guidelines at the constant displacement rate of 30 mm/min. Membranes were cut along three directions: the machine direction (MD), the cross direction (CD, i.e. the direction orthogonal to the MD) and at 45 degrees (XD) with respect to the machine direction. In addition, the influence of the sample conditioning in different solutions and for a different amount of time was addressed. In particular, samples were kept for 1 day or 1 week in solutions of tap water, salt solutions of 0.5 M and 4.5M of pure NaCl.

With regard to loading and un-loading tests, samples were conditioned 1 day in tap water and the analysis was performed at a constant displacement rate of 30 mm/min both in loading and unloading steps. The load was increased of steps of 2 MPa till reaching the tensile stress of 14 MPa. No dwell time was set.

### 5.2.1) Uniaxial tensile tests

The engineering stress-strain curves for anion and cation exchange membranes conducted for all the three directions are shown in Figure 5. 3. Results are reported in terms of engineering stresses and strains. In particular, engineering stresses are calculated as ratio between the tensile force and the original cross-sectional area of the sample. Moreover, strains are calculated as the ratio between sample longitudinal elongation and the its original length.

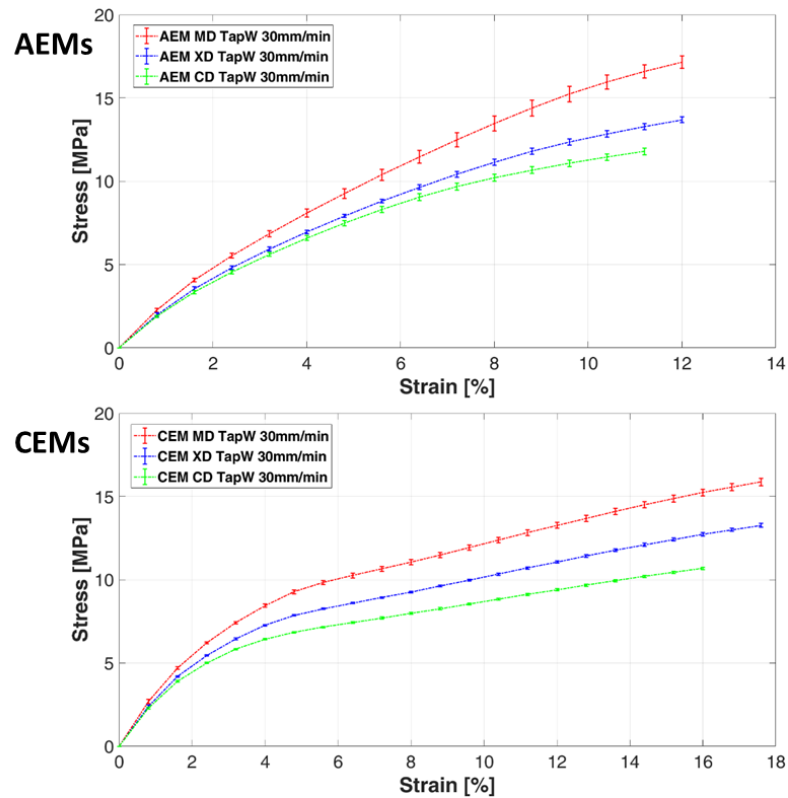


**Figure 5. 3** Engineering stress-strain curves for anion (AEM) and cation (CEM) exchange membranes tested in the MD (red dotted lines), XD (blue dotted lines) and CD (green dotted lines) directions. Samples were conditioned 1 day in tap water (TapW) and tests were run at 30 mm/min.

Both membranes do not have a well-defined linear elastic region except over a small range of strain. CEM membranes have a higher elongation at break of 18% compared to that of 12% of AEMs. On the other hand, values of stresses at



break are similar for both membranes. In particular, membranes cut along the MD, CD and XD directions show values of stress at break of 16, 14 and 11 MPa, respectively. In addition, CEM membranes present a gradual rollover yield occurring over a strain ranging from almost 1 to 5%. Post-yield strain hardening is then observed with the strain hardening slope increasing slightly with increasing strain.

Membranes show different mechanical responses at the three directions investigated, thus indicating an anisotropic behaviour of the membranes. However, mechanical properties do not much differ in the three directions especially in the small strain region.

As far as the linear elastic region is concerned, Figure 5. 4 presents the stress-strain curves of Figure 5. 3 in a magnified region up to 0.8% of strain.

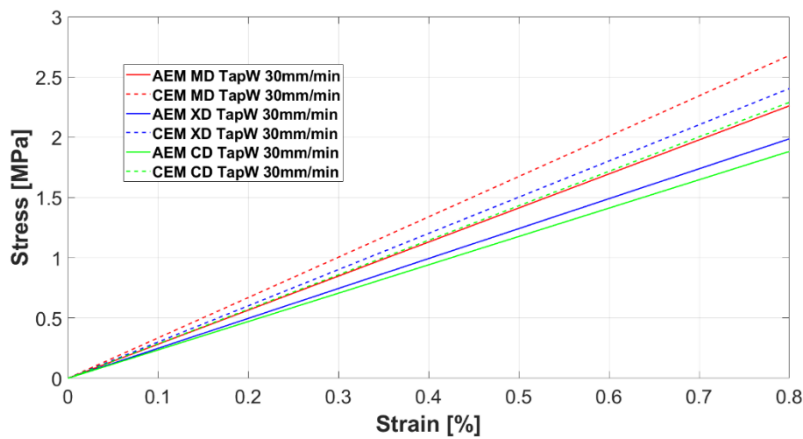


**Figure 5. 4** Magnified region of the stress-strain curves of Figure 5. 3 up to 0.8% of strain.

CEMs are found to be stiffer than AEMs. Moreover, they present higher yielding stresses. Young's moduli for the two membranes at all the directions are reported in Table 5. 1.

**Table 5. 1** Identified Young's moduli for both AEM and CEM membranes tested in tap water.

Quantities	MD Direction	XD Direction	CD Direction
AEMs Young's modulus	284	258	245
CEMs Young's modulus	360	320	305

### 5.2.1.1) Uniaxial tensile tests of samples conditioned in different solutions

The mechanical response of the AEMs and CEMs conditioned for one day in tap water and salt solutions of concentrations of 0.5M and 4.5M, are reported in Figure 5. 5. Solutions were prepared using deionized water and pure NaCl salt.

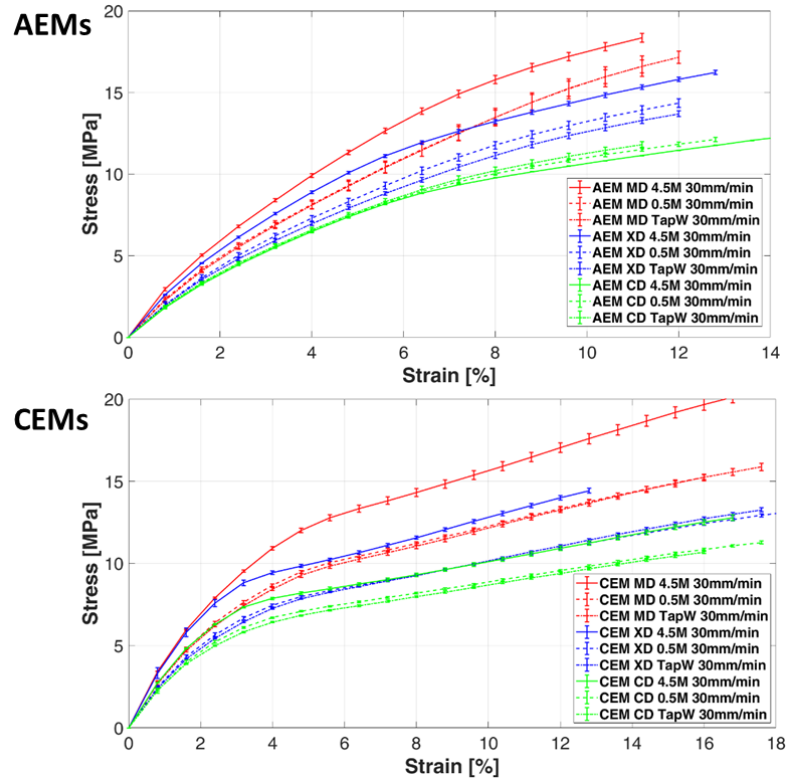


**Figure 5. 5** Engineering stress-strain curves for anion (AEMs) and cation (CEMs) exchange membranes conditioned in tap water (fine dotted lines), in salt solution of 0.5M (course dotted lines) and in salt solution of 4.5M (straight lines). Membranes are tested along MD (red lines), XD (blue lines) and CD (green lines) directions. Tests were run at 30 mm/min.

Interestingly, the characteristics of conditioned membranes in the salt solution of 0.5M are similar to those of membranes conditioned in tap water. On the other hand, the membranes conditioned in the salt solution of 4.5M are found to be stiffer than those conditioned in tap water.

Further, CEMs properties vary more than those of AEMs. As an example, the Young's modulus of CEMs, along the MD direction, conditioned in the salt

solution of 4.5M is almost 22% higher than that of membranes conditioned in tap water (463 MPa and 360 MPa, respectively).

### 5.2.1.2) Uniaxial tensile tests of samples conditioned at different conditioning time

For the sake of brevity, in Figure 5. 6 a comparison between the mechanical response of the AEMs and CEMs conditioned for one week and one day in the salt solution of 4.5M is shown.

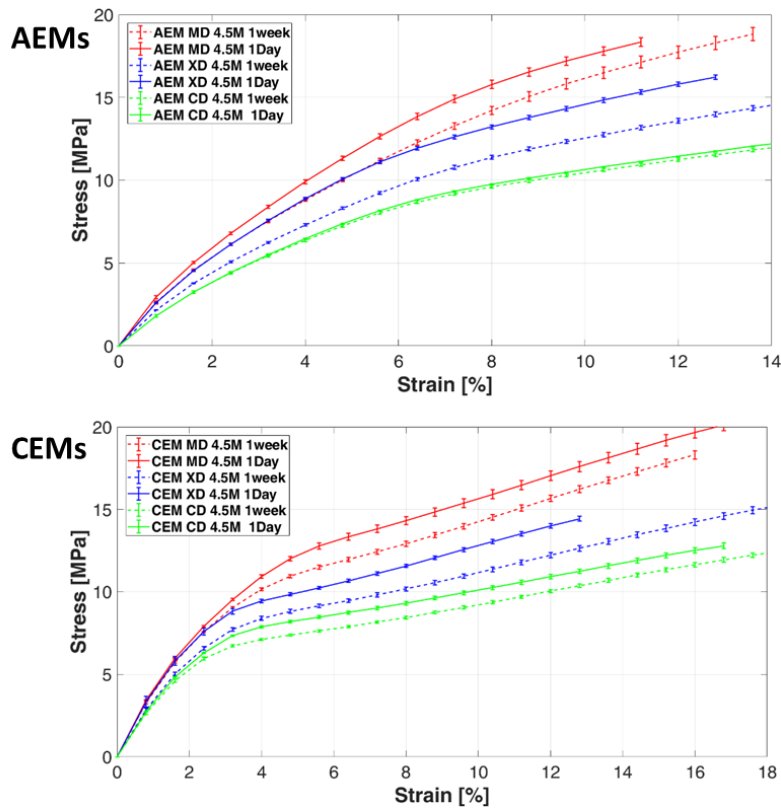


**Figure 5. 6** Engineering stress-strain curves for anion (AEMs) and cation (CEMs) exchange membranes conditioned in the salt solution of 4.5M for one week (dotted lines) and one day (straight lines). Membranes are tested along MD (red lines), XD (blue lines) and CD (green lines) directions. Tests were run at 30 mm/min.

After one week, membranes show a reduction of their mechanical properties. The effect is higher in the MD direction with respect to the CD direction. Measurements conducted for samples conditioned in tap water or salt solution of 0.5M did not show any change in their mechanical response. This can be due to faster membrane aging in high concentrate salt solutions that can deteriorate membrane polymeric structure. On the other hand, a conditioning time of one day may be not enough for a proper conditioning in concentrate solutions, thus affecting the measurements.

To further investigate the effect of the conditioning time, Figure 5.7 presents the mechanical behaviour of AEMs and CEMs conditioned in the salt solution of 4.5M for one week and in tap water for one day. AEMs conditioned in the salt solution show the same properties of the AEMs conditioned in tap water. On the other hand, CEMs still show an improvement of the mechanical properties when membranes are conditioned in the high concentrate solution. This may be due to different ion interactions between the polymeric matrix of the CEM and AEM membranes, which in turn may make the membrane stiffer.

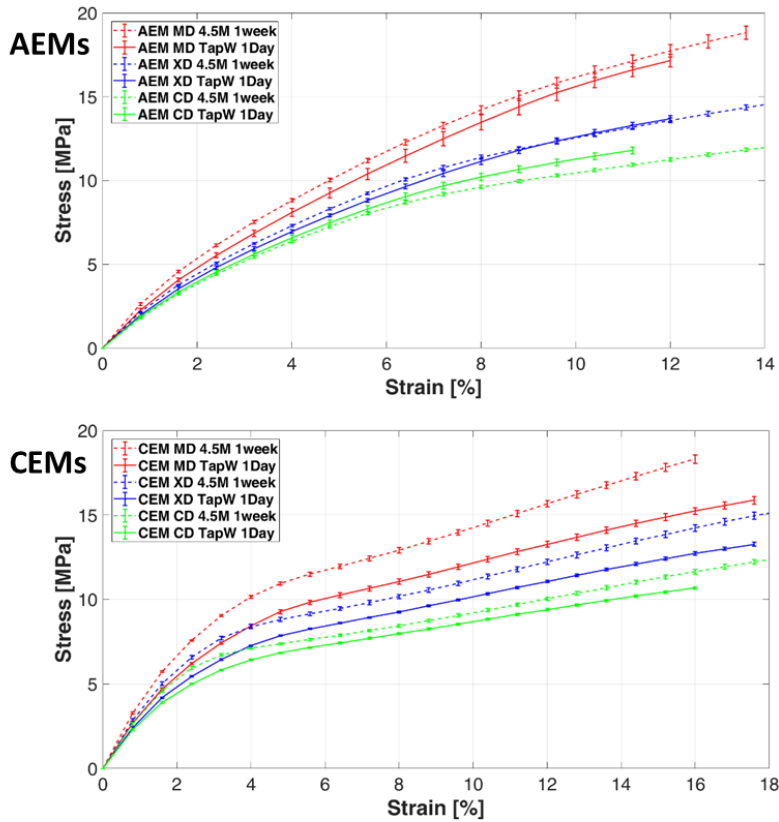


**Figure 5. 7** Engineering stress-strain curves for anion (AEMs) and cation (CEMs) exchange membranes conditioned in the salt solution of 4.5M for one week (dotted lines) and one day in tap water (straight lines). Membranes are tested along MD (red lines), XD (blue lines) and CD (green lines) directions. Tests were run at 30 mm/min.

### 5.2.2) Loading and un-loading tests

The mechanical response of the AEMs and CEMs to uniaxial loading-unloading-reloading tests are shown in Figure 5. 8. Results concern only membranes conditioned in tap water for one day and cut along the MD direction. The linear elastic region of the membranes is confirmed to be in the region of stresses of almost 2 MPa, i.e. the first loading condition. In this case, no residual plastic deformations are identified. Overall, the AEMs show smaller hysteresis and lower residual deformations compared to CEMs. At the last applied load of

14 MPa, the residual strains of the CEM membranes are the doubled with respect to the AEMs, thus showing that CEMs dissipate more energy compared to AEMs.

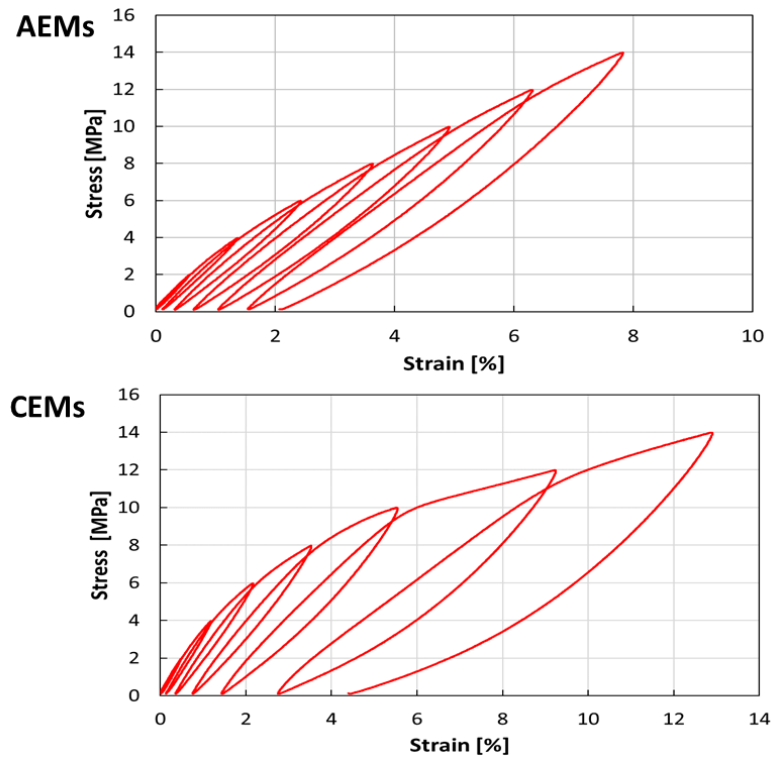


**Figure 5. 8.** Engineering stress-strain curves for anion (AEMs) and cation (CEMs) exchange membranes conditioned in the salt solution of 4.5M for one week (dotted lines) and one day in tap water (straight lines). Membranes are tested along MD (red lines), XD (blue lines) and CD (green lines) directions. Tests were run at 30 mm/min.

### 5.3) Finite element model of profiled AEMs and CEMs

Taking into account the mechanical behavior of ion exchange membranes discussed in Section 5.2, a finite element model was developed to study the deformation of profiled membranes in ED and RED systems. Specifically, two profiled membranes type were investigated: Overlapped Crossed Filaments (OCF) and round pillar (RP) types, in Figure 5. 9. OCF are made by an array of semi-cylinders on both membrane sides, placed at 90° each other. Instead, RP

membranes bear on one side flat cylindrical protrusions. To reduce the computational effort and study accurately the deformation of the profiled membranes, a periodic portion of the whole membrane was studied, enlarged in Figure 5. 9.

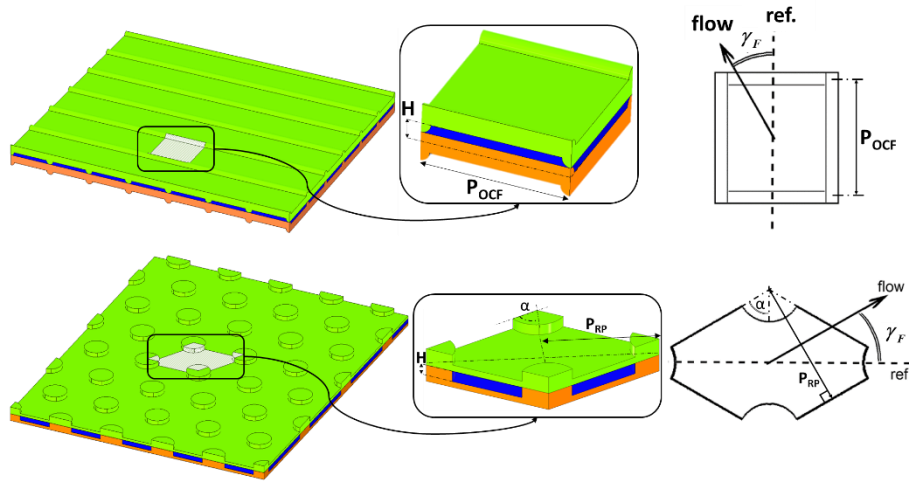


**Figure 5. 9** First row) Profiled membranes of the Overlapped Crossed Filaments (OCF) type. Second row) Round pillar (RP) profiled membranes. For each membrane type, the corresponding repetitive unit (periodic portion) of profiled membranes is shown, enlarged, in the central inset. The geometric parameters  $H$  (channel thickness),  $P_{OCF}$  and  $P_{RP}$  (pitches),  $\alpha$  (intrinsic angle) and  $\gamma_F$  (flow attack angle) are indicated.

OCF type present a square planform and profiles of adjacent membranes were assumed to be aligned on top of one another; in practice, this arrangement may not be precisely achieved since, in operation, shifts would be likely to occur. In this case, the pitch ( $P_{OCF}$ ) was defined as the distance between two profiles on the same membrane side, while the channel height ( $H$ ) was the distance between the two undeformed membranes. Three different pitch ( $P$ ) to channel height ratio  $P/H$  values were considered. With regard to the RP membranes, Pillars were assumed to be arranged in a regular hexagonal lattice ( $\alpha=60^\circ$ ) and the pitch was the normal distance between adjacent pillar rows and the pillar diameter was fixed to five times the channel thickness  $H$ , while the pitch to channel height ratio  $P/H$  was made to vary. The undeformed channel thickness  $H$  was assumed to be 0.2 mm and the undeformed membrane thickness 0.12 mm, for both OCF and RP

cases. These values are representative of advanced membrane-channel configurations currently being considered for ED and RED applications [114, 159, 160, 163]. The channel thickness  $H$  ranges usually from  $\sim 0.1$  to  $\sim 0.4$  mm in RED applications [141], while a larger thickness is typically adopted in ED units, i.e. from  $\sim 0.3$  to  $\sim 2$  mm, especially in commercial stacks [114]. However, several recent researches on ED modelling and experiments have been focused on the use of thin spacers [164-166]. Therefore, the value of  $200 \mu\text{m}$  can be considered representative of both RED and ED applications.

As discussed above, the mechanical properties of the membrane depend on manufacturing method, nature of co-polymers, cross-linking degree, ageing, etc. Therefore, instead of using the Young's modulus values determined from the experimental campaign, a lower conservative value of  $150 \text{ MPa}$  for the Young's modulus ( $E$ ) was chosen and a Poisson ratio ( $\nu$ ) of  $0.4$  was used as suggested by the producer. Cation and anion exchange membranes were assumed to have the same mechanical properties and, for the sake of simplicity, were treated as linearly elastic, homogeneous and isotropic media.

The geometrical and mechanical quantities for both the OCF and RP profiled membrane types are summarized in Table 5. 2.

**Table 5. 2** Geometrical and mechanical quantities for OCF and RP membranes.

Quantity	Value	Units
Membrane Young's modulus, $E$	150	MPa
Membrane Poisson ratio, $\nu$	0.4	-
Membrane thickness, $H^{EM}$	120	$\mu\text{m}$
Channel thickness, $H$	200	$\mu\text{m}$
OCF-Pitch-to-height ratio, $P/H$	7-9	-
OCF-Angle between filaments	90	deg
RP-Pitch-to-height ratio, $P/H$	9-11	-
RP-Pillar diameter, $d$	1	mm
RP-Intrinsic angle of pillar lattice, $\alpha$	60	deg



All these properties are assumed to hold for swollen membranes, because this is the actual condition under which membranes find themselves in a real operating ED/RED stack.

The linearly elastic hypothesis is quite reasonable for ED/RED membranes within the mild load conditions considered in this study: for  $TMP = \pm 40$  kPa, the maximum computed von Mises stress is  $\sim 2$  MPa, which is close to the limit stress for linearly elastic behavior generally exhibited by ion exchange membranes [152-156], including findings of the experimental campaign (Section 5.2).

The homogeneity assumption is based on the membrane structure and on the preparation technique adopted, as described by the manufacturer (FujiFilm Manufacturing Europe B.V.).

In regard to the isotropy assumption, results of Figure 5. 4 evidence that in the linear elastic region, the behavior of the membrane do not differ much along the different membrane directions. In view of this modest degree of anisotropy, it was decided to neglect this feature, which would have complicated the computations of the representative test cases without changing significantly the results.

### **5.3.1) Boundary Conditions and computational grids**

Figure 5. 10 reports the computational domains of both OCF and RP profiled membranes, where the mechanical boundary conditions are evidenced.

1. Each of the four segments representing the external vertical edges of the domain (1) was clamped, i.e., zero displacement and rotation were imposed to all points belonging to it.
2. Each of the four side faces of the domain (2) was imposed zero displacement in the direction normal to itself, so that a single computational domain is representative of a periodic array of repetitive units.
3. The trans-membrane pressure  $TMP$  (relative to that of the internal fluid channel) was applied to the whole outer surface of the domain (3). Please note that  $TMP > 0$  for compression conditions, while  $TMP < 0$  for expansion conditions.

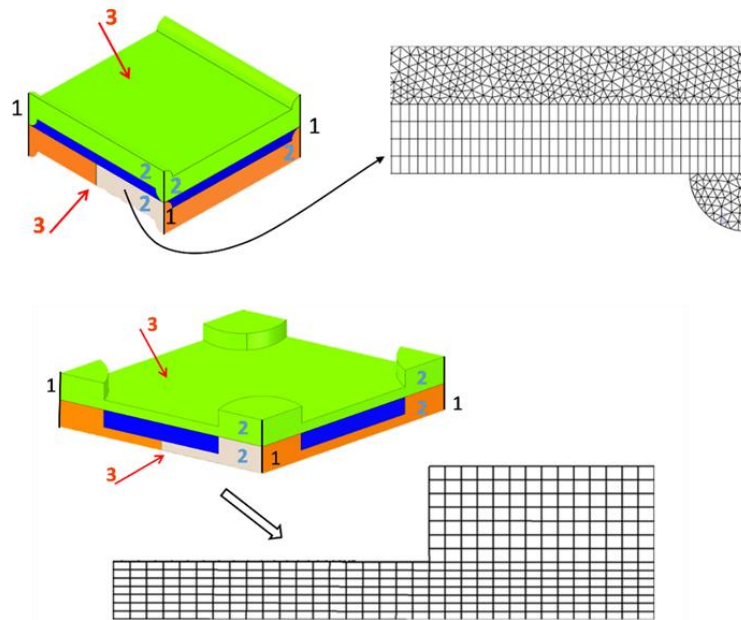


**Figure 5. 10** Upper row) The computational domain the OCF profiled membrane and a detail of the finite element mesh used. Lower row) The computational domain the RP profiled membrane and its detail of the finite element mesh adopted. Numbers 1–3 indicate the mechanical boundary conditions (see text).

In addition, Figure 5. 10 shows insights of the computational grids used for the two membranes cases. Specifically, in the case of OCF membrane, a hybrid (hexahedral-tetrahedral) grid was necessary, while for the RP completely hexahedral and block-structured grid was used. Grid dependence for both cases was preliminary assessed.

Tables 5. 3 and 5. 4 report the maximum displacement at the outer surface of the domain computed for  $TMP = 80$  kPa and  $P/H = 8$  and  $P/H = 10$ , for OCF and Pillars respectively, with increasingly fine meshes.

**Table 5. 3** Grid dependence results ( $TMP = +80$  kPa) for OCF with  $P/H=8$  type membrane.

FE mesh	No. elements	Maximum displacement [ $\mu\text{m}$ ]
OCF-I	$200 \times 10^3$	67.04
OCF-II	$500 \times 10^3$	67.38
OCF-III	1 million	67.53

**Table 5. 4** Grid dependence results for the mechanical simulations (TMP=+80 kPa,  $P/H=10$ ) for Pillar type membrane.

FE mesh	No. elements	Maximum displacement [ $\mu\text{m}$ ]
RP-I	$21 \times 10^3$	67.69
RP-II	$60 \times 10^3$	67.97
RP-III	$180 \times 10^3$	68.06

On the basis of results of Table 5. 3, computational mesh of  $500 \times 10^3$  elements (OCF-II) was used in all the simulations for the OCF membrane type as a compromise between accuracy and computational effort.

Moreover, taking into account results of Table 5. 4, the computational mesh of  $6 \times 10^4$  elements (RP-II) was chosen for the RP membrane type. The same element size was adopted in all the simulations. The simulations were conducted by the Finite Element code Ansys-Mechanical®. Equilibrium, compatibility and constitutive equations were numerically solved by using a FE method in order to find the deformed configuration of the bodies, large deflections were taken into account.

### 5.3.2) Model validation

To validate the FE model, experimental bulge tests were conducted for a  $10 \times 10 \text{ cm}^2$  square samples of flat anion exchange membranes (AEM) of the same type of those investigated in Section 5.2. Moreover, a comparison between FE results and an analytical solution was also carried out to investigate the FE predictions of the deflection of smaller membrane areas.

#### 5.3.2.1) Bulge tests of an anion exchange membrane

A custom-designed bulge test equipment was built (Figure 5. 11). Two square plexiglas® plates of 20 cm side and 2 cm thickness were used. Six circular holes with a diameter of 1.2 cm were drilled in one of the two plates (Plate 1) in order to allow water entrance and exit. The inlet and outlet manifolds were then installed into the holes. Moreover, a square hole of 10 cm side was milled in the other plate (Plate 2), to serve as a window allowing the membrane expansion. An

anion exchange membrane of the same type of those analysed in the Section 5.2, was conditioned for 24 h in tap water and then cut into square sheets of 20 cm side. A silicone gasket 1 mm thick creating the space for the liquid was interposed between the membrane sample and Plate 1. The two plates were clamped by 8 bolts and nuts. The bottom manifolds were connected to a water column. Once the channel was filled and air bubbles were carefully removed, a valve placed in the exit pipe was closed.

Membrane wrinkling was observed when no pre-stretching was applied. This is a common phenomenon, which happens for very thin sheets with negligible flexural stiffness if compressive residual stresses are present. Applying in-plane tensile forces (i.e., pre-stretching the membrane biaxially in its plane) would reduce this phenomenon. However, it would require a suitable equipment that was not available. Therefore, the membrane was slightly pre-stretch by applying an initial hydrostatic load of  $\sim 1$  kPa (10 cm water column). The initial maximum displacement of the central point of the membrane was measured to be  $\sim 7.3$  mm. The membrane was then pressurized by increasing the liquid height. The central membrane displacement was measured by a highly accurate laser scanner vibrometer (Polytech® PSV-400) and recorded at various levels of applied pressure increasing in 2 kPa steps up to 10 kPa. Tests were repeated five times for repeatability purposes. Corrected displacements were obtained by subtracting the initial displacement from the measured values.

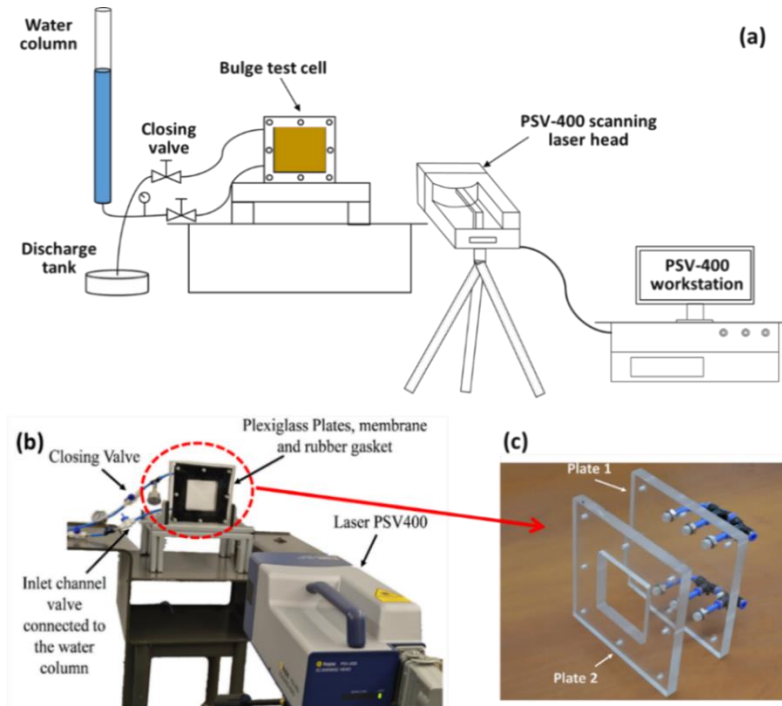


**Figure 5. 11** Experimental setup. a) Overall layout; b) Bulge test cell and laser head; c) Detail of the Plexiglas plates making up the bulge test cell.

### 5.3.2.2) Comparison between experimental and FE bulge test results

Membrane bulging was simulated by the FE model. As mentioned above, the membrane was considered to be isotropic. Therefore, the mechanical properties and thickness experimentally determined for the anion exchange membrane along the XD direction (Young's modulus 258 MPa, thickness 148  $\mu\text{m}$ ), investigated in the Section 5.2, were provided as input to the model, taking into account the non-linear elastic behaviour. A Poisson ratio of 0.4 was again considered, as suggested by the producer. As boundary conditions, all edges of the square membrane were clamped. The small deformation approximation was not used. First, the deformed stretched configuration (no-wrinkles) was numerically determined, knowing the maximum central displacement value. Then, a uniform pressure was applied to the pre-stretched configuration. The comparison between the numerical results and the corrected measured displacements is shown in Figure 5. 12 (a). Figure 5. 12 (a) compares the predicted and experimental maximum displacements (placed

at the central point of the membrane) as functions of the trans-membrane pressure. Error bars are reported for the experimental data. A fairly good agreement can be observed.

### 5.3.2.3) Comparison between FE predictions and an analytical solution

A further validation of the FE model was performed by comparing numerical predictions with an analytical solution of structural mechanics for a two-dimensional domain [167] to investigate FE predictions for smaller membrane areas compared to that of bulge test. A square body loaded with a uniform pressure and with all the edges clamped was considered. Since the membrane deflection overcomes the “small deflection” range, a suitable analytical solution was used for the comparison. In particular, Figure 5. 12 (b) reports the maximum deflection as a function of the trans-membrane pressure. The broken line is the first-order approximated analytical solution reported by Iyengar and Naqvi [167], the solid line is the present FE numerical solution. In this case, the square membrane is 2 mm wide and 0.120 mm thick and Young’s modulus is 150 MPa. The Poisson ratio is 0.316, as the analytical solution proposed in reference [167] was specifically obtained for this value. Figure 5. 12 (b) shows that numerical simulations are in good agreement with the approximate theoretical solution, the discrepancy increasing with TMP and being only ~3% at 80 kPa.

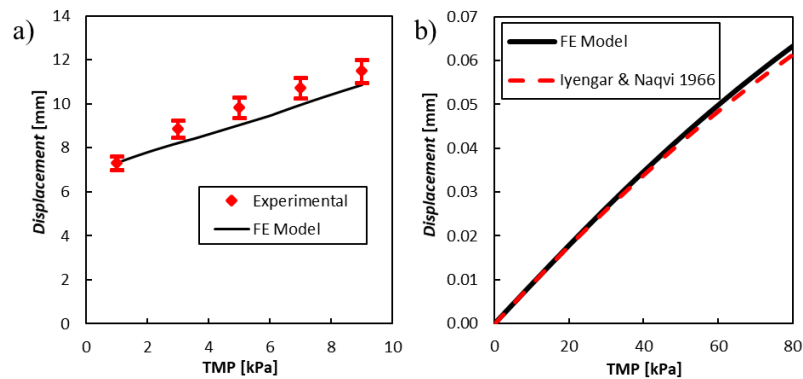


**Figure 5. 12** Maximum displacement for a square, edge-clamped membrane as a function of the trans-membrane pressure. Comparison of FE predictions (solid line) with (a) experimental results (symbols) of bulge tests on a  $10 \times 10 \text{ cm}^2$  sample and (b) the first-order analytical solution by Iyengar and Naqvi [167] for a  $2 \times 2 \text{ mm}^2$  membrane (dashed line).

### 5.3.3) Results

The mechanical investigation of the deformation of the periodic portion of OCF and RP profiled membrane types was carried out in two steps:

1. First, the influence of the pitch-to-height ratio ( $P/H$ ) was addressed. A TMP of 80 kPa was applied, and the geometry with the largest value of  $P/H$  still able to withstand this load without collapsing (i.e., without exhibiting a contact between opposite membranes) was identified. The figure of 80 kPa was conservatively chosen as a value comfortably larger than the highest TMP actually expected in real RED/ED applications. The search for the largest admissible  $P/H$  was motivated by the fact that small values of  $P/H$  are associated with large pressure drops: many studies [126, 129, 143, 168-170] have highlighted the importance of reducing pressure drop and thus mechanical power losses in the channels, especially in RED applications. It is true that the increase of  $P/H$  may also cause a reduction in mass transfer coefficients, but its effect on stack performance is usually less important.
2. The geometry thus identified was then investigated under expansion and compression conditions corresponding to TMP varying from -40 to +40 kPa. As discussed in the Section 5.1.3, this range encompasses most of the conditions that are likely to occur in actual ED/RED applications.

#### 5.3.3.1) Influence of Pitch to Height Ratio ( $P/H$ ) and limiting values

Computational results for the deformation of periodic portions with different pitch ( $P$ ) to channel height ( $H$ , distance between the two undeformed membranes) ratios under the conservative value of TMP = + 80 kPa (the “+” sign refers to compression) are presented in Figures 5. 13 and 5. 14 for the OCF and Pillar profiled membranes, respectively. Three values of  $P/H$  were investigated for both the membranes. Specifically, the  $P/H$  values of 7, 8 and 9; and 9, 10 and 11 were studied for the OCF and RP membranes, respectively. In the case of OCF membrane type (see Figure 5. 13), the first contact between the two membranes approximately occurs for  $P/H = 9$  and is located at the centres of the side ridges

(note that an inter-membrane clearance of  $\sim 60 \mu\text{m}$  is still preserved at the centre of the periodic unit). Therefore, the value  $P/H = 8$  was chosen as the largest admissible one.

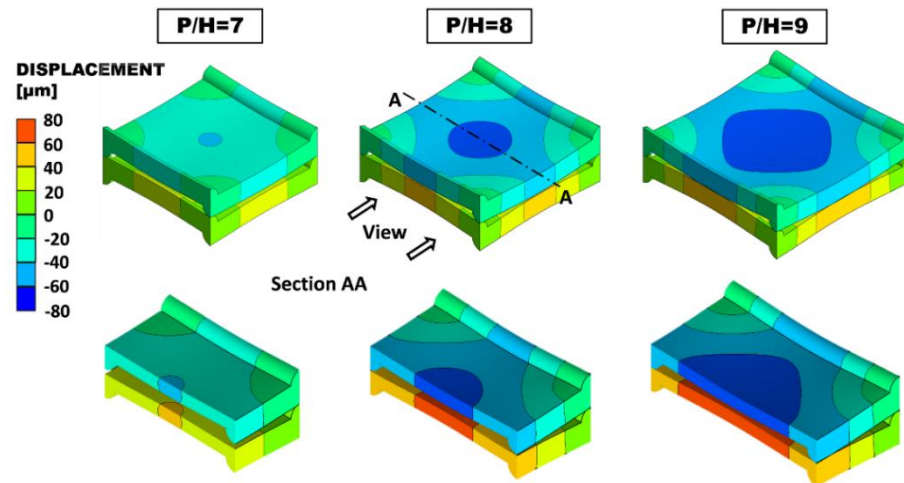


**Figure 5.13** Deformation of OCF membranes with different  $P/H$  ratios under  $\text{TMP} = +80 \text{ kPa}$ . The quantity shown is the displacement in the direction orthogonal to the undeformed membranes. Top: external view; bottom: view after sectioning by a mid-plane A-A.

In the case of RP membranes (Figure 5.14), the first contact between the two membranes approximately occurs for  $P/H=11$  at two points located on the long diagonal of the unit diamond somewhere in between the central point and the pillars, symmetrically with respect to the short diagonal. The immediately lower value  $P/H=10$  was thus selected as the largest admissible one.

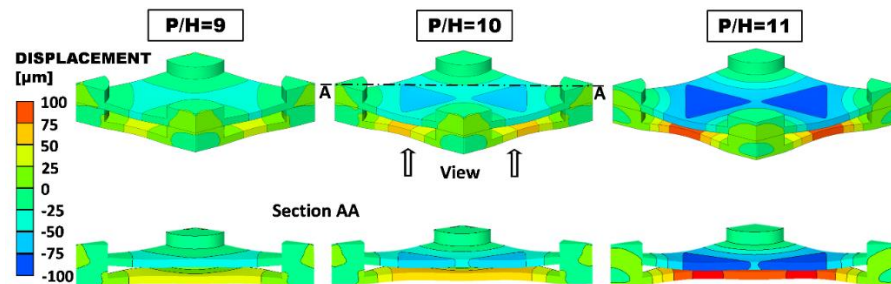


**Figure 5.14** Deformation for RP membranes with different  $P/H$  ratios under  $\text{TMP} = +80 \text{ kPa}$ . The quantity shown is the displacement in the direction orthogonal to the undeformed membranes. Top: external view; bottom: view after sectioning by a diagonal plane A-A.



### 5.3.3.2) Membrane and Channel Deformation for the Selected Geometries

The geometries characterized by the maximum admissible  $P/H$  ratio, (being 8 and 10, for OCF and RP membranes, respectively) were subjected to TMP varying in 10 kPa steps from  $-40$  kPa (expansion) to  $+40$  kPa (compression), and the corresponding deformation was computed. In the case of OCF membranes, Figure 5. 15 shows the deformed configuration for  $P/H = 8$  under  $TMP = \pm 40$  kPa. The insets on the right show the deformed fluid volumes. The maximum relative variation of the clearance occurs at the centres of the ridges. Here, the distance between the two opposite membranes (thickness of the fluid passage), which is  $H/2 = 100 \mu\text{m}$  in the undeformed configuration, decreases to  $\sim 53.7 \mu\text{m}$  in the compression case and increases to  $\sim 148.4 \mu\text{m}$  in the expansion case. The distance between opposite membranes at the centre of the domain, which is  $H = 200 \mu\text{m}$  in the undeformed configuration, decreases to  $\sim 130 \mu\text{m}$  under compression or increases to  $\sim 272 \mu\text{m}$  in expansion (i.e., the maximum deflection at the centre is  $\sim \pm 70 \mu\text{m}$ ).

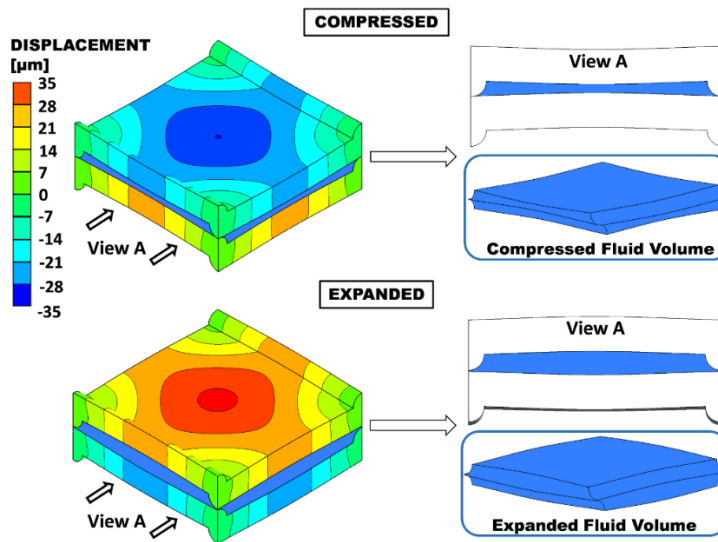


**Figure 5. 15** Deformation of OCF membranes with  $P/H = 8$  for the compressed and the expanded cases at  $TMP = \pm 40$  kPa. The quantity shown is the displacement in the direction orthogonal to the undeformed membranes. The corresponding deformed fluid volume is shown in the insets.

In the case of RP profiled membranes, Figure 5. 16 presents the deformed configurations calculated for  $TMP=\pm 40$  kPa for the geometry with the maximum admissible  $P/H$  ratio (10).

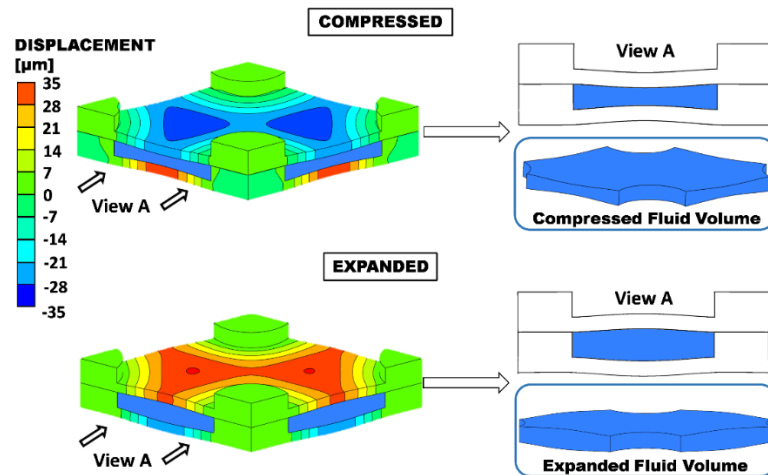


**Figure 5. 16** Deformation for the RP with  $P/H=10$  in both the compressed and the expanded cases at  $TMP=\pm 40$  kPa. The quantity shown is the displacement in the direction orthogonal to the undeformed membranes. The corresponding deformed configuration of the fluid volume is shown in the insets on the right.

Under compression, the minimum clearance occurs at two points with maximum displacement located on the long diagonal of the unit diamond symmetrically with respect to the short diagonal. It amounts to  $\sim 128$   $\mu\text{m}$ , corresponding to a vertical displacement of  $\sim 36$   $\mu\text{m}$  for each membrane. Under expansion, the maximum inter-membrane distance increases to  $\sim 268$   $\mu\text{m}$  (vertical displacement  $\approx 34$   $\mu\text{m}$  for each membrane).

Figure 5. 17 provides information concerning the TMP effects, in the whole range studied, on the fluid volume. In particular, in the case of OCF with  $P/H=8$  (Figure 5. 17 a), the volume follows a linear trend and exhibits an almost perfect symmetry between compression and expansion; the volume changes by  $\pm 25\%$  for  $TMP = \pm 40$  kPa.

In the case of RP with  $P/H=10$  (Figure 5. 17 b), a slight deviation from a perfectly symmetric behavior can be observed: the volume decreases by 22.7% for  $TMP= +40$  kPa and increases by 21% for  $TMP= -40$  kPa.

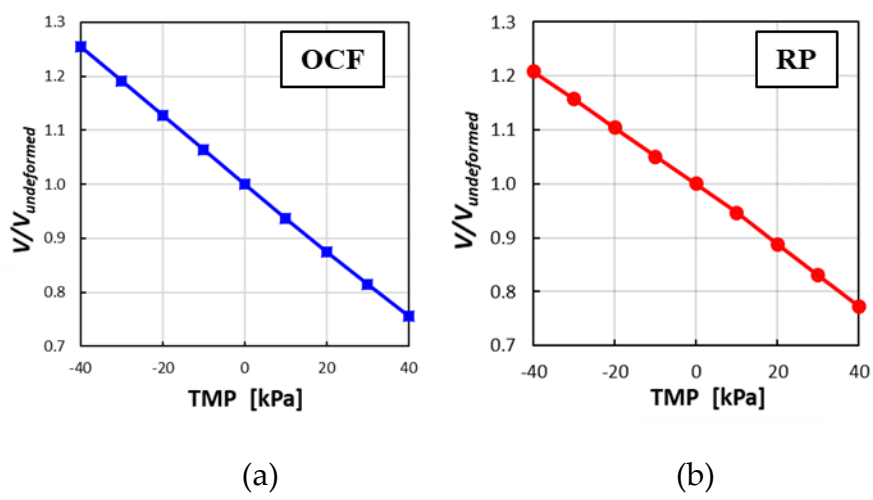


Figure 5. 17 Fluid volume (normalized by the undeformed volume) as a function of trans-membrane pressure for: (a) OCF with  $P/H = 8$  and (b) RP with  $P/H=10$ .

## CHAPTER VI

# INVESTIGATION ON FLUID DYNAMICS AND MASS TRANSFER IN DEFORMED CHANNELS

### 6.1) Introduction

The hydrodynamics and mass transport phenomena in channels of membrane modules have been systematically addressed by experimental and computational methods [168, 171-177]. Computational Fluid Dynamics (CFD) has been largely employed as a powerful tool for hydrodynamic simulations and predictions of both spacer-filled [178-181] and profiled bounded channels [121-123]. 2D and 3D models have been developed and, in particular, 3D simulations have allowed considerable insight into fluid flow phenomena. The effects of the geometry of spacers or profiles and of their orientation with respect to the flow have also been investigated [123, 129, 181, 182].

In this chapter, in order to evaluate the effects of membrane deformation on fluid dynamics and mass transport in deformed channels, CFD simulations were carried out in the undeformed, compressed and expanded channel configurations bounded by the periodic portion of OCF and RP profiled membranes investigated in Chapter V (see Figure 5. 9). Only one fluid channel at a time was simulated at the different TMP values and the governing equations were solved by the finite volume code Ansys-CFX®. From the numerical solution of these equations, velocity, pressure and electrolyte concentration fields are obtained. Raw results are then elaborated in order to calculate friction factor and Sherwood number.

## 6.2) Governing Equations and Definitions

Assumptions of steady laminar flow and constant-property fluid were assumed for the fluid dynamics / mass transfer problem. The steady laminar flow is amply justified by the low Reynolds numbers investigated ( $<100$  in most cases). Moreover, unsteadiness was observed only for  $Re > 300$  in experimental and direct numerical simulation studies conducted for spacer-filled channels [183], which geometry was closely related to that of the OCF profiled membrane type of Chapter V. In particular, a much lower pitch to height ratio  $P/H=2$  was studied and thus larger values of the transitional Reynolds number can be expected for the geometry investigated. The same consideration can be also applied for the case of RP pillars, since round pillars have lower effects on the hydrodynamics of membrane bounded channels, as also pointed out in ref [123].

As far as constant-property assumption is concerned, it is justified by the small concentration changes occurring in a generic portion of the channel (the assumption is also verified by the results shown in polarization coefficients  $c_b / c_w$  ranging from 0.97 to 1.03, in Sections 6.4.1.2 and 6.4.2.2).

With regard to the ionic transport, it was simulated assuming the local electroneutrality condition in the whole fluid domain. Under this hypothesis, from the Nernst-Planck equations and the mass balances of the two ions of a binary electrolyte, a convective-diffusive transport equation can be derived [181, 184-186]. This simplifies the calculations, requiring only the need for a choice concerning the boundary condition at the membrane-solution interface (uniform concentration, uniform flux, or mixed condition); however, the influence of the boundary conditions on the mass transfer coefficient is small [121, 187]. The potential is eliminated from the transport equation, and therefore the electric field and associated phenomena (e.g., Ohmic resistance) are not calculated by this simulation approach. Moreover, electroneutrality conditions are assumed and the electric double layer at the membrane-solution interface is not simulated, so that special conditions in which an extended space charge region occurs (e.g., electroconvection under overlimiting conditions) are not taken into consideration.

Under these assumptions, three-dimensional continuity, Navier-Stokes and scalar transport equations were numerically solved.

The continuity equation (with implicit summation) is simply

$$\frac{\partial \tilde{u}_i}{\partial x_i} = 0 \quad (6.1)$$

where  $\tilde{u}_i$  is the  $i$ -th velocity component of the fluid.

All simulations were carried out under the hypothesis of fully developed flow and concentration field, thus employing the Unit Cell approach [181]. In this approach, periodic boundary conditions are imposed to all variables between the inlet and outlet faces of the computational domain. At the same time, it is necessary to allow for the variation of pressure and bulk concentration along the main flow direction  $s$ , due to frictional losses and solute inflow or outflow through the channel walls, respectively. These apparently contradictory requirements are reconciled as follows.

- Consider pressure  $p$  first. In the fully developed region of a channel,  $p$  can be decomposed into a periodic component  $\tilde{p}$ , whose spatial distribution repeats itself identically in each unit cell, and a large-scale component  $K_p(\mathbf{x} \cdot \mathbf{s})$  which decreases linearly along the main flow direction whose unit vector is  $s$  ( $\mathbf{x}$  is the position vector of components  $x_i$ ). By substituting  $\tilde{p} - K_p(\mathbf{x} \cdot \mathbf{s}) = \tilde{p} - K_p x_i s_i$  for  $p$  in the  $i$ -th steady-state Navier-Stokes equation:

$$\frac{\partial \rho \tilde{u}_j \tilde{u}_i}{\partial x_j} = -\frac{\partial p}{\partial x_i} + \frac{\partial}{\partial x_j} \mu \frac{\partial \tilde{u}_i}{\partial x_j} \quad (6.2)$$

(where  $\rho$  and  $\mu$  are the fluid's density and viscosity), it becomes

$$\frac{\partial \rho \tilde{u}_j \tilde{u}_i}{\partial x_j} = -\frac{\partial \tilde{p}}{\partial x_i} + \frac{\partial}{\partial x_j} \mu \frac{\partial \tilde{u}_i}{\partial x_j} + K_p s_i \quad (6.3)$$

Eq. (6.3) is similar to Eq. (6.2), but (a) the “true” pressure  $p$  is replaced by its periodic component  $\tilde{p}$ , and (b) a body force per unit volume (mean pressure gradient) acting along the main flow direction  $s$  appears at the right hand side. If required, the “true” pressure  $p$  can always be reconstructed from the simulation results as  $p = \tilde{p} - K_p(\mathbf{x} \cdot \mathbf{s})$ .

- In regard to the concentration  $c$ , by definition of fully developed conditions it can be decomposed into a periodic component  $\tilde{c}$  and a large-scale component  $K_c(\mathbf{x} \cdot \mathbf{s})$ , where  $K_c$  can now be either positive (net inflow of electrolyte into the channel) or negative (net outflow of electrolyte from the channel). By substituting  $\tilde{c} + K_c(\mathbf{x} \cdot \mathbf{s}) = \tilde{c} + K_c x_i s_i$  for  $c$  in the transport equation

$$\frac{\partial \tilde{u}_j c}{\partial x_j} = \frac{\partial}{\partial x_j} D_{Salt} \frac{\partial c}{\partial x_j} \quad (6.4)$$

(where  $D_{Salt}$  is the salt diffusivity), after some manipulation one obtains:

$$\frac{\partial \tilde{u}_j \tilde{c}}{\partial x_j} = \frac{\partial}{\partial x_j} D_{Salt} \frac{\partial \tilde{c}}{\partial x_j} - K_c \tilde{u}_s \quad (6.5)$$

in which  $\tilde{u}_s = \tilde{\mathbf{u}} \cdot \mathbf{s}$  is the local velocity component along the main flow direction  $s$ . The large-scale gradient  $K_c$  can be obtained by an elementary balance as:

$$K_c = \frac{A}{V} \frac{j}{\langle \tilde{u}_s \rangle} \quad (6.6)$$

in which  $j$  is the molar salt flux at walls (imposed in the simulation),  $A$  is the membrane surface active area in a fluid unit cell (so that  $jA$  is the molar flow per unit time, mol/s),  $V$  is the cell volume and  $\langle \tilde{u}_s \rangle$  is the volume average of  $\tilde{u}_s$ .

In the present study, the (bulk) Reynolds number was conventionally defined as:

$$Re = \frac{\rho U 2H}{\mu} \quad (6.7)$$

i.e., it was based on the hydraulic diameter  $2H$  of a void (profile-less) and undeformed channel of thickness  $H$  in the limit of indefinite width, and on the approach velocity

$$U = \frac{Q}{S} \quad (6.8)$$

in which  $Q$  is the volume flow rate through a cross section of the channel orthogonal to the main flow direction and  $S$  is the cross sectional area of a void (profile-less) and undeformed channel of thickness  $H$ . The above definitions of  $U$  and  $Re$  are consistent with those adopted in many works on undeformed spacer-filled channels or profiled membranes [123, 129, 181, 182].

The Darcy friction coefficient  $f_{Darcy}$  was defined with reference to the above approach velocity  $U$  and hydraulic diameter  $2H$ , i.e., as:

$$f_{Darcy} = \left| \frac{dp}{ds} \right| \frac{4H}{\rho U^2} \quad (6.9)$$

In the simulations, the driving pressure gradient  $Kp=|dp/ds|$  in Eq. (6.3) was imposed, while the flow rate was obtained as part of the solution. Please note that  $|dp/ds|$  can be expressed in terms of the friction velocity Reynolds number

$$Re_{\tau} = \frac{\tilde{u}_{\tau} \rho H}{\mu} \quad (6.10)$$

in which  $\tilde{u}_{\tau}$  is the friction velocity,

$$\tilde{u}_{\tau} = \sqrt{\frac{H}{2\rho} \left| \frac{dp}{ds} \right|} \quad (6.11)$$

Therefore, in the parametrical analyses illustrated above, results were obtained for a given  $Re_{\tau}$  (friction velocity Reynolds number) rather than for a given  $Re$  (bulk Reynolds number). Please note that according to the present definitions, between  $Re$ ,  $Re_{\tau}$  and  $f_{Darcy}$  the following relation holds:

$$f_{Darcy} = 128 \left( \frac{Re_{\tau}}{Re} \right)^2 \quad (6.12)$$

To separate the effects of profile shape and channel deformation from the effects of varying the flow rate (and thus  $Re$ ), the Darcy friction coefficient was normalized by that holding for parallel laminar flow in a void plane channel of indefinite width, i.e.,  $96/Re$ . Therefore, the following quantity ( $F$ -ratio) was reported:

$$F = \frac{f_{Darcy}}{96/Re} \quad (6.13)$$



The local concentration polarization coefficient  $\theta$  was defined as:

$$\theta = \frac{c_b}{c_w} \quad (6.14)$$

where  $c_b$  is the molar bulk concentration and  $c_w$  is the local molar concentration at the membrane surface. Please note that defining the average polarization coefficient in such a way that it is lower than 1 [123, 129, 181] the local polarization coefficient in Eq. (6.14) refers to the case of either a dilute channel of RED or a concentrate channel of ED, where the flux enters from membrane's walls.

The mass transfer coefficient was defined as

$$k_c = \frac{jA}{(c_b - \langle c_w \rangle) A_{proj}} \quad (6.15)$$

and the Sherwood number was defined as

$$\text{Sh} = k_c \frac{2H}{D_{Salt}} = \frac{jA}{(c_b - \langle c_w \rangle) A_{proj}} \frac{2H}{D_{Salt}} \quad (6.16)$$

in which  $A_{proj}$  is the projected membrane surface area and  $\langle c_w \rangle$  is the area average of  $c_w$  on the same membrane. Please note that the Sherwood numbers on the two membranes facing a channel may differ depending on the flow direction.

### 6.3) Boundary Conditions and FV Mesh for CFD Simulations

As mentioned in discussing the unit cell approach, translational periodicity was imposed for  $\tilde{\mathbf{u}}$ ,  $p$  and  $c$  between opposite inlet-outlet boundaries. At the membrane surfaces, no slip conditions were imposed for velocity and a uniform value of  $2.6 \times 10^{-4}$  mol/(m<sup>2</sup>s) for the molar salt flux entering the fluid, corresponding to a current density of 50 A/m<sup>2</sup>. An NaCl aqueous solution at a bulk concentration of 500 mol/m<sup>3</sup> was considered (i.e., seawater, see physical properties reported in Table 6. 1). Please note that these choices on flux and bulk concentration affect directly the polarization coefficient (Eq. (6.14)), while, the Sherwood number depends only on geometry, Re and Schmidt (Sc), due to the linearity of the transport equation (6.5).

**Table 6. 1** Physical properties of the 500 mol/m<sup>3</sup> NaCl solution at 25 °C.

Property	Value	Units
Density, $\rho$	1017	kg m <sup>-3</sup>
Viscosity, $\mu$	$0.931 \times 10^{-3}$	N s m <sup>-2</sup>
Salt diffusivity, $D_{Salt}$	$1.47 \times 10^{-9}$	m <sup>2</sup> s <sup>-1</sup>
Schmidt number, $(\mu / \rho) / D$	622	-

As far as computational details are concern, all simulations were conducted in double precision. The “High Resolution” (higher-order upwind) interpolation scheme was adopted for the advection terms. In regard to convergence, iterations were interrupted when the residuals of all variables became less than  $10^{-10}$ .

### 6.3.1) FV Mesh for OCF

Mainly hexahedral meshes were adopted in the CFD simulations of the OCF membrane type. Small regions at the corners of the domain were discretized by tetrahedra (~4.4% of the total volumes), pyramids (~0.13%) and wedges (~0.03%). Grid dependence was evaluated for  $P/H = 8$  in the undeformed configuration at  $Re_\tau \approx 5$ , corresponding to a bulk Reynolds number of ~20. Therefore, the test case selected for the grid-independence assessment lies well above the creeping flow range and close to the highest Reynolds numbers investigated. Results are shown in Table 6. 2, where the computed values of the Darcy friction coefficient  $f_{Darcy}$  and of the Sherwood number Sh are reported as functions of the number of finite volumes.

**Table 6. 2** Grid dependence results for the OCF profiled membrane of  $P/H=8$  computed for  $Re_\tau = 5.2$  and  $\gamma_F = 0^\circ$ .

FV CFD Mesh	No. Finite Volumes	Darcy Friction Coefficient	Sherwood Number (Upper Wall)	Sherwood Number (Lower Wall)
OCF-A	$2.252 \times 10^6$	10.985	5.685	9.122
OCF-B	$3.833 \times 10^6$	11.062	5.519	8.771
OCF-C	$7.502 \times 10^6$	11.117	5.491	8.596

The mesh adopted for the final simulations (OCF-B) was characterized by about 4 million volumes. The channel height  $H$  was resolved by 40 finite volumes. Details of the same mesh are presented in Figure 6. 1.

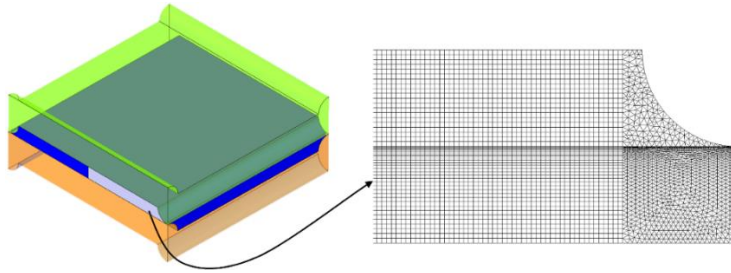


**Figure 6. 1** Details of the mesh chosen for the OCF with  $P/H=8$  (undeformed configuration).

### 6.3.2) FV Mesh for RP

In the case of RP profiled membranes almost completely hexahedral meshes were adopted in the CFD simulations. Only a minimal fraction ( $\sim 0.23\%$ ) of the volumes were wedges. Grid dependence was evaluated for  $P/H=10$  in the undeformed configuration at  $Re_\tau \approx 5$ , corresponding to a bulk Reynolds number of  $\sim 30$ , well above the creeping flow range and close to the highest Reynolds numbers investigated. Results are shown in Table 6. 3, where the computed values of Darcy friction coefficient  $f_{Darcy}$  and of the Sherwood number are reported as functions of the number of finite volumes. Please note that the distributions of all quantities on the upper and lower wall are identical due to symmetry reasons.

**Table 6. 3** Grid dependence results for the RP profiled membrane of  $P/H=10$  computed for  $Re_\tau = 5$  and  $\gamma_F = 90^\circ$ .

FV CFD Mesh	No. Finite Volumes	Darcy Friction Coefficient	Sherwood Number
RP-A	$2.576 \times 10^6$	6.941	13.769
RP-B	$4.142 \times 10^6$	6.965	13.719
RP-C	$6.091 \times 10^6$	6.976	13.689

The mesh selected for the final simulations (RP-B) consisted of  $\sim 4$  million volumes and 40 divisions along the channel height  $H$ . Details of the mesh are shown in Figure 6. 2.

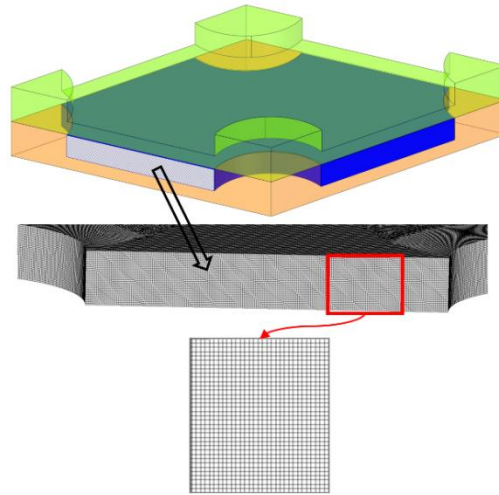


**Figure 6. 2** Details of the mesh chosen for RP with  $P/H=10$  (undeformed configuration).

## 6.4) Results

### 6.4.1) OCF profiled membrane type of $P/H = 8$

Fluid investigation in deformed and the undeformed channel were carried out by investigating different flow attack angle  $\gamma_F$ . Specifically, in the case of OCF profiled membrane type,  $\gamma_F$  is defined (Figure 5. 9) as the angle formed by the flow direction with the membrane ridges belonging to the upper wall of the channel under consideration. Three  $\gamma_F$  values of  $0^\circ$ ,  $45^\circ$  and  $90^\circ$  were studied.

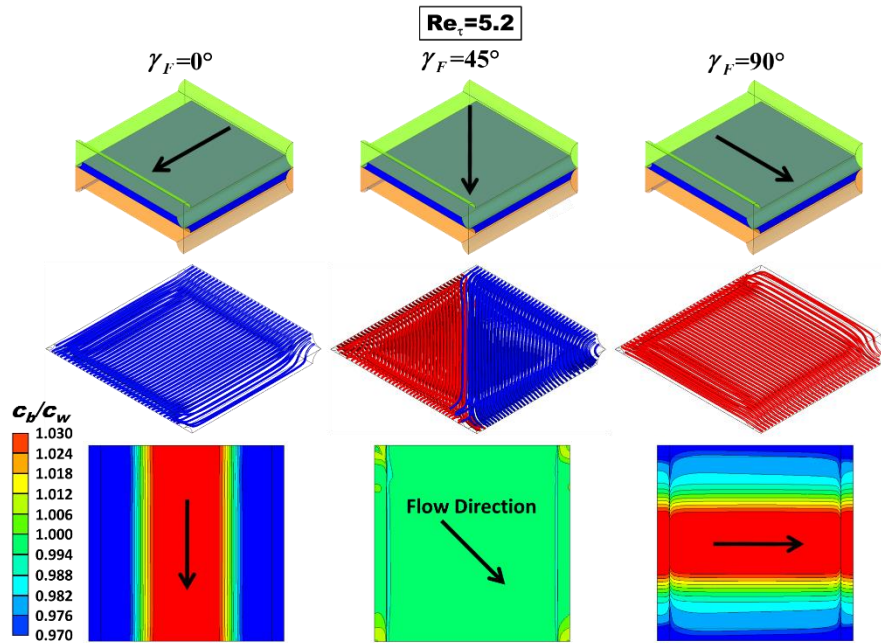
#### 6.4.1.1) Undeformed Configuration

Figure 6. 3 shows 3-D streamlines and maps of the polarization coefficient  $\theta$  in the undeformed configuration characterized by  $P/H = 8$  for a friction velocity Reynolds number  $Re_\tau = 5.2$  (bulk Reynolds number  $Re \approx 17.6$ , approach

velocity  $\sim 4$  cm/s) and all three values of the flow attack angle investigated. The flow direction is indicated by arrows.

The streamlines show that the flow is regular and parallel at this low value of  $Re$ . The corresponding plots for  $\gamma_F = 0^\circ$  and  $\gamma_F = 90^\circ$  are identical apart from a  $90^\circ$  rotation and a top-bottom reflection. For  $\gamma_F = 45^\circ$ , streamlines were shown in two colours according to the face from which they enter the unit cell; the graph shows that there is no mixing between the two inlet streams.

The maps of  $\theta$  in the bottom row show that the case  $\gamma_F = 45^\circ$  provides a more uniform distribution of the wall salt concentration, while the other two cases exhibit a very strong spanwise non-uniformity; the concentration is lower in the central region of the wall, where it becomes less than the bulk value despite the net overall salt flux being into the channel, and larger in the lateral regions of the channel walls, where low fluid velocities (stagnation zones) occur. Please note that the distribution of  $\theta$  on the upper wall for  $\gamma_F = 0^\circ$ , once rotated by  $90^\circ$ , would become the corresponding lower wall distribution for  $\gamma_F = 90^\circ$  and vice versa. Also, remember that the values of the polarization coefficient depend on the flux imposed at the boundary and on the bulk concentration considered. Therefore, for example, much lower values would be obtained for dilute solutions.



**Figure 6. 3** CFD results for the undeformed configuration of OCF with  $P/H = 8$  at  $Re_\tau = 5.2$  (approach velocity  $\sim 4$  cm/s). Top row: sketches illustrating the flow direction; middle row: 3-D streamlines; bottom row: maps of the concentration polarization coefficient  $\theta = c_b/c_w$  on the upper wall.  $c_b = 500$  mol/m<sup>3</sup>, flux corresponding to a current density of 50 A/m<sup>2</sup> entering the fluid domain (dilute channel of RED or concentrate channel of ED).

#### 6.4.1.2) Deformed Configurations

For the sake of brevity, the influence of deformation on flow and mass transfer in OCF membranes with  $P/H = 8$  is illustrated in Figure 6. 4 only for a friction velocity Reynolds number  $Re_\tau = 5.2$  (corresponding to bulk Reynolds numbers between  $\sim 7$  and  $\sim 35$ , approach velocity  $\sim 1.6$  and  $\sim 7.8$  cm/s, depending on the load conditions) and a flow attack angle  $\gamma_F = 90^\circ$  (flow orthogonal to the profile ridges adjacent to the upper wall of the fluid channel), as evidenced in the inset.

Three configurations are examined: compressed by a trans-membrane pressure  $TMP = +40$  kPa (left column), undeformed (middle column), and expanded by a trans-membrane pressure  $TMP = -40$  kPa (right column). The

top row reports contour plots of the velocity component along the main flow direction in the central cross section of the channel, while the middle and bottom rows report contour plots of the polarization coefficient  $\theta$  on both the upper and the lower wall of the fluid-filled channel, as clarified by the sketches in the rightmost part of the figure. The corresponding values of the  $F$  ratio and of the Sherwood number are also reported. In the deformed channels, the normalized axial velocity component exhibits larger maximum values, which are located closer to the longitudinal ridges in the case of the compressed channel.

The  $F$  ratio increases from  $\sim 2.04$  to  $\sim 4.96$  with compression and decreases from  $\sim 2.04$  to  $\sim 1.03$  with expansion. In regard to the Sherwood numbers that on the upper wall (flow orthogonal to the profile ridges) increases significantly with compression (from 8.77 to 11.46, i.e., by  $\sim 30\%$ ) and increases, but negligibly, also with expansion (from 8.77 to 8.92, i.e., by  $\sim 2\%$ ). That on the lower wall (flow parallel to the profile ridges) increases significantly with compression (from 5.52 to 7.63, i.e., by  $\sim 38\%$ ) and increases less, but still appreciably, also with expansion (from 5.52 to 6.17, i.e., by  $\sim 12\%$ ).

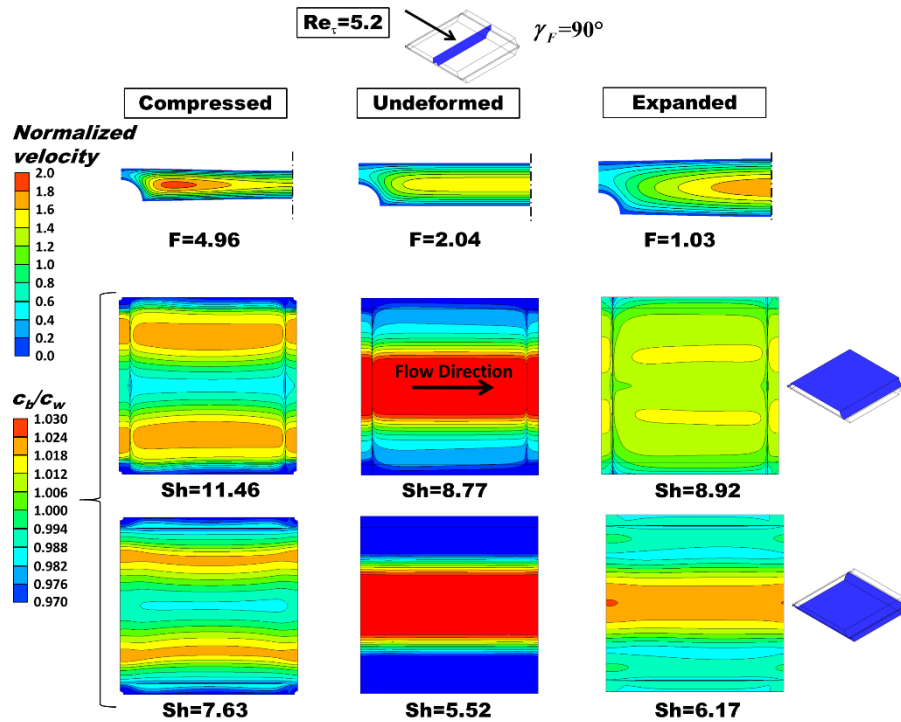


**Figure 6. 4** Influence of deformation on flow and mass transfer for OCF with  $P/H = 8$ ,  $\gamma_F = 90^\circ$ . Left column: compressed (TMP = +40 kPa); middle column: undeformed; right column: expanded (TMP = - 40 kPa). Top row: distribution of the streamwise velocity component in the central cross section of the channel (for symmetry reasons, only half map is shown); middle and bottom rows: distribution of the polarization coefficient on the upper and lower walls (see sketches on the right).  $c_b = 500 \text{ mol/m}^3$ , flux corresponding to a current density of  $50 \text{ A/m}^2$  entering the fluid domain (dilute channel of RED or a concentrate channel of ED).  $F$  ratio and Sherwood number are also reported.

For greater readability of the results, the dimensioned values of the approach velocity  $U$  and of the mass transfer coefficient  $k$  for the three conditions in Figure 6. 4 (TMP = 0 or  $\pm 40$  kPa) are summarized in Table 6. 4. In all three cases the friction velocity Reynolds number  $Re_\tau$  is  $\sim 5.2$ , corresponding to an inlet-outlet pressure drop in a unit cell (1.6 mm in side) of  $\sim 34.36$  Pa.



**Table 6. 4** Approach velocity and mass transfer coefficients for the load conditions in Figure 6. 4.

Quantities	Compressed	Undeformed	Expanded
	+40 kPa		-40 kPa
$U$ [cm/s]	~1.6	~4	~7.8
$(k_c)$ , upper wall [m/s]	$\sim 3.72 \times 10^{-5}$	$\sim 2.84 \times 10^{-5}$	$\sim 2.89 \times 10^{-5}$
$(k_c)$ , lower wall [m/s]	$\sim 2.47 \times 10^{-5}$	$\sim 1.78 \times 10^{-5}$	$\sim 2.00 \times 10^{-5}$

Distributions of the polarization coefficient  $\theta$  are deeply affected by deformation. In the compressed configuration, both on the upper and on the lower wall the region of high  $\theta$  (i.e., low concentration) observed in the undeformed case splits into two smaller regions, symmetrically located about the midline parallel to the flow direction, whereas the central region of the wall close to this midline exhibits low values of  $\theta$  (i.e., high values of concentration). In the expanded configuration, the concentration distribution on the lower wall remains similar to that observed in the undeformed case, with a single large central strip where  $c_w < c_b$ , which is consistent with the fact that the longitudinal velocity exhibits a single central maximum as in the undeformed case (see top row). The  $\theta$  distribution on the upper wall becomes flat, with two shallow  $\theta$  maxima (i.e.,  $c_w$  minima) symmetrically located about the longitudinal midline.

By comparing the polarization coefficient maps and the velocity maps in Figure 6. 4, it can be observed that under the present assumption of mass flux entering the channel, higher concentration levels on the wall correspond to stagnation regions, whereas low values of concentration occur in regions of high streamwise velocity as an effect of axial advection.

#### 6.4.1.3) Global Parameters

Among the performance parameters of greatest interest which can be affected by deformation, the friction coefficient and the Sherwood number were taken into account [129, 182].

Figure 6. 5 reports the normalized Darcy friction coefficient, i.e., the  $F$  ratio, as a function of Re for OCF membranes with  $P/H = 8$  at different values of

TMP. Graph (a) is for flow attack angles  $\gamma_F$  of  $0^\circ$  or  $90^\circ$  (equivalent in regard to friction), while graph (b) is for  $\gamma_F = 45^\circ$ . Please note that the results of each series of simulations performed at a given  $Re_\tau$  appear as an inclined row of symbols since they correspond to different values of  $Re$ .

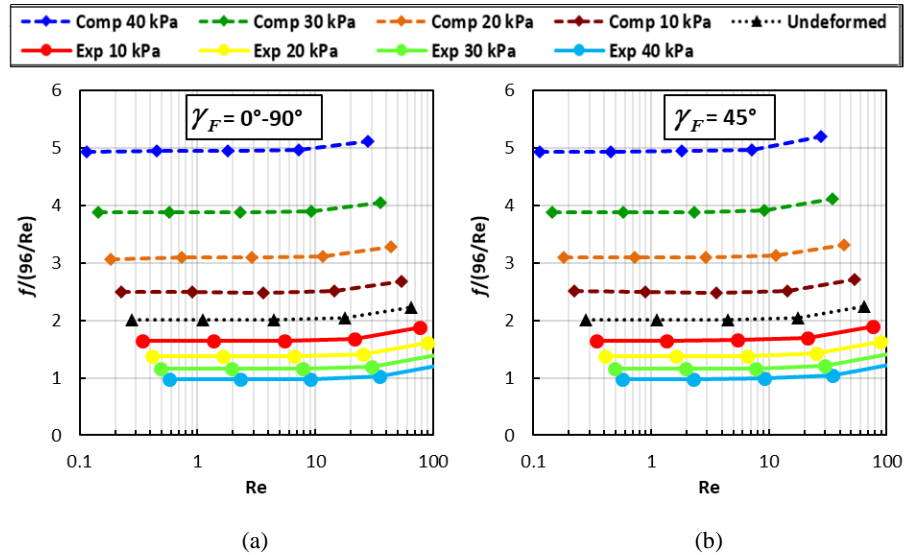


**Figure 6. 5** Normalized Darcy friction coefficient ( $F$  ratio) as a function of  $Re$  for OCF with  $P/H = 8$ , different values of the trans-membrane pressure TMP and two values of the flow attack angle  $\gamma_F$ . (a)  $\gamma_F = 0^\circ$  or  $90^\circ$ ; (b)  $\gamma_F = 45^\circ$ .

For any  $\gamma_F$  and applied TMP,  $F$  is flat up to  $Re \approx 10$ , indicating that inertial effects are negligible (self-similar flow). A significant departure from the void channel behavior is observed only for  $Re \gg 10$ . The influence of TMP is to enhance friction under compression and to reduce it under expansion. This effect is expected because, for any given  $Re$ , in a compressed channel the cross section is reduced, local velocities increase and thus pressure drops are higher (the opposite occurs in an expanded channel). For the same absolute value of TMP, the influence of compression is slightly larger than that of expansion: TMP = +40 kPa leads to an increase in  $F$  by a factor of  $\sim 2.5$ , while TMP = - 40 kPa leads only to a halving of  $F$ . The influence of the angle  $\gamma_F$  is negligible (graphs (a) and

(b) are practically identical), indicating a substantial isotropy of the profiled membrane lattice in terms of hydraulic friction. This behavior is typical in the case of low Reynolds numbers, as largely documented in the literature [121, 129, 181, 182]. Figure 6. 6 reports the Sherwood number on the upper channel wall, for  $P/H = 8$  as a function of the Reynolds number and for different values of the trans-membrane pressure. Graphs (a), (b) and (c) are for flow attack angles  $\gamma_F$  of  $0^\circ$ ,  $45^\circ$  and  $90^\circ$ , respectively. Please note that the cases  $\gamma_F = 0^\circ$  and  $90^\circ$  are equivalent in regard to friction but not in regard to mass transfer on a specified wall. However, for symmetry reasons, the Sherwood number on the lower wall of the channel at a given  $\gamma_F$  is identical to that on the upper wall at the complementary flow attack angle  $\gamma_F = 90^\circ$  (also the distributions of wall quantities such as concentration and mass transfer coefficient would be the same, apart from rotations and reflections). Therefore, values of Sh for the lower wall were not separately reported.

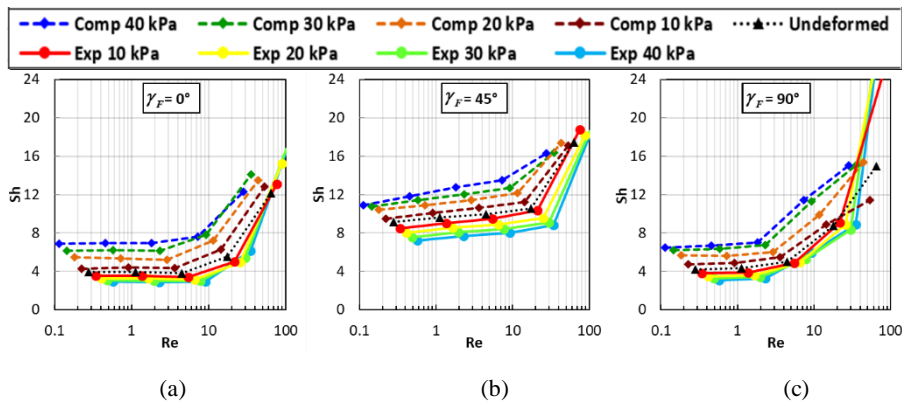


**Figure 6. 6** Sherwood number on the upper wall as a function of the Reynolds number for OCF with  $P/H = 8$  and different values of the trans-membrane pressure and of the flow attack angles. (a)  $\gamma_F = 0^\circ$ ; (b)  $\gamma_F = 45^\circ$ ; (c)  $\gamma_F = 90^\circ$ .

When  $\gamma_F = 0^\circ$ , Figure 6. 6 (a), for any applied TMP the Sherwood number on the upper wall changes little with Re up to  $\sim 10$ , while for  $\gamma_F = 90^\circ$ , Figure 6. 6 (c), the departure from this flat behavior occurs earlier ( $Re \approx 2$ ). For  $\gamma_F = 0^\circ$  or  $90^\circ$ , the Sherwood number at low Reynolds numbers ranges between  $\sim 3$  and  $\sim 7$

and thus is less than the theoretical value for a void plane channel of indefinite width ( $\sim 8.24$  under uniform mass flux conditions [187]). This indicates that in this Reynolds number range, the “shadow” effects of the profiles hinder mass transfer. The behaviour of  $Sh$  is different for a flow attack angle of  $45^\circ$ , Figure 6. 6 (b), for which, even at very low Reynolds numbers,  $Sh$  increases with  $Re$  and is larger than in a void channel for all compressed configurations, while it becomes slightly lower only for the expanded ones. Under all conditions,  $Sh$  increases rapidly as  $Re$  exceeds some critical value and, at  $Re \approx 30\text{--}100$ , it becomes much larger than in a void channel. The most peculiar behaviour is exhibited by the upper wall Sherwood number in the expanded cases and  $\gamma_F = 90^\circ$ , which jumps to very high values (up to  $\sim 40$  for  $TMP = -40$  kPa) as  $Re$  exceeds  $\sim 50$  due to the increasing importance of flow recirculation.

The influence of trans-membrane pressure on  $Sh$  is more complex than that on  $F$ . On the whole, compression enhances mass transfer and expansion reduces it; the influence of channel deformation on mass transfer is less marked than on friction. Some anomalous behaviour of  $Sh$  is observed only in the cases characterized by  $\gamma_F = 90^\circ$  and  $Re > \sim 50$ , in which the highest values of  $Sh$  are obtained for the largest expansion. Under all deformation conditions, the flow orientation  $\gamma_F = 45^\circ$  yields the highest values of  $Sh$ . This is in contrast with the behaviour of the friction coefficient, see Figure 6. 5, which is only minimally affected by the flow attack angle.

#### 6.4.2) RP pillar type of $P/H = 10$

In the case of RP profiled membrane type, also three values of the flow attack angle  $\gamma_F$  were investigated:  $\gamma_F = 0^\circ$  (flow parallel to the longer diagonal),  $\gamma_F = 30^\circ$  (flow parallel to two of the sides) and  $\gamma_F = 90^\circ$  (flow parallel to the shorter diagonal).

### 6.4.2.1) Undeformed Configuration

Figure 6. 7 shows 3-D streamlines and distributions of the polarization coefficient  $\theta$  for the RP profiled membrane of  $P/H=10$  undeformed configuration at a friction velocity Reynolds number of 2.5 (the resulting bulk Reynolds number was  $Re=5.1$ ) and all three flow attack angles investigated ( $\gamma_F=0^\circ$ ,  $30^\circ$  and  $90^\circ$ ). The flow direction is shown in the top row.

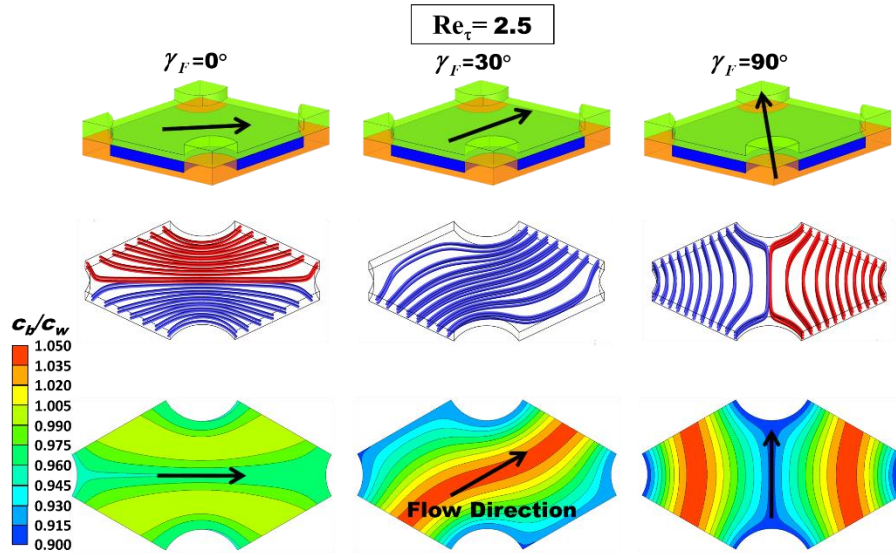


**Figure 6. 7** Sketches illustrating the flow direction (top row), 3-D streamlines (middle row) and maps of the concentration polarization coefficient  $\theta = c_b/c_w$  on either of the walls (bottom row) for the RP with  $P/H=10$  undeformed configuration and a friction velocity Reynolds number of 2.5 ( $Re=5.1$ ).  $c_b = 500 \text{ mol/m}^3$ , flux corresponding to a current density of  $50 \text{ A/m}^2$  entering the fluid domain (dilute channel of RED or concentrate channel of ED).

The streamlines show that the flow is regular at this low value of  $Re$ . In the cases  $\gamma_F=0^\circ$  and  $\gamma_F=90^\circ$ , streamlines were shown in different colors according to the face from which they enter the fluid domain; the graphs show that there is essentially no mixing between the two inlet streams, as expected. In regard to the maps of  $\theta = c_b/c_w$  (bottom row), it should be observed that the distributions of all quantities on the upper and lower wall are identical due to symmetry reasons and to the boundary conditions adopted. The comparison of the  $\theta$  maps relevant to

the three angles investigated shows that the case  $\gamma_F=0^\circ$  provides a fairly uniform distribution of the wall salt concentration, while for  $\gamma_F=90^\circ$  the wall concentration is strongly non-uniform in the lateral (spanwise) direction and becomes lower than the bulk concentration in two curved regions, symmetrically located about the flow direction, despite the net overall salt flux being into the channel. The case  $\gamma_F=30^\circ$  exhibits a non-uniform distribution, with one S-shaped central region characterized by large values of  $\theta$ . The significant non-uniformity of the polarization coefficient maps exhibited by the cases with flow attack angle  $\gamma_F=30^\circ$  and  $\gamma_F=90^\circ$  are associated to inhomogeneous distributions of the fluid velocity. The occurrence of marked stagnant regions and restricted zones with high fluid velocity, results in uneven  $\theta$  distributions.

#### 6.4.2.2) Deformed Configurations

Figure 6. 8 illustrates an example of the effect of deformation on flow and mass transfer. The cases at  $Re_\tau = 2.5$  and  $\gamma_F=90^\circ$  (flow parallel to the shorter diagonal of the unit rhombus) are shown, as evidenced in the inset. Only the undeformed (middle column,  $Re=5.1$ ), the most compressed (TMP = +40 kPa, left column,  $Re=2.4$ ) and the most expanded (TMP = - 40 kPa, right column,  $Re=8.9$ ) configurations are examined.

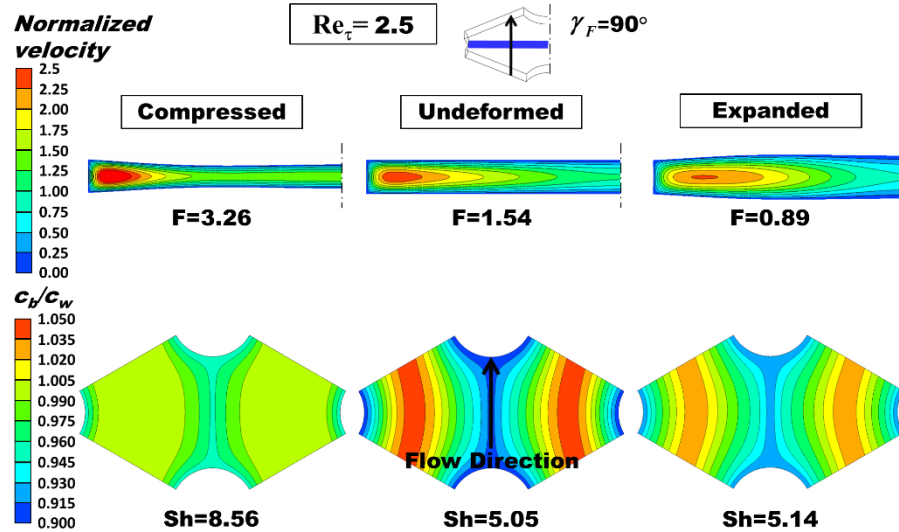


**Figure 6. 8** Influence of deformation on flow and mass transfer for RP with  $P/H=10$ ,  $\gamma_F=90^\circ$ ,  $Re_\tau=2.5$ . Left column: compressed (TMP = +40 kPa,  $Re=2.4$ ); middle column: undeformed ( $Re=5.1$ ); right column: expanded (TMP = -40 kPa,  $Re=8.9$ ). Top row: distribution of the streamwise velocity component in the central cross section of the channel (for symmetry reasons, only half map is shown); bottom row: distribution of the polarization coefficient on either of the walls.  $c_b = 500$  mol/m<sup>3</sup>, flux corresponding to a current density of 50 A/m<sup>2</sup> entering the fluid domain (dilute channel of RED or a concentrate channel of ED).  $F$  ratio and Sherwood number are also reported.

The top row reports contour plots of the velocity component along the main flow direction in the central cross section of the channel (for symmetry reasons, only the left half of this section is shown), while the bottom row reports contour plots of the polarization coefficient  $\theta = c_b/c_w$  on either of the walls of the fluid-filled channel (see above discussion on the symmetry between upper and lower wall). The corresponding values of the normalized Darcy friction coefficient ( $F$  ratio) and of the Sherwood number are also indicated.

In the central cross section, the maximum values of normalized axial velocity component occur approximately in the same region in all the three configuration examined, close to the lateral pillars, but exhibit larger values going from the expanded channel to the undeformed and the compressed ones. It can be observed that the  $F$  ratio increases more than twice (from  $\sim 1.54$  to  $\sim 3.26$ ) with compression and decreases, but less markedly (from  $\sim 1.54$  to  $\sim 0.89$ ), with expansion. The Sherwood number increases by 70% (from  $\sim 5.05$  to  $\sim 8.56$ ) with

compression and increases slightly (from  $\sim 5.05$  to  $\sim 5.14$ ) with expansion. Distributions of  $\theta$  become much more uniform with compression and only slightly more uniform with expansion.

### 6.4.2.3) Global quantities

Also for RP membrane case, the friction coefficient and the Sherwood number were investigated. The normalized Darcy friction coefficient, i.e. the  $F$  ratio as defined by Eq. (6.13), is reported as a function of the Reynolds number for different values of TMP in Figure 6. 9. Graph (a) is for a flow attack angle  $\gamma_F$  of  $0^\circ$ , graph (b) is for  $\gamma_F=30^\circ$  and graph (c) is for  $\gamma_F=90^\circ$ . For any applied TMP and  $\gamma_F$ ,  $F$  remains practically constant with Re up to  $Re \approx 10-20$ , which indicates that, in this range, inertial effects are negligible and the flow is self-similar. A marked departure from the void channel behavior occurs only for  $Re > 20$ . The influence of trans-membrane pressure is to enhance friction under compression conditions and to reduce it (but to a lesser extent) under expansion conditions. For example, a value of TMP of +40 kPa leads to a more than twofold increase in  $F$ , while a value of -40 kPa leads only to a 40% decrease.

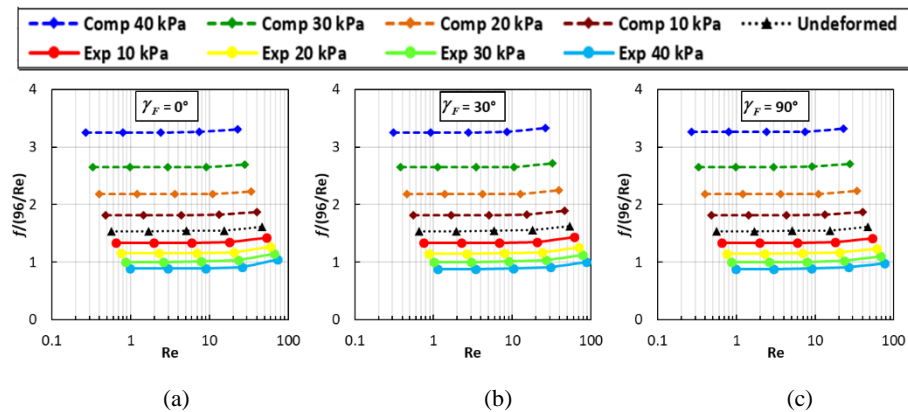


**Figure 6. 9** Normalized Darcy friction coefficient ( $F$  ratio) for RP with  $P/H=10$  as a function of the Reynolds number for different values of the trans-membrane pressure and three values of the flow attack angle  $\gamma_F$ . a)  $\gamma_F=0^\circ$ ; b)  $\gamma_F=30^\circ$ ; c)  $\gamma_F=90^\circ$ .



In the range of  $Re$  investigated, the flow attack angle does not influence hydraulic friction (i.e., graphs (a), (b) and (c) are practically identical), indicating a substantially isotropic behavior of the profiled membrane lattice for the pressure drop. Figure 6. 10 reports the Sherwood number on either of the channel walls, defined by Eq. (6.16), as a function of the Reynolds number for different values of TMP. Graphs (a), (b) and (c) are for a flow attack angle  $\gamma_F$  of  $0^\circ$ ,  $30^\circ$  and  $90^\circ$ , respectively. As already stated, the Sherwood numbers on the upper and lower walls are practically identical for symmetry reasons.

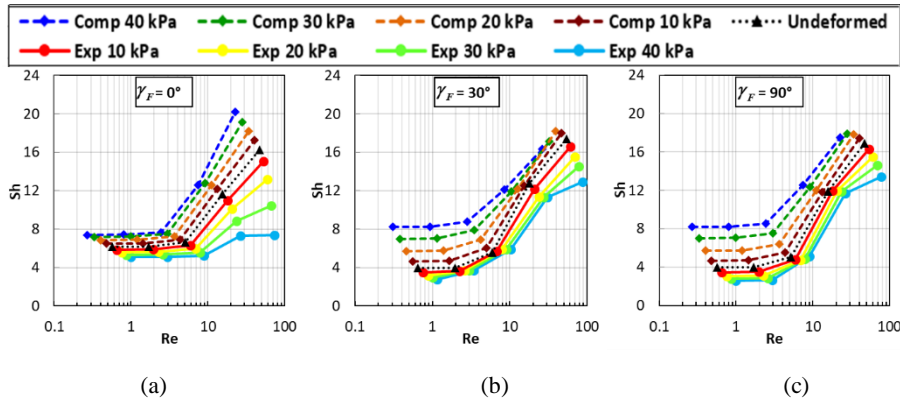


**Figure 6. 10** Sherwood number on either of the walls as a function of the Reynolds number for RP with  $P/H=10$  at different trans-membrane pressures and flow attack angles. a)  $\gamma_F=0^\circ$ ; b)  $\gamma_F=30^\circ$ ; c)  $\gamma_F=90^\circ$ .

At the left end of the  $Re$  interval investigated (up to a few units),  $Sh$  changes little with  $Re$  and ranges between  $\sim 3$  and  $\sim 8$ , thus being lower than the theoretical  $Sh$  for a void plane channel of indefinite width ( $\sim 8.24$  under uniform mass flux conditions). These results suggest that, in this low  $Re$  range, the “shadow” effect of the profiles hinders mass transfer. On the other hand, for  $Re$  larger than a few units,  $Sh$  increases significantly. Only in the most expanded configurations (TMP =  $-30$  and  $-40$  kPa), the increase of  $Sh$  with  $Re$  is less marked, especially for  $\gamma_F=0^\circ$ .

In regard to the influence of trans-membrane pressure, for all flow attack angles  $Sh$  increases with compression and decreases with expansion; the

influence of compression is larger than the influence of expansion at low Reynolds numbers, while the opposite is true at higher Re. For  $\gamma_F=0^\circ$ , the reduction of Sh caused by expansion at high Re is particularly significant. The behaviours of Sh for  $\gamma_F=30^\circ$  and  $90^\circ$  are less sensitive to TMP and are similar to each other. Unlike the case of the  $F$  ratio, the flow attack angle affects the Sherwood number at any Re.

### 6.4.3) Comparison between OCF and RP profiled membranes

A comparison between the influence of TMP on the RP profiled membranes with  $P/H=10$  and on the OCF ones with  $P/H=8$ , is reported in Table 6. 5. Approach velocity, Darcy friction factor and mass transport coefficient for both the upper and the lower wall are listed for a flow attack angle of  $\gamma_F=90^\circ$  and  $Re_\tau=2.5$ . The definition of  $\gamma_F$  for the two geometries is shown in Figure 5. 9.

**Table 6. 5** Approach velocity, Darcy friction factor and mass transfer coefficients for the undeformed, +40 kPa compressed and -40 kPa expanded configurations for RP with  $P/H=10$  and OCF with  $P/H=8$  geometries for  $\gamma_F=90^\circ$  and  $Re_\tau=2.5$ .

Quantities	Compressed +40 kPa		Undeformed		Expanded -40 kPa	
	RP	OCF	RP	OCF	RP	OCF
$U$ [cm/s]	0.5	0.4	1.1	1.0	2.0	2.0
$f_{Darcy}$	129.0	260.5	28.9	43.2	9.5	10.3
$k_c$ [m/s] upper wall	$3.2 \cdot 10^{-5}$	$2.6 \cdot 10^{-5}$	$1.9 \cdot 10^{-5}$	$1.9 \cdot 10^{-5}$	$1.9 \cdot 10^{-5}$	$2.2 \cdot 10^{-5}$
$k_c$ [m/s] lower wall	$3.2 \cdot 10^{-5}$	$2.6 \cdot 10^{-5}$	$1.9 \cdot 10^{-5}$	$1.4 \cdot 10^{-5}$	$1.9 \cdot 10^{-5}$	$1.1 \cdot 10^{-5}$

In the undeformed configuration, the RP arrangement exhibits lower friction coefficients than the OCF one. As TMP varies, the friction coefficient varies slightly less than in the OCF arrangement.

With regard to the mass transport properties, in the undeformed configuration the RP arrangement exhibits mass transport coefficients  $k_c$  similar to the OCF. Under compression, the  $k_c$  coefficients increase more than in the OCF; under expansion, they remain about unchanged, while  $k_c$  vary in a complex way in the OCF (increasing on the upper wall and decreasing on the lower one).

## CHAPTER VII

# FLOW REDISTRIBUTION IN ED AND RED CHANNELS IN THE PRESENCE OF LOCAL MEMBRANE DEFORMATIONS

### 7.1) Introduction

The CFD investigation presented in the Chapter VI has shown that membrane deformation induced by TMP may significantly affects the hydrodynamics and mass transport properties in ED and RED channels. The study was conducted at a small scale of a periodic portion of a profiled membrane bounded channel. In order to investigate the deformation effect at the higher scale of the entire channel dimension level, CFD applicability is limited due to the large computational effort and long computation time required by a very fine discretization in the presence of geometrical complexities in the whole channels.

Some authors, e.g. Dirkse et al. [188], Kostoglou and Karabelas [189, 190], Kodým et al. [191] and Pánek et al. [192], have proposed simplified models allowing the simulation of an entire channel of different membrane systems. However, the hydrodynamic in those channels has been investigated assuming undeformed (reference, or nominal) geometries.

In the present chapter a novel iterative Fluid-Structure Interaction model is presented to predict flow redistribution in channels where local membrane deformation occurs. In particular, the continuity and Darcy equations are solved in two adjacent channels by treating them as porous media and using the previous results of the CFD analysis of Chapter VI to express their hydraulic permeability as a function of the local TMP.

## 7.2) From a small- to a large-scale description of membrane-bounded channels

In the following section, some of the quantities already defined in Chapters V and VI are recalled together with the introduction of new ones, which are needed to scale up the analysis of ED and RED channels from a small to a large scale.

First, the *channel thickness*  $H$  is defined under undeformed conditions as the distance between the plane regions of opposite membranes. The *equivalent channel thickness*  $h$  is defined as the ratio of the fluid volume in the small periodic portion bounded by profiled membranes to the projected membrane area ( $P^2$  for a square-planform unit cell). Note that, in an undeformed channel, one has  $h < H$  due to the volume occupied by the membrane profiles; in a compressed channel  $h$  is always  $< H$ ; in an expanded channel, one can have  $h < H$ ,  $h = H$  or even  $h > H$ . Values of  $h$  under different load conditions are reported in Table B1 of Appendix B.

The *superficial velocity*  $U_s$  along a generic direction  $s$  is defined, in accordance with Eq. (6.8), as the ratio between the flow rate through a cross section of the channel orthogonal to  $s$ , having width  $W$ , and its undeformed and void area  $HW$ . The *interstitial velocity*  $U_{s,inter}$  along the same generic direction  $s$  is defined as the volume average of the  $s$ -component of the actual fluid velocity in the unit cell portion and can be computed as  $U_s H / h$ . It takes into account both the presence of membrane profiles and the possible deformation (compression or expansion) of the channel.

The analysis is carried out for channels bonded by the OCF profiled membranes of  $P/H=8$  presented in the previous Chapters V and VI.

The investigation at the small scale of the friction characteristics of the channel bounded by OCF profiled membranes (see, Figure 6. 5) showed that up to  $Re \approx 100$  the equivalent friction coefficient varied in a negligible way with the flow attack angle  $\gamma_F$ , thus exhibiting an isotropic behaviour, and that no pressure gradient orthogonal to the main flow direction arose. Moreover, up to  $Re \approx 10$  the

equivalent friction coefficient was proportional to  $Re^{-1}$  (*i.e.*, the relation between velocity and pressure drop was linear), indicating a regime of creeping flow characterized by the self-similarity of the flow field. At higher  $Re$ , the dependence of the pressure drop on the velocity became nonlinear due to inertial effects.

At the larger scale of a whole stack, the flow can be described as flow in a porous medium [171, 189]. Under the assumption of flat channels, the generic channel can be treated as a two-dimensional domain. In view of the above-discussed invariance of the equivalent friction coefficient with the flow attack angle, the permeability can be assumed to be isotropic and the relation between the pressure gradient and the superficial velocity is a generalized Darcy equation:

$$-\frac{\partial p}{\partial s} = \frac{\mu}{K_{app}} U_s \quad (7.1)$$

where  $\mu$  is the fluid viscosity and  $K_{app}$  is a (scalar) apparent permeability, independent of the flow direction  $s$ . At low Reynolds numbers (*i.e.*  $< 10$ )  $K_{app}$  attains a constant value  $K$ , independent of the velocity  $U_s$ , and Eq. (7.1) takes the form of the classical Darcy law. At higher Reynolds numbers, when inertial effects occur, the Darcy law is replaced by the Darcy-Forchheimer equation:

$$-\frac{\partial p}{\partial s} = \frac{\mu}{K_{app}} U_s + \rho C_F U_s^2 \quad (7.2)$$

containing two characteristics of the porous medium, namely a Darcy permeability  $K$  and a Forchheimer coefficient  $C_F$  [193]. Eq. (7.2) can still be expressed in the form of Eq. (7.1) provided the apparent permeability is expressed as  $K_{app} = K(1 + \rho K C_F U_s / \mu)$ .

The apparent permeability is related to the friction factor  $f_{Darcy}$  by:

$$K_{app} = \frac{4\mu H}{\rho U_s} \frac{1}{f_{Darcy}} \quad (7.3)$$

The value of  $K_{app}$  deduced from the friction coefficient using Eq. (7.3) can then be employed in Eq. (7.1) to estimate the superficial velocity associated with a given pressure gradient in the fluid domain. A straightforward solution of Eq. (7.1) is not possible if the channel permeability varies in space as a function of

the local trans-membrane pressure. Therefore, a novel mathematical model was developed which adopts an iterative approach to deal with this issue, thus computing the steady-state fluid distribution in the channels in the presence of membrane deformation.

### 7.3) Computational domain and modelling assumptions

The model simulates two adjacent channels, a diluate (DIL, low electrolyte concentration) and a concentrate (CON, high electrolyte concentration), together with the associated AEM and CEM membranes (the “cell pair”). Figure 7. 1 shows a schematic representation of a cell pair equipped with Overlapped Crossed Filaments (OCF) profiled membranes and a sketch of the computational “molecules” adopted in the present model for the formulation of balance equations in discrete form.

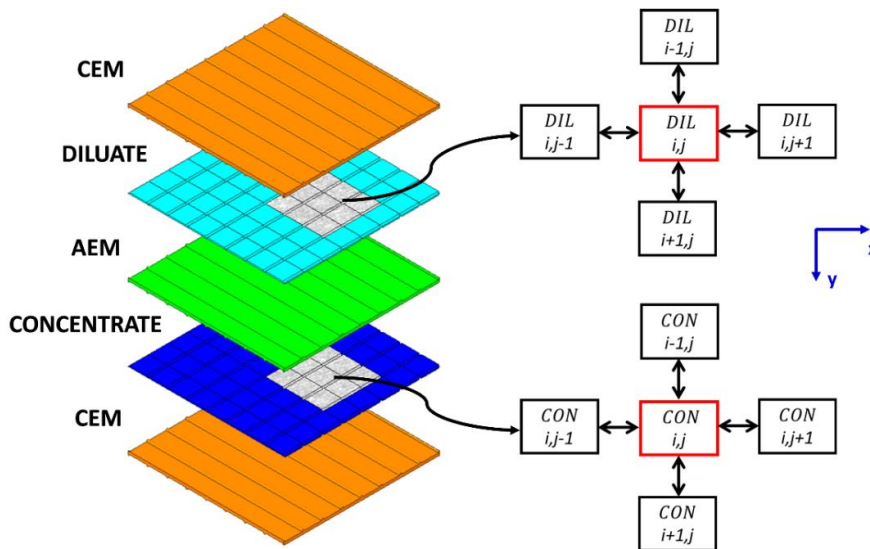


**Figure 7. 1** Sketch of a cell pair with dilute (DIL) and concentrate (CON) channels. Membranes are shown only for the sake of clarity, but are not part of the computational domain. The bottom row reports a representation of the computational “molecules” adopted for the formulation of discrete balance equations in both channels.

Membranes are not actually included in the computational domain. The hydrodynamic effects of the profiled membranes and of their deformation are taken into account using constitutive equations expressing the channel's apparent permeability as a function of trans-membrane pressure and superficial velocity.

As discussed above, such equations can be derived using Eq. (7.3) and the results of the friction factor obtained from the investigation at the lower scale level of a periodic unit cell (Figure 6. 5). The apparent permeability  $K_{app}$  of the concentrate channel is reported in Figure 7. 2 as a function of the superficial velocity  $U_s$  for different TMP values.

It can be observed that the assumption of Darcyan flow (*i.e.*, of a linear dependence of velocity on pressure gradient, with  $K$  independent of  $U_s$ ) is well satisfied only for velocities of the order of a few cm/s ( $Re \approx 10$  for  $H=200 \mu\text{m}$ ), which are common in RED but rather low in ED.

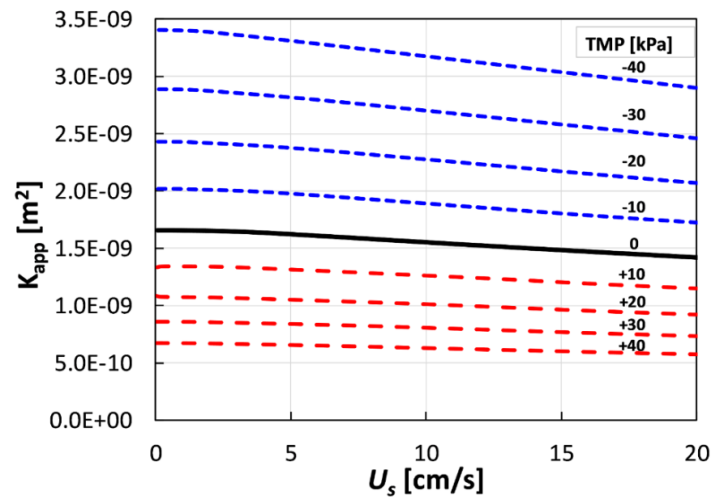


**Figure 7. 2** Apparent permeability  $K_{app}$  of the concentrate channel as a function of the equivalent velocity  $U_s$  at different values of the trans-membrane pressure for OCF profiled membranes with  $P/H=8$ . The sign convention for TMP adopted is the same of that used in Chapter V and VI: TMP is positive if the concentrate channel is compressed and negative if the concentrate channel is expanded.



The other assumptions made in the model are:

- a) The flow field is steady.
- b) The fluid properties are constant and are the same in both channels both the DIL and the CON channels (see Table 6. 1).
- c) AEM and CEM membranes share the same mechanical properties and profiles geometry, so that the same correlation for the channel apparent permeability applies to both channels.
- d) Trans-membrane water transport (due to osmotic flow and electro-osmotic drag) is neglected. Therefore, the inlet flow rate coincides with the outlet flow rate. This assumption is justified by the fact that the trans-membrane water flow rate is much less than the main water flow rate along the channels. For example, even in the extreme case of ED with a large concentration gradient (seawater-freshwater), a high current density ( $100 \text{ A/m}^2$ ), a large channel length/thickness ratio (3000, e.g.  $L=0.6 \text{ m}$ ,  $H=200 \text{ }\mu\text{m}$ ), a low superficial velocity ( $1 \text{ cm/s}$ ) in both channels, a large membrane osmotic permeability ( $10 \text{ ml}/(\text{m}^2 \text{ h bar})$ ) and a hydration number of 7 (water molecules/ion), the total trans-membrane water flow rate estimated by elementary balances is less than 8% of the axial flow rate of each solution.

In addition, the following conventions are adopted:

- I. Flow rates exiting a computational block are assumed positive, while flow rates entering a block are assumed negative.
- II. The TMP is calculated as the difference between the local pressures in the DIL and CON compartments ( $TMP_{i,j} = P_{i,j}^{DIL} - P_{i,j}^{CONC}$ ), so that, as mentioned above, it is positive when DIL is expanded and CON compressed. By definition, if the CON compartment locally experiences a given value of TMP, at the corresponding location the DIL compartment is subjected to -TMP. The convection is in accordance with the TMP definition used in Chapter V and VI.

The model was implemented in the Matlab® environment.

## 7.4) Discretized governing equations

### 7.4.1) Discretized continuity equation

In the model each of the two coupled CON and DIL channels, of overall size  $L \times W$ , are assumed divided into  $N_{Block}^x \times N_{Block}^y$  rectangular blocks of size  $\Delta x = L / N_{Block}^x$ ,  $\Delta y = W / N_{Block}^y$ , where  $L$  and  $W$  are the length and the width of the channels. Each channel is treated as a continuous, porous, two-dimensional medium, and the block size, being an arbitrary computational construct, is unrelated to the size of the individual periodic fluid portion.

For either channel, considering a steady state flow regime and making reference to the sketch in Figure 7. 1, the continuity equation at the generic computational block  $i, j$  can be written as:

$$U_{i,j+1}^{i,j} + U_{i+1,j}^{i,j} - U_{i,j}^{i-1,j} - U_{i,j}^{i,j-1} = 0 \quad (7.4)$$

in which each  $U$  is the volume flow rate through the corresponding block interface divided by  $H \Delta x$  or  $H \Delta y$  (undeformed and void-channel area of the same interface). Superscripts indicate the grid block from which the flow exits, while subscripts indicate the block into which the flow is entering. Signs are attributed according to convention I.

### 7.4.2) Discretized Darcy equation for the case of low velocity

In the limit of low  $U_s$ , the apparent permeability in Figure 7. 2 becomes a function of trans-membrane pressure only and is shown in Figure 7. 3.

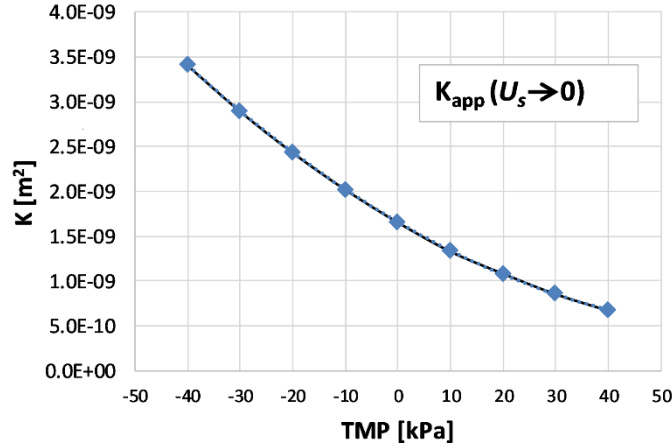


**Figure 7. 3** Permeability  $K$  at  $U_s \rightarrow 0$  as a function of trans-membrane pressure for OCF profiled membranes with  $P/H=8$ .

The function  $K(\text{TMP})$  can well be approximated by a quadratic function:

$$K = 2.405 \cdot 10^{-13} \text{TMP}^2 - 3.4 \cdot 10^{-11} \text{TMP} + 1.656 \cdot 10^{-9} \quad (7.5)$$

in which  $K$  is in  $\text{m}^2$  and  $\text{TMP}$  in  $\text{kPa}$ .

The non-Darcyan range of higher velocities, in which  $K_{app}$  depends not only on  $\text{TMP}$  but also on  $U_s$ , requires a slightly more complex treatment and it is separately discussed in Section 7.4.3.

By approximating the derivatives in the Darcy equation (7.1) with reference to the block sizes  $\Delta x$  or  $\Delta y$ , the superficial velocities of the fluid can be expressed as:

$$U_{i,j+1}^{i,j} = -\frac{K_{i,j}}{\mu} \cdot \frac{P_{i,j+1} - P_{i,j}}{\Delta x}$$

$$U_{i+1,j}^{i,j} = -\frac{K_{i,j}}{\mu} \cdot \frac{P_{i+1,j} - P_{i,j}}{\Delta y} \quad (7.6-7)$$

By substituting Eqs. (7.6) and (7.7) into Eq. (7.4), and considering for simplicity  $\Delta x = \Delta y$ , the pressure in the block  $(i, j)$  can be expressed as:

$$P_{i,j}^{Calc} = \frac{K_{i,j} \cdot P_{i+1,j} + K_{i,j} \cdot P_{i,j+1} + K_{i-1,j} \cdot P_{i-1,j} + K_{i,j-1} \cdot P_{i,j-1}}{K_{i-1,j} + 2K_{i,j} + K_{i,j-1}} \quad (7.8)$$

The steady-state pressure distribution in deformed channels must simultaneously satisfy Eq. (7.8) (which was derived from the continuity and Darcy equations) and the constitutive law, e.g. Eq. (7.5), expressing the dependence of the channel's permeability on the local TMP. An iterative algorithm was developed in order to perform this coupling; its flow chart is schematically shown in Figure 7. 4.

First, a guess for pressure is imposed in both channels at each grid block ( $P_{i,j}^{Guess}$ ). Random values distributed between -40 and +40 kPa were used in the present applications. Then, the local TMP is calculated by using convention II, and the  $K_{i,j}$  values in both channels are determined by using Eq. (7.5). A new pressure value  $P_{i,j}^{Calc.}$  is computed at each block ( $i, j$ ) by using Eq. (7.8). Finally, under-relaxation is applied before starting a new iteration:

$$P_{i,j}^{New} = P_{i,j} + c_r (P_{i,j}^{Calc.} - P_{i,j}) \quad (7.9)$$

where  $c_r$  is an under-relaxation factor for which a value of 0.7 was chosen as a reasonable trade-off between computing time and convergence stability. The algorithm terminates when the maximum difference between old and new pressures over all grid blocks becomes less than a prescribed small value, i.e.  $10^{-9}$  kPa. Once convergence is attained, superficial velocities are computed from Eqs. (7.6)-(7.7). The model was implemented in the Matlab® environment.

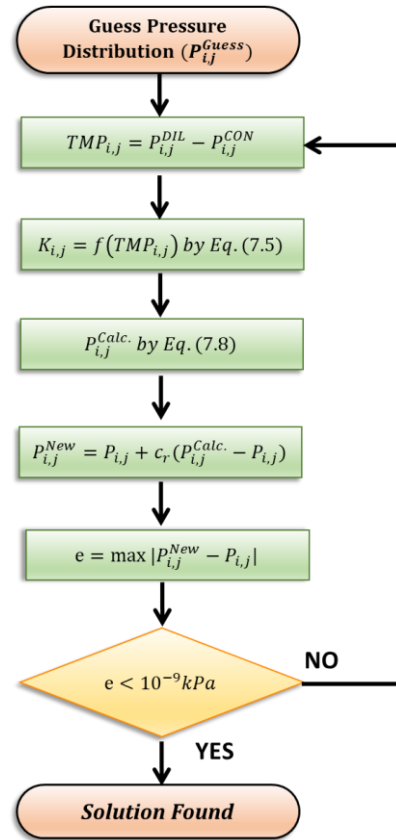
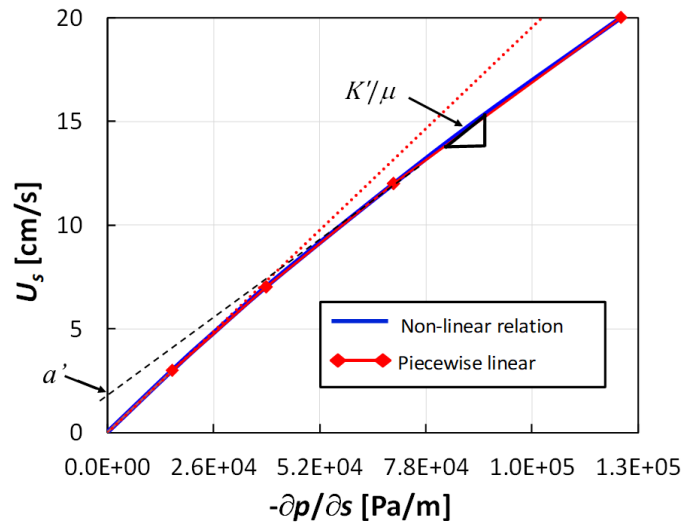


Figure 7. 4 Flow chart of the iterative algorithm for the case of low velocity.

### 7.4.3) Model adjustment for non-Darcyan flow regime

Industrial electro-membrane processes, especially ED, often experience fluid velocities larger than a few cm/s and channel thicknesses larger than 200  $\mu\text{m}$  [114, 117]. Under these conditions, yielding Reynolds numbers of the order of  $10^2$ , the linear relation between velocity and pressure gradient expressed by the Darcy law is no longer valid, *i.e.*  $K_{app}$  depends on  $U_s$ . For the sake of clarity, the relation between velocity and pressure gradient is reported in Figure 7. 5 for the undeformed case; in the presence of deformation, a similar graph applies for each value of TMP. The blue solid line represents the  $U_s$  vs.  $\partial p/\partial s$  relation computed

by CFD, while the dotted red line represents the linear extrapolation of the behaviour observed in the limit of low velocity. A significant departure from the linear behaviour is observed for velocities larger than  $\sim 10$  cm/s. Therefore, in order to investigate higher flow regimes without excessively modifying the proposed model, a piecewise linear fitting (represented in Figure 7. 5 by red line segments separated by symbols) was applied to capture the dependence of the apparent channel permeability on the velocity. Each linear segment is identified by its slope  $K'/\mu$  and its intercept  $a'$  as shown in Figure 7. 5, with  $K'=K$  and  $a'=0$  in the first segment.



**Figure 7. 5** Dependence of superficial velocity on pressure gradient for the undeformed channel case (solid blue line). The dotted red line represents the linear relation valid at low velocities. The straight red segments separated by symbols represent a piecewise linear fitting. As an example, the intercept  $a'$  and the slope  $K'/\mu$  of the 4<sup>th</sup> segment are indicated.

The same procedure was repeated for all the values of TMP investigated between  $-40$  and  $+40$  kPa; Tables B2.1 and B2.2 in Appendix B report the slopes and intercepts of each straight line segment.

Accordingly, the Darcy equation (7.1) can be replaced by:

$$U_s = -\frac{K'}{\mu} \left( -\frac{\partial p}{\partial s} \right) + a' \quad (7.10)$$

in which  $K'$  and  $a'$  are constant for each segment of the piecewise linear approximation.

In discretized form, Eqs. (7.6) and (7.7) are modified as follows:

$$\begin{aligned} U_{i,j+1}^{i,j} &= -\frac{K_{i,j}^{\prime x}}{\mu} \cdot \frac{P_{i,j+1} - P_{i,j}}{\Delta x} - \text{sgn}(P_{i,j+1} - P_{i,j}) \cdot a_{i,j}^{\prime x} \\ U_{i+1,j}^{i,j} &= -\frac{K_{i,j}^{\prime y}}{\mu} \cdot \frac{P_{i+1,j} - P_{i,j}}{\Delta y} - \text{sgn}(P_{i+1,j} - P_{i,j}) \cdot a_{i,j}^{\prime y} \end{aligned} \quad (7.11-12)$$

where the terms  $a_{i,j}^{\prime x}$ ,  $a_{i,j}^{\prime y}$  and  $K_{i,j}^{\prime x} / \mu$ ,  $K_{i,j}^{\prime y} / \mu$  are the intercepts and the slopes of the straight line segments, respectively. The terms  $a_{i,j}^{\prime x}$  and  $a_{i,j}^{\prime y}$  are multiplied by the sign of the pressure difference between two consecutive computational blocks to account for the direction of the flow. The terms  $K_{i,j}^{\prime x}$  and  $K_{i,j}^{\prime y}$  may be different despite the isotropy of the medium because of the different values of the velocity along  $x$  and  $y$ . At low velocity both  $K_{i,j}^{\prime x}$  and  $K_{i,j}^{\prime y}$  reduce to  $K_{i,j}$ , which is the proportionality constant of the Darcy equation (7.1), while the terms  $a_{i,j}^{\prime}$  vanish.

Substituting Eqs. (7.11) and (7.12) into Eq. (7.4), and considering for simplicity  $\Delta x = \Delta y$ , one obtains:

$$\begin{aligned} P_{i,j}^{Calc} &= \frac{K_{i,j}^{\prime y} \cdot P_{i+1,j} + K_{i,j}^{\prime x} \cdot P_{i,j+1} + K_{i-1,j}^{\prime y} \cdot P_{i-1,j} + K_{i,j-1}^{\prime x} \cdot P_{i,j-1}}{K_{i-1,j}^{\prime y} + K_{i,j}^{\prime y} + K_{i,j}^{\prime x} + K_{i,j-1}^{\prime x}} + \\ &+ \mu \Delta x \left[ \frac{a_{i,j}^{\prime x} \cdot \text{sgn}(P_{i,j+1} - P_{i,j}) + a_{i,j}^{\prime y} \cdot \text{sgn}(P_{i+1,j} - P_{i,j})}{K_{i-1,j}^{\prime y} + K_{i,j}^{\prime y} + K_{i,j}^{\prime x} + K_{i,j-1}^{\prime x}} + \right. \\ &\left. - \frac{a_{i,j-1}^{\prime x} \cdot \text{sgn}(P_{i,j} - P_{i,j-1}) - a_{i-1,j}^{\prime y} \cdot \text{sgn}(P_{i,j} - P_{i-1,j})}{K_{i-1,j}^{\prime y} + K_{i,j}^{\prime y} + K_{i,j}^{\prime x} + K_{i,j-1}^{\prime x}} \right] \end{aligned} \quad (7.13)$$

Eq. (7.13) must be employed instead of Eq. (7.8) to evaluate the pressure value at each computational block in either channel. It requires an initial distribution of  $a_{i,j}^{\prime x}$ ,  $a_{i,j}^{\prime y}$  and  $K_{i,j}^{\prime x}$ ,  $K_{i,j}^{\prime y}$  to calculate the flow velocity at each computational block. Therefore, some additional steps must be added to the algorithm, as illustrated by the flowchart in Figure 7. 6.

First, initial (guess) values  $P_{i,j}^{Guess}$ ,  $K_{i,j}^{Guess}$  and  $a_{i,j}^{Guess}$  of pressures and non-Darcyan parameters are set in both channels at each grid block and the corresponding TMP and velocities are calculated by using convention II and Eqs. (7.11) -(7.12), respectively. On the basis of the local TMP and superficial velocities, new  $a_{i,j}^{x}$ ,  $a_{i,j}^{y}$  and  $K_{i,j}^{x}$ ,  $K_{i,j}^{y}$  are computed by linear interpolation of data reported in using Tables B2.1 and B2.2. Then, pressures  $P_{i,j}^{Calc}$  are calculated by using Eq. (7.13). Finally, after applying under-relaxation using Eq. (7.9) (as in the Darcyan case), the error is evaluated and, until it decreases below the prescribed value, a new iteration is performed. Guess values  $K_{i,j}^{Guess}$  and  $a_{i,j}^{Guess}$  too far from the equilibrium values may hinder the convergence of the algorithm. Therefore, the guess pressure distribution  $P_{i,j}^{Guess}$  was obtained by running the simplified (Darcyan) model, while the guess  $a_{i,j}^{x}$  and  $a_{i,j}^{y}$  values were set to zero at each block and the guess  $K_{i,j}^{x}$  and  $K_{i,j}^{y}$  values were assumed equal to the  $K_{i,j}$  values of the simplified model.



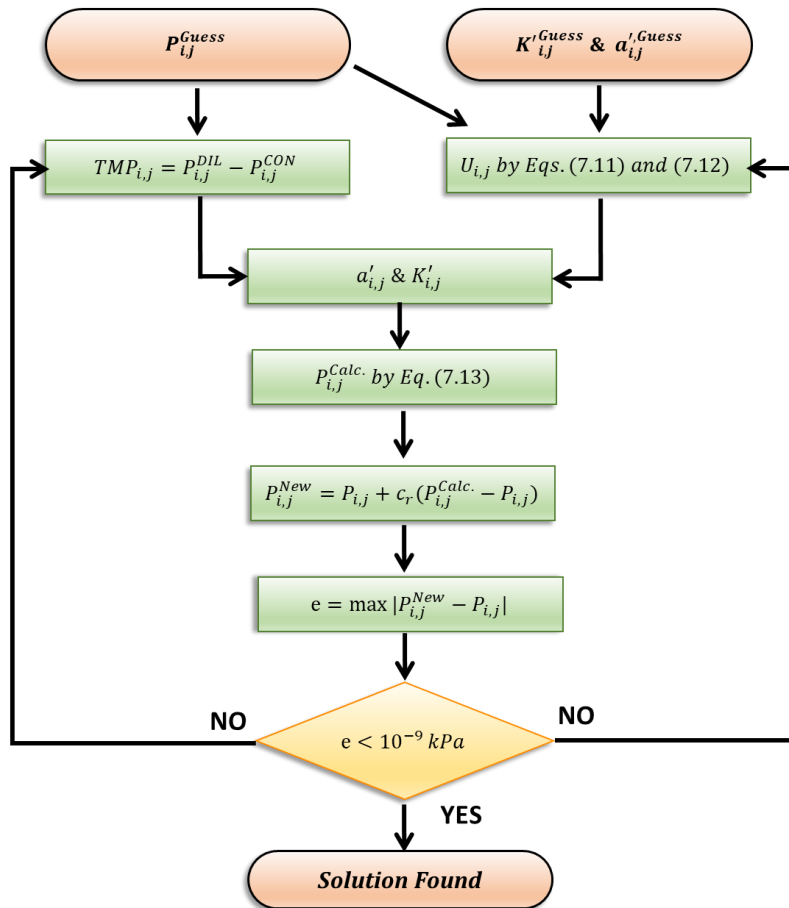


Figure 7. 6 Algorithm flow chart in the case of non-Darcyan flow regime

### 7.5) Flow arrangement and boundary conditions

Three are the most common fluid flow arrangements employed in RED and ED applications: (i) parallel flow, (ii) counter flow and (iii) cross flow. Advantages and disadvantages of these layouts have amply been discussed in the literature [114, 163]. Parallel flow assures the lowest TMP values between fluid channels, thus minimizing leakages and membrane deformation issues (ideally  $TMP=0$  if the two solutions share the same velocity and physical properties and the channels share the same geometrical configuration). On the other hand, the

parallel flow arrangement suffers from a strong axial variation of concentration difference, which, in its turn, reduces the driving force in RED and increases the energy consumption in ED. Counter flow is characterized by a more uniform distribution of the concentration difference along the channel length, but exhibits the largest TMP. Finally, the cross flow layout has shown a more uniform electric current distribution and promising process performances in RED [194].

In the following section, fluid flow distribution in a square stack of 0.6 m side was analysed in the cross flow and counter flow arrangements. For the aforementioned reasons, parallel flow does not pose significant TMP issues and therefore was not investigated. A channel length of 0.6 m allows the investigation of superficial velocities up to ~10 cm/s with an inlet-outlet pressure drop below 40 kPa, corresponding to the highest TMP value for which correlations for  $K$  were obtained. This size is close to that of square prototype stacks that have actually been used in RED applications [194, 195]. The choice of a square stack simplifies the calculations and the interpretation of the results obtained. Of course, the model could also be applied to rectangular geometries, which are often employed in industrial ED units [143].

The two flow arrangements investigated are shown in Figure 7. 7. In cross flow, fluid enters and exits each channel through two opposite slots of height  $H$  in the lateral gasket located beside the channel area where membrane profiles are, running through the whole width  $W$  of each channel. In the case of counter flow, inlets and outlets are shorter slots connecting the channels with manifolds orthogonal to the membranes; they were simulated as straight segments, three at the inlet and two at the outlet. The inlet slots were placed 3 cm away from the upper and lower side walls and the outflow ones 14 cm away. All slots were 10 cm wide and the distance between adjacent slots was 12 cm.

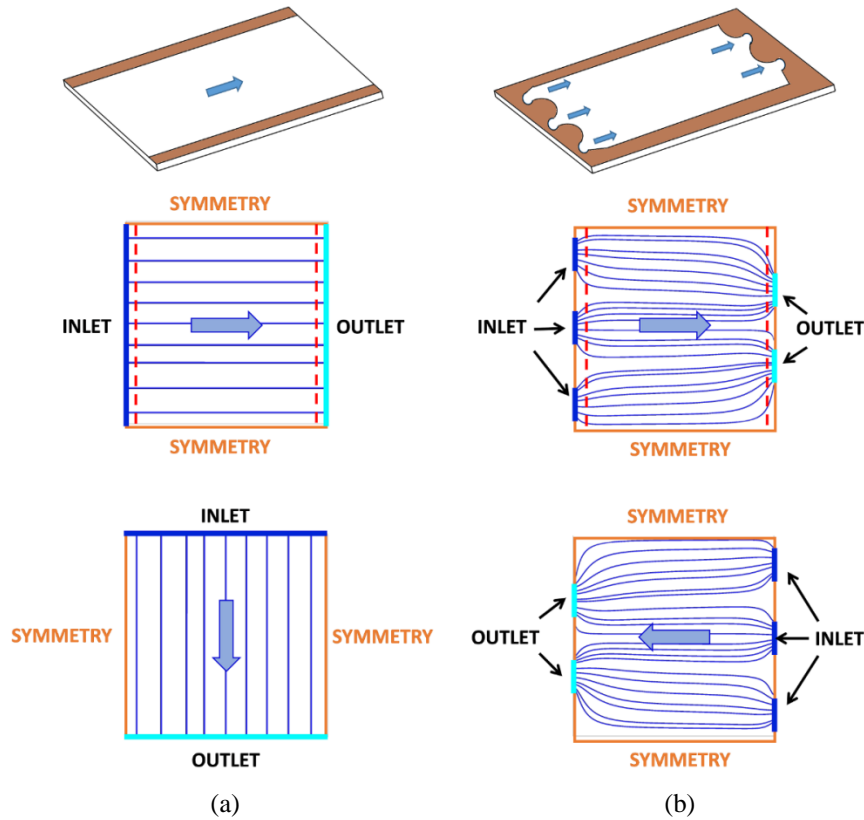


**Figure 7.7** Flow arrangements analysed: (a) cross flow; (b) counter flow. The insets in the top row show the actual geometry of inlets and outlets. The second and third rows report the approximated geometry simulated which apply to the two solutions (e.g., concentrate and diluate). The broken lines in the middle graphs are those along which velocity and pressure profiles obtained with different grids have been compared (Appendix C).

In all cases, pressure was set to zero at the outlet boundaries and to a uniform value  $P_{in}$  at the inlet boundaries. In the cross-flow case, values of 3.12, 16.29 and 34.3 kPa were set for  $P_{in}$ , yielding superficial velocities in the undeformed channels of 1, 5 and 10 cm/s, respectively. Only the value  $P_{in}=34.3$  kPa was investigated in the case of the counter flow configuration, where it yielded a superficial velocity in the undeformed channels of  $\sim 8.5$  cm/s.

In regard to the side boundaries, where neither inlet nor outlet boundaries were specified, the most physically appropriate boundary condition would be the no slip one. However, since no slip conditions are not fully consistent with the

Darcy approximation, pressure symmetry conditions were used instead. CFD simulations for the counter flow configuration were performed in which either symmetry or no-slip wall conditions were imposed on the side boundaries, and discrepancies of less than 1% were observed in the computed pressure distribution.

Grid dependence, i.e. the effect of the number of channel blocks on the model's results, was analysed by comparing five grids of increasing resolution. Results for a single undeformed channel were also compared with the CFD predictions obtained using the Ansys-CFX code. Results show that, for the case of cross-flow, 2-D grids with just 60×60 blocks are sufficient to yield satisfactory results. For the case of counter-flow, the presence of small details in the geometry of the inlets and outlets made finer grids, e.g. 120×120 blocks, necessary. Details of these comparisons are reported in Appendix C.

## **7.6) Results**

### **7.6.1) Cross Flow arrangement**

#### **7.6.1.1) Low velocity case ( $U_s \approx 1$ cm/s)**

Pressure maps and TMP for cross flow configuration with an inlet pressure of 3.12 kPa (yielding  $U_s \approx 1$  cm/s, being  $s$  either  $x$  for the CON channel or  $y$  for the DIL channel) are shown in Figure 7. 8 for the case in which membrane deformation effects are *not* taken into account.

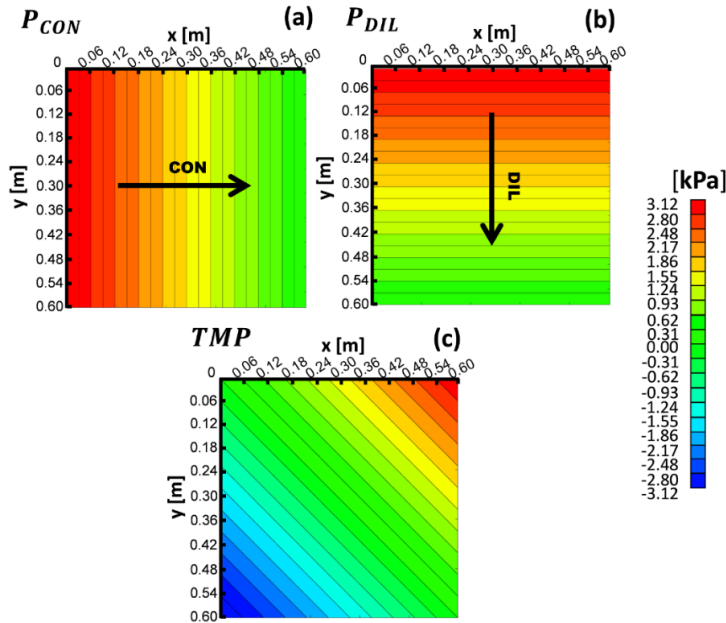


**Figure 7. 8** Results for a cross flow stack of 0.6 m side at  $P_{in}-P_{out}=3.12$  kPa ( $U_s=1$  cm/s) in the absence of membrane deformation: relative pressure maps for the CON (a) and DIL (b) channels, and TMP (c).

In each channel, pressure decreases linearly along the flow direction. The resulting TMP exhibits an anti-symmetric behaviour about the descending diagonal of the channel, attaining its lowest value at the bottom left corner and the highest value at the top right corner. Velocity maps are not shown since a flat distribution exists. Results obtained for the same cross flow stack of Figure 7. 8, but taking membrane deformation into account, are shown in Figure 7. 9. Note that, at the low velocity considered here, the behaviour of the channel regarded as a porous medium is purely Darcyan (see Figure 7. 5). The effects of membrane deformation are too small to be seen in the pressure maps (a), (b), and also the TMP is almost the same as in the undeformed case, Figure 7. 8(c). Figure 7. 9 (d) reports the equivalent height  $h$  of the concentrate channel, which exhibits an anti-symmetric trend about the channel's descending diagonal (as TMP), but attains its lowest value at the top right corner and its highest value at the bottom left corner (opposite to TMP), and changes by only about  $\pm 2\%$  with respect to the undeformed channel equivalent height ( $180 \mu\text{m}$ ). This modest membrane

deformation affects only slightly the distribution of the streamwise superficial velocity component ( $U_x$ ), which is shown in map (e) for the concentrate channel. This quantity exhibits a stratification in the direction orthogonal to the main flow direction, with a mean value ( $U_x$ ) of  $\sim 0.976$  cm/s (almost the same as in the undeformed case) and a variation of about  $\pm 3\%$ . For the sake of completeness, also the superficial velocity component along the direction orthogonal to the main flow ( $U_y$ ) is reported in map (f).  $U_y$  is  $\sim 4$  orders of magnitude lower than the streamwise component  $U_x$  and exhibits a symmetric distribution about the channel's descending diagonal. Finally, map (g) reports the interstitial velocity. This quantity presents relative variations of about  $\pm 3-4\%$ , similar to those observed for the superficial velocity, but a different distribution, which results from the combined variations of superficial velocity  $U_s$  and channel equivalent height  $h$ .

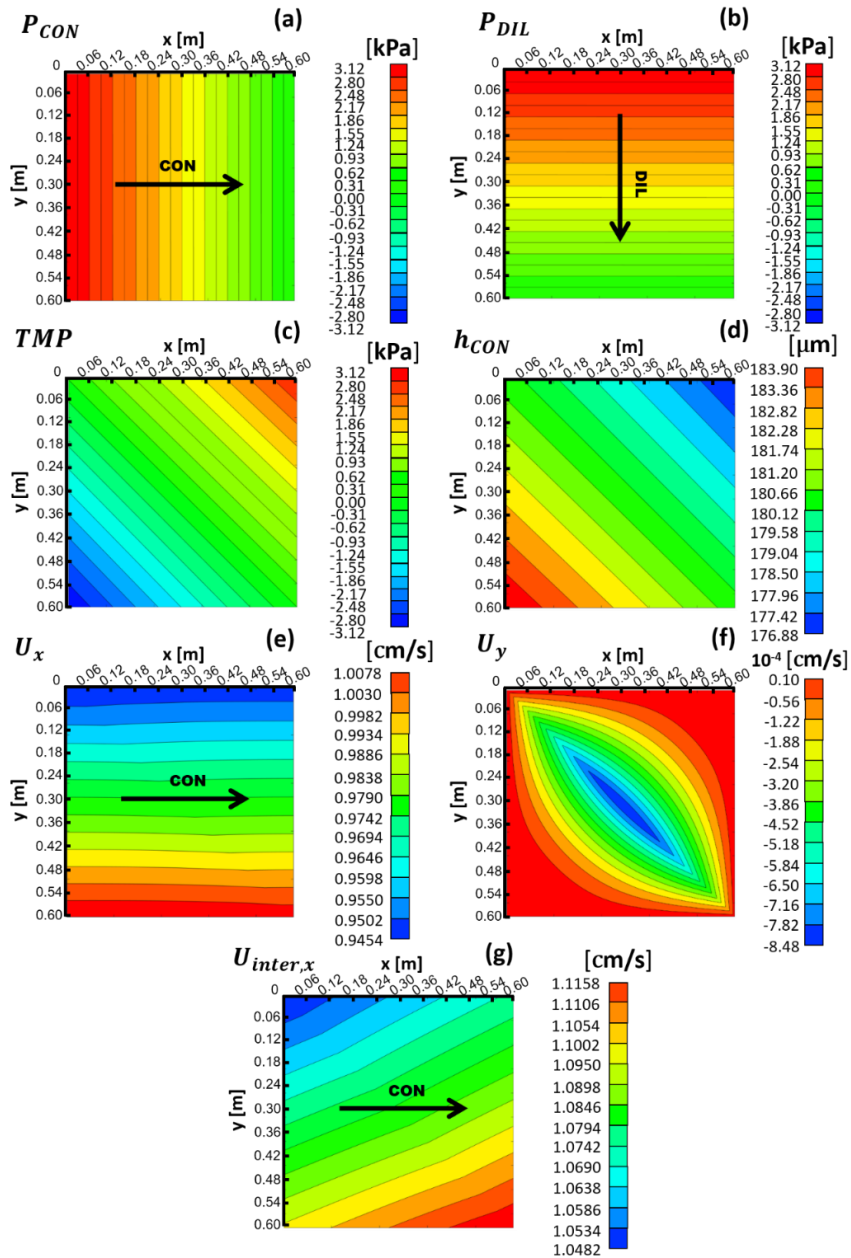


**Figure 7.9** Results for a cross flow stack of 0.6 m side at  $P_{in}-P_{out}=3.12$  kPa ( $U_s=1$  cm/s) in the presence of membrane deformation: relative pressure maps for the CON (a) and DIL (b) channels, TMP (c), and concentrate channel equivalent height (d), superficial velocity components along the x (e) and y (f) directions, and interstitial velocity along the x direction (g).

### 7.6.1.2 Higher velocity case ( $U_s=10$ cm/s)

The same cross flow configuration considered above, see Figures 7. 8 and 7. 9, was also investigated for an inlet pressure of 34.3 kPa, yielding  $U_s \approx 10$  cm/s along the main flow direction.

Results for the case in which membrane deformation effects are not taken into account are shown in Figure 7. 10. In the absence of membrane deformation, the pressure in the channels decreases linearly along the flow directions as in the lower velocity case, and TMP shows the same anti-symmetric behaviour about the descending diagonal of the channel.

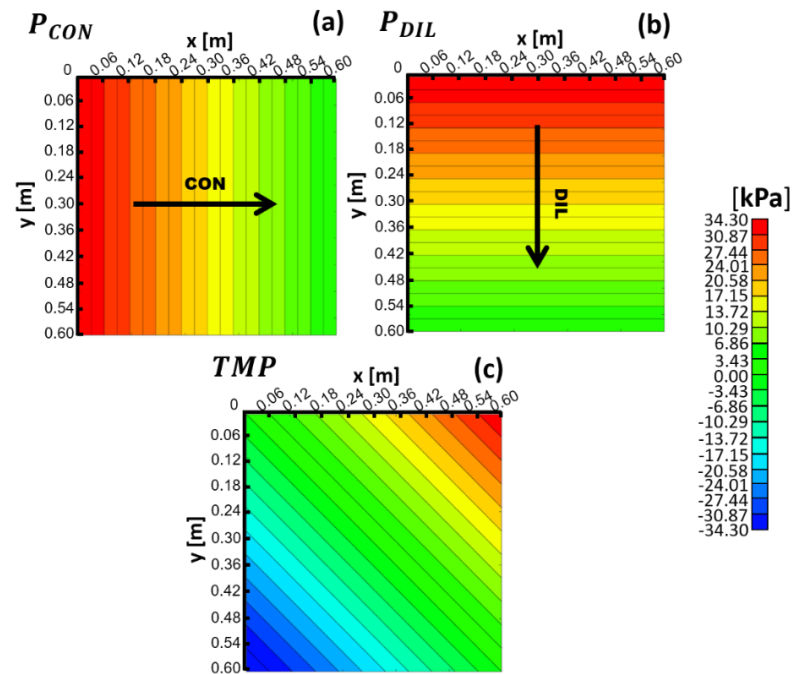


**Figure 7. 10** Results for a cross flow stack of 0.6 m side at  $P_{in}-P_{out}=34.3$  kPa ( $U_s=10$  cm/s) in the absence of membrane deformation: relative pressure maps for the CON (a) and DIL (b) channels, and TMP (c).

Results for the case in which membrane deformation effects are taken into account are reported in Figure 7. 11. In this case, the behaviour of the channel regarded as a porous medium is significantly non-Darcyan, as can be observed in Figure 7. 5.



Membrane deformation significantly affects the pressure distribution in the channels, as can be seen in maps (a) and (b). Specifically, the pressure distribution is not linear, but the pressure gradient increases as the fluid approaches the outlet regions. The TMP, map (c), is still anti-symmetric about the descending diagonal, but now the iso-TMP lines are no more parallel to this diagonal, but converge towards the bottom right corner.

Map (d) reports the concentrate channel's equivalent height  $h$ , which varies by about  $\pm 20\%$  with respect to that of the undeformed channel ( $180\ \mu\text{m}$ ). As shown in map (e), the higher membrane deformation (compared to the low velocity case) enhances the stratification along  $y$  of the superficial velocity  $U_x$ , with a mean value  $\langle U_x \rangle$  of  $9.82\ \text{cm/s}$  (1.8% reduction with respect to the undeformed case) and a maximum variation of +39% in the lower region of the stack (close to  $y=0.6\ \text{m}$ ) and -27% in the upper region (close to  $y=0$ ). Map (f) reports the secondary superficial velocity component along the direction orthogonal to the main flow direction ( $U_y$ , in the concentrate channel). This quantity is now only two-three orders of magnitude lower than the streamwise component  $U_x$  and exhibits a more complex distribution than in the lower velocity case of Figure 7.9 (f).

Finally, map (g) reports the interstitial velocity. It shows a similar trend as for the  $U_s = 1\ \text{cm/s}$  case, but presents much larger relative variations (about  $\pm 35\%$ ) and a much more non-uniform gradient.

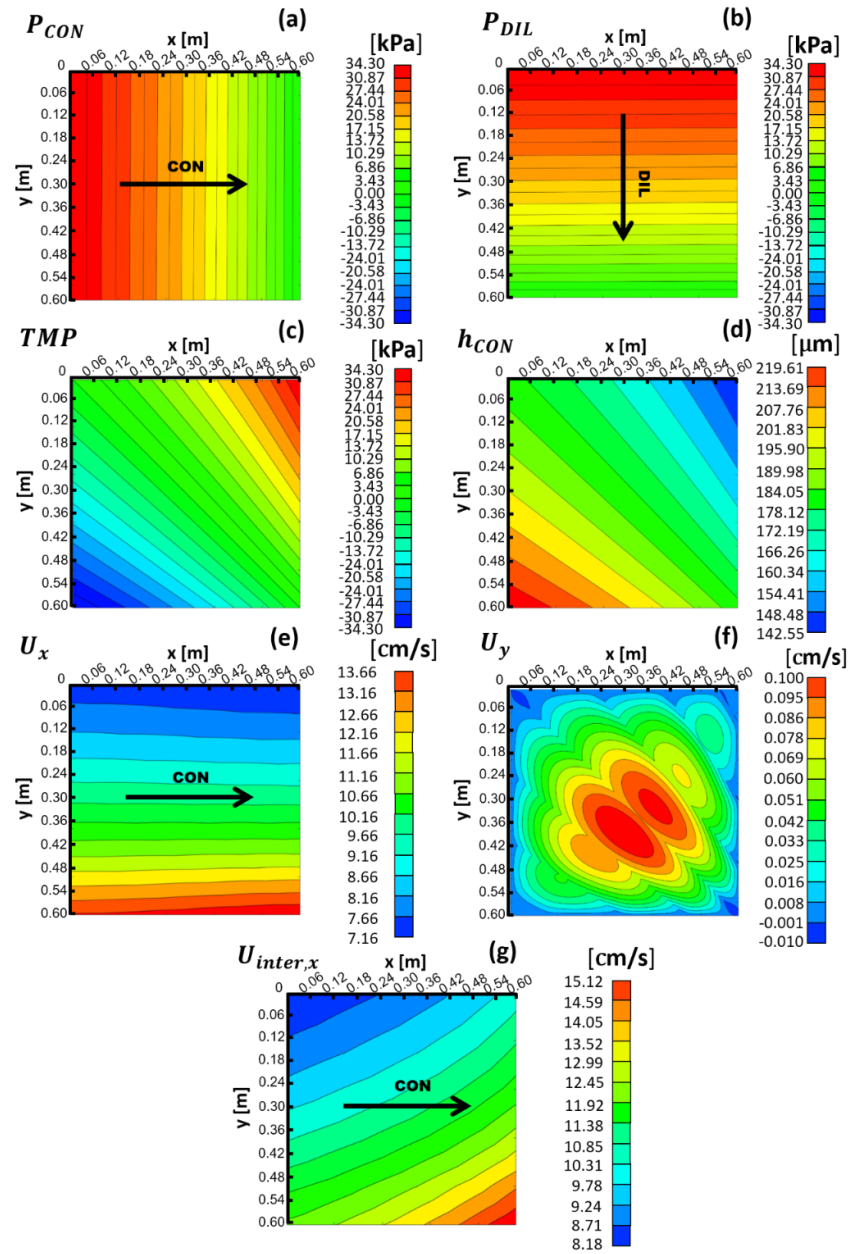


**Figure 7. 11** Results for a cross flow stack of 0.6 m side at  $P_m - P_{out} = 34.3$  kPa ( $U_s = 10$  cm/s) in the presence of membrane deformation: relative pressure maps for the CON (a) and DIL (b) channels, TMP (c), and concentrate channel equivalent height (d), superficial velocity components along the x (e) and y (f) directions, and interstitial velocity along the x direction (g).

For the same test case (cross flow at  $U_s \approx 10$  cm/s in the presence of membrane deformation), a better understanding of the behaviour of the different quantities in Figure 7. 11 can be achieved by considering the profiles of different variables along the main flow direction ( $x$  for the concentrate channel). Figure 7. 12 reports such profiles as obtained at two spanwise locations, namely,  $y=0.05$  m (upper region of the maps in Figure 7. 12) and  $y=0.55$  m (lower region of the same maps).

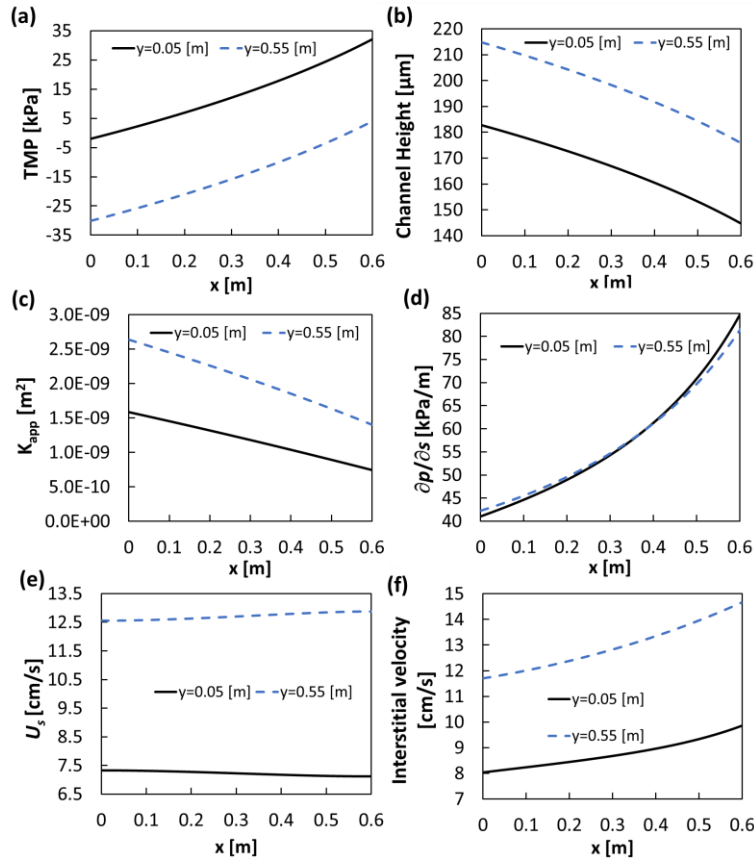


**Figure 7. 12** Results for a cross flow stack of 0.6 m side at  $P_m - P_{out} = 34.3$  kPa ( $U_s = 10$  cm/s) in the presence of membrane deformation: profiles of TMP (a), and concentrate channel equivalent height (b), apparent permeability (c), pressure gradient (d), superficial velocity (e) and interstitial velocity (f) along the  $x$  direction at  $y=0.05$  m and 0.55 m. Corresponding results would be obtained for the diluate channel.

The trans-membrane pressure TMP (graph a) increases along the  $x$  direction at both  $y$  locations, and varies from about zero to about 28 kPa along the line  $y=0.05$  m and from about -34 kPa to zero along the line  $y=0.55$  m. As a

consequence, the concentrate channel equivalent height, graph (b), decreases from  $\sim 180 \mu\text{m}$  to  $\sim 145 \mu\text{m}$ , *i.e.* from undeformed to compressed, at  $y=0.05 \text{ m}$ , and from  $\sim 215 \mu\text{m}$  to  $\sim 180 \mu\text{m}$ , *i.e.* from expanded to undeformed, at  $y=0.55 \text{ m}$ . Thus, the channel is compressed in the upper region of the stack and expanded in the lower one.

As shown in graph (c), the channel's apparent permeability decreases along the  $x$  direction following the trend of the channel's equivalent height, in accordance with Figure 7. 2. The streamwise pressure gradient, graph (d), increases along the flow direction  $x$  (by about the same amount at both  $y$  locations) to compensate for the decreasing permeability while the mass flow rate remains constant. The superficial velocity  $U_s$ , graph (e), can be calculated as the product of the pressure gradient by the channel's apparent permeability. As a result,  $U_s$  is lower at  $y=0.05 \text{ m}$  than at  $y=0.55 \text{ m}$ , since the pressure gradient is almost the same at the two locations while the permeability is lower in the upper-compressed region of the channel than in the lower-expanded one.

Graph (f) shows profiles of the interstitial velocity, *i.e.*  $U_s H/h$ . This quantity increases along the flow direction  $x$  at both  $y$  locations because the superficial velocity, graph (e), varies much less than the channel equivalent height, graph (b). Moreover, the interstitial velocity is lower at  $y=0.05 \text{ m}$  (upper, compressed region of the channel) than at  $y=0.55 \text{ m}$  (lower, expanded region) because the superficial velocity varies along  $y$  more than the equivalent channel height.

### 7.6.1.3) Pressure profiles for all cross flow cases

Pressure profiles along the  $x$  direction near the lower edge of the concentrate channel ( $y=0.6 \text{ m}$ ) are shown in Figure 7. 13 for  $U_s$  values of 1, 5 and 10 cm/s. Both the undeformed and the deformed conditions are considered.

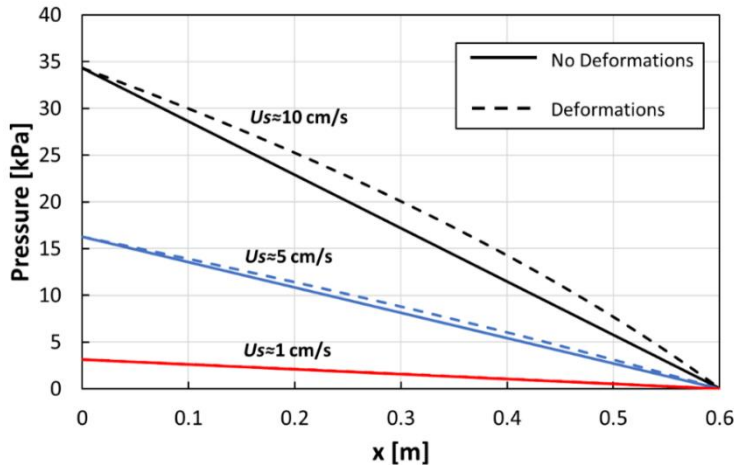


**Figure 7. 13** Pressure profiles along the x-direction near the lower edge ( $y=0.55$  m) of the concentrate channel for the cross flow configuration and  $\langle U_s \rangle = 1, 5$  and  $10$  cm/s. Profiles are reported both in the presence and in the absence of membrane deformation.

Note that the same pressure drops are imposed in undeformed and deformed conditions. The reduction of the mean fluid velocity  $\langle U_s \rangle$  under deformed conditions is small (1.8% for  $P_{in}-P_{out} = 34.3$  kPa, as mentioned in section 7.6.1.2, and practically negligible for lower pressure drops).

In the absence of deformation, pressure decreases linearly with  $x$ . At  $\langle U_s \rangle \approx 1$  cm/s, membrane deformation is small, as already discussed in Section 7.6.1.1, and does not significantly affect the pressure profile. As the velocity, and thus the TMP, increases, pressure profiles depart from the linear trend. Cubic polynomial functions are found to fit well the pressure profiles when membrane deformation becomes considerable.

### 7.6.2) Counter Flow arrangement

In the counter flow arrangement, only one pressure inlet value (34.3 kPa) was investigated. This pressure value is the same used for the cross flow case discussed in Section 7.6.1.2, where it yielded  $U_s \approx 10$  cm/s. In the present case, due to the different inlet-outlet geometry of inlet and outlet regions (see Figure 7.

7), the resulting superficial velocity in the absence of membrane deformation is  $U_s \approx 8.5$  cm/s (with  $s$  corresponding to  $x$ ). Note that pressure changes due to abrupt area variations, present in this configuration, are not taken into account by the model, but this is not a severe limitation because, at the present low velocity, these terms (proportional to the kinetic pressure  $\rho U_s^2 / 2$ ) are negligible compared to the distributed losses (order of 0.01 kPa, compared to the imposed inlet-outlet pressure variation of 34.3 kPa). This conclusion is also supported by the comparison with CFD results in Appendix C.

For the case of no membrane deformation, maps of pressure in both channels, TMP, and superficial velocity along the main flow direction in the concentrate channel are shown in Figure 7. 14. In each channel, inlet and outlet regions can be observed in which the geometry of the openings significantly affects the pressure distribution, see maps (a) and (b); outside these regions,  $p$  is mainly stratified with a uniform gradient along the flow direction  $x$ . Of course, the two distributions are identical apart from a reflection about the vertical midline. As a result, TMP in map (c) is anti-symmetric with respect to the vertical midline and ranges from negative to positive values spanning an interval twice that exhibited by pressure in each of the separate channels. The streamwise superficial velocity in the concentrate channel, map (d), exhibits complex details in the inlet and outlet regions and is about flat in the central region.

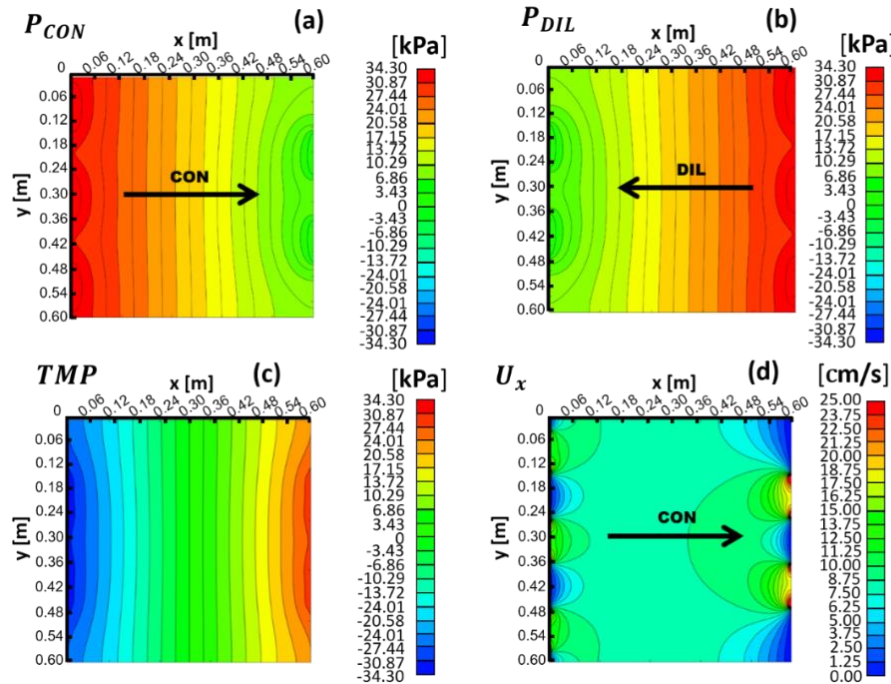


**Figure 7. 14** Results for a cross flow stack of 0.6 m side at  $P_{in}-P_{out}=34.3$  kPa ( $\langle U_s \rangle = 8.5$  cm/s) in the absence of membrane deformation: maps of relative pressure in the CON (a) and DIL (b) channels, TMP (c) and superficial velocity along the x direction in the concentrate channel (d).

Figure 7. 15 reports results obtained in the presence of membrane deformation. Pressure distributions (see maps (a) and (b)) show that the pressure gradient along  $x$  increases towards the outlet regions, where the channel is compressed. In each channel, a larger pressure non-uniformity is observed near the (two) outlet openings than near the (three) inlet ones. The non-uniform pressure gradient trends partially compensate when the pressure difference, i.e. TMP, is computed, yielding a more uniform gradient, map (c). Note that the shape of the TMP iso-lines reflects the geometry of the outlets more than that of the inlets. The channel equivalent height in the concentrate compartment exhibits the opposite trend as TMP, decreasing from its highest value of  $\sim 218$   $\mu\text{m}$  in the inlet region to its lowest value of  $\sim 144$   $\mu\text{m}$  in the outlet region. The superficial velocity distribution, map (e), is qualitatively similar to that obtained in the undeformed

case, Figure 7. 15 (d), but its mean value  $\langle U_s \rangle$  is now  $\sim 7.5$  cm/s,  $\sim 12\%$  lower than that computed in the undeformed case ( $\sim 8.5$  cm/s). This result can be attributed to the asymmetric behaviour of the hydraulic permeability, which varies less under compression than under expansion.

Finally, map (f) shows the interstitial velocity in the concentrate channel. This quantity changes slightly with respect to the superficial velocity without significantly fluid redistribution phenomena.

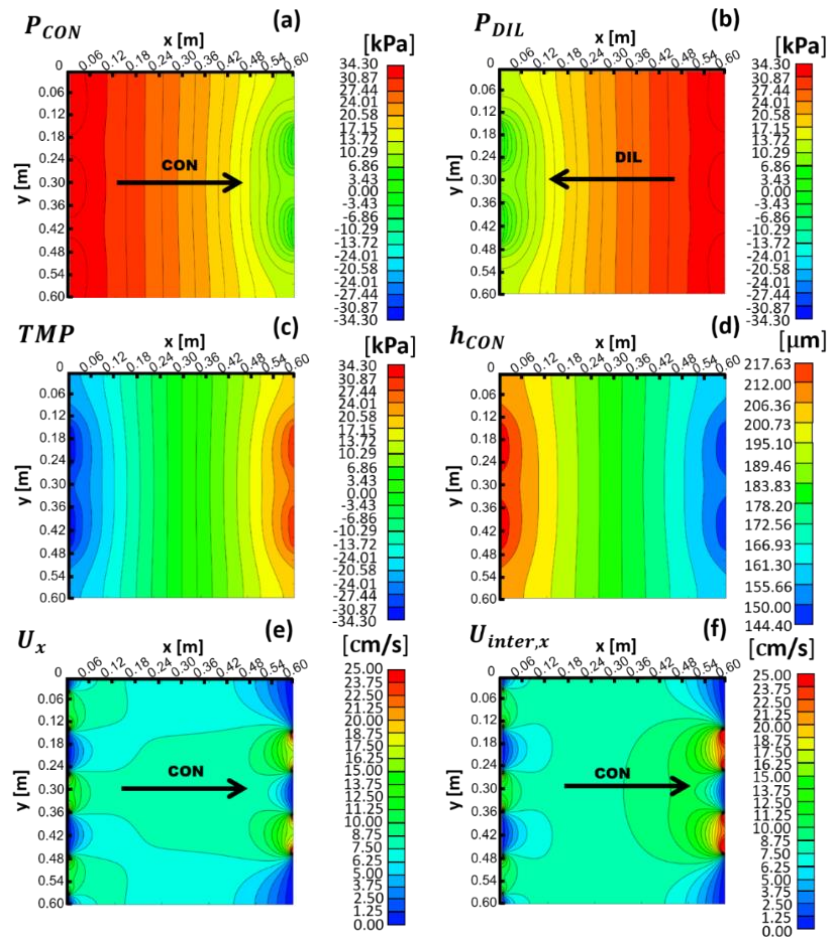


**Figure 7. 15** Results for a cross flow stack of 0.6 m side at  $\langle U_s \rangle = 7.5$  cm/s in the presence of membrane deformation: maps of relative pressure in the CON (a) and DIL (b) channels; TMP (c); and channel equivalent height (d), superficial velocity (e) and interstitial velocity (f) along the x direction in the concentrate channel.



## CHAPTER VIII

# IMPACT OF MEMBRANE DEFORMATION ON THE PERFORMANCES OF CROSS-FLOW ELECTRODIALYSIS UNITS FOR WATER DESALINATION

### 8.1) Introduction

Several modelling approaches have been proposed to describe RED and ED processes and predict the process's performances, spanning from simple models based on empirical correlations, to advanced comprehensive process models [114].

The first category consists of simplified models, where many assumptions are generally made and lumped parameters are considered for a preliminary design [196] or to study a very specific system relying on experimentally determined parameters [197].

The second category is represented by advanced models, which account for a number of non-ideal phenomena. Advanced models can also be divided into two sub-categories: theoretical and semi-empirical models. Theoretical models aim to describe key phenomena based on the solution of rigorous equations [198-202] (i.e. Nerst-Planck, or even the more complex Stefan-Maxwell equations). However, these models require a large amount of computational power and a number of thermodynamic and electrochemical parameters that cannot be easily determined. Thus, they are often applied for the analysis of simplified geometries or to study specific phenomena.

On the other hand, semi-empirical models are fast, comprehensive and robust simulation tools, based on some empirical information such as the membrane's

properties (e.g., transport numbers, ohmic resistance, salt permeability, osmotic permeability, etc.) and require a lower computational effort.

Thus, they are more suitable for the investigation of channels with complex configurations and for simulations of entire stack operation.

Some advanced semi-empirical models are based on a multi-scale approach treating the lower scale fluid flow and mass transfer phenomena (Darcy friction factor, Sherwood number and, thus, concentration polarization) by means of empirical information [143, 203-205] or small-scale theoretical analysis, e.g. by means of Computational Fluid Dynamics tools [121, 129, 165, 206].

Semi-empirical models can be based either on lumped or distributed parameters. The former have limited prediction capabilities, while the latter models are more accurate, but at the cost of a large computational effort. A few 2-D models have been developed for the study of (R)ED systems [194]. In particular, a 2-D approach allows studying different stack configurations beside the classical parallel-flow and counter-flow arrangements. Moreover, neither simplified or advanced models have been presented to account for the effects of membrane/channel deformation, induced by a transmembrane pressure (TMP) difference between fluid channels, on the ED process' performance. In the following chapter, a novel semi-empirical, multi-scale 2-D model is presented to address the performance of ED cross-flow configurations in the presence of local membrane deformations. The model is combined with the method presented in the previous chapter (VII) to take into account the fluid flow and the channel height distributions induced by local membrane deformations.

## **8.2) 2-D process simulator of ED units: model and methods**

The 2-D process model which was developed allows for the investigation of ED units in the presence and in the absence of local membrane deformation in different stack configurations, e.g. parallel-, counter- and cross- flow. In particular, the model simulates transport and electrochemical phenomena occurring in ED units, computing the distribution of the main variables in a cell pair ( and thus in a stack) and assessing process' performance, e.g. the energy consumption.

The 2-D process model is based on a multi-scale approach and employs results presented in Chapters V, VI and the fluid redistribution algorithm introduced in Chapter VII. Specifically:

- (i) at the lowest scale, CFD results regarding the friction factor, Sherwood number and channel equivalent height as functions of the transmembrane pressure (TMP) in the fluid channels are employed to evaluate the overall pressure drop, polarization phenomena and electrical channel resistances.
- (ii) at a higher scale, considering the entire channel dimension; mass balances, transport phenomena, solutions properties and electrical parameters are addressed in a single repeating unit of the ED stack, i.e. the cell pair (see, Figure 5. 1), taking into account flow redistribution in channels with local deformation.
- (iii) Finally, at the highest scale, the performances of ED stacks are predicted for any number of cell pairs, taking into account the resistance of the electrode compartments.

The following assumptions are used in the model:

1. Salt solutions of NaCl are simulated;
2. Steady-state regime is assumed;
3. All cell pairs behave in the same way and are subject to the same constant voltage drop;
4. Limiting current density conditions are not considered;
5. The effect of parasitic currents via manifolds is not considered;
6. Pressure drops in the manifolds are neglected.

### **8.2.1) Mass balances and fluxes**

In a two-dimensional approach, the distribution of the variables is evaluated over the length ( $L$ ) and width ( $W$ ) of a channel. Considering a cross-flow arrangement, as shown in Figure 8. 1, the concentrate solution (CON) may be assumed to flow ideally from the left to the right side of its channel, parallel to

the  $x$ -axis, while the diluate solution (DIL) may be assumed to flow from the top to the bottom of its channel ideally parallel to the  $y$ -axis.

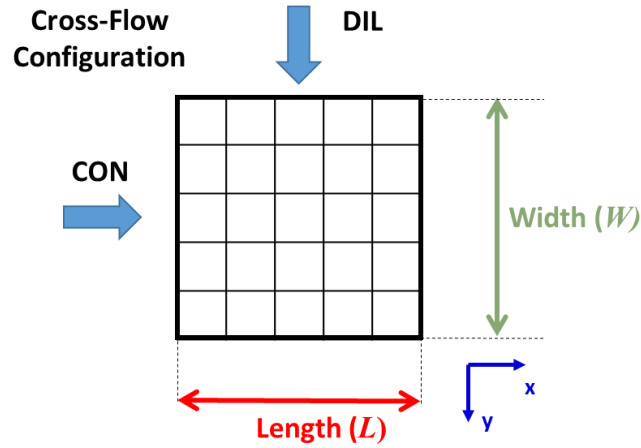


**Figure 8. 1** Computational domain of the developed model for a 2-D cross-flow configuration.

Under the assumption of constant solution density, differential mass balances for the salt and water species in the concentrate and diluate channel can be written as:

$$\begin{aligned} \frac{\partial(Q^{CON}(x,y)C^{CON}(x,y))}{\partial x \partial y} &= +J_{SALT}^{TOT}(x,y); \\ \frac{\partial(Q^{CON}(x,y))}{\partial x \partial y} &= +J_{WATER}^{TOT}(x,y); \\ \frac{\partial(Q^{DIL}(x,y)C^{DIL}(x,y))}{\partial x \partial y} &= -J_{SALT}^{TOT}(x,y) \\ \frac{\partial(Q^{DIL}(x,y))}{\partial x \partial y} &= -J_{WATER}^{TOT}(x,y) \end{aligned} \quad (8.1-4)$$

where  $Q^{CON}(x,y)$  and  $Q^{DIL}(x,y)$  are the flow rates of the CON and DIL solutions;  $C^{CON}(x,y)$  and  $C^{DIL}(x,y)$  are the salt concentrations in the CON and DIL solutions;  $J_{SALT}^{TOT}(x,y)$  and  $J_{WATER}^{TOT}(x,y)$  are the total transmembrane salt and water fluxes, respectively, which pass through the two membranes.

The total transmembrane water flux accounts for both osmotic  $J_{WATER}^{OSM}(x, y)$  and electro-osmotic  $J_{WATER}^{E.OSM}(x, y)$  transport mechanisms:

$$J_{WATER}^{TOT}(x, y) = J_{WATER}^{OSM}(x, y) + J_{WATER}^{E.OSM}(x, y) \quad (8.5)$$

The osmotic term describes the water transport due to the interfacial osmotic pressure gradient between concentrate and diluate solutions over the membranes:

$$J_{WATER}^{OSM}(x, y) = L_{p,AEM}(\pi_{CEM}^{CON}(x, y) - \pi_{AEM}^{DIL}(x, y)) + L_{p,CEM}(\pi_{CEM}^{CON}(x, y) - \pi_{AEM}^{DIL}(x, y)) \quad (8.6)$$

where  $L_{p,IEM}$  is the water permeability coefficients of the generic Ion Exchange Membrane (IEM), i.e. either the cation- or the anion-exchange membrane (CEM or AEM), whose value is usually given in ml/(m<sup>2</sup> h bar), but in SI units is m<sup>3</sup>/(m<sup>2</sup> s Pa).  $\pi_{IEM}^{SOL}(x, y)$  is the osmotic pressure related to the interfacial solution (SOL) concentration at the generic IEM membrane. Osmotic pressure can be calculated by employing the van't Hoff law [165], in which osmotic coefficients can be accurately estimated by Pitzer's correlations [207, 208]. However, in the present model, the osmotic coefficients were considered to be unitary.

The second transport mechanism, i.e. electro-osmosis, refers to the water transport coupled with the ions' movement. The electro-osmotic term can be expressed as:

$$J_{WATER}^{E.OSM}(x, y) = n_h J_{SALT}^{TOT}(x, y) \frac{M_w}{\rho_w} \quad (8.7)$$

Where  $n_h$  is the hydration number, here assumed to be equal to 7;  $J_{SALT}^{TOT}(x, y)$  is the total salt flux through the membranes;  $M_w$  and  $\rho_w$  are the water molecular weight and density.

As far as the total salt flux  $J_{SALT}^{TOT}(x, y)$  is concerned, it accounts for conductive flux  $J_{Cond.}^{TOT}(x, y)$  and diffusive  $J_{Diff.}^{TOT}(x, y)$  flux:

$$J_{SALT}^{TOT}(x, y) = J_{Cond.}^{TOT}(x, y) + J_{Diff.}^{TOT}(x, y) \quad (8.8)$$

The conductive flux represents the main salt transport contribution, which is proportional to the local ionic current density  $i_c$ . For monovalent ions, under the

assumption of perfect membrane perm-selectivity, the  $\text{Na}^+$  ions flux ( $J_{Cond.}^{\text{Na}^+}(x, y)$ ) through a CEM, or the  $\text{Cl}^-$  ions flux ( $J_{Cond.}^{\text{Cl}^-}(x, y)$ ) through an AEM, can be written as:

$$J_{Cond.}^{\text{Na}^+ \text{ or } \text{Cl}^-}(x, y) = \frac{i_c(x, y)}{z_{\text{Na}^+ \text{ or } \text{Cl}^-} F_{Faraday}} \quad (8.9)$$

where  $F_{Faraday}$  is the Faraday constant,  $i_c(x, y)$  is the local current density and  $z_{\text{Na}^+ \text{ or } \text{Cl}^-}$  is the ion valence, i.e. +1 and -1 for  $\text{Na}^+$  and  $\text{Cl}^-$ , respectively. In a cell pair the total salt conductive flux coincides with the  $\text{Na}^+$  or  $\text{Cl}^-$  ion flux, thus  $J_{Cond.}^{TOT}(x, y) = J_{Cond.}^{\text{Na}^+}(x, y) = -J_{Cond.}^{\text{Cl}^-}(x, y)$ .

The diffusive flux describes the salt back-diffusion through the membrane due to the concentration difference between the channels. The diffusive flux through a single membrane can be written as:

$$J_{Diff}^{IEM}(x, y) = \frac{D_{Salt}^{IEM}}{H^{IEM}} (C_{IEM}^{CON}(x, y) - C_{IEM}^{DIL}(x, y)) \quad (8.10)$$

where  $D_{Salt}^{IEM}$  is the salt diffusion permeability in a generic IEM membrane of a thickness  $H^{IEM}$ .  $C_{IEM}^{SOL}(x, y)$  is the generic salt concentration at the membrane interface, solution side. As for the conductive flux, two diffusive fluxes, one at the AEM and one at the CEM, have to be taken into account, thus  $J_{Diff}^{TOT}(x, y) = J_{Diff}^{AEM}(x, y) + J_{Diff}^{CEM}(x, y)$ .

### 8.2.2) Electric variables, ohmic and non-ohmic resistances

The overall voltage drop over a cell pair ( $V_{cp}$ ) can be expressed as:

$$V_{cp} = \eta(x, y) + R_{TOT}(x, y) i_c(x, y) \quad (8.11)$$

The term  $\eta(x, y)$  is the non-ohmic voltage drops and  $R_{TOT}(x, y) i_c(x, y)$  is the ohmic losses in the cell pair.  $R_{TOT}$  is the total areal resistance of the cell pair, that can be expressed as

$$R_{TOT}(x, y) = R^{CEM}(x, y) + R^{AEM}(x, y) + R^{DIL}(x, y) + R^{CON}(x, y) \quad (8.12)$$

where  $R^{CEM}(x, y)$  and  $R^{AEM}(x, y)$  are the areal electrical resistances of the membranes;  $R^{DIL}(x, y)$  and  $R^{CON}(x, y)$  are the areal electrical resistances of the channels.

By following the results of the experimental measurements performed by Galama et al. [209],  $R^{IEM}(x, y)$  can be approximated as:

$$R^{IEM}(x, y) = a^{IEM} + b^{IEM} (C_{IEM}^{DIL}(x, y))^{-c^{IEM}} \quad (8.13)$$

where  $a^{IEM}$ ,  $b^{IEM}$ ,  $c^{IEM}$  are constants, which can be empirically determined. In the present simulations,  $a$  is equal to 1.89 and 1.77  $\Omega \text{ cm}^2$ , for the CEM and AEM membranes, respectively. These values are the areal membrane resistances measured at the standard concentration of 0.5M NaCl. Moreover,  $b$  and  $c$  are equal to  $7 \times 10^{-3}$  and 1.25, for both AEM and CEM membranes. The constants for AEM and CEM membranes were taken from [165].  $C_{IEM}^{DIL}(x, y)$  is the diluate concentration at the interface of a generic membrane.

With regard to the channel resistance, it can be estimated by:

$$R^{SOL}(x, y) = \frac{h^{SOL}(x, y)}{\kappa^{SOL}(x, y)} \quad (8.14)$$

where  $h^{SOL}(x, y)$  is the equivalent channel thickness (defined in Section 7.2) and  $\kappa^{SOL}(x, y)$  is the electrical conductivity of the solution, which is a function of the local salt concentration (here estimated by using a correlation proposed in [129]). Note that,  $h^{SOL}$  accounts for the deformed channel height in the case of membrane deformation, while it corresponds to the equivalent undeformed channel height in the absence of local deformations. In Eq. (8.14),  $h^{SOL}$  takes into account the so-called *shadow factor*  $f_{shadow}$ , which estimates the increase of the channel resistance due to the presence of spacer filaments or membrane profiles. In general, the  $f_{shadow}$  is simply calculated as the reciprocal of the channel volume porosity.

In the present chapter, OCF profiled membranes with  $P/H=8$  (see first row of Figure 5. 9) like those of chapters V, VI and VII are simulated. For the sake of simplicity, OCFs were considered non-conductive for the calculation of  $f_{shadow}$

. This assumption is well justified by the fact that the present OCF geometry is characterized by a channel porosity close to 0.9, thus the filaments occupy a very small portion of the channels.

The non-ohmic voltage drop  $\eta(x, y)$  (Eq.(8.11)), given by the back electromotive force originated from the salt concentration gradient over the permselective membranes, can be divided into two contributions associated with (i) the concentration gradient between the two solutions bulks  $\varphi(x, y)$  and (ii) its increment due to concentration polarization phenomena  $\eta_{BL}(x, y)$ .

Therefore, the total non-ohmic voltage drop can be written as:

$$\eta(x, y) = \varphi(x, y) + \eta_{BL}(x, y) \quad (8.15)$$

The first contribution for a single membrane IEM is calculated as:

$$\varphi_{IEM}(x, y) = (\alpha_{IEM}) \frac{RT}{F_{Faraday}} \ln \left( \frac{\gamma^{CON}(x, y) C_{Bulk}^{CON}(x, y)}{\gamma^{DIL}(x, y) C_{Bulk}^{DIL}(x, y)} \right) \quad (8.16)$$

where  $\alpha_{IEM}$  is the perm-selectivity of a generic membrane, which is correlated to the ability of the membrane to block the passage of co-ion through itself (assumed constant in the model);  $T$  is the temperature;  $R$  is the gas constant;  $\gamma^{CON}$  and  $\gamma^{DIL}$  are the salt activity coefficients in the CON and DIL solutions, which depend on the solution bulk concentration ( $C_{Bulk}^{CON}(x, y)$  and  $C_{Bulk}^{DIL}(x, y)$ ). Taking into account both AEM and CEM membranes, one has:  $\varphi(x, y) = \varphi_{AEM}(x, y) + \varphi_{CEM}(x, y)$ .

As far as the concentration polarization phenomena are concerned, they are caused by the different kinetics of transport in solutions and in membranes. In particular, polarization phenomena can be defined as: “the concentration profile that has a higher (or lower) level of solute nearest to the upstream membrane surface compared with the more-or-less well-mixed bulk fluid far from the membrane surface” [164]. In the case of the ED process, the resulting increase of salt concentration at the membrane surface in the concentrate channel and the reduction of the salt concentration at the membrane surface in the diluate channel cause a reduction of the process’ performance.



The non-ohmic voltage drop due to concentration polarization can be calculated as the sum of the contributions of the four boundary layers in a cell pair:

$$\eta_{BL}(x, y) = \eta_{AEM}^{CON}(x, y) + \eta_{CEM}^{CON}(x, y) + \eta_{AEM}^{DIL}(x, y) + \eta_{AEM}^{DIL}(x, y) \quad (8.17)$$

where the voltage drop  $\eta_{IEM}^{SOL}(x, y)$  at the generic IEM membrane, i.e. AEM or CEM, in contact with the generic solution SOL (CON or DIL), can be calculated as:

$$\eta_{IEM}^{SOL}(x, y) = -\alpha_{IEM} \frac{RT}{F_{Faraday}} \ln(\theta_{IEM}^{SOL}(x, y)) \quad (8.18)$$

where  $\theta_{IEM}^{SOL}(x, y)$  is the so-called polarization coefficient determined at the membrane-solution interface as:

$$\theta_{IEM}^{CON}(x, y) = \frac{C_{Bulk}^{CON}(x, y)}{C_{IEM}^{CON}(x, y)} \quad \text{and} \quad \theta_{IEM}^{DIL}(x, y) = \frac{C_{IEM}^{DIL}(x, y)}{C_{Bulk}^{DIL}(x, y)} \quad (8.19)$$

where  $C_{Bulk}^{CON}(x, y)$  and  $C_{Bulk}^{DIL}(x, y)$  are the CON and DIL bulk concentrations,  $C_{IEM}^{CON}(x, y)$  and  $C_{IEM}^{DIL}(x, y)$  are the solution concentrations at the generic IEM membrane-solution SOL (CON or DIL) interface. Note that,  $\theta_{IEM}^{CON}(x, y)$  and  $\theta_{IEM}^{DIL}(x, y)$  are always smaller than one. Moreover, the effects of polarization on the activity coefficients are neglected. Introducing the *Sherwood* number as [129]:

$$Sh_{IEM}^{SOL}(x, y) = \left| \frac{(J_{Diff}^{IEM}(x, y) + 0.5 \times J_{Cond.}^{TOT}(x, y)) 2H^{SOL}}{(C_{Bulk}^{SOL}(x, y) - C_{IEM}^{SOL}(x, y)) D_{Salt}^{SOL}(x, y)} \right| \quad (8.20)$$

where  $H^{SOL}$  is the channel thickness of a generic solution (SOL) and  $D_{Salt}^{SOL}(x, y)$  is the salt diffusivity in the generic solution SOL. It has to note that the term  $(J_{Diff}^{IEM}(x, y) + 0.5 \times J_{Cond.}^{TOT}(x, y))$  represents the diffusive salt flux in the generic solution SOL in contact with the generic membrane IEM, which can be found by taking into account the flux continuity at the solution-membrane interface.

Therefore, the polarization coefficients for the two solutions can be calculated by [129]:

$$\theta_{IEM}^{CON}(x, y) = 1 / \left[ 1 + \frac{\left( J_{Diff}^{IEM}(x, y) + 0.5 \times J_{Cond.}^{TOT}(x, y) \right) 2H^{CON}}{Sh_{IEM}^{CON}(x, y) C_{Bulk}^{CON}(x, y) D_{Salt}^{CON}(x, y)} \right] \quad (8.21)$$

$$\theta_{IEM}^{DIL}(x, y) = 1 - \frac{\left( J_{Diff}^{IEM}(x, y) + 0.5 \times J_{Cond.}^{TOT}(x, y) \right) 2H^{DIL}}{Sh_{IEM}^{DIL}(x, y) C_{Bulk}^{DIL}(x, y) D_{Salt}^{DIL}(x, y)} \quad (8.22)$$

Thus, the voltage drop  $\eta_{IEM}^{SOL}(x, y)$  of Eq. 8.18 can be obtained.

### 8.2.3) Stack simulation

In the ED system, a potential voltage drop  $V_{Applied}$  is applied by a power supply to the electrodes in order to obtain the desired desalination degree of the diluate (DIL) feed solution. In the model, the potential voltage drop  $V_{Applied}$  is assumed to be constant (i.e. independent of  $x$  and  $y$ ). At the stack level, the number of cell pairs and the electrode compartments have to be taken into account in order to simulate the whole electrical circuit.

The local generated current density  $i_c(x, y)$  can be expressed as (Kirchhoff's second law):

$$i_c(x, y) = \frac{V_{Applied} - \eta(x, y) N_{cp}}{R_{blank} + R_{TOT}(x, y) N_{cp}} \quad (8.23)$$

where  $V_{Applied}$  is the voltage drop applied by a power supply to the electrodes,  $N_{cp}$  is the total number of cell pairs and  $R_{blank}$  is the electric resistance of the electrode compartments.

The total power consumption of the process  $P_{el}$  can be expressed as:

$$P_{el} = V_{Applied} I + \frac{\Delta p_{tot}^{CON} Q_{TOT.av}^{CON} + \Delta p_{tot}^{DIL} Q_{TOT.av}^{DIL}}{\eta_{Pump}} \quad (8.24)$$

where  $I$  is the overall current calculated as the integral of the current density ( $i_c$ ) over the active area of the membrane.  $\Delta p_{tot}^{CON}$  and  $\Delta p_{tot}^{DIL}$  are the total pressure

drops in the CON and DIL channels and  $\eta_{Pump}$  is the efficiency of the pump.  $Q_{TOT,av}^{CON}$  and  $Q_{TOT,av}^{DIL}$  are the average solution flow rates calculated as the integral of the flow rate over one channel and multiplied by the total number of cell pairs ( $N_{cp}$ ).

The distributed pressure drops of a generic solution SOL are evaluated as:

$$\Delta p_{dist.}^{Sol} = \int_0^L \int_0^W f_{Darcy}(x, y) \frac{1}{2H^{SOL}} \rho^{SOL} \frac{(U^{SOL}(x, y))^2}{2} dx dy \quad (8.25)$$

where,  $f_{Darcy}(x, y)$  is the Darcy friction coefficient and  $U^{SOL}(x, y)$  is the *superficial velocity*. These quantities were already introduced in Chapter VI.  $\rho^{SOL}$  is the density of the generic solution. Please note that, in the simulations where membrane deformation is taken into account,  $\Delta p_{dist.}^{Sol}$  is simply the difference between the imposed boundary pressure at the inlet ( $P_{in}$ ) and outlet ( $P_{outlet}$ ) of the generic channel, as described in Chapter VII. Therefore, Eq. (8.25) is evaluated only in the case of undeformed channels.

Finally, two other important parameters can be introduced to quantify the efficiency of an ED stack:

- 1) The energy consumption per unit volume of product  $E_{spec}$  (kWh/m<sup>3</sup>):

$$E_{spec} = \frac{P_{el}}{Q_{TOT,OUTLET}^{DIL}} \quad (8.26)$$

where  $Q_{TOT,OUTLET}^{DIL}$  is the overall diluate outlet flowrate, calculated as the mean flow rate at the outlet of the diluate channel and multiplied by the total number of cell pairs ( $N_{cp}$ ).

- 2) The apparent product flux  $J_p$  (l/m<sup>2</sup> h):

$$J_p = \frac{Q_{TOT,OUTLET}^{DIL}}{2LWN_{cp}} \quad (8.27)$$

which can be useful in order to calculate the area required to obtain a certain flowrate of desalinated water.

For the sake of clarity, Table 8. 1 summarises all the constants employed for membrane and channels features. Moreover, the correlations used for the physical and transport properties of NaCl solutions are reported in the Appendix D.

**Table 8. 1** Values of the quantities employed in the model.

Quantity	Value	Unit
Nominal channel height (DIL and CON)	$200 \times 10^{-6}$	m
$R_{\text{blank}}$	$2 \times 10^{-3}$ [210]	$\Omega \text{ m}^2$
Membrane thickness (AEM and CEM)	$120 \times 10^{-6}$	m
Salt permeability (AEM and CEM)	$4e^{-12}$ [210]	$\text{m}^2/\text{s}$
AEM permselectivity (constant)	0.97 [210]	-
CEM permselectivity (constant)	0.98 [210]	-
Water permeability (AEM and CEM)	8 [210]	$\text{ml}/\text{m}^2 \text{ h bar}$
$f_{\text{Shadow}}$	1.11	-

### 8.3) Algorithm of solution

In order to solve Eqs. (8.1-23), an approach similar to that presented in Section 7.4 was adopted. Each of the two coupled CON and DIL channels, of overall size  $L \times W$ , is divided into  $N_{\text{Block}}^x \times N_{\text{Block}}^y$  rectangular blocks of size  $\Delta x = L / N_{\text{Block}}^x$ ,  $\Delta y = W / N_{\text{Block}}^y$ .

With reference to the computational molecules presented in Figure 7. 1, the mass balances (Eqs. (8.1-4)) at the generic  $i, j$  block are discretized as:

$$\begin{aligned}
& C_{\text{Bulk};i,j+1}^{\text{CON};i,j} \cdot Q_{i,j+1}^{\text{CON};i,j} + C_{\text{Bulk};i+1,j}^{\text{CON};i,j} \cdot Q_{i+1,j}^{\text{CON};i,j} + \\
& -C_{\text{Bulk};i,j}^{\text{CON};i,j-1} \cdot Q_{i,j}^{\text{CON};i,j-1} - C_{\text{Bulk};i,j}^{\text{CON};i-1,j} \cdot Q_{i,j}^{\text{CON};i-1,j} + J_{\text{SALT};i,j}^{\text{TOT}} \cdot \Delta x \cdot \Delta y = 0 \\
& Q_{i,j+1}^{\text{CON};i,j} + Q_{i+1,j}^{\text{CON};i,j} - Q_{i,j}^{\text{CON};i,j-1} - Q_{i,j}^{\text{CON};i-1,j} + J_{\text{WATER};i,j}^{\text{TOT}} \cdot \Delta x \cdot \Delta y = 0 \\
& C_{\text{Bulk};i,j+1}^{\text{DIL};i,j} \cdot Q_{i,j+1}^{\text{DIL};i,j} + C_{\text{Bulk};i+1,j}^{\text{DIL};i,j} \cdot Q_{i+1,j}^{\text{DIL};i,j} + \\
& -C_{\text{Bulk};i,j}^{\text{DIL};i,j-1} \cdot Q_{i,j}^{\text{DIL};i,j-1} - C_{\text{Bulk};i,j}^{\text{DIL};i-1,j} \cdot Q_{i,j}^{\text{DIL};i-1,j} - J_{\text{SALT};i,j}^{\text{TOT}} \cdot \Delta x \cdot \Delta y = 0 \\
& Q_{i,j+1}^{\text{DIL};i,j} + Q_{i+1,j}^{\text{DIL};i,j} - Q_{i,j}^{\text{DIL};i,j-1} - Q_{i,j}^{\text{DIL};i-1,j} - J_{\text{WATER};i,j}^{\text{TOT}} \cdot \Delta x \cdot \Delta y = 0 \quad (8.28-31)
\end{aligned}$$

Superscripts indicate the grid block from which the flow exits, while subscripts indicate the block which the flow is entering. As in Chapter VII, signs are in accordance with convention I of Section 7.3: flow rates exiting a computational block are assumed positive, while flow rates entering a block are assumed negative.

Under the assumption of negligible components of the velocity along the direction orthogonal to the main flow direction, and taking into account the flow configuration of Figure 8. 1, Eqs.(8.28-31) can be rewritten as:

$$\begin{aligned}
 C_{Bulk;i,j+1}^{CON;i,j} \cdot Q_{i,j+1}^{CON;i,j} - C_{Bulk;i,j}^{CON;i,j-1} \cdot Q_{i,j}^{CON;i,j-1} + J_{SALT;i,j}^{TOT} \cdot \Delta x \cdot W &= 0 \\
 Q_{i,j+1}^{CON;i,j} - Q_{i,j}^{CON;i,j-1} + J_{WATER;i,j}^{TOT} \cdot \Delta x \cdot W &= 0 \\
 C_{Bulk;i+1,j}^{DIL;i,j} \cdot Q_{i+1,j}^{DIL;i,j} - C_{Bulk;i,j}^{DIL;i-1,j} \cdot Q_{i,j}^{DIL;i-1,j} - J_{SALT;i,j}^{TOT} \cdot \Delta y \cdot L &= 0 \\
 Q_{i+1,j}^{DIL;i,j} - Q_{i,j}^{DIL;i-1,j} - J_{WATER;i,j}^{TOT} \cdot \Delta y \cdot L &= 0 \quad (8.32-35)
 \end{aligned}$$

This assumption is justified even in the presence of considerable membrane deformations, as shown by the results reported in Section 7.6.1.2. In particular, the secondary superficial velocity component along the direction orthogonal to the main flow direction was still three orders of magnitude lower than the streamwise component.

With regard to Eqs. (8.5-23), these are algebraic equations that are evaluated at each grid block taking into account the local value of the solution concentrations.

To couple Eqs. (8.1-4) and (8.5-23), thus determining the steady-state distributions of all variables for a chosen ED unit configuration, an iterative procedure was employed. The algorithm can be divided into three main steps:

- I. The flow and channel height distributions are calculated by using the simplified (Darcyan) model of Section 7.4.2 and employing Eq. (B1) of Annex B, which gives the dependence of the channel height as function of the TMP values. Velocities up to 5 cm/s were investigated, which do not require the more accurate, yet more complex non-Darcyan model (Section 7.4.3).

- II. All the other distributed variables are then computed by the ED process model solving Eqs. (8.5-23) and (8.32, 8.34) for the chosen value of the applied voltage and of the number of cell pairs.
- III. Flow rates of step I are adjusted taking into account the transmembrane water fluxes calculated in step II.
- IV. Finally, the process' performances are evaluated by solving Eqs. (8.24-8.27)

Step I is performed following the algorithm previously illustrated in Figure 7. 4. Then Steps II and III are iteratively solved until a desired convergence criterion is attained, as depicted by the flow chart of Figure 8. 2.

First, uniform block concentrations, equal to the inlet values ( $C_{Inlet}^{DIL}, C_{Inlet}^{CON}$ ) are imposed in both channels at each grid block, and the same values are also assumed for the membrane-solution interfacial concentrations (no concentration polarization).

Then, the solution's properties and activity coefficients are calculated by equations in Annex 1 [129]. Consequently, channels' ohmic resistances are evaluated by Eq. (8.14), taking into account the channel height distribution of step I. Moreover, membranes resistances are calculated by Eq. (8.13) and thus the cell pair resistance can be obtained by Eq. (8.12). Then, the non-ohmic voltage drop  $\varphi(x, y)$  is evaluated by Eq. (8.16) at each grid block. Note that the voltage drop due to concentration boundary layers  $\eta_{BL}$  and also  $\varphi(x, y)$  are zero at the first iteration, since bulk and interfacial concentrations are the same. Consequently, the local current density  $i_c$  can be found by Eq. (8.23).

By knowing the current density and solution concentrations, total salt and water fluxes are calculated using Eqs. (8.5-10). Thus, polarization factor coefficients and  $\eta_{BL}$  can be found by Eqs. (8.17-22).

Finally, rearranging Eqs. (8.32) and (8.34), new concentration values at each  $i, j$  block can be found. Step II terminates when the maximum difference between old and new concentrations over all grid blocks ( $e = |C_{New}^{SOL} - C_{Old}^{SOL}|$ ) becomes less than  $10^{-3}$  M.

At this point, step III begins and new values for the solution flow rates are calculated using Eqs. (8.33) and (8.35), considering water and salt fluxes of step II. Then, the solution concentrations are again calculated from the mass balances of Eqs. (8.32) and (8.34), taking into account the new flow distribution. Finally, the difference between the new concentration values and those of step II are calculated over all grid blocks using the same equation as was used to find the error  $e$ . If the maximum difference is higher than  $10^{-3}$  M, the flow distribution is updated in step II and new concentrations are found. Otherwise, the final solution is attained. The algorithm terminates when step II and step III are fulfilled. It should be noted that, in a more complete procedure, membrane deformation would be updated (step I) considering the calculated flow rate of step III, which take into account water transmembrane fluxes. However, this step has been neglected following the assumption d of Section 7.3, which points out the small influence of the trans-membrane water flow rate with respect to the main water flow rate along the channels.

The procedure was implemented in the Matlab environment.

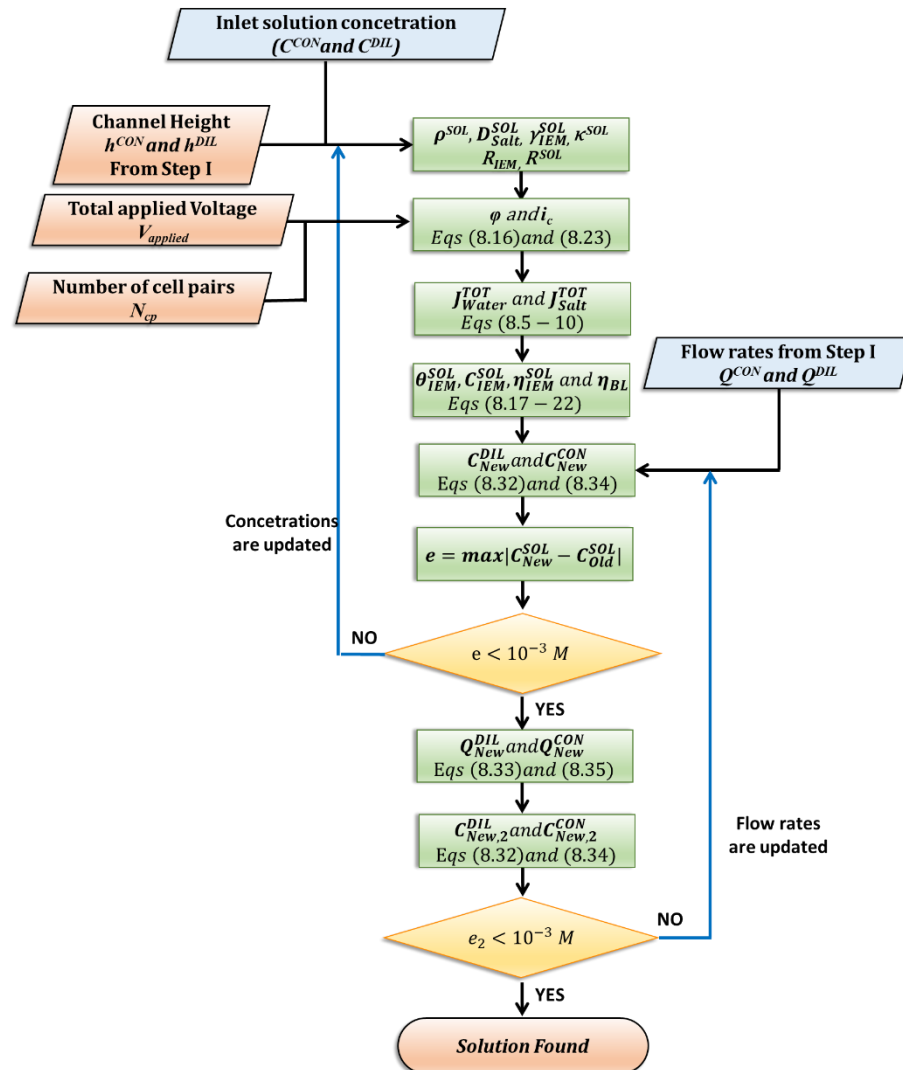


**Figure 8. 2** Flow chart of steps II and III of the iterative algorithm used for the 2-D process model of ED units.

#### 8.4) Grid dependence analysis and model validation for the parallel flow configuration

The proposed model has been validated comparing results with those obtained using the model presented in ref [129] for a parallel flow configuration.



It has to be noted that no membrane deformation effects were taken into consideration, since the model in ref [129] has been developed for undeformed channels only, thus step I is not computed. Since parallel flow is investigated, diluate and concentrate solutions are both assumed to flow ideally from the left to the right of their channels. Consequently, Eqs. (8.32-35) become:

$$\begin{aligned}
 C_{Bulk;j+1}^{CON;j} \cdot Q_{j+1}^{CON;j} - C_{Bulk;j}^{CON;j-1} \cdot Q_j^{CON;j-1} + J_{SALT;j}^{TOT} \Delta x W &= 0 \\
 Q_{j+1}^{CON;j} - Q_j^{CON;j-1} + J_{WATER;j}^{TOT} \Delta x W &= 0 \\
 C_{Bulk;j+1}^{DIL;j} \cdot Q_{j+1}^{DIL;j} - C_{Bulk;j}^{DIL;j-1} \cdot Q_j^{DIL;j-1} - J_{SALT;j}^{TOT} \Delta x W &= 0 \\
 Q_{j+1}^{DIL;j} - Q_j^{DIL;j-1} - J_{WATER;j}^{TOT} \Delta x W &= 0
 \end{aligned} \tag{8.36-39}$$

All the other equations do not need any adjustment, since they only depend on the concentration of the solutions at each  $j$  block.

The comparison was carried out considering:

- Inlet solution concentrations of 513.34 mol/m<sup>3</sup>, i.e. seawater concentration.
- Length and width of the stack of 0.6 m.
- 400 cell pairs.
- Inlet solution flow rates of 57.60 l/min.
- Non-conductive spacers with  $f_{shadow}$  value of 1.33.
- A voltage drop applied  $V_{Applied}$  able to desalinate the diluate solution up to an outlet concentration of 7.94 mol/m<sup>3</sup>, corresponding to a salt concentration of almost 500 ppm, which is considered to be a standard for potable water.

Parameters in Table 8. 1 were used except for the  $f_{shadow}$ .

First, to assess the accuracy of the present model, a grid dependence analysis was conducted and results are reported in Table 8. 2 . In particular, six grids were analysed with 40, 80, 120, 180, 240 and 480 blocks, respectively.

**Table 8. 2** Grid dependence for the parallel flow configuration case.

Quantities	40	80	120	180	240	480
$C_{OUTLET}^{CON}$ [M]	937.53	938.80	939.21	939.48	939.61	939.81
<b>Discrepancy %</b>	-0.24	-0.11	-0.06	-0.03	-0.02	
$Q_{TOT,OUTLET}^{CON}$ [l min <sup>-1</sup> ]	62.63	62.55	62.52	62.50	62.49	62.48
<b>Discrepancy %</b>	0.25	0.11	0.06	0.04	0.02	
$Q_{TOT,OUTLET}^{DIL}$ [l min <sup>-1</sup> ]	52.57	52.65	52.68	52.70	52.71	52.72
<b>Discrepancy %</b>	-0.29	-0.13	-0.08	-0.04	-0.03	
$V_{Applied}$ [V]	133.75	131.14	130.26	129.73	129.44	129.04
<b>Discrepancy %</b>	3.52	1.60	0.94	0.53	0.31	
$i_c$ [A m <sup>-2</sup> ]	349.91	341.83	339.20	337.48	336.61	335.33
<b>Discrepancy %</b>	4.17	1.90	1.14	0.64	0.38	

The highest discrepancy of 4.17 % with respect to the finest discretization is detected by using the 40-block grid. By increasing the grid discretization, the discrepancies reduce at the cost of higher computational effort. Therefore, the 80-block grid was selected as representative of the best compromise which satisfies the trade-off between model accuracy and computational effort.

As far as the model validation is concerned, the comparison between the voltage drop  $V_{Applied}$ , the overall current density  $i_c$ , the concentrate outlet concentration  $C_{OUTLET}^{CON}$  and diluate and concentrate outlet flow rates  $Q_{TOT,OUTLET}^{CON/DIL}$ , computed using the present model and the model in ref [129], are reported in Table 8. 3. Eighty blocks were used in the simulations, i.e.  $N_{Block}^x = 80$ . Concentrate and diluate concentration, non-ohmic voltage drop ( $\varphi(x, y)$ ) and current density profiles along the channel length are also reported in Figure 8. 3.

**Table 8. 3** Comparison between results of the present model and the model in ref [129].

Quantity	Model in [129]	Present model with $N_{Block}^x = 80$	Discrepancy %
$V_{Applied}$	128.96 [V]	131.13 [V]	<b>1.66</b>
$i_c$	338.96 [A m <sup>-2</sup> ]	341.82 [A m <sup>-2</sup> ]	<b>-0.83</b>
$Q_{OUTLET}^{CON}$	918.54 [M]	938.80 [M]	<b>2.16</b>
$Q_{TOT,OUTLET}^{DIL}$	51.28 [l/min]	52.65 [l/min]	<b>-2.67</b>
$Q_{TOT,OUTLET}^{CON}$	63.92 [l/min]	62.55 [l/min]	<b>-2.14</b>

In Table 8. 3,  $Q_{TOT,OUTLET}^{CON}$  and  $Q_{TOT,OUTLET}^{DIL}$  are the overall outlet flowrates of the concentrate and diluate solutions, obtained by multiplying the outlet flow rate by the total number of cell pairs ( $N_{cp}$ ).

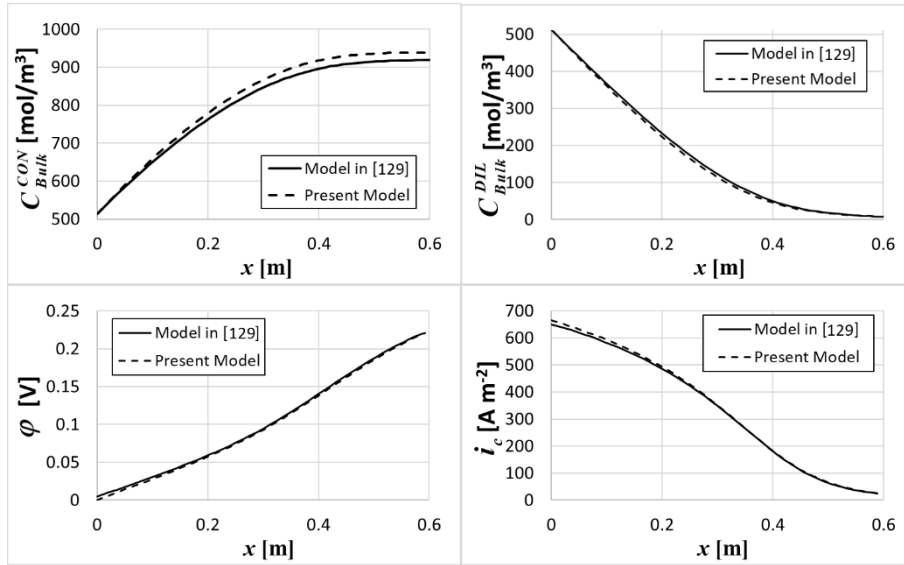


**Figure 8. 3** Comparison between results of the present model and the model in ref [129]; concentrate and diluate bulk concentrations, non-ohmic voltage drop  $\phi$  and current density profiles along the channel length.

Results show a very good agreement between the two models' predictions.

### 8.5) Grid dependence analysis for the Cross Flow configuration

In order to determine the most suitable grid size that satisfies the trade-off between computing time and accuracy in the simulation of cross-flow configurations, a sensitivity analysis of the model predictions on the grid resolution was carried out. In this grid dependence analysis, membrane deformation effects were taken into account. Six grids were investigated: 40 x 40, 80 x 80, 120 x 120, 180 x 180, 240 x 240 and 480 x 480 blocks. OCF membranes of the same type as in Chapters V, VI and VII were simulated.

The comparison was carried out, considering:

- Inlet solutions concentrations of 513.34 mol/m<sup>3</sup>.
- A length and a width of the stack of 0.6 m.
- Inlet mean concentrate and diluate velocities of 5 cm/s.
- 400 cell pairs.
- A voltage drop applied  $V_{Applied}$  able to desalinate the diluate solution up to an outlet diluate concentration of 8.5 mol/m<sup>3</sup>.

Parameters in Table 8. 1 were used. Table 8. 4 and Figure 8. 4 present the results of the above mentioned grid analysis.

**Table 8. 4** Grid dependence for the cross-flow configuration.

	40	80	120	180	240	480
$C_{OUTLET}^{CON}$ [M]	969.41	966.59	965.76	965.21	964.93	963.39
<b>Discrepancy %</b>	0.62	0.33	0.25	0.19	0.16	
$Q_{TOT,OUTLET}^{CON}$ [l min <sup>-1</sup> ]	151.16	152.52	152.96	153.27	153.43	152.71
<b>Discrepancy %</b>	-1.02	-0.34	0.04	0.30	0.43	
$Q_{TOT,OUTLET}^{DIL}$ [l min <sup>-1</sup> ]	130.11	131.67	132.16	132.51	132.69	132.11
<b>Discrepancy %</b>	-1.54	-0.12	0.16	0.37	0.47	
$V_{Applied}$ [V]	260.15	254.99	253.70	252.90	252.50	250.00
<b>Discrepancy %</b>	3.90	1.96	1.46	1.15	0.99	
$i_c$ [A m <sup>-2</sup> ]	839.75	831.52	828.73	827.19	826.43	820.24
<b>Discrepancy %</b>	2.32	1.36	1.02	0.84	0.75	

Please note that,  $C_{OUTLET}^{CON}$  is calculated as the mean concentration value at the outlet of the concentrate channel;  $Q_{TOT,OUTLET}^{CON}$  is the overall concentrate outlet flowrate, calculated as the mean flow rate at the outlet of the channel and multiplied by the total number of cell pairs ( $N_{cp}$ ).

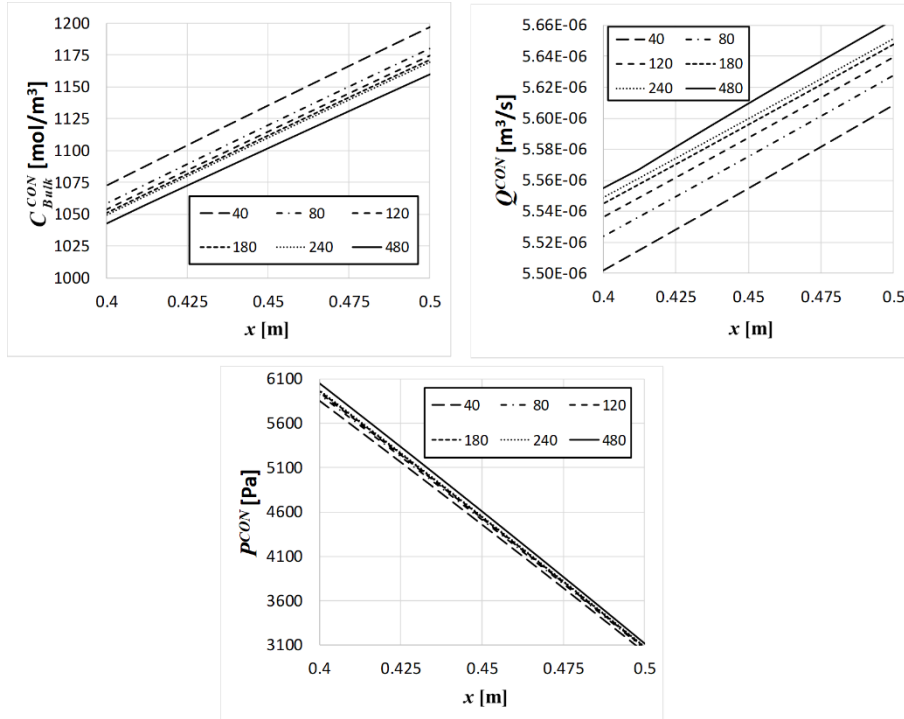


**Figure 8. 4** Comparison among results of the present model obtained with different discretization degrees: concentration, pressure and flow rate profiles of the concentrate solution along a line placed at 2.5 cm from the top of the channel. Quantities in the region of the channel between 0.4 and 0.5 m are reported.

Results show that the 80 x 80 grid can be employed, as discrepancies lower than 3% are obtained with respect to the finest grid. This is in accordance with the grid dependence conducted for the fluid redistribution model (see Appendix C).

## 8.6) Results

### 8.6.1) No membrane deformation

A sensitivity analysis was carried out to investigate the process' performances of cross-flow stacks changing the size and the operating conditions and neglecting deformation effects. In particular, the length ( $L$ ) and the width ( $W$ ) of the stack were let to vary between 0.1 and 0.6 m. Moreover, the inlet velocity of the concentrate,  $v_c$ , and diluate,  $v_d$ , solutions were changed between 1 and 5 cm/s. The number of cell pairs was fixed at 400 for each case. The total voltage drop over the stack electrodes  $V_{Applied}$  suitable to reach an outlet diluate concentration of  $8.5 \text{ mol/m}^3$  was assessed in each simulated case. Parameters in Table 8. 1 were used. In all cases OCF membranes of the same type as used in Chapter V, VI and VII were simulated.

Eight different cases were investigated:

- 1)  $L=0.2 \text{ m}$ ,  $W=0.6 \text{ m}$ ,  $v_c=5 \text{ cm s}^{-1}$ ,  $v_d=1 \text{ cm s}^{-1}$ ;
- 2)  $L=0.4 \text{ m}$ ,  $W=0.6 \text{ m}$ ,  $v_c=5 \text{ cm s}^{-1}$ ,  $v_d=1 \text{ cm s}^{-1}$ ;
- 3)  $L=0.6 \text{ m}$ ,  $W=0.6 \text{ m}$ ,  $v_c=5 \text{ cm s}^{-1}$ ,  $v_d=1 \text{ cm s}^{-1}$ ;
- 4)  $L=0.6 \text{ m}$ ,  $W=0.35 \text{ m}$ ,  $v_c=5 \text{ cm s}^{-1}$ ,  $v_d=1 \text{ cm s}^{-1}$ ;
- 5)  $L=0.6 \text{ m}$ ,  $W=0.15 \text{ m}$ ,  $v_c=5 \text{ cm s}^{-1}$ ,  $v_d=1 \text{ cm s}^{-1}$ ;
- 6)  $L=0.6 \text{ m}$ ,  $W=0.6 \text{ m}$ ,  $v_c=3 \text{ cm s}^{-1}$ ,  $v_d=1 \text{ cm s}^{-1}$ ;
- 7)  $L=0.6 \text{ m}$ ,  $W=0.6 \text{ m}$ ,  $v_c=1 \text{ cm s}^{-1}$ ,  $v_d=1 \text{ cm s}^{-1}$ ;
- 8)  $L=0.6 \text{ m}$ ,  $W=0.6 \text{ m}$ ,  $v_c=1 \text{ cm s}^{-1}$ ,  $v_d=3 \text{ cm s}^{-1}$ .

Results in terms of specific energy consumption  $E_{spec}$ , apparent flux  $J_p$ , overall electric current  $I$ , voltage drop  $V_{Applied}$  and diluate outlet flow rate  $Q_{TOT,OUTLET}^{DIL}$  are reported in Table 8. 5.

**Table 8.5** Specific energy consumption  $E_{spec}$ , apparent flux  $J_p$ , electric current  $I$ , voltage drop  $V_{Applied}$  and diluate outlet flow rate  $Q_{TOT,OUTLET}^{DIL}$  for eight cross-flow cases.

<i>Case</i>	$E_{spec}$ [kWh/m <sup>3</sup> ]	$J_p$ [l/m <sup>2</sup> h]	$I$ [A]	$V_{Applied}$ [V]	$Q_{TOT,OUTLET}^{DIL}$ [l min <sup>-1</sup> ]
#1	3.34	5.40	20.18	84.99	8.64
#2	3.34	5.39	40.38	85.06	17.26
#3	3.35	5.41	60.79	85.17	25.95
#4	4.13	9.39	60.19	107.80	26.30
#5	7.87	22.79	61.66	209.38	27.35
#6	3.43	5.35	60.84	85.33	25.90
#7	3.43	5.35	61.08	86.42	25.67
#8	6.41	16.38	180.82	167.14	78.65

Results suggest that, the stack length ( $L$ , which is the length of the concentrate channel and the width of the diluate channel) does not significantly affect process performances ( $E_{spec}$  and  $J_p$ ). In fact,  $E_{spec}$  and  $J_p$  are almost the same for the *cases* #1-3. However, the diluate outlet flow rate  $Q_{TOT,OUTLET}^{DIL}$  changes, since the diluate width varies (see Figure 8. 1), while the inlet fluid velocity is fixed.

The stack width ( $w$ , which is the width of the concentrate channel and the length of the diluate channel) considerably influences the process' parameters, see results of the *cases* #3-5. Specifically,  $E_{spec}$  and  $J_p$  are found to increase as the stack width  $w$  decreases.

Finally, the specific energy consumption and the apparent flux slightly change by varying the concentrate solution velocity  $v_c$ , the *cases* #3, 6-7. Conversely,  $E_{spec}$  and  $J_p$  are significantly affected by the diluate velocity  $v_d$  (*cases* #7-8). The effects of  $v_d$  show an opposite trend with respect to that of the stack width  $w$ . Specifically, an increase of the diluate velocity causes a reduction of both  $E_{spec}$  and  $J_p$ .

### **8.6.2) Effects of membrane deformation**

The ED process' performances analysed for the above presented eight cases were also investigated taking into account membrane deformation effects. In particular, two membrane deformation conditions were investigated: (i) mild deformation effects and (ii) heavy deformation effects. In all cases OCF membranes as Chapters V, VI and VII were simulated.

#### **8.6.2.1) Mild deformation effects**

Flow and channel height distributions were evaluated for the above mentioned eight cross-flow cases by following step I of Section 8.3, before performing steps II and III. Interestingly, membrane deformation does not significantly impair process' performance. Specifically, the specific energy consumption and the apparent flux increase only by almost 2 % in deformed channels with respect to the values found for undeformed configurations reported in Table 8. 5.

In this sub-section, only results for the *case #2*, which was considered to be the most representative among those analysed, will be reported. Moreover, for the sake of brevity, only diluate concentration and current density maps are shown in Figure 8.5, comparing undeformed and deformed channels, as these variables are the most affected by the membrane deformation phenomena.



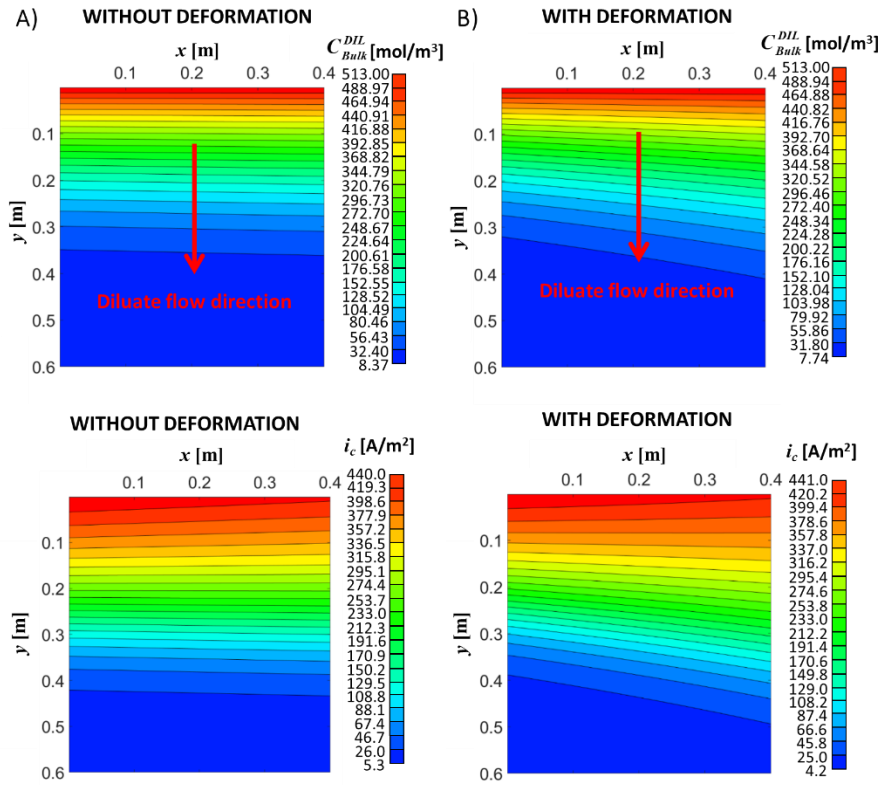


**Figure 8. 5** Diluate concentration ( $C_{Bulk}^{DIL}$ ) and current density ( $i_c$ ) maps for the cross-flow case #2: a) without membrane deformation; b) with membrane deformation.

As can be seen in Figure 8. 5, concentration and current density isolines are not straight anymore in presence of deformation. In particular, iso-lines show a significant deflection close to the channel outlet. To better understand this behaviour, diluate superficial velocity, along the main flow direction ( $y$ -axis), and channel height maps in the presence of membrane deformation are shown in Figure 8. 6.

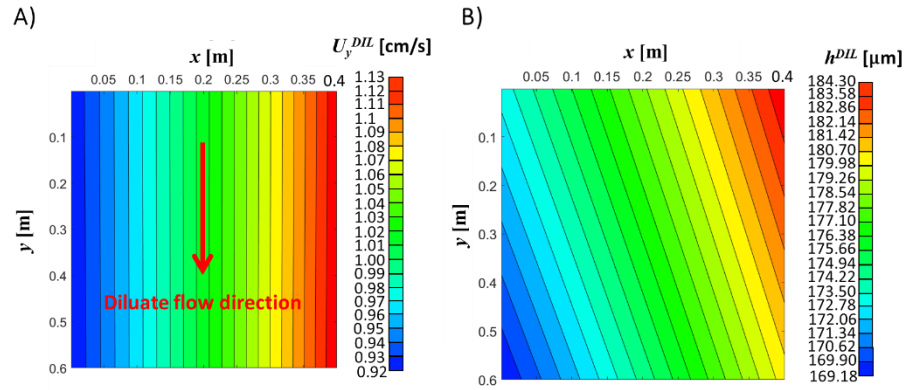


**Figure 8. 6** Diluate superficial velocity (a) along the main flow direction (  $y$ -axis) and channel height (b) maps for the cross-flow *case #2* in the presence of membrane deformation.

The superficial velocity is 18% lower in the left side of the channel with respect to the right side. As a consequence, the residence time is higher in the left part of the stack compared to the right part. This favours the desalination process in the left side, where local concentrations are lower than those of the right side (see, Figure 8. 5 b), since the voltage drop applied by a power supply is assumed to be equal over all the channel, as would occur at an electrode. As a result, the overall electrical resistance of the diluate channel increases, thus requiring higher applied voltage at the electrodes.

### 8.6.2.2) Heavy deformation effects

Based on previous results, it may be concluded that membrane deformation has a small effect under the conditions simulated in terms of mechanical properties and geometrical features of the OCF profiled membrane investigated in chapters V-VII. However, more severe deformations can occur in other profiled membrane configurations with a lower membrane Young's modulus and thickness. In order to avoid the large computational effort that would be required by further numerical simulations for solid and fluid mechanics (see Chapter V and VI), a preliminary study of severe membrane deformation effects was

performed assuming a fictitious correlation between the hydraulic permeability ( $K_{app}$ ) in deformed channels and the TMP. In particular, the  $K_{app}$  values at TMP of  $\pm 30$  kPa of Eq. (7.5) were assumed to occur for TMP of  $\pm 10$  kPa.

In this case, only results for the *case #4*, which showed the highest membrane deformation effects, will be reported. Table 8. 6 reports the specific energy consumption  $E_{spec}$ , the apparent flux  $J_p$ , the overall electric current  $I$ , the voltage drop  $V_{Applied}$  and the diluate outlet flow rate  $Q_{TOT,OUTLET}^{DIL}$  computed either in the absence or in the presence of membrane effects. Diluate concentration and current density maps are also reported in Figure 8. 7.

**Table 8. 6** Specific energy consumption  $E_{spec}$ , apparent flux  $J_p$ , overall electric current  $I$ , applied voltage drop  $V_{Applied}$  and diluate outlet flow rate  $Q_{TOT,OUTLET}^{DIL}$  for the cross-flow case #4 either in the absence or in the presence of severe membrane effects.

	UNDEFORMED	DEFORMED	Variation %
$E_{spec}$ [kWh/m <sup>3</sup> ]	4.13	4.39	<b>6.07</b>
$J_p$ [l/m <sup>2</sup> h]	9.39	9.51	1.21
$I$ [A]	60.19	60.75	0.91
$V_{Applied}$ [V]	107.80	115.21	<b>6.44</b>
$Q_{TOT,OUTLET}^{DIL}$ [l min <sup>-1</sup> ]	26.30	26.62	1.21

Results in Table 8. 6 show that heavy membrane deformation conditions can significantly impair the process' performances. Specifically, the voltage drop increases by 6.44% in the presence of deformations, along with an increase of 6% of the  $E_{spec}$ . The reason for this behavior relies on the strong redistribution of the fluid velocity. In fact, the diluate superficial velocity along the y-axis is found to be almost two times higher in the right side of the channel with respect to the left side, thus strongly influencing the residence time. As a result, concentration and current density iso-lines are much more deflected in a stack suffering severe deformations.

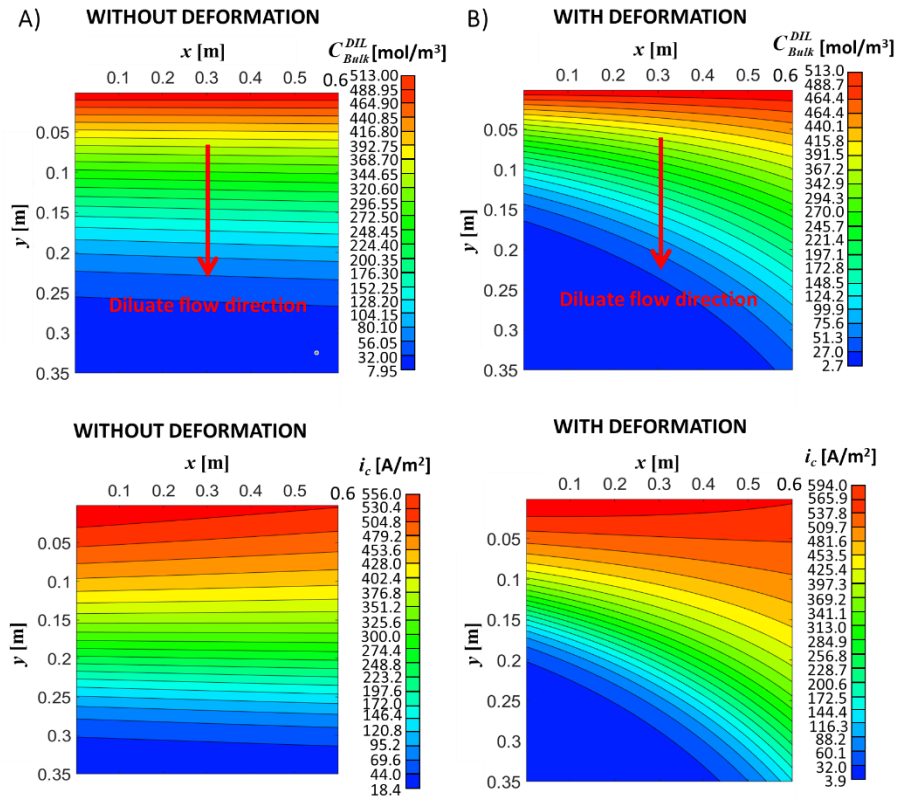


**Figure 8. 7** Diluate concentration ( $C_{Bulk}^{DIL}$ ) and current density ( $i_c$ ) maps for the cross-flow case #4 in the absence (a) or in the presence of severe membrane effects (b).

## CONCLUSIONS

ED and RED are two promising membrane-based technologies for saline water desalination and electric energy harvesting from renewable resources, respectively. A pressure difference between adjacent channels (transmembrane pressure, TMP) may arise in many ED and RED applications, e.g. non-parallel arrangements, thus causing membrane/channel deformations. Despite the relevance of membrane deformations, this phenomenon has always been neglected in the design of ED and RED systems.

In this PhD thesis, for the first time, the impact of membrane deformation on the performance of Electrodialysis (ED) and Reverse Electrodialysis (RED) processes was assessed.

To this aim, knowledge of solid mechanics, fluid dynamics and electrochemistry was combined to investigate profiled membrane-bounded fluid channels of ED and RED systems. First, thin plates have been studied developing novel tools for the analysis of isotropic and orthotropic arbitrarily shaped thin plates with small and large deflections (membranes). Then, membrane behaviour in ED and RED channels was investigated by developing a multi-scale model.

In chapter II an innovative method was presented for the analysis of isotropic plates of arbitrary shapes and boundary conditions. The method does not require any boundary or domain discretization and employs only line integrals. In the procedure, the deflection function of the plates is approximated by a series expansion in terms of harmonic polynomials. The procedure was applied for the analysis of various plate configurations, for which exact solutions are available. The exact analytical solutions were detected using only a few expansion coefficients. Further, plates of complex geometries, subjected to arbitrary boundary conditions were also analysed and the results were compared with those obtained by finite element code. A very good agreement was found, thus proving the accuracy of the proposed procedure.

In Chapter III, the pb2-Rayleigh Ritz method, commonly employed for the study of isotropic thin plates, was extended for the analysis of orthotropic arbitrarily shaped plates. Two-dimensional integrals were converted into line

integrals by taking advantage of the Green Lemma. The method was employed to determine the modal parameters of an elliptical clamped orthotropic plate and a triangular plate with mixed boundary conditions. Discrepancies between calculated frequencies and those found in literature of less than 2% were detected, thus showing the accuracy of the method.

In Chapter IV, the abovementioned method was combined with a Particle Swarm Optimization algorithm to identify the mechanical parameters of orthotropic thin plates based on vibration data. To primarily assess the procedure's reliability, the mechanical parameters of the plate configurations from chapter III were investigated and compared with literature data. Very satisfactory results were obtained, especially when ten frequencies were considered with discrepancies between model and literature data lower than 10%.

To further assess the algorithm's reliability, an extensive experimental campaign was conducted at the Laboratory of Experimental Dynamics of the University of Palermo. Specifically, the modal parameters of different structurally thin plates made by 3D printer were identified. The comparison between results obtained from experimental testing, finite element analysis and the proposed procedure highlighted the accuracy of the proposed procedure.

In Chapter IV attention was also focused on the analysis of membranes. Specifically, an optimization procedure was presented to identify the mechanical characteristics of orthotropic membranes based on bulge test measurements. In this case, the principle of minimum energy was combined with an optimization genetic algorithm. A finite element code was used to obtain virtual bulge test data of two orthotropic membranes. An excellent agreement was found between identified membrane properties and those from literature with discrepancies lower than 10%.

Based on the aforementioned studies, in Chapter V, attention was focused on the analysis of membrane deformation in ED and RED systems.

Specifically, membrane deformation was investigated in a periodic portion of two adjacent membranes through finite element three-dimensional simulations. Two different profiled membranes were studied: one with Overlapped Cross Filaments (OCF) and another with Round Pillars (RP). The

model employed the membrane's mechanical characteristics determined by conducting uniaxial tensile tests at the Laboratory of FujiFilm Europe B.V. Further, the model was also validated by performing experimental and analytical comparisons.

First, a high (conservative) transmembrane pressure value (TMP) of 80 kPa was considered and the largest profiled membrane configuration, which was able to withstand to this TMP value without the two membranes touching each other, was determined. The largest configuration with a pitch over channel height ratio ( $P/H$ ) of 8 and 10 was found for OCF and RP configurations, respectively.

The identified configurations were then studied under applied TMP values of  $\pm 40$  kPa. The fluid volume bounded by the two the adjacent membranes was found to vary by almost  $\pm 25\%$  in the most compressed and expanded configurations with respect to the volume of the undeformed channel.

In Chapter VI, fluid dynamics and mass transport properties were fully addressed through finite volume three-dimensional simulations in the periodic region of the fluid channel bounded by the two adjacent membranes, whose deformations were determined in chapter V. The Darcy friction factor was found to almost double in the most compressed configurations and to decrease by almost 50% in most expanded channels, with respect to the friction characteristics of the undeformed configuration. The Sherwood number increased in compressed channels and reduced in expanded ones, but with a more complex behaviour compared to that of the friction coefficient.

In Chapter VII an original fluid-structure two-dimensional model was developed to determine the flow redistribution in ED and RED channels at the higher scale of the entire channel dimensions. The model, based on the Darcy and continuity equations, used results obtained in chapter VI for the dependence of fluid channel properties as a function of TMP. A significant fluid redistribution is detected for cross-flow square stacks of 0.6 m sides fed by a mean superficial velocity of 10 cm/s. The superficial velocity was found to stratify along the main flow direction and locally vary between -27% and +39% with respect to the mean superficial velocity value.

Finally, in Chapter VIII electrochemical and transport phenomena of ED and RED processes were simulated by a two-dimensional multi-scale process model which was coupled with the fluid-structure model of the previous chapter. Mass balances, water and salt fluxes, and electrical parameters were considered to investigate the performance of ED systems in the presence and in the absence of membrane deformation considering also the electrode compartments. Mild membrane deformations altered the process' performance slightly. However, heavy membrane deformations were found to significantly affect ED process' performance. The specific energy consumption was 6% higher than that of the corresponding ED unit without deformation.

Overall, in Chapters V-VIII a novel tool was presented to fully study and design profiled membranes and to address their application in RED and ED processes. The tool can also be easily employed for the analysis of spacer-filled channels.

The largest pitch over height ratio ( $P/H$ ) of a profiled membrane or a net spacer can be assessed in order to reduce pressure drops in channels, without causing excessive membrane deformation.

Moreover, large  $P/H$  values can reduce both the amount of membrane area covered by spacers, decreasing the shadow effect, and the amount of material for making the profiles on the membranes, decreasing membrane cost. On the other hand, the effects on mass transport in the channels have to be taken into account. In fact, large  $P/H$  ratios may lead to a poor mixing in the channels, thus increasing the concentration polarization phenomena.

All of these considerations have to be taken in mind during the design and fabrication of spacers and especially for the case of profiled membranes. In particular, attention has to be focused on both membrane thickness and membranes' mechanical characteristics. For example, the adoption of thinner membranes can reduce the electrical resistance of a stack, but membranes will be much more prone to deform under the action of a TMP. Therefore, manufacturers should improve membrane properties (Young's modulus) or change spacer/profiled membrane geometries if thinner membranes would be employed.



The effects of membrane deformation analysed in this thesis call for future studies on the development of experimental approaches to further validate the models developed for the analysis of the effects of membrane deformation on RED and ED systems at large scale, considering the total dimensions of an ED or RED unit.

Moreover, the membrane deformation could be also assessed in net-spacers filled channels and a sensitivity analysis in terms of both geometries and membrane features (thickness and mechanical characteristics) can be carried out to address the effects of membrane deformation in several conditions.

Finally, the limiting current density phenomenon in both undeformed and deformed channels could be also considered by introducing empirical correlations in the model.

## Appendix A: Expression of the Boundary Conditions in terms of Harmonic Polynomials

In this appendix, the compact form expressions of the BCs used in Eqs. (2.73)-(2.76) of the Chapter II are reported. Specifically, taking into account Eq. (2.72) and the properties of the harmonic polynomials in Eqs. (2.15) and (2.16), it is possible to directly give explicit expressions of the BCs in terms of the previously introduced functions. In this regard, let the deflection function in Eq. (2.72) can be rewritten as

$$w(x, y) = \mathbf{r}_m \boldsymbol{\mu} + w_p(x, y, \tilde{\boldsymbol{\eta}}_i) \quad (\text{A.1})$$

where  $\mathbf{r}_m$  is a row vector containing the harmonic polynomials, as given in Eq. (2.44), while  $\boldsymbol{\mu}$  is a column vector of coefficients, given as

$$\boldsymbol{\mu} = -\mathbf{Q}_m^{-1} \boldsymbol{\lambda} + \sum_{i=1}^{N_y} \mathbf{Q}_m^{-1} \tilde{\mathbf{Q}}_{m,i} \tilde{\boldsymbol{\xi}}_i \quad (\text{A.2})$$

In this manner, omitting henceforth variable dependence, derivatives of the deflection function can be expressed as

$$\frac{\partial w}{\partial x} = \frac{\partial \mathbf{r}_m}{\partial x} \boldsymbol{\mu} + \frac{\partial w_p}{\partial x} \quad (\text{A.3})$$

and

$$\frac{\partial w}{\partial y} = \frac{\partial \mathbf{r}_m}{\partial y} \boldsymbol{\mu} + \frac{\partial w_p}{\partial y} \quad (\text{A.4})$$

Recalling the properties of the harmonic polynomials as in Eq. (2.16), Eqs. (A.3) and (A.4) can be directly expressed in compact form as

$$\frac{\partial w}{\partial x} = \mathbf{r}_{m,x}^{(1)} \mathbf{Z}_x^{(1)} \boldsymbol{\mu} + \frac{\partial w_p}{\partial x} \quad (\text{A.5})$$

And

$$\frac{\partial w}{\partial y} = \mathbf{r}_{m,y}^{(1)} \mathbf{Z}_y^{(1)} \boldsymbol{\mu} + \frac{\partial w_p}{\partial y} \quad (\text{A.6})$$

where  $\mathbf{Z}_x^{(1)}$  and  $\mathbf{Z}_y^{(1)}$  are diagonal matrices of coefficients given respectively as  $\mathbf{Z}_x^{(1)} = [\bar{0} \ 1 \cdots m \ 1 \ 2 \cdots m]$  and  $\mathbf{Z}_y^{(1)} = [\bar{0} \ 1 \cdots (-m) \ 1 \ 2 \cdots m]$ , while  $\mathbf{r}_{m,x}^{(1)}$  and  $\mathbf{r}_{m,y}^{(1)}$  are vectors containing the corresponding derivatives of  $\mathbf{r}_m$ , given as

$$\mathbf{r}_{m,x}^{(1)} = [P_{-1} \cdots P_{m-1} \ Q_0 \cdots Q_{m-1}] \quad (\text{A.7})$$

and

$$\mathbf{r}_{m,y}^{(1)} = [Q_{-1} \cdots Q_{m-1} \ P_0 \cdots P_{m-1}] \quad (\text{A.8})$$

On this base, second order derivatives can be directly obtained as

$$\frac{\partial^2 w}{\partial x^2} = \mathbf{r}_{m,x}^{(2)} \mathbf{Z}_x^{(1)} \mathbf{Z}_x^{(2)} \boldsymbol{\mu} + \frac{\partial^2 w_p}{\partial x^2} \quad (\text{A.9})$$

$$\frac{\partial^2 w}{\partial y^2} = \mathbf{r}_{m,y}^{(2)} \mathbf{Z}_y^{(1)} \mathbf{Z}_y^{(2)} \boldsymbol{\mu} + \frac{\partial^2 w_p}{\partial y^2} \quad (\text{A.10})$$

$$\frac{\partial^2 w}{\partial x \partial y} = \mathbf{r}_{m,xy}^{(2)} \mathbf{Z}_y^{(1)} \mathbf{Z}_x^{(2)} \boldsymbol{\mu} + \frac{\partial^2 w_p}{\partial x \partial y} \quad (\text{A.11})$$

where  $\mathbf{Z}_x^{(2)} = [\bar{-1} \ 0 \cdots (m-1) \ 0 \ 1 \cdots (m-1)]$  and

$\mathbf{Z}_y^{(2)} = [\bar{-1} \ 0 \cdots (m-1) \ 0 \ -1 \cdots -(m-1)]$ , while

$$\mathbf{r}_{m,x}^{(2)} = [P_{-2} \cdots P_{m-2} \ Q_{-1} \cdots Q_{m-2}] \quad (\text{A.12})$$

$$\mathbf{r}_{m,xy}^{(2)} = [Q_{-2} \cdots Q_{m-2} \ P_{-1} \cdots P_{m-2}] \quad (\text{A.13})$$

and  $\mathbf{r}_{m,y}^{(2)} = \mathbf{r}_{m,x}^{(2)}$ .

Finally, third order derivatives can be rewritten as

$$\frac{\partial^3 w}{\partial x^3} = \mathbf{r}_{m,x}^{(3)} \mathbf{Z}_x^{(1)} \mathbf{Z}_x^{(2)} \mathbf{Z}_x^{(3)} \boldsymbol{\mu} + \frac{\partial^3 w_p}{\partial x^3} \quad (\text{A.14})$$

$$\frac{\partial^3 w}{\partial y^3} = \mathbf{r}_{m,y}^{(3)} \mathbf{Z}_y^{(1)} \mathbf{Z}_y^{(2)} \mathbf{Z}_y^{(3)} \boldsymbol{\mu} + \frac{\partial^3 w_p}{\partial y^3} \quad (\text{A.15})$$

$$\frac{\partial^3 w}{\partial x \partial y^2} = \mathbf{r}_{m,xy}^{(3)} \mathbf{Z}_x^{(1)} \mathbf{Z}_y^{(2)} \mathbf{Z}_y^{(3)} \boldsymbol{\mu} + \frac{\partial^3 w_p}{\partial x \partial y^2} \quad (\text{A.16})$$

$$\frac{\partial^3 w}{\partial y \partial x^2} = \mathbf{r}_{m,yx}^{(3)} \mathbf{Z}_y^{(1)} \mathbf{Z}_x^{(2)} \mathbf{Z}_x^{(3)} \boldsymbol{\mu} + \frac{\partial^3 w_p}{\partial y \partial x^2} \quad (\text{A.17})$$

where  $\mathbf{Z}_x^{(3)} = \begin{bmatrix} -2 & -1 \cdots (m-2) & -1 & 0 \cdots (m-2) \end{bmatrix}$  and

$$\mathbf{Z}_y^{(3)} = \begin{bmatrix} 2 & 1 \cdots (m-2) & -1 & 0 \cdots (m-2) \end{bmatrix}.$$

Further

$$\mathbf{r}_{m,x}^{(3)} = [P_{-3} \cdots P_{m-3} \ Q_{-2} \cdots Q_{m-3}] \quad (\text{A.18})$$

$$\mathbf{r}_{m,y}^{(3)} = [Q_{-3} \cdots Q_{m-3} \ P_{-2} \cdots P_{m-3}] \quad (\text{A.19})$$

while  $\mathbf{r}_{m,xy}^{(3)} = \mathbf{r}_{m,x}^{(3)}$  and  $\mathbf{r}_{m,yx}^{(3)} = \mathbf{r}_{m,y}^{(3)}$

In this manner, taking into account Eqs. (1.42-44) and (1.57-58) and manipulating yields the bending and twisting moments as

$$M_x = -D \left[ \left( \mathbf{r}_{m,x}^{(2)} \mathbf{Z}_x^{(1)} \mathbf{Z}_x^{(2)} + \nu \mathbf{r}_{m,y}^{(2)} \mathbf{Z}_y^{(1)} \mathbf{Z}_y^{(2)} \right) \boldsymbol{\mu} + \left( \frac{\partial^2 w_p}{\partial x^2} + \nu \frac{\partial^2 w_p}{\partial y^2} \right) \right] \quad (\text{A.20})$$

$$M_y = -D \left[ \left( \mathbf{r}_{m,y}^{(2)} \mathbf{Z}_y^{(1)} \mathbf{Z}_y^{(2)} + \nu \mathbf{r}_{m,x}^{(2)} \mathbf{Z}_x^{(1)} \mathbf{Z}_x^{(2)} \right) \boldsymbol{\mu} + \left( \frac{\partial^2 w_p}{\partial y^2} + \nu \frac{\partial^2 w_p}{\partial x^2} \right) \right] \quad (\text{A.21})$$

$$M_{xy} = -D(1-\nu) \left( \mathbf{r}_{m,xy}^{(2)} \mathbf{Z}_y^{(1)} \mathbf{Z}_x^{(2)} \boldsymbol{\mu} + \frac{\partial^2 w_p}{\partial x \partial y} \right) \quad (\text{A.22})$$

while the shearing forces are given as

$$V_x = -D \left[ \left( \mathbf{r}_{m,x}^{(3)} \mathbf{Z}_x^{(1)} \mathbf{Z}_x^{(2)} \mathbf{Z}_x^{(3)} + \mathbf{r}_{m,xy}^{(3)} \mathbf{Z}_x^{(1)} \mathbf{Z}_y^{(2)} \mathbf{Z}_y^{(3)} \right) \boldsymbol{\mu} + \left( \frac{\partial^3 w_p}{\partial x^3} + \frac{\partial^3 w_p}{\partial x \partial y^2} \right) \right] \quad (\text{A.23})$$

$$V_y = -D \left[ \left( \mathbf{r}_{m,y}^{(3)} \mathbf{Z}_y^{(1)} \mathbf{Z}_y^{(2)} \mathbf{Z}_y^{(3)} + \mathbf{r}_{m,yx}^{(3)} \mathbf{Z}_y^{(1)} \mathbf{Z}_x^{(2)} \mathbf{Z}_x^{(3)} \right) \boldsymbol{\mu} + \left( \frac{\partial^3 w_p}{\partial y^3} + \frac{\partial^3 w_p}{\partial y \partial x^2} \right) \right] \quad (\text{A.24})$$

Further, normal stresses  $\sigma_x$  and  $\sigma_y$ , given as

$$\sigma_x = -\frac{Ez}{1-\nu^2} \left( \frac{\partial^2 w}{\partial x^2} + \nu \frac{\partial^2 w}{\partial y^2} \right) \quad (\text{A.25})$$

and

$$\sigma_y = -\frac{Ez}{1-\nu^2} \left( \frac{\partial^2 w}{\partial y^2} + \nu \frac{\partial^2 w}{\partial x^2} \right) \quad (\text{A.26})$$

can be directly expressed as

$$\sigma_x = -\frac{Ez}{1-\nu^2} \left[ \left( \mathbf{r}_{m,x}^{(2)} \mathbf{Z}_x^{(1)} \mathbf{Z}_x^{(2)} + \nu \mathbf{r}_{m,y}^{(2)} \mathbf{Z}_y^{(1)} \mathbf{Z}_y^{(2)} \right) \boldsymbol{\mu} + \left( \frac{\partial^2 w_p}{\partial x^2} + \nu \frac{\partial^2 w_p}{\partial y^2} \right) \right] \quad (\text{A.27})$$

And

$$\sigma_y = -\frac{Ez}{1-\nu^2} \left[ \left( \mathbf{r}_{m,y}^{(2)} \mathbf{Z}_y^{(1)} \mathbf{Z}_y^{(2)} + \nu \mathbf{r}_{m,x}^{(2)} \mathbf{Z}_x^{(1)} \mathbf{Z}_x^{(2)} \right) \boldsymbol{\mu} + \left( \frac{\partial^2 w_p}{\partial y^2} + \nu \frac{\partial^2 w_p}{\partial x^2} \right) \right] \quad (\text{A.28})$$

Similarly, shear stresses  $\tau$

$$\tau = -\frac{E}{1+\nu} \left( \frac{\partial^2 w}{\partial x \partial y} z \right) \quad (\text{A.29})$$

can be given as

$$\tau = -\frac{E}{1+\nu} z \left[ \mathbf{r}_{m,xy}^{(2)} \mathbf{Z}_y^{(1)} \mathbf{Z}_x^{(2)} \boldsymbol{\mu} + \frac{\partial^2 w_p}{\partial x \partial y} \right] \quad (\text{A.30})$$

Note that Eqs. (A.3), (A.4), (A.20)-(A.24) are then useful to directly express the BCs in Eqs. (1.85)-(1.90) in terms of harmonic polynomials. These expressions can be then used in the functionals in Eqs. (2.73)-(2.76).

## Appendix B: Dependence of equivalent channel height and channel hydraulic permeability on TMP

In this appendix, the dependence of equivalent channel height and channel hydraulic permeability as a function of TMP discussed in the Chapter VII are reported.

### B1) Equivalent channel height

As discussed in Section 7.2, the equivalent channel height is defined here as the ratio between fluid volume and projected area. Table B1 reports fluid volumes and corresponding equivalent channel heights for the periodic portion of channels delimited by OCF profiled membranes characterized by  $H=200\ \mu\text{m}$ ,  $P=1600\ \mu\text{m}$  ( $P/H=8$ , projected area  $P^2=2.56\ \text{mm}^2$ ) for TMP varying between  $-40$  and  $+40\ \text{kPa}$ . Channel height values were fit by a second-order polynomial, which was implemented in the Matlab® program ( $h$  is in  $\mu\text{m}$ , TMP in  $\text{kPa}$ ):

$$h = 6.0025 \times 10^{-4} \times \text{TMP}^2 - 1.1285 \times 10^{-7} \times \text{TMP} + 180 \quad (\text{B1})$$

**Table B1** Channel fluid volume and equivalent height as a function of TMP.

TMP [kPa]	V [mm <sup>3</sup> ]	h [ $\mu\text{m}$ ]
40	0.349	136
30	0.376	147
20	0.404	158
10	0.432	169
0	0.462	180
-10	0.491	192
-20	0.521	203
-30	0.550	215
-40	0.579	226

## B2) Channel permeability for non-Darcyan flow

The slopes and intercepts of each linear segment of the piecewise linear fitting (discussed in Section 7.4.3) used to capture the dependence of the channel permeability on the velocity at different values of TMP are reported in Tables B2.1 and B2.2.

**Table B2.1** Slopes and intercepts for superficial velocity ranging between 0 cm/s and 7 cm/s.

TMP [kPa]	0 < U < 3 cm/s		3 < U < 7 cm/s	
	K [m <sup>2</sup> ]	a' [cm/s]	K' [m <sup>2</sup> ]	a' [cm/s]
40	6.754 · 10 <sup>-10</sup>	0	6.289 · 10 <sup>-10</sup>	0.20677
30	8.651 · 10 <sup>-10</sup>	0	8.052 · 10 <sup>-10</sup>	0.20784
20	1.088 · 10 <sup>-9</sup>	0	1.012 · 10 <sup>-9</sup>	0.20885
10	1.356 · 10 <sup>-9</sup>	0	1.261 · 10 <sup>-9</sup>	0.20938
0	1.670 · 10 <sup>-9</sup>	0	1.553 · 10 <sup>-9</sup>	0.20934
-10	2.034 · 10 <sup>-9</sup>	0	1.891 · 10 <sup>-9</sup>	0.20973
-20	2.439 · 10 <sup>-9</sup>	0	2.271 · 10 <sup>-9</sup>	0.20753
-30	2.893 · 10 <sup>-9</sup>	0	2.693 · 10 <sup>-9</sup>	0.20727
-40	3.397 · 10 <sup>-9</sup>	0	3.163 · 10 <sup>-9</sup>	0.20678

**Table B2.2** Slopes and intercepts for superficial velocity ranging between 7 cm/s and 20 cm/s.

TMP [kPa]	7 < U < 12 cm/s		12 < U < 20 cm/s	
	K' [m <sup>2</sup> ]	a' [cm/s]	K' [m <sup>2</sup> ]	a' [cm/s]
40	5.777 · 10 <sup>-10</sup>	0.7598	5.169 · 10 <sup>-10</sup>	1.9422
30	7.393 · 10 <sup>-10</sup>	0.7634	6.612 · 10 <sup>-10</sup>	1.9506
20	9.287 · 10 <sup>-10</sup>	0.7668	8.302 · 10 <sup>-10</sup>	1.9584
10	1.158 · 10 <sup>-9</sup>	0.7686	1.034 · 10 <sup>-9</sup>	1.9625
0	1.425 · 10 <sup>-9</sup>	0.7684	1.274 · 10 <sup>-9</sup>	1.9622
-10	1.735 · 10 <sup>-9</sup>	0.7697	1.551 · 10 <sup>-9</sup>	1.9651
-20	2.085 · 10 <sup>-9</sup>	0.7623	1.865 · 10 <sup>-9</sup>	1.9483
-30	2.473 · 10 <sup>-9</sup>	0.7615	2.213 · 10 <sup>-9</sup>	1.9462
-40	2.905 · 10 <sup>-9</sup>	0.7598	2.600 · 10 <sup>-9</sup>	1.9425

## Appendix C: Grid dependence and validation against CFD results

In this appendix, details of the grid dependence carried out for the fluid redistribution model of Chapter VII are described.

### C1) Grid dependence

As mentioned in Section 7.5, the effect of the number of channel divisions ( $N_{Block}^x$  and  $N_{Block}^y$ ) on the model's results was systematically addressed by comparing 5 grids characterized by: A) 30×30; B) 60×60; C) 120×120; D) 240×240; E) 480×480 blocks, with a total number of 900, 3600, 14,400, 57,600 and 230,400 blocks, respectively.

For the cross flow configuration at  $P_{in}=34.3$  kPa, Figure C1.1 reports profiles of the  $x$ -velocity component along a line orthogonal to the main flow direction and located 2 cm away from the inlet side, see left broken line in Figure 7.7 (a). The inset shows an enlarged portion of the same plot. It can be observed that maximum differences (grids A vs. E) are less than 0.25 cm/s, and grids C-E yield practically identical results. The discrepancies between consecutive grids decrease with the number of blocks, indicating an asymptotic convergence.

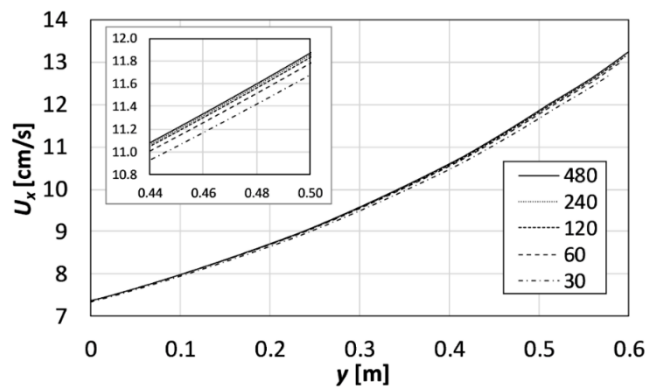


**Figure C1.1** Cross flow configuration at  $P_{in}=34.3$  kPa: profiles of the  $x$  velocity component along a line orthogonal to the main flow direction and located 2 cm away from the inlet, see Figure 7.7 (a). Results obtained with five grids of increasing resolution are reported. The inset shows a magnified portion of the same plot.



A similar comparison for the counter flow configuration is reported in Figure C1.2, which shows profiles of the x-velocity component along a line orthogonal to the main flow direction and located 2 cm upstream of the outlet side, see right broken line in Figure 7. 7 (b). The maximum grid-dependent differences (grids A vs. E) are higher than for the cross flow case (up to  $\sim 4$  cm/s), but are concentrated near the outflow slots. Grids C-E yield very similar results, with maximum differences of  $\sim 0.5$  cm/s ( $\sim 3\%$ ).

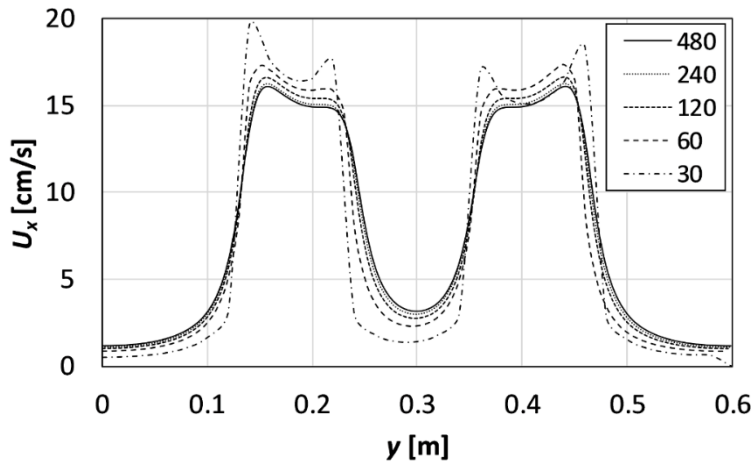


**Figure C1.2** Counter flow configuration at  $P_{in}=34.3$  kPa: pressure profiles along a line orthogonal to the main flow direction and located 2 cm upstream of the outlet, see Figure 7. 7 (b). Results obtained with five grids of increasing resolution are reported.

As far as the computing time is concerned, it typically increased from a few seconds for grid A to  $\sim 80$  h for grid E when simulations were run on a desktop computer equipped with an Intel Core i7-6700 CPU with 32 GB memory. The computing time was significantly lower (about 50%) in the absence of deformation.

## C2) Comparison with CFD results

The reliability of the present mathematical model was verified by comparing results for undeformed channel configurations (TMP=0) with those provided by computational fluid dynamics (CFD) simulations. The commercial software

Ansys CFX® 18.1 was employed. Both cross-flow and counter-current configurations were simulated. The CFD settings were as follows:

- The porous media model was assumed and steady state simulations were performed.
- Values of the permeability and of the resistance loss coefficient were determined by means of a quadratic regression of the undeformed channel characteristics (Figure 7. 5). The permeability was set to  $1.65 \cdot 10^{-9} \text{ m}^2$  and the resistance loss coefficient to  $989 \text{ m}^{-1}$ .
- Free slip wall boundary conditions were set at the upper and lower walls of the channel (representative of membrane surfaces). The latter condition was imposed to avoid viscous fluid-wall interaction, which would lead to erroneous results; in fact, the friction characteristics of the membrane surfaces and profiles are already taken into account by the permeability and resistance coefficients.
- Symmetry or no slip boundary conditions were imposed at the lateral edges of the domain.
- In the case of cross-flow configuration, mean inlet flow velocities of 1, 5 and 10 cm/s were investigated. For the counter flow arrangement, only a mean inlet flow velocity of 10 cm/s was considered.

CFD predictions for pressure and velocity were evaluated and compared with the results of the present model. For example, Figure C2 reports profiles of the relative pressure computed along a line orthogonal to the main flow direction and located 2 cm away from the inlet of a channel in the counter flow configuration at  $P_{in}=18.64 \text{ kPa}$ . Only the three finest grids C, D and E were considered. It can be observed that CFD predictions are practically coincident with the results provided by the finest grid (E,  $480 \times 480$  blocks) but agree fairly well also with those obtained by coarser ( $120 \times 120$  or  $240 \times 240$ ) grids. A similar agreement was obtained also for other locations, the other configuration (*i.e.* cross flow) and various flow velocities, thus confirming the reliability of the present model.

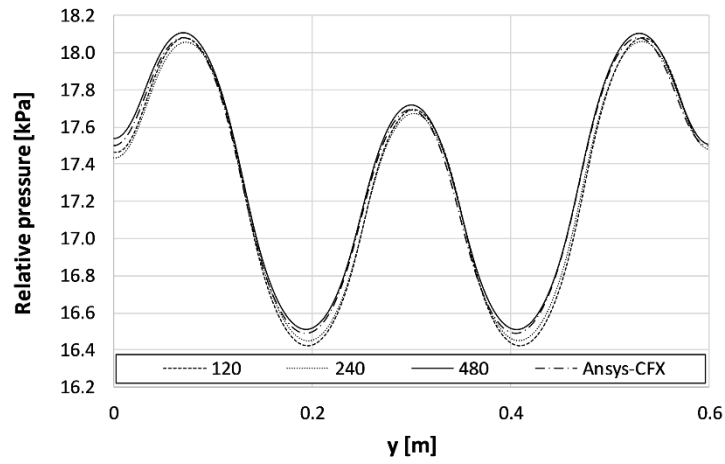


**Figure C2.** Single undeformed channel in counter flow configuration at  $P_{in}=18.64$  kPa: pressure profiles along a line orthogonal to the main flow direction and located 2 cm away from the inlet, see Figure 7. 7 (b). Results obtained with three grids of increasing resolution are compared with CFD predictions.

## **Appendix D: Correlations used for the physical and transport properties of NaCl solutions.**

This appendix reports the correlations for the physical and transport properties of NaCl solutions, used in the model presented in Chapter VIII. In the following equations, the quantities referred to a generic solution SOL, e.g. salt concentration  $C^{SOL}$ , are shortened avoiding the superscripts, thus  $C^{SOL}$  becomes  $C$ .

- Solution density  $\rho$  (kg/m<sup>3</sup>), from [129]:

$$\rho = 5.94 \times 10^{-11} C^3 - 1.032 \times 10^{-6} C^2 + 4.097 \times 10^{-2} C + 997$$

- Solution electrical conductivity  $\kappa$  (S/m), from [129]:

$$\log_{10}(\kappa) = -0.0027373(\log_{10}(C))^3 - 0.0059675(\log_{10}(C))^2 + 0.98994(\log_{10}(C)) - 1.9074 \quad (C \leq 1000)$$

$$\log_{10}(\kappa) = -1.3893(\log_{10}(C))^3 + 13.252(\log_{10}(C))^2 - 41.277(\log_{10}(C)) + 43.011 \quad (C > 1000)$$

- Salt diffusion  $D_{Salt}$  (m<sup>2</sup>/s), from [129]:

$$D_{Salt} = 1.47 \times 10^{-9} + 0.13 \times 10^{-9} C^2 e^{(-C/70)} \quad (C \leq 400)$$

$$D_{Salt} = -2.87262 \times 10^{-21} C^3 + 2.03219 \times 10^{-17} C^2 - 8.44113 \times 10^{-15} C + 1.4705 \times 10^{-9} \quad (C > 400)$$

- Salt activity coefficients  $\gamma$  (dimensionless), from [129]:

$$\gamma = 0.64 + 0.189e^{-C/260} + 0.1605e^{-C/20} \quad (C \leq 1200)$$

$$\gamma = 0.64 + 0.189e^{-C/260} + 0.1605e^{-C/20} + 1.051 \times 10^{-7} (C - 1200)^{1.8} \quad (C > 1200)$$

## NOMENCLATURE

$A$	Area of <i>midplane</i> or membrane active area
$A_k$	Unknown coefficients
$A_{proj}$	Projected membrane surface area
$a$	Side of plate
$\mathbf{a}$	Vector of unknown coefficients
$a'$	Intercepts of piecewise linear approximations
$a_k, \tilde{a}_k$	Unknown coefficients
$B$	Effective torsional rigidity
$b$	Side of plate
$\mathbf{b}$	Vector of unknown coefficients
$b_k, \tilde{b}_k, B_k$	Unknown coefficients
$C^{DIL}, C^{CON}$	Concentration of DIL and CON solutions
$C_{Bulk}^{SOL}, C_{IEM}^{SOL}$	Concentration of generic solution SOL in the bulk and at the membrane-solution interface of a generic IEM
$c, \tilde{c}$	Concentration and periodic concentration component
$c_b, c_w$	Bulk and wall concentrations
$c_i, c_k$	Unknown constants
$D$	Flexural rigidity of isotropic plate
$D_x, D_y$	Plate flexural rigidities associated with $x$ and $y$ directions, respectively
$D_{Salt}$	Salt diffusivity in solution
$D_{Salt}^{IEM}, D_{Salt}^{SOL}$	Salt diffusivity in a generic membrane IEM and in the generic solution SOL
$D_t$	Torsional rigidity of plate
$d_k$	Unknowns coefficients
$E$	Young's modulus of elasticity
$E_{spec}$	Energy consumption per unit volume of product
$E_x, E_y, E_z$	Young's modulus of elasticity associated with $x, y, z$ directions, respectively
$F$	Darcy coefficient normalized to that of void plane channel

$f_{Darcy}$	Darcy coefficient
$\tilde{f}_k$	Plate frequencies
$f_{shadow}$	Shadow factor
$G, G_{xy}, G_{xz}, G_{yz}$	Shear modulus
$H$	Undeformed spacer-less channel thicknesses
$H^{IEM}, H^{SOL}$	Generic IEM membrane and solution SOL thickness
$h$	Thickness of plates and membranes
$h^{SOL}$	Equivalent fluid channel thickness of generic solution SOL
$I$	Overall current
$i_c$	Ionic current density
$J_{Cond.}^{TOT}$	Total conductive salt flux
$J_{Diff}^{TOT}$	Total diffusive salt flux
$J_p$	Apparent product flux
$J_{SALT}^{TOT}$	Total salt flux
$J_{WATER}^{TOT}$	Total water flux
$J_{WATER}^{E.OSM}$	Electro-osmotic flux
$J_{WATER}^{OSM}$	Osmotic water flux
<b>K</b>	Stiffness Matrix
$K_{app}, K$	Apparent permeability and Hydraulic permeability
$K'_{i,j}$	Slopes of piecewise linear approximations
$K_p, K_c$	Large-scale components
$k$	Positive integer
$k_c$	Mass transfer coefficient
$L$	Fluid channel length
$L_{p,IEM}$	Water permeability constant
$l$	Generic length
<b>M</b>	Mass matrices
$M_w$	Water molecular weight
$M_x, M_y, M_{xy}$	Bending and twisting moments of plates
$M, \tilde{M}$	Moment sum functions
$m$	Positive integers
$N_x, N_y,$	In-plane forces
$N_{xy}, N_{yx}$	

$N_x^0, N_y^0,$ $N_{xy}^0, N_{yx}^0$	Initial in-plane forces
$N$	Positive integers
$N_{Block}^x, N_{Block}^y$	Number of rectangular block
$N_{cp}$	Total number of cell pair
$N_p$	Number of points of the deflection functions
$\mathbf{n}$	Outward normal vector
$n, \tilde{n}$	Positive integers
$n_f$	Number of frequencies
$n_h$	Hydration number
$n_x, n_y$	Components of the unitary vector $\mathbf{n}$
$P$	Profiled membrane pitch
$P_{el}$	Electric power consumption
$P_{i,j}$	Pressure value at $i,j$ computing block
$P_{int}, P_{ext}, P_{c,ext}$	Internal, external and concentrated external forces
$\mathbf{p}_n$	Vector of harmonic polynomials
$p, \tilde{p}$	Pressure and periodic pressure component
$Q$	Solution volume flow rate
$\bar{Q}$	Concentrated load
$Q^{CON}, Q^{DIL}$	CON and DIL solution flow rates
$Q_{TOT,av}^{CON}$ and $Q_{TOT,av}^{DIL}$	Average CON and DIL solution flow rates
$Q_k$	Harmonic polynomials
$Q_{TOT,OUTLET}^{DIL}$	Overall diluate outlet flow rate
$\mathbf{q}_n$	Vector of harmonic polynomials
$q$	Vertical distributed load
$\mathbf{R}^{(de,pq)}$	Matrix of elements of partial derivatives of Ritz functions
$R^{CON}, R^{DIL}, R^{SOL}$	Areal resistance of CON, DIL and generic SOL solutions
$R^{CEM}, R^{AEM}, R^{IEM}$	Areal resistance of CEM, AEM and generic IEM membranes
$R_{TOT}, R_{blank}$	Total areal resistance of a cell pair and electrode compartments
$Re$	Reynolds number

$Re_{\tau}$	Friction velocity Reynolds number
Sc	Schmidt number
Sh	Sherwood number
$s$	Main flow direction
$T$	Temperature or Kinetic energy
$t$	time
$U$	Superficial or Approach fluid velocity
$U_{pre-stress}$	External energy of pre-tensioning forces
$U_s$	Superficial velocity associated with $s$ direction
$U_{s,inter}$	Interstitial velocity associated with $s$ direction
$U_{Strain}$	Strain energy
$U_x, U_y$	Superficial velocity associated with $x$ and $y$ directions, respectively
$u$	displacements component
$u_0$	Initial extensions of the body
$W$	Fluid channel Width
$W_{ext}, W_{int}$	Work of external and internal forces
$w$	Displacements components (deflection)
$\mathbf{x}$	Position vector
$x$	Component of Cartesian coordinate system
$y$	Component of Cartesian coordinate system
$V$	Volume of plates or of fluid channels
$V_{Applied}$	Potential voltage drop applied by a power supply
$V_{cp}$	Overall voltage drop over a cell pair
$V_x, V_y$	Shear forces
$v$	Displacements components of plates
$v_0$	Initial extensions of the body
$v_c, v_d$	Velocity of the CON and DIL solutions
$z$	Component of Cartesian coordinate system

**Greek symbols**

$\alpha$	Intrinsic angle of RP profiled membranes
$\alpha_{IEM}$	Perm-selectivity of a generic IEM membrane



$\beta$	Angle of twist rotation
$\gamma$	Curvilinear abscissa
$\gamma_{IEM}^{CON}, \gamma_{IEM}^{DIL}$	Salt activity coefficients in CON and DIL solutions at the interface of a generic IEM membrane
$\gamma_F$	Flow attack angle
$\gamma_{xy}, \gamma_{xz}, \gamma_{yz}$	Shear strains
$\varepsilon_x, \varepsilon_y$	Normal strains in $x$ and $y$ directions
$\boldsymbol{\eta}, \tilde{\boldsymbol{\eta}}$	Vectors of unknown coefficients
$\eta, \eta_{IEM}^{SOL}$	Non-ohmic voltage drop
$\vartheta$	Angle
$\theta$	Polarization coefficient
$\kappa^{SOL}$	Electrical conductivity of the generic SOL
$\lambda$	Eigenvalues
$\mu$	Fluid viscosity
$\nu, \nu_{xy}, \nu_{xz}, \nu_{yz}$	Poisson ratios
$\xi, \tilde{\xi}_i$	Vector of unknown coefficients
$\pi$	Osmotic pressure
$\rho$	Fluid or plate density
$\varsigma$	Angle
$\sigma_x, \sigma_y$	Normal stresses in $x$ and $y$ directions
$\tau, \tau_{xy}, \tau_{xz}, \tau_{yz}$	Shear stresses
$\varphi$	Non-ohmic voltage drop due to fluid concentration gradient
$\phi_j$	pb-2 Rayleigh-Ritz functions
$\chi_x, \chi_y, \chi_{xy}$	Curvature of the <i>midplane</i>
$\psi$	Prandtl function
$\omega$	Warping function
$\tilde{\omega}$	Angular frequency of vibration
$\Gamma$	Generic contour
$\Delta x, \Delta y$	Length and width of rectangular blocks
$\Delta p_{tot}^{CON}, \Delta p_{tot}^{DIL}$	Total pressure drops in the CON and DIL channels
$\Delta p_{dist}^{SOL}$	Distributed pressure drops of a generic solution SOL
$\Pi_{tot}$	Total potential energy
$\Omega$	Area of domain

$\Omega_{ex}$  Potential of external forces

### **Acronyms**

AEM	Anion Exchange membranes
BEM	Boundary element method
BL	Related to concentration boundary layer
Blank	Electrode compartments
CD	Cross direction
CEM	Cation Exchange Membranes
CFD	Computational fluid dynamics
CON	Concentrate solution
CP	Cell pair
DIL	Diluate solution
ED	Electrodialysis
FEM	Finite Element Method
IEM	Generic Ion Exchange Membrane (AEM and CEM)
LEM	Line Element-less Method
MD	Machine direction
PSO	Particle Swarm Optimization
RED	Reverse Electrodialysis
SOL	Generic Solution (CON and DIL)
TMP	Transmembrane pressure
XD	Tensile test at 45° degree direction

## **BIBLIOGRAPHY**

- [1] S. Timoshenko and S. Woinowsky-Krieger, Theory of thin plates and shells, McGraw-Hill, 1959.
- [2] R. Szilard, Theories and Applications of Plate Analysis, John Wiley & Sons, Inc., 2004.
- [3] A. Leissa, Vibrations of plates (NASA SP-160), Washington, DC: Government Printing Office, 1969.
- [4] E. Ventsel and T. Krauthammer, Thin Plates and Shells, Marcel Dekker, Inc., 2001.
- [5] M. Geradin and D. J. Rixen, Mechanical Vibrations: Theory and Application to Structural Dynamics, Chichester: John Wiley & Sons, Ltd, 2015.
- [6] M. Amabili, Nonlinear Vibrations and Stability of Shells and Plates, New York, United States of America: Cambridge University Press, 2008.
- [7] R. M. Jones, Mechanics of composite materials, Taylor & Francis Ltd., 1999.
- [8] S. G. Lekhnitskii, Anisotropic Plates, New York: Gordon and Breach Science Publisher , 1968.
- [9] S. Marcus, Die theorie elastischer gewebe, Berlin, Germany, 1932.
- [10] K. Liew, K. Lam and S. Chow, "Free vibration analysis of rectangular plates using orthogonal plate function," *Computers & Structures*, vol. 34, pp. 79-85, 1990.
- [11] O. Zienkiewicz, The finite element method in engineering science, New York: McGraw-Hill, 1984.
- [12] J. Katsikadelis, Boundary elements: theory and applications, UK: Elsevier Science Ltd, 2002.

- [13] G. Liu, *Meshfree Methods: Moving Beyond the Finite Element Method*, Boca Raton: CRC Press, 2010.
- [14] A. M. Zenkour, "Bending of thin plates with variable-thickness in a hygrothermal environment," *Thin-Walled Structures*, vol. 123, pp. 333-340, 2018.
- [15] A. Reali and H. Gomez, "A modified Kirchhoff plate theory for analyzing thermo-mechanical static and buckling responses of functionally graded material plates," *Thin-Walled Structures*, vol. 117, pp. 113-126, 2017.
- [16] F. Maurin, F. Greco, L. Coox, D. Vandepitte and W. Desmet, "Isogeometric collocation for Kirchhoff-Love plates and shells," *Computer Methods Applied Mechanics*, vol. 329, pp. 396-420, 2018.
- [17] S. Li and W. Liu, "Meshfree and particle methods and their applications," *Applied Mechanics Reviews*, vol. 55, pp. 1-34, 2002.
- [18] J. S. Chen, M. Hillman and S. W. Chi, "Meshfree methods: progress made after 20 years," *Journal of Engineering Mechanics*, vol. 143, 2017.
- [19] S. Çeribaşı, G. Altay and M. Dökmeci, "Static analysis of super elliptical clamped plates by Galerkin's method," *Thin-Walled Structures*, vol. 46, p. 122–127, 2008.
- [20] T. Belytschko, D. Organ and Y. Krongauz, "A coupled finite element–element-free Galerkin method," *Computational Mechanics*, vol. 17 , p. 186–195, 1995.
- [21] S. Atluri and T. Zhu, "New concepts in meshless methods," *International Journal for Numerical Methods in Engineering*, vol. 47, p. 537–556, 2000.
- [22] C. Duarte and J. Oden, "An hp adaptive method using clouds," *Computer Methods in Applied Mechanics and Engineering*, vol. 139, p. 237–262, 1996.
- [23] L. Chen, Y. Cheng and H. Ma, "The complex variable reproducing kernel particle method for the analysis of Kirchhoff plates," *Computational Mechanics*, vol. 55, p. 591–602, 2015 .
- [24] S. Sadamoto, S. Tanaka, K. Taniguchi, M. Ozdemir, T. Bui, C. Murakami and D. Yanagihara, "Buckling analysis of stiffened plate structures by an

- improved meshfree flat shell formulation,” *Thin-Walled Structures*, vol. 117, p. 303–313, 2017.
- [25] V. Leitaó, “A meshless method for Kirchhoff plate bending problems,” *International Journal for Numerical Methods in Engineering*, vol. 52, p. 1107–1130, 2001.
- [26] S. Sadamoto, M. Ozdemir, S. Tanaka, K. Taniguchi, T. Yu and T. Bui, “An effective meshfree reproducing kernel method for buckling analysis of cylindrical shells with and without cutouts,” *Computational Mechanics*, vol. 59, p. 919–932, 2017.
- [27] C. Thai, T. Nguyen, T. Rabczuk and H. Nguyen-Xuan, “An improved moving Kriging meshfree method for plate analysis using a refined plate theory,” *Computers & Structures*, vol. 176, p. 34–49, 2016.
- [28] M. Bitaraf and S. Mohammadi, “Large deflection analysis of flexible plates by the meshless finite point method,” *Thin-Walled Structures*, vol. 48, p. 200–214, 2010.
- [29] C. Thai, A. Ferreira and H. Nguyen-Xuan, “Naturally stabilized nodal integration meshfree formulations for analysis of laminated composite and sandwich plates,” *Composite Structures*, vol. 178, p. 260–276, 2017.
- [30] Y. Liu, Y. Hon and L. Liew, “A meshfree Hermite-type radial point interpolation method for Kirchhoff plate problems,” *International Journal for Numerical Methods in Engineering*, vol. 66, p. 1153–1178, 2006.
- [31] T. Bui, M. Nguyen and C. Zhang, “Buckling analysis of Reissner–Mindlin plates subjected to in-plane edge loads using a shear-locking-free and meshfree method,” *Engineering Analysis with Boundary Elements*, vol. 35, p. 1038–1053, 2011.
- [32] W. Jin, Y. Cheung and O. Zienkiewicz, “Trefftz method for Kirchhoff plate bending problems,” *International Journal for Numerical Methods in Engineering*, vol. 36, p. 765–781, 1993.
- [33] K. Liew and C. Wang, “p2- Rayleigh-Ritz method for general plate analysis,” *Engineering Structures*, vol. 15, pp. 55–60, 1993.

- [34] M. Saadatpou and M. Azhari, "The Galerkin method for static analysis of simply supported plates of general shape," *Computers & Structures*, vol. 69, p. 1–9, 1998.
- [35] M. Di Paola, A. Pirrotta and R. Santoro, "Line element-less method (LEM) for beam torsion solution (truly no-mesh method)," *Acta Mechanica*, pp. 349-364, 2008.
- [36] M. Di Paola, A. Pirrotta and R. Santoro, "De Saint-Venant flexure-torsion problem handled by Line Element-less Method (LEM)," *Acta Mechanica*, pp. 101-118, 2011.
- [37] A. Pirrotta, "LEM for twisted re-entrant angle sections," *Computers and Structures*, pp. 149-155, 2014.
- [38] R. Santoro, "The line element-less method analysis of orthotropic beam for the Saint Venant torsion problem," *International Journal of Mechanical Sciences*, pp. 43-55, 2010.
- [39] R. Santoro, "Solution of De Saint Venant flexure-torsion problem for orthotropic beam via LEM (Line Element-less Method)," *European Journal of Mechanics A/Solids*, pp. 924-939, 2011.
- [40] G. Barone, A. Pirrotta and R. Santoro, "Comparison among three boundary element methods for torsion problems: CPM, CVBEM, LEM," *Engineering Analysis with Boundary Elements*, pp. 895-907, 2011.
- [41] E. Murtha-Smith, "Plate analogy for the torsion problem," *Journal of Engineering Mechanics*, vol. 116, no. 1, pp. 1-17, 1990.
- [42] H. Irschik, "Analogies between bending of plates and torsion problem," *Journal of Engineering Mechanics*, vol. 117, no. 11, pp. 2503-2508, 1991.
- [43] R. Barretta, "Analogies between kirchhoff plates and Saint-Venant beams under torsion," *Acta Mechanica*, vol. 224, pp. 2955-2964, 2013.
- [44] A. Pirrotta and C. Bucher, "Innovative straight formulation for plate in bending," *Computers and Structures*, vol. 180, pp. 117-124, 2017.

- [45] A. Pirrotta, "Evaluation of deflection of a plate using line integrals," *Proceedings of the twelfth international conference on computational structures technology.*, p. Paper 215., 2014.
- [46] A. Pirrotta, "Complex potential function in elasticity theory: shear and torsion solution through line integrals," *Acta Mechanica*, vol. 223, pp. 1251-1259, 2012.
- [47] C. S. Chen, A. S. Muleshkov and M. Golger, "The numerical evaluation of particular solutions for Poisson's equation-a revisit," *Trans. Model Simul.*, vol. 24, 1999.
- [48] M. Golberg, A. Muleshkov, A. Muleshkov, C. Chen and A. Cheng, "Polynomial particular solutions for certain partial differential operators," *Numerical Methods for Partial Differential Equations*, vol. 19, pp. 112-133, 2003.
- [49] A. Abramowitz and L. Stegun, *Handbook of Mathematical Functions: With Formulas, Graphs, and Mathematical Tables*, New York: Dover Publications, 1972.
- [50] S. Lekhnitskii, *Anisotropic plates*, New York: Gordon and Breach, 1968.
- [51] O. Bedair, "Analysis and limit state design of stiffened plates and shells: a world view," *Applied Mechanics Review*, vol. 62:020801, 2009.
- [52] Y. Xing and B. Liu, "New exact solutions for free vibrations of thin orthotropic rectangular plates," *Composite Structures*, vol. 89, pp. 567-74, 2009.
- [53] M. Biancolini, C. Brutti and L. Reccia, "Approximate solution for free vibrations of thin orthotropic plates," *Journal of Sound and Vibration*, vol. 288, p. 321-44., 2005.
- [54] R. Bhat, "Natural frequencies of rectangular plates using characteristic orthogonal polynomials in the Rayleigh-Ritz method," *Journal of Sound and Vibration*, vol. 102, p. 493-9., 1985.
- [55] S. Dickinson and A. Di Blasio, "On the use of orthogonal polynomials in the Rayleigh-Ritz method for the study of the flexural vibration and

- buckling of isotropic and orthotropic rectangular plates,” *Journal of Sound and Vibration*, vol. 108, p. 51–62, 1986.
- [56] C. Tsay and J. Reddy, “Bending, stability and free vibrations of thin orthotropic plates by simplified mixed finite elements,” *Journal of Sound and Vibration*, vol. 59, p. 307–11, 1978.
- [57] H. AL-Khaiat, “Free vibration analysis of orthotropic plates by the initial value method,” *Computers & Structures*, vol. 33, p. 1431–5, 1989.
- [58] Y. Chen, “Evaluation of fundamental vibration frequency of an orthotropic bending plate by using an iterative approach,” *Computer Methods in Applied Mechanics and Engineering*, vol. 161, p. 289–96, 1998.
- [59] N. Bardell, J. Dunsdon and R. Langley, “Free vibration analysis of thin coplanar rectangular plate assemblies – Part I: theory, and initial results for specially orthotropic plates,” *Composite Structures*, vol. 34, p. 129–43, 1996.
- [60] C. Kim, “Natural frequencies of orthotropic, elliptical and circular plates,” *Journal of Sound and Vibration*, vol. 259, pp. 733-745, 2003.
- [61] C. Kim and S. Dickinson, “The free flexural vibration of isotropic and orthotropic general triangular shaped plates,” *Journal of Sound and Vibration*, pp. 383-403, 1992.
- [62] A. Farag and A. Ashour, “Free vibration of orthotropic skew plates,” *Journal of Vibration and Acoustics*, vol. 122, p. 313–7, 2000.
- [63] K. Liew and L. K.Y., “A Rayleigh-Ritz approach to transverse vibration of isotropic and anisotropic trapezoidal plates using orthogonal plate functions,” *International Journal of Solids and Structures*, vol. 27, p. 189–203, 1991.
- [64] K. Liew, “Response of plates of arbitrary shape subject to static loading,” *Journal of Engineering Mechanics*, vol. 118, p. 1783–94, 1992.
- [65] K. Liew, “Vibration analysis of plates by the pb-2 Rayleigh-Ritz method: mixed boundary conditions, reentrant corners, and internal curved



- supports.,” *Mechanics of Structures and Machines*, vol. 20, p. 281–92, 1992.
- [66] A. Milazzo and V. Oliveri, “Post-buckling analysis of cracked multilayered composite plates by pb-2 Rayleigh-Ritz method,” *Composite Structures*, vol. 132, p. 75–86, 2015.
- [67] C. Kim and C. Hong, “Buckling of unbalanced anisotropic sandwich plates with finite bending stiffness,” *AIAA Journal*, vol. 26, pp. 982-988, 1988.
- [68] L. Carlsson and P. R.B., *Experimental characterization of advanced composite materials*, New York: Prentice-Hall, 1987.
- [69] F. Moussu and M. Nivoit, “Determination of elastic constants of orthotropic plates by a modal analysis/method of superposition,” *Journal of Sound and Vibration*, vol. 165, pp. 149-163, 1993.
- [70] L. G. R. Deobald, “Determination of elastic constants of orthotropic plates by a modal analysis/Rayleigh-Ritz technique,” *Journal of Sound and Vibration*, vol. 124, pp. 269-283, 1988.
- [71] C. Mota Soares, M. Moreira de Freitas, A. Araujo and P. Pedersen, “Identification of material properties of composite plate specimens,” *Composite Structures*, vol. 25, pp. 277-285, 1993.
- [72] D. Larsson, “Using modal analysis for estimation of anisotropic material constants,” *Journal of Engineering Mechanics*, vol. 123, pp. 222-229, 1997.
- [73] J. Cunha, S. Cogan and C. Berthod, “Application of genetic algorithm for the identification of elastic constants of composite materials from dynamic tests,” *International Journal for Numerical Method in Engineering*, vol. 30, pp. 279-289, 1999.
- [74] R. Rikards, A. Chate, W. Steinchen, A. Kessler and A. Bledzki, “Method for identification of elastic properties of laminates based on experiment design,” *Composites Part B: Engineering*, vol. 30, pp. 279-289, 1999.
- [75] S. Hwang and C. Chang, “Determination of elastic constants of materials by vibration testing,” *Composites Structures*, vol. 49, pp. 183-190, 2000.

- [76] S. Chakraborty, M. Mukhopadhyay and O. Sha, "Determination of physical parameters of stiffened plates using genetic algorithm," *Journal of Computing in Civil Engineering*, vol. 16, pp. 206-221, 2002.
- [77] C. Maletta and L. Pagnotta, "On the determination of mechanical properties of composite laminates using genetic algorithm," *International Journal of Mechanics and Materials in Design*, vol. 1, pp. 199-211, 2004.
- [78] S. Hwang, J. Wu and R. He, "Determination Identification of effective elastic constants of composite plates based on a hybrid genetic algorithm," *Composite Structures*, vol. 90, pp. 217-224, 2009.
- [79] F. Daghia, S. De Miranda, F. Ubertini and E. Viola, "Estimation of elastic constants of thick laminated plates within a Bayesian framework," *Composite Structures*, vol. 80, pp. 461-473, 2007.
- [80] J. Auzins, A. Chate, R. Rikards and E. Skukis, "Metamodeling and robust minimization approach for the identification of elastic properties of composites by vibration method," *ZAMM - Journal of Applied Mathematics and Mechanics*, vol. 10, pp. 1012-1026, 2015.
- [81] J. Kennedy and R. Eberhart, "Particle swarm optimization," *Proceedings of IEEE international conference on neural networks*, vol. IV, pp. 1942-1948, November, 1995.
- [82] R. Perez and K. Behdinan, "Particle swarm approach for structural design optimization," *Computers & Structures*, vol. 85, pp. 1579-1588, 2007.
- [83] V. Plevris and M. Papadrakakis, "A hybrid particle swarm-gradient algorithm for global structural optimization," *Computer-Aided Civil and Infrastructure Engineering*, vol. 26, p. 48-68, 2011.
- [84] A. Di Matteo, F. Lo Iacono, G. Navarra and A. Pirrotta, "Direct evaluation of the equivalent linear damping for TLCD systems in random vibration for pre-design purposes," *International Journal of Non-Linear Mechanics*, vol. 63, pp. 19-30, 2014.
- [85] A. Di Matteo, T. Furtmuller, C. Adam and A. Pirrotta, "Optimal design of tuned liquid column dampers for seismic response control of base-isolated structures," *Acta Mechanica*, vol. 229, pp. 437-454, 2018.

- [86] M. Dorigo, V. Maniezzo and A. Colorni, "The ant system: optimization by a colony of cooperating agents," *IEEE Transactions on Systems, Man, and Cybernetics, Part B*, vol. 26, p. 29–41, 1996.
- [87] G. Cottone, G. Fileccia Scimemi and A. Pirrotta, " $\alpha$ -stable distributions for better performance of ACO in detecting damage on not well spaced frequency systems," *Probabilistic Engineering Mechanics*, vol. 35, pp. 29-36, 2014.
- [88] M. Grediac and P. Paris, "Direct identification of elastic constants of anisotropic plates by modal analysis: theoretical and numerical aspects," *Journal of Sound and Vibration*, vol. 193, pp. 401-415, 1996.
- [89] Y. Aoki and W. Maysenholder, "Experimental and numerical assessment of the equivalent-orthotropic-thin-plate model for bending of corrugated panels," *International Journal of Solids and Structures*, vol. 108, pp. 11-23, 2017.
- [90] N. Huffington, "Theoretical determination of rigidity properties of orthogonally stiffened plates," *Journal of Mechanics*, vol. 26, pp. 15-20, 1956.
- [91] H. Hoppman, N. Huffington and L. Magness, "A study of orthogonally stiffened plates," *Journal of Applied Mechanics*, vol. 23, pp. 243-250, 1956.
- [92] W. Hoppmann and M. Baltimore, "Bending of orthogonally stiffened plates," *Journal of Applied Mechanics*, vol. 22, pp. 267-271, 1955.
- [93] W. Hoppmann, L. Magness and M. Baltimore, "Nodal patterns of the free flexural vibrations of stiffened plates," *Journal of Applied Mechanics*, vol. 22, pp. 526-530, 1956.
- [94] Y. Luan, M. Ohlrich and F. Jacobsen, "Improvements of the smearing technique for cross-stiffened thin rectangular plates," *Journal of Sound and Vibration*, vol. 330, pp. 4274-4286, 2011.
- [95] H. Irschik, "A boundary-integral equation method for bending of orthotropic plates," *International Journal of Solids and Structures*, vol. 20, pp. 245-255, 1984.

- [96] H. Yoshihara and M. Yoshinobu, "Effects of specimen configuration and measurement method of strain on the characterization of tensile properties of paper," *Journal of Wood Science*, vol. 60, p. 287–293, 2014.
- [97] G. A. Baum and C. Habeger, "On-line measurement of paper mechanical properties," *IPC technical paper series*, no. 91, 1980.
- [98] R. W. Mann, G. A. Baum and C. C. Habeger, "Determination of all nine orthotropic elastic constants," *IPC technical paper series*, no. 84, 1979.
- [99] T. Yokoyama and K. Nakai, "Evaluation of in-plane orthotropic elastic constants of paper and paperboard," *2007 SEM Annual Conference & Exposition on Experimental and Applied Mechanics*, 2007.
- [100] T. Yokoyama, k. Nakai and T. Jnagaki, "Orientation Dependence of In-plane Tensile Properties of Paper: Experiments and Theories," *Journal of mechanical engineering and sciences*, vol. 9, pp. 86-91, 2009.
- [101] J. Vlassak and W. Nix, "A new bulge test technique for the determination of Young's modulus and Poisson's ratio of thin films," *Journal of Material Research*, vol. 7, pp. 3242-3249, 1992.
- [102] D. Maier-Schneider, J. Maibacj and E. Obermeier, "A New Analytical Solution for the Load-Deflection of Square Membranes," *Journal of Microelectromechanical systems*, vol. 4, no. 4, pp. 238-241, 1995.
- [103] F. M. Davis, Y. Luo, S. Avril, A. Duprey and J. Lu, "Local mechanical properties of human ascending thoracic aneurysms," *Journal of the Mechanical Behaviour of biomedical materials*, vol. 61, pp. 235-249, 2016.
- [104] T. K. Tonge, L. S. Atlan, L. M. Voo and T. D. Nguyen, "Full-field bulge test for planar anisotropic tissues: Part I- Experimental methods applied to human skin tissue," *Acta Biomaterialia*, vol. 9, pp. 5913-5925, 2013.
- [105] H. Youssef, A. Ferrand, P. Calmon, P. Pons and R. Plana, "Methods to improve reliability of bulge test technique to extract mechanical properties of thin films," *Microelectronics Reliability*, vol. 50, pp. 1888-1893, 2010.
- [106] O. Pabst, M. Schiffer, E. Obermeier, T. Tekin, K. D. Lang and H. Hgo, "Measurement of Young's modulus and residual stress of thin SiC layers

- for MEMS high temperature applications,” *Microsystem Technologies*, vol. 18, pp. 945-953, 2012.
- [107] M. D. Larson, C. J. Simonson, R. W. Besant and P. W. Gibson, “The elastic and moisture transfer properties of polyethylene and polypropylene membranes for use in liquid-to-air energy exchangers,” *Journal of Membrane Science*, vol. 302, pp. 136-149, 2007.
- [108] O. Tabata, K. Kawahata, S. Sugiyama and I. Igarashi, “Mechanical Property Measurements of thin films using Load-Deflection of Composite Rectangular Membranes,” *Sensors and Actuators*, vol. 20, pp. 135-141, 1989.
- [109] J. Y. Pan, P. Lin and F. Maseeh, “Verification of fem analysis of load-deflection methods for measuring mechanical properties of thin films,” *Microsystems Technology Laboratories*, pp. 70-73, 1990.
- [110] S. Chucheepsakul, S. Kaewunruen and A. Suwanarat, “Large deflection analysis of orthotropic, elliptic membranes,” *Structural Engineering and Mechanics*, vol. 31, no. 6, pp. 625-638, 2009.
- [111] R. Bouzidi and A. L. Van, “Numerical solution of hyperelastic membranes by energy minimization,” *Computers and Structures*, vol. 82, pp. 1961-1969, 2004.
- [112] J. Valdés, J. Miquel and E. Oñate, “Non linear finite element analysis of orthotropic and prestressed membrane structures,” *Finite Elements in Analysis and Design*, vol. 45, pp. 395-404, 2009.
- [113] T. Yokoyama and K. Nakai, “Evaluation of in-plane orthotropic elastic constants of paper and paperboard,” *SEM Annual Conference & Exposition on Experimental and Applied Mechanics*, 2007.
- [114] A. Campione, L. Gurreri, M. Ciofalo, G. Micale, A. Tamburini and A. Cipollina, “Electrodialysis for water desalination: A critical assessment of recent developments on process fundamentals, models and applications,” *Desalination*, vol. 434, pp. 121-160, 2018.
- [115] G. Dufton, S. Mikhaylin, S. Gaaloul and L. Bazinet, “Positive Impact of Pulsed Electric Field on Lactic Acid Removal, Demineralization and

- Membrane Scaling during Acid Whey Electrodialysis,” *International Journal of Molecular Sciences*, vol. 20, no. 797, 2019.
- [116] R. Tufa, J. Hnát, M. Němeček, R. Kodým, E. Curcio and K. Bouzek, “Hydrogen production from industrial wastewaters: An integrated reverse electrodialysis-Water electrolysis energy system,” *Journal of Cleaner Production*, vol. 203, pp. 418-426, 2018.
- [117] H. Strathmann, “Electrodialysis, a mature technology with a multitude of new applications,” *Desalination*, vol. 264, pp. 268-288, 2010.
- [118] Y. Mei and C. Tang, “Recent developments and future perspectives of reverse electrodialysis technology: A review,” *Desalination*, vol. 425, pp. 156-174, 2018.
- [119] S. Pawlowski, J. Crespo and S. Velizarov, “Profiled Ion Exchange Membranes: A Comprehensible Review,” *International Journal of Molecular Sciences*, vol. 20, no. 165, 2019.
- [120] V. Nikonenko, A. Kovalenko, M. Urtenov, N. Pismenskaya, J. Han, P. Sistat and G. Pourcelly, “Desalination at overlimiting currents: State-of-the-art and perspectives,” *Desalination*, vol. 342, pp. 85-106, 2014.
- [121] S. Pawlowski, V. Geraldes, J. Crespo and S. Velizarov, “Computational fluid dynamics (CFD) assisted analysis of profiled membranes performance in reverse electrodialysis,” *Journal of Membrane Science*, vol. 502, pp. 179-190, 2016.
- [122] J. Tadimeti, V. Kurian, A. Chandra and S. Chattopadhyay, “Corrugated membrane surfaces for effective ion transport in electrodialysis,” *Journal of Membrane Science*, vol. 499, pp. 418-428, 2016.
- [123] L. Gurreri, M. Ciofalo, A. Cipollina, A. Tamburini, W. Van Baak and G. Micale, “CFD modelling of profiled-membrane channels for reverse electrodialysis,” *Desalination and Water Treatment*, vol. 55, pp. 3404-3423, 2015.
- [124] C. Larchet, V. Zabolotsky, N. Pismenskaya, V. Nikonenko, A. Tskhay, K. Tastanov and G. Pourcelly, “Comparison of different ED stack

- conceptions when applied for drinking water production from brackish waters,” *Desalination*, vol. 222, pp. 489-496, 2008.
- [125] D. Vermaas, M. Saakes and K. Nijmeijer, “Power generation using profiled membranes in reverse electrodialysis,” *Journal of Membrane Science*, Vols. 385-386, pp. 234-242, 2011.
- [126] D. Vermaas, M. Saakes and K. Nijmeijer, “Enhanced mixing in the diffusive boundary layer for energy generation in reverse electrodialysis,” *Journal of Membrane Science*, vol. 453, pp. 312-319, 2014.
- [127] E. Güler, R. Elizen, M. Saakes and K. Nijmeijer, “Micro-structured membranes for electricity generation by reverse electrodialysis,” *Journal of Membrane Science*, vol. 458, pp. 136-148, 2014.
- [128] S. Pawlowski, T. Rijnaarts, M. Saakes, K. Nijmeijer, J. Crespo and S. Velizarov, “Improved fluid mixing and power density in reverse electrodialysis stacks with chevron-profiled membranes,” *Journal of Membrane Science*, vol. 531, pp. 111-121, 2017.
- [129] M. La Cerva, M. Di Liberto, L. Gurreri, A. Tamburini, A. Cipollina, G. Micale and M. Ciofalo, “Coupling CFD with a one-dimensional model to predict the performance of reverse electrodialysis stacks,” *Journal of Membrane Science*, vol. 541, pp. 595-610, 2017.
- [130] Q. She, X. Jin and C. Tang, “Osmotic power production from salinity gradient resource by pressure retarded osmosis: Effects of operating conditions and reverse solute diffusion,” *Journal of Membrane Science*, Vols. 401-402, pp. 262-273, 2012.
- [131] Q. She, D. Hou, J. Liu, K. Tan and C. Tang, “Effect of feed spacer induced membrane deformation in the performance of pressure retarded osmosis (PRO): Implications for PRO process operation,” *Journal of Membrane Science*, vol. 445, pp. 170-182, 2013.
- [132] A. Karabelas, C. Koutsou and D. Sioutopoulos, “Comprehensive performance assessment of spacers in spiral-wound membrane modules accounting for compressibility effects,” *Journal of Membrane Science*, vol. 549, pp. 602-615, 2018.

- [133] S. Huang, "Laminar flow and heat transfer in plate membrane channels: Effects of the deformation heights," *International Journal of Thermal Sciences*, vol. 109, pp. 44-53, 2016.
- [134] Z. Shi and X. Wang, "A numerical study of flow crossover between adjacent flow channels in a proton exchange membrane fuel cell with serpentine flow field," *Journal of Power Sources*, vol. 185, pp. 985-992, 2008.
- [135] Y. Zhou, K. Jiao, Q. Du, Y. Yin and X. Li, "Gas diffusion layer deformation and its effect on the transport characteristics and performance of proton exchange membrane fuel cell," *International Journal of Hydrogen Energy*, vol. 38, pp. 12891-12903, 2013.
- [136] J. Hereijgers, H. Ottevaere, T. Breugelmans and W. De Malsche, "Membrane deflection in a flat membrane microcontactor: Experimental study of spacer features," *Journal of Membrane Science*, vol. 504, pp. 153-161, 2016.
- [137] J. Moreno, E. Slouwerhof, D. Vermaas, M. Saakes and K. Nijmeijer, "The Breathing Cell: Cyclic Intermembrane Distance Variation in Reverse Electrodialysis," *Environmental Science & Technology*, vol. 50, pp. 11386-11393, 2016.
- [138] Y. Tanaka, "Pressure distribution, hydrodynamics, mass transport and solution leakage in an ion-exchange membrane electro dialyzer," *Journal of Membrane Science*, vol. 234, pp. 23-39, 2004.
- [139] Y. Tanaka, "Overall mass transport and solution leakage in an ion-exchange membrane electro dialyzer," *Journal of Membrane Science*, vol. 235, pp. 15-24, 2004.
- [140] S. Hong, C. Kim, K. Hwang, J. Han, H. Kim, N. Jeong and K. Choi, "Experimental and numerical studies on pressure drop in reverse electro dialysis: Effect of unit cell configuration," *Journal of Mechanical Science and Technology*, vol. 30, pp. 5287-5292, 2016.
- [141] A. Tamburini, A. Cipollina, M. Tedesco, L. Gurreri, M. Ciofalo and G. Micale, "The REAPower Project: Power Production From Saline Waters and Concentrated Brines," in *Current Trends and Future Developments*



- on (*Bio-*) *Membranes*, Amsterdam, The Netherlands, Elsevier, 2019, p. 407–448.
- [142] M. Tedesco, A. Cipollina, A. Tamburini and G. Micale, “Towards 1 kW power production in a reverse electrodialysis pilot plant with saline waters and concentrated brines,” *Journal of Membrane Science*, vol. 522, pp. 226-236, 2017.
- [143] N. Wright, S. Shah, S. Amrose and A. Winter, “A robust model of brackish water electrodialysis desalination with experimental comparison at different size scales,” *Desalination*, vol. 443, pp. 27-43, 2018.
- [144] R. Long, B. Li, Z. Liu and W. Liu, “Performance analysis of reverse electrodialysis stacks: Channel geometry and flow rate optimization,” *Energy*, vol. 158, pp. 427-436, 2018.
- [145] M. Ciofalo, M. La Cerva, M. Di Liberto, L. Gurreri, A. Cipollina and G. Micale, “Optimization of net power density in Reverse Electrodialysis,” *Energy*, vol. 181, pp. 576-588, 2019.
- [146] M. Bdiri, L. Dammak, C. Larchet, F. Hellal, M. Porozhnyy, E. Nevakshenova, N. Pismenskaya and V. Nikonenko, “Characterization and cleaning of anion-exchange membranes used in electrodialysis of polyphenol-containing food industry solutions; comparison with cation-exchange membranes,” *Separation and Purification Technology*, vol. 210, pp. 636-650, 2019.
- [147] W. Garcia-Vasquez, L. Dammak, C. Larchet, V. Nikonenko, N. Pismenskaya and D. Grande, “Evolution of anion-exchange membrane properties in a full scale electrodialysis stack,” *Journal of Membrane Science*, vol. 446, pp. 255-265, 2013.
- [148] W. Garcia-Vasquez, R. Ghalloussi, L. Dammak, C. Larchet, V. Nikonenko and D. Grande, “Structure and properties of heterogeneous and homogeneous ion-exchange membranes subjected to ageing in sodium hypochlorite,” *Journal of Membrane Science*, vol. 452, pp. 104-116, 2014.
- [149] W. Garcia-Vasquez, L. Dammak, C. Larchet, V. Nikonenko and D. Grande, “Effect of acid-base cleaning procedure on structure and

- properties of anion-exchange membranes used in electrodialysis,” *Journal of Membrane Science*, vol. 507, pp. 12-23, 2016.
- [150] C. Klaysom, S. Moon, B. Ladewig, G. Lu and L. Wang, “Preparation of porous ion-exchange membranes (IEMs) and their characterizations,” *Journal of Membrane Science*, vol. 371, pp. 37-44, 2011.
- [151] J. Křivčík, D. Neděla and R. Válek, “Ion-exchange membrane reinforcing,” *Desalination and Water Treatment*, vol. 56, pp. 3214-3219, 2015.
- [152] A. Kusoglu, A. Karlsson, M. Santare, S. Cleghorn and W. Johnson, “Mechanical behavior of fuel cell membranes under humidity cycles and effect of swelling anisotropy on the fatigue stresses,” *Journal of Power Sources*, vol. 170, pp. 345-358, 2007.
- [153] E. Safronova, D. Golubenko, N. Shevlyakova, M. D’yakova, V. Tverskoi, L. Dammak, D. Grande and A. Yaroslavtsev, “New cation-exchange membranes based on cross-linked sulfonated polystyrene and polyethylene for power generation systems,” *Journal of Membrane Science*, vol. 515, pp. 196-203, 2016.
- [154] R. Solasi, Y. Zou, X. Huang and K. Reifsnider, “A time and hydration dependent viscoplastic model for polyelectrolyte membranes in fuel cells,” *Mechanics of Time-Dependent Materials*, vol. 12, pp. 15-30, 2008.
- [155] Y. Tang, A. Karlsson, M. Santare, M. Gilbert, S. Cleghorn and W. Johnson, “An experimental investigation of humidity and temperature effects on the mechanical properties of perfluorosulfonic acid membrane,” *Materials Science and Engineering: A*, vol. 425, pp. 297-304, 2006.
- [156] M. Vandiver, B. Caire, J. Carver, K. Waldrop, M. Hibbs, J. Varcoe, A. Herring and M. Liberatore, “Mechanical Characterization of Anion Exchange Membranes by Extensional Rheology under Controlled Hydration,” *Journal of The Electrochemical Society*, vol. 161, p. H677–H683, 2014.
- [157] R. Ghalloussi, W. Garcia-Vasquez, N. Bellakhal, C. Larchet, L. Dammak, P. Huguet and D. Grande, “Ageing of ion-exchange membranes used in electrodialysis: Investigation of static parameters, electrolyte permeability

and tensile strength,” *Separation and Purification Technology*, vol. 80, pp. 270-275, 2011.

- [158] R. Narducci, J. Chailan, A. Fahs, L. Pasquini, M. Di Vona and P. Knauth, “Mechanical properties of anion exchange membranes by combination of tensile stress-strain tests and dynamic mechanical analysis,” *Journal of Polymer Science Part B: Polymer Physics*, vol. 54, pp. 1180-1187, 2016.
- [159] R. Nagarale, G. Gohil and V. Shahi, “Recent developments on ion-exchange membranes and electro-membrane processes,” *Advances in Colloid and Interface Science*, vol. 119, pp. 97-130, 2006.
- [160] J. Ran, L. Wu, Y. He, Z. Yang, Y. Wang, C. Jiang, L. Ge, E. Bakangura and T. Xu, “Ion exchange membranes: New developments and applications,” *Journal of Membrane Science*, vol. 522, pp. 267-291, 2017.
- [161] J. Hong, B. Zhang, S. Glabman, N. Uzal, X. Dou, H. Zhang, X. Wei and Y. Chen, “Potential ion exchange membranes and system performance in reverse electrodialysis for power generation: A review,” *Journal of Membrane Science*, vol. 486, pp. 71-88, 2015.
- [162] M. Tedesco, H. Hamelers and P. Biesheuvel, “Nernst-Planck transport theory for (reverse) electrodialysis: III. Optimal membrane thickness for enhanced process performance,” *Journal of Membrane Science*, vol. 565, pp. 480-487, 2018.
- [163] R. Tufa, S. Pawlowski, J. Veerman, K. Bouzek, E. Fontananova, G. Di Profio, S. Velizarov, J. Goulao Crespo, K. Nijmeijer and E. Curcio, “Progress and prospects in reverse electrodialysis for salinity gradient energy conversion and storage,” *Applied Energy*, vol. 225, pp. 290-331, 2018.
- [164] M. La Cerva, L. Gurreri, M. Tedesco, A. Cipollina, M. Ciofalo, A. Tamburini and G. Micale, “Determination of limiting current density and current efficiency in electrodialysis units,” *Desalination*, vol. 445, pp. 138-148, 2018.
- [165] A. Campione, A. Cipollina, I. Bogle, L. Gurreri, A. Tamburini, M. Tedesco and G. Micale, “A hierarchical model for novel schemes of electrodialysis desalination,” *Desalination*, vol. 465, pp. 79-93, 2019.

- [166] G. Doornbusch, M. Tedesco, J. Post, Z. Borneman and K. Nijmeijer, “Experimental investigation of multistage electro dialysis for seawater desalination,” *Desalination*, vol. 464, pp. 105-114, 2019.
- [167] K. Iyengar and M. Naqvi, “Large deflections of rectangular plates,” *International Journal of Non-Linear Mechanics*, vol. 1, pp. 109-122, 1966.
- [168] J. Chiapello and M. Bernard, “Improved spacer design and cost reduction in an electro dialysis system,” *Journal of Membrane Science*, vol. 80, pp. 251-256, 1993.
- [169] D. Vermaas, M. Saakes and K. Nijmeijer, “Doubled power density from salinity gradients at reduced intermembrane distance,” *Environmental Science & Technology*, vol. 45, pp. 7089-7095, 2011.
- [170] A. von Gottberg, “New High-Performance Spacers in Electro- Dialysis Reversal (EDR) Systems,” in *In Proceedings of the 1998 AWWA Annual Conference*, Dallas, TX, USA., 21–25 June 1998..
- [171] G. Schock and A. Miquel, “Mass transfer and pressure loss in spiral wound modules,” *Desalination*, vol. 64, pp. 339-352, 1987.
- [172] F. Li, W. Meindersma, A. B. de Haan and T. Reith, “Optimization of commercial net spacers in spiral wound membrane modules,” *Journal of Membrane Science*, vol. 208, p. 289–302, 2002.
- [173] F. Li, W. Meindersma, A. de Haan and T. Reith, “Experimental validation of CFD mass transfer simulations in flat channels with non-woven net spacers,” *Journal of Membrane Science*, vol. 232 , p. 19–30, 2004.
- [174] A. Da Costa, A. Fane and D. Wiley, “Spacer characterization and pressure drop modelling in spacer-filled channels for ultrafiltration,” *Journal of Membrane Science*, vol. 87, pp. 79-98, 1994.
- [175] C. Koutsou, S. Yiantsios and A. Karabelas, “Direct numerical simulation of flow in spacer-filled channels: effect of spacer geometrical characteristics,” *Journal of Membrane Science*, vol. 291 , p. 2007, 53-69.
- [176] G. Fimbres-Weihs and D. Wiley, “Review of 3D CFD modeling of flow and mass transfer in narrow spacer-filled channels in membrane

- modules,” *Chemical Engineering and Processing*, vol. 49, pp. 759-781, 2010.
- [177] Y. Winograd, A. Solan and M. Toren, “Mass transfer in narrow channels in the presence of turbulence promoters,” *Desalination*, vol. 13, pp. 171-186, 1973.
- [178] S. K. Karode and A. Kumar, “Flow visualization through spacer filled channels by computational fluid dynamics I. Pressure drop and shear rate calculations for flat sheet geometry,” *Journal of Membrane Science*, vol. 193, pp. 69-84, 2001.
- [179] C. P. Koutsou, S. Yiantsios and A. J. Karabelas, “A numerical and experimental study of mass transfer in spacer-filled channels: Effects of spacer geometrical characteristics and Schmidt number,” *Journal of Membrane Science*, vol. 326, pp. 234-251, 2009.
- [180] J. Schwinge, D. Wiley and D. Fletcher, “Simulation of the Flow around Spacer Filaments between Channel Walls. 2. Mass-Transfer Enhancement,” *Industrial & Engineering Chemistry Research*, vol. 41, pp. 4879-4888, 2002.
- [181] L. Gurreri, A. Tamburini, A. Cipollina, G. Micale and M. Ciofalo, “CFD prediction of concentration polarization phenomena in spacer-filled channels for reverse electro dialysis,” *Journal of Membrane Science*, vol. 468, pp. 133-148, 2014.
- [182] L. Gurreri, A. Tamburini, A. Cipollina, G. Micale and M. Ciofalo, “Pressure drop at low Reynolds numbers in woven-spacer-filled channels for membrane processes: CFD prediction and experimental validation,” *Desalination and Water Treatment*, vol. 61, pp. 170-182, 2017.
- [183] M. Ciofalo, F. Ponzio, A. Tamburini, A. Cipollina and G. Micale, “Unsteadiness and transition to turbulence in woven spacer filled channels for Membrane Distillation,” *Journal of Physics: Conference Series*, vol. 796, no. 012003, 2017.
- [184] A. Sonin and R. Probstein, “A hydrodynamic theory of desalination by electro dialysis,” *Desalination*, vol. 5, pp. 293-329, 1968.

- [185] J. Newman and K. Thomas-Alyea, *Electrochemical Systems*, Hoboken, NJ, USA: John Wiley & Sons, Inc., 2004.
- [186] A. Nakayama, Y. Sano, X. Bai and K. Tado, "A boundary layer analysis for determination of the limiting current density in an electro dialysis desalination," *Desalination*, vol. 404, pp. 41-49, 2017.
- [187] M. Ciofalo, M. La Cerva, M. Di Liberto and A. Tamburini, "Influence of the boundary conditions on heat and mass transfer in spacer-filled channels," *Journal of Physics: Conference Series*, vol. 923, no. 012053, 2017.
- [188] M. Dirkse, W. V. Loon, J. W. Post, J. Veeman and G. Bot, "Extending potential flow modelling of flat-sheet geometries as applied in membrane-based systems," *Journal of Membrane Science*, vol. 325, pp. 537-545, 2008.
- [189] M. Kostoglou and A. J. Karabelas, "On the Fluid Mechanics of Spiral-Wound Membrane Modules," *Industrial & Engineering Chemistry Research*, vol. 48, pp. 10025-10036, 2009.
- [190] M. Kostoglou and A. Karabelas, "Mathematical analysis of the meso-scale flow field in spiral-wound membrane modules," *Industrial & Engineering Chemistry Research*, vol. 50, pp. 4653-4666, 2011.
- [191] R. Kodým, F. Vlasák, D. Šnita, A. Černín and K. Bouzek, "Spatially two-dimensional mathematical model of the flow hydrodynamics in a channel filled with a net-like spacer," *Journal of Membrane Science*, vol. 368, pp. 171-183, 2011.
- [192] P. Pánek, R. Kodým, D. Šnita and K. Bouzeka, "Spatially two-dimensional mathematical model of the flow hydrodynamics in a spacer-filled channel – The effect of inertial forces," *Journal of membrane science*, vol. 492, pp. 588-599, 2015.
- [193] S. Irmay, "On the theoretical derivation of Darcy and Forchheimer formulas," *Eos Transactions American Geophysical Union*, vol. 39, pp. 702-707, 1958.
- [194] M. Tedesco, P. Mazzola, A. Tamburini, G. Micale, I. Bogle, M. Papapetrou and A. Cipollina, "Analysis and simulation of scale-up

- potentials in reverse electrodialysis,” *Desalination and Water Treatment*, vol. 55, pp. 3391-3403, 2014.
- [195] J. Moreno, S. Grasman, R. Van Engelen and K. Nijmeijer, “Upscaling Reverse Electrodialysis,” *Environmental Science & Technology*, vol. 52, pp. 10856-10863, 2018.
- [196] H. Lee, F. Sarfert, H. Strathmann and S. Moon, “Designing of an electrodialysis desalination plant,” *Desalination*, vol. 142, p. 267–286, 2002.
- [197] M. Sadrzadeh, A. Kaviani and T. Mohammadi, “Mathematical modeling of desalination by electrodialysis,” *Desalination*, vol. 206, p. 538–546, 2007.
- [198] P. Pintauro and D. Bennion, “Mass transport of electrolytes in membranes. 1. Development of mathematical transport model,” *Industrial & Engineering Chemistry Fundamentals*, vol. 23, p. 230–234, 1984.
- [199] J. Wesselingh, P. Vonk and G. Kraaijeveld, “Exploring the Maxwell-Stefan description of ion exchange,” *Chemical Engineering Journal and the Biochemical Engineering Journal*, vol. 57, p. 75–89, 1995.
- [200] Z. Zourmand, F. Faridirad, N. Kasiri and T. Mohammadi, “Mass transfer modeling of desalination through an electrodialysis cell,” *Desalination*, vol. 359, p. 41–51, 2015.
- [201] M. Tedesco, H. Hamelers and P. Biesheuvel, “Nernst-Planck transport theory for (reverse) electrodialysis: I. effect of co-ion transport through the membranes,” *Journal of Membrane Science*, vol. 510, p. 370–381, 2016.
- [202] L. Gurreri, G. Battaglia, A. Tamburini, A. Cipollina, G. Micale and M. Ciofalo, “Multiphysical modelling of reverse electrodialysis,” *Desalination*, vol. 423, p. 52–64, 2017.
- [203] M. Fidaleo and M. Moresi, “Optimal strategy to model the electroalytic recovery of a strong electrolyte,” *Journal of Membrane Science*, vol. 260, p. 90–111, 2005.

- [204] R. McGovern, S. Zubair and J. Lienhard V, "The cost effectiveness of electro dialysis for diverse salinity applications," *Desalination*, vol. 348 , p. 57–65, 2014.
- [205] S. Shah, N. Wright, P. Nepsky and A. Winter, "Cost-optimal design of a batch electro dialysis system for domestic desalination of brackish groundwater," *Desalination*, vol. 443 , p. 198–211, 2018.
- [206] M. Tedesco, A. Cipollina, A. Tamburini, I. Bogle and G. Micale, "A simulation tool for analysis and design of reverse electro dialysis using concentrated brines," *Chemical Engineering Research and Design*, vol. 93, p. 441–456, 2015.
- [207] K. Pitzer, "Thermodynamics of electrolytes: I. Theoretical basis and general equations," *Journal of Physics Chemistry*, vol. 77, pp. 268-277, 1973.
- [208] K. Pitzer and G. Mayorga, "Thermodynamics of electrolytes. II Activity and osmotic coefficients for strong electrolytes with one or both ions univalent," *Journal of Physical Chemistry*, vol. 77, pp. 2300-2308, 1973.
- [209] A. Galama, N. Hong and D. Yntema, "Method for determining ion exchange membrane resistance for electro dialysis systems," *Desalination*, vol. 380, pp. 1-11, 2016.
- [210] M. La Cerva, L. Gurreri, A. Cipollina, A. Tamburini, M. Ciofalo and G. Micale, "Modelling and cost analysis of hybrid systems for seawater desalination: Electromembrane pre-treatments for Reverse Osmosis," *Desalination*, vol. 467, pp. 175-195, 2019.



## LIST OF ISI PUBLICATIONS AND INTERNATIONAL CONFERENCES PAPERS AND ABSTRACTS

### Papers published in international journals

- Battaglia G., Gurreri L., Cipollina A., Pirrotta A., Velizarov S., Ciofalo M., Micale G., Fluid-structure interaction and flow redistribution in membrane-bounded channels, 2019, *Energies*, 12, 4259, <https://doi.org/10.3390/en12224259>.
- Battaglia G., Gurreri L., Airò Farulla G., Cipollina A., Pirrotta A., Micale G., Ciofalo M., Pressure-Induced Deformation of Pillar-Type Profiled Membranes and Its Effects on Flow and Mass Transfer, 2019, *Computation*, 7, 32, <https://doi.org/10.3390/computation7020032>.
- Battaglia, G., Gurreri, L., Airò Farulla, G., Cipollina, A., Pirrotta, A., Micale, G., Ciofalo, M., 2019, Membrane Deformation and Its Effects on Flow and Mass Transfer in the Electromembrane Processes, *International Journal of Molecular Sciences*, 20, 1840, <https://doi.org/10.3390/ijms20081840>.
- Battaglia G., Di Matteo A., Micale G., Pirrotta A., 2018, Arbitrarily shaped plates analysis via Line Element-Less Method (LEM), *Thin-Walled Structures*, 133, 235-248, <https://doi.org/10.1016/j.tws.2018.09.018>.
- Battaglia G., Di Matteo A., Micale G., Pirrotta A., 2018, Vibration-based identification of mechanical properties of orthotropic arbitrarily shaped plates: Numerical and experimental assessment, *Composites Part B: Engineering*, 150, 212-225, <https://doi.org/10.1016/j.compositesb.2018.05.029>.
- Gurreri L., Battaglia G., Tamburini A., Cipollina A., Micale G., Ciofalo M., 2017, Multi-physical modelling of reverse electrodialysis, *Desalination*, 423, 52-64, <https://doi.org/10.1016/j.desal.2017.09.006>

### **Papers Uder Preparation**

- Battaglia G., Gurreri L., Cipollina A., Pirrotta A., D. Bogle, Ciofalo M., Micale G., Membrane deformation effects on Electrodialysis Cross-Flow industrial units.
- Battaglia G., Di Matteo A., Micale G., Pirrotta A, Novel identification approach for the mechanical properties of orthotropic rectangular membranes using bulge test technique.
- Kaynardag K., Battaglia G., Ebrahimkhanlou A., Pirrotta A, Salamone S., Identification of Bending Modes of Vibration in Rails by a laser doppler vibrometer on a moving platform.

### **Conference Papers and Abstracts**

- Battaglia G., Gurreri L., Cipollina A., Pirrotta A., Micale G., Tamburini A., Ciofalo M., Analisi numerica degli effetti della deformazione di membrane a scambio ionico sulla distribuzione dei fluidi in canali di Elettrodialisi. *GRICU 2019*, 30 June-3 July 2019, Palermo, Italy.
- Battaglia G., Gurreri L., Tamburini A., Cipollina A., Ciofalo M., Micale G.; Integrated modelling of membrane deformation, fluid dynamics and mass transfer in electromembrane processes. *13<sup>th</sup> SDEWES Conference*, 30 September-4 October 2018, Palermo, Italy.
- Battaglia G., Gurreri L., Tamburini A., Cipollina A., Ciofalo M., Micale G.; Fluid-structure interaction in electromembrane processes: modelling of membrane deformation, fluid dynamics and mass transfer. *Desalination for the Environment: Clean Water and Energy Science, Research, Innovation, Industry, Business*, 3-6 September 2018, Athens, Greece.
- Battaglia G., Ciofalo M., Cipollina A., Di Matteo A., Gurreri L., Pirrotta A. Tamburini A., Micale G.; Mechanical-fluid dynamics coupled model for profiled Ion Exchange Membranes design. *Euromembrane 2018*, 9-13 July 2018, Valencia, Spain.
- Battaglia G., Di Matteo A., Micale G., Pirrotta A.; LEM method for plates of general shape. *EMI 2017*. 3-7 June 2017, San Diego, USA.

- Battaglia G., Di Matteo A., Micale G., Pirrotta A.; Analysis of arbitrarily shaped plates via meshfree LEM solution. *AIMETA17*, 4-7 September 2017, Salerno, Italy.
- Battaglia G., Di Matteo A., Pirrotta A., Micale G.; Dynamic response of equivalent orthotropic plate model for stiffened plate: numerical-experimental assessment. *EURODYN*, 10-13 September 2017, Rome, Italy.
- Battaglia G., Cipollina A., Di Matteo A., Gurreri L., Micale G., Pirrotta A., Tamburini A.; Ion Exchange membrane deformation and its relevance in Reverse ElectroDialysis. *EUROMED 2017*, 9-12 May 2017, Tel Aviv, Israel.
- Gurreri L., Battaglia G., Cipollina A., Tamburini A., Micale G., Ciofalo M., Investigation of Reverse Electrodialysis Units by Multiphysical Modelling. *Comsol Conference 2016 Munich*, 12-14 October 2016, Munich, Germany.

## **ACKNOWLEDGEMENTS**

In these few lines, I wish to express my regards to all the people, who have followed me through this adventure.

First, I would like to express my deepest gratitude to my supervisors: Prof. Antonina Pirrotta and Prof. Giorgio Micale. They have believed in me, since the beginning of this experience, and guided me through the beautiful and the bad times that I have faced.

My sincere and deep gratitude goes to Prof. Michele Ciofalo. I want to thank him for all the days spent together discussing problems and ordinary daily life matters. He infused me the love for research and knowledge.

I wish to express special thanks to Prof. Andrea Cipollina and Dott. Alessandro Tamburini, who have always pushed me and taught me to never stop even at the highest points.

I am very grateful to Prof. Salvatore Salamone, who welcomed me at the University of Texas at Austin, giving me the opportunity to live one of the biggest experiences of my life. I will never forget my time in the U.S.

I am very grateful to Prof. David Bogle, who gave me the opportunity of studying at the University of College London. I revalued the beautifulness, which characterizes London.

Special thanks go to Dott. Luigi Gurreri. He has always listened to me and given me advice and suggestions.

My warmest gratitude goes to Dott. Alberto Di Matteo, for guiding me through subjects, which I have never heard before in my life. He demonstrated me his love for research, teaching me carefully and patiently.

I wish to thank all the colleagues of the REvivED project, and especially those who welcomed me at the Fujifilm Laboratories.

I want to show grateful feeling to all my colleagues of the chemical engineering department (Mimma, Daniele, Fabrizio, MariaGiorgia, Ninni, Serena, Nunzio, Carmelo, Salvatore, Francesco, Maurizio, Andrea, Alessandro, Javier), with who I have spent lunchtime many times.

With my all gratitude, I want to thank the guys of the Structural Dynamics Laboratory: Chiara, Salvatore, Iain and Andrea (especially for having printed the plates). I will always remember the days spent together.

I wish to express my deepest gratitude to my Austin brotherhood: Stylianos, Daniele and Korkut. I have unforgettable memories of the time in the U.S. thanks to them.

My sincere gratitude goes to my closest friends: Carlo, Antonio, Salvatore, Andrea, Michele. They have always been ready to listen to me and help me. I know, they will always be with me. I want to thank also Salvatore and Giacoma who gave me the honour of being one of their best men. I will never forget those days and that emotion.

A special thanks goes to my always present chemical engineering group: Martina, Luigi and Giuseppe. Despite it has already been four years since we graduated, we are still friends like we were.

Last but not the least, my sincere thanks go to my family (uncles, aunts and cousins). My mother and my father, who have always supported me and taught me how to live a fulfilled and fruitful life. I want to thank my sister Concetta, her husband, Gianluca, and my two little, beautiful nieces Giulia and Elena. They remind me to be always a child surprised by life.

I want to thank Stefano and Francesca Giglio, for considering me as a brother. Giovanni and Mariella Giglio, the father and mother of my sweet girlfriend, to have given birth to her.

I want to end these lines, with the most important and deepest thank to my girlfriend Deborah Giglio, for having made my days beautiful and colourful, despite all the difficulties that I have faced during this experience. I will always thank you for all the love you gave to me.